Universitat
de les Illes Balears

DOCTORAL THESIS

2025

DECODING GRAVITATIONAL WAVE SIGNALS FROM COMPACT BINARY COALESCENCES: TOWARDS NEXT-GENERATION DETECTORS

Maria de Lluc Planas Llompart

Universitat
de les Illes Balears

DOCTORAL THESIS

2025

Doctoral Programme in Physics

DECODING GRAVITATIONAL WAVE SIGNALS FROM COMPACT BINARY COALESCENCES: TOWARDS NEXT-GENERATION DETECTORS

Maria de Lluc Planas Llompart

Thesis Supervisor: Dr. Sascha Husa.

Thesis Supervisor: Dr. Antoni Ramos Buades.

Thesis tutor: Dr. Carlos Palenzuela.

Doctor by the Universitat de les Illes Balears

Dr. Sascha Husa, of the Institute of Space Sciences and the University of the Balearic Islands,

I DECLARE:

That the thesis titled *"Decoding gravitational wave signals from compact binary coalescences: towards next-generation detectors"*, submitted by **Maria de Lluc Planas Llompart** in pursuit of a Doctoral Degree, has been completed under the joint supervision of Antoni Ramos Buades and myself, and fulfills the requirements for the distinction of an International Doctorate.

For all intents and purposes, I hereby sign this document.

Signature:

Dr. Antoni Ramos Buades, of the University of the Balearic Islands

I DECLARE:

That the thesis titled *"Decoding gravitational wave signals from compact binary coalescences: towards next-generation detectors"*, submitted by **Maria de Lluc Planas Llompart** in pursuit of a Doctoral Degree, has been completed under the joint supervision of Sascha Husa and myself, and fulfills the requirements for the distinction of an International Doctorate.

For all intents and purposes, I hereby sign this document.

Signature:

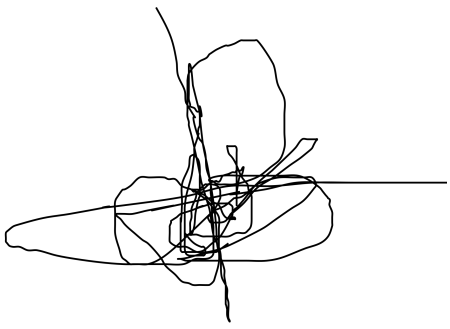

Palma de Mallorca, April 30, 2025

Publications derived from the thesis

- Maria de Lluc Planas, Joan Llobera-Querol, and Sascha Husa. "*Building a bridge between comparable and extreme mass ratio black hole binaries: A single spin precessing model for the final state*", **Phys. Rev. D 109.12 (2024), p. 124028**. DOI: 10.1103/PhysRevD.109.124028, arXiv: 2401.13342 [gr-qc].

- Maria de Lluc Planas, Antoni Ramos-Buades, Cecilio García-Quirós, Héctor Estellés, Sascha Husa, and Maria Haney. "*Time-domain phenomenological multipolar waveforms for aligned-spin binary black holes in elliptical orbits*", arXiv: arXiv:2503.13062[gr-qc] (Submitted to Physical Review D)

- Maria de Lluc Planas, Antoni Ramos-Buades, Cecilio García-Quirós, Héctor Estellés, Sascha Husa, and Maria Haney. "*Eccentric or circular? A reanalysis of gravitational wave events for orbital eccentricity signatures*", arXiv: arXiv:2504.15833[gr-qc] (Submitted to Physical Review D)

- Maria de Lluc Planas, Sascha Husa, Antoni Ramos-Buades, Jorge Valencia. "*First eccentric inspiral-merger-ringdown analysis of neutron star-black hole mergers*", arXiv: arXiv:2506.01760[astro-ph] (Submitted to The Astrophysical Journal Letters)

Glossary of abbreviations

- **ADM** : Arnowitt-Deser-Misner
- **AS** : Aligned-Spin
- **BSSN** : Baumgarte-Shapiro-Shibata-Nakamura
- **BBH** : Binary Black Hole
- **BH** : Black Hole
- **BHPT** : Black Hole Perturbation Theory
- **BNS** : Binary Neutron Star
- **CBC** : Compact Binary Coalescence
- **CE** : Cosmic Explorer
- **CW** : Continuous Wave
- **EFE** : Einstein's Field Equations
- **EMRI** : Extreme Mass Ratio Inspiral
- **EOB** : Effective-One-Body
- **ET** : Einstein Telescope
- **ETK** : Einstein Toolkit
- **FFT** : Fast Fourier Transform
- **GHG** : Generalized Harmonic Gauge
- **GSF** : Gravitational Self Force
- **GR** : General Relativity
- **GW** : Gravitational Wave
- **HM** : Higher Mode

- **IMBH** : Intermediate-Mass Black Hole
- **IMR** : Inspiral-Merger-Ringdown
- **ISCO** : Innermost Stable Circular Orbit
- **ISSO** : Innermost Stable Spherical Orbit
- **KAGRA** : Kamioka Gravitational Wave Detector
- **LIGO** : Laser Interferometer Gravitational-Wave Observatory
- **LISA** : Laser Interferometer Space Antenna
- **LVK** : LIGO-Virgo-KAGRA
- **MHG** : Modified Harmonic Gauge
- **MCMC** : Markov Chain Monte Carlo
- **NR** : Numerical Relativity
- **NSBH** : Neutron Star-Black Hole binary
- **PBH** : Primordial Black Hole
- **PE** : Parameter Estimation
- **PISNe** : Pair-Instability Supernovae
- **PN** : Post-Newtonian
- **PSD** : Power Spectral Density
- **PTA** : Pulsar Timing Array
- **QC** : Quasi-Circular
- **QK** : Quasi-Keplerian
- **QNM** : Quasinormal Mode
- **RR** : Radiation Reaction
- **ROM** : Reduced-Order Model
- **SBH** : Supermassive Black Hole
- **SMBH** : Stellar-Mass Black Hole
- **SMBBH** : Supermassive Binary Black Hole
- **SGWB** : Stochastic Gravitational Wave Background
- **SNR** : Signal-to-Noise Ratio
- **SO** : Spin-Orbit

- **SS** : Spin-Spin
- **SWSH** : Spin-Weighted Spherical Harmonic
- **SXS** : Simulating eXtreme Spacetimes
- **SPA** : Stationary Phase Approximation
- **SUA** : Shifted Uniform Asymptotics
- **TOV** : Tolman–Oppenheimer–Volkoff
- **TT** : Transverse-Traceless
- **3G** : Third Generation

Abstract (English)

The detection of gravitational waves (GWs) has opened a new era in astrophysics. The first three observing runs of the Advanced LIGO and Advanced Virgo detectors (O1, O2, and O3) have led to the detection of over 90 GW events [1–4], all originating from compact object binaries. While the majority of these events have been identified as binary black hole (BBH) mergers, several binary neutron star (BNS) and neutron star–black hole (NSBH) mergers have also been observed [5–9]. The final part of this thesis coincides with the ongoing fourth observing run (O4), which has already achieved a significantly higher detection rate, surpassing 200 detections halfway through the run [10]. As detector sensitivities continue to improve, future observations by the LIGO–Virgo–KAGRA (LVK) Collaboration, along with upcoming facilities such as the Einstein Telescope (ET) [11, 12], Cosmic Explorer [13], and the LISA space mission [14–17], are expected to uncover a broader range of source properties. These observations will provide crucial insights into the strong-field regime of gravity, the population and evolution of compact objects, galaxy formation, cosmology, and fundamental tests of general relativity [15].

Accurate and computationally efficient waveform models are essential for extracting the physical parameters of GW signals. As detector sensitivities improve, the demand for more accurate and versatile waveform templates becomes increasingly critical, see e.g. reviews on the challenges for ET [11] and LISA [17]. This thesis contributes to the advancement of waveform modeling in three directions that are essential for improving model accuracy and extending coverage across the BBH parameter space. Although current inspiral-merger-ringdown (IMR) waveform models can accurately describe BBHs on quasi-circular (QC) orbits with aligned spins, several key regions of the parameter space remain poorly explored. These include binaries with generic spin orientations (which lead to orbital precession), systems with high or extreme mass ratios, and binaries on eccentric orbits – all of which are astrophysically motivated and relevant for upcoming GW observatories. This thesis aims to address these limitations and support the development of physically robust, generic BBH waveform models that will be essential for GW data analysis with future third-generation ground-based detectors and the LISA space mission.

First, we present a model for predicting the remnant properties (final mass and spin) of spin-precessing BBHs in QC orbits across a wide range of mass ratios [18]. By combining insights from numerical relativity and black hole perturbation theory, this model helps bridge the gap between the extreme and comparable mass ratio regimes. This work lays groundwork for the development of waveform models that are applicable across the full mass-ratio spectrum, which is particularly relevant for LISA, as it will be sensitive to high-

and extreme-mass-ratio inspirals in the millihertz frequency band.

Second, we introduce IMRPhenomTEHM [19], a new IMR phenomenological waveform model for aligned-spin, eccentric BBHs. This model incorporates post-Newtonian corrections atop the QC baseline IMRPhenomTHM and significantly reduces computational cost compared to other state-of-the-art eccentric models [20, 21]. Its computational efficiency makes it well-suited for large-scale Bayesian inference studies and a strong candidate for standard parameter estimation pipelines in current and future detector networks.

Motivated by the performance and accuracy of the model, in the last part of the thesis we apply IMRPhenomTEHM to a reanalysis of selected GW events, investigating the detectability of eccentricity and assessing the robustness of current QC assumptions in GW parameter estimation. Our BBH parameter estimation studies [22] identify evidence for eccentricity in two GW events from O3 [4], GW200129 and GW200208_22, and reveal that the high-mass events GW190701 and GW190929 exhibit potentially eccentric features. Due to the proven efficiency of IMRPhenomTEHM, we reanalyze three NSBH events from GWTC-3 [8, 9], finding support for eccentricity in GW200105 and quasi-circular consistency for GW200115 and GW230529, while also highlighting the impact of systematic uncertainties related to signal duration, waveform model degeneracies, and data quality [23]. These results underscore the importance of including eccentric waveform models in future analyses, particularly as the BBH population becomes increasingly diverse with upcoming observations. Accounting for these effects is crucial to mitigate potential biases in parameter estimation and to maximize the scientific output of next-generation GW detectors.

Abstract (Spanish)

La detección de ondas gravitacionales (OGs) ha inaugurado una nueva era en la astrofísica. Los tres primeros periodos de observación de los detectores LIGO y Virgo (O1, O2 y O3) han dado lugar a la detección de más de 90 eventos de OGs [1–4], todos ellos originados por sistemas binarios de objetos compactos. Aunque la mayoría de estos eventos han sido identificados como fusiones de agujeros negros binarios (BBH), también se han observado varias fusiones de estrellas de neutrones binarias (BNS) y sistemas estrella de neutrones–agujero negro (NSBH)[5–9]. La parte final de esta tesis coincide con el cuarto periodo de observación (O4), actualmente en curso, que ya ha alcanzado una tasa de detección significativamente mayor, superando las 200 detecciones a mitad de la campaña [10]. A medida que la sensibilidad de los detectores continúa mejorando, se espera que futuras observaciones por parte de la colaboración LIGO–Virgo–KAGRA (LVK), junto con instalaciones en desarrollo como el Einstein Telescope (ET) [11, 12], Cosmic Explorer [13] y la misión espacial LISA [14–17], revelen una gama más amplia de propiedades de las fuentes de OGs. Estas observaciones ofrecerán información crucial sobre el régimen de campos fuertes de la gravedad, la población y evolución de objetos compactos, la formación de galaxias, la cosmología y permitirán realizar pruebas fundamentales de la relatividad general [15].

Los modelos de forma de onda precisos y computacionalmente eficientes son esenciales para la extracción de los parámetros físicos de señales de OG. A medida que la sensibilidad de los detectores mejora, la necesidad de plantillas de forma de onda más precisas y versátiles se vuelve cada vez más crítica; véanse, por ejemplo, las revisiones sobre los desafíos para ET [11] y LISA [17]. Esta tesis contribuye al avance de la modelización de formas de onda en tres direcciones clave, con el objetivo de mejorar la precisión de los modelos y ampliar la cobertura dentro del espacio de parámetros de los sistemas BBH. Aunque los modelos actuales de tipo inspiral-merger-ringdown (IMR) describen con precisión fusiones de BBHs en órbitas cuasi-circulares con espines alineados, existen aún regiones importantes del espacio de parámetros poco exploradas. Estas incluyen sistemas con orientaciones de espín genéricas (que inducen precesión orbital), sistemas con razones de masa altas o extremas y sistemas con órbitas excéntricas, todos ellos motivados desde el punto de vista astrofísico y relevantes para los detectores de OGs de próxima generación. Esta tesis busca abordar estas limitaciones y contribuir al desarrollo de modelos de forma de onda para BBHs genéricos, físicamente robustos, que serán fundamentales para el análisis de datos de OGs con los futuros detectores terrestres de tercera generación y la misión espacial LISA.

En primer lugar, presentamos un modelo para predecir las propiedades del remanente (masa y espín finales) de sistemas BBH en órbitas cuasi-circulares con precesión de espines, abarcando el completo rango de razones de masa [18]. Combinando resultados de relatividad numérica y teoría de perturbaciones de agujeros negros, este modelo ayuda a conectar el régimen de masas comparables con el de razón de masa extrema. Este trabajo sienta las bases para el desarrollo de modelos de forma de onda aplicables a todo el espectro de razones de masa, lo cual es especialmente relevante para LISA, dado que será sensible a inspirales con razones de masa altas o extremas en la banda de frecuencia del milihertz.

En segundo lugar, introducimos IMRPhenomTEHM [19], un nuevo modelo fenomenológico IMR para BBHs con espines alineados y en órbitas excéntricas. Este modelo incorpora correcciones post-newtonianas sobre la base del modelo cuasi-circular IMRPhenomTHM y reduce significativamente el coste computacional en comparación con otros modelos excéntricos de última generación [20, 21]. Su eficiencia lo hace especialmente adecuado para estudios bayesianos a gran escala y un candidato sólido para ser integrado en los análisis estándar de estimación de parámetros, tanto en redes actuales como futuras de detectores.

Motivados por el rendimiento y la precisión del modelo, en la última parte de esta tesis aplicamos IMRPhenomTEHM a un reanálisis de eventos seleccionados de OGs, investigando la detectabilidad de la excentricidad y evaluando la robustez de las suposiciones actuales de cuasi-circularidad en la estimación de parámetros. Nuestros estudios de estimación de parámetros para sistemas BBH [22] identifican evidencia de excentricidad en dos eventos de la tercera campaña de observación [4], GW200129 y GW200208_22 y revelan que los eventos de alta masa GW190701 y GW190929 podrían presentar características excéntricas. Gracias a la eficiencia demostrada de IMRPhenomTEHM, reanalizamos tres eventos NSBH del catálogo GWTC-3 [8, 9], encontrando soporte para excentricidad en GW200105 y una evolución cuasi-circular compatible en GW200115 y GW230529, al tiempo que destacamos el impacto de incertidumbres sistemáticas relacionadas con la duración de la señal, las degeneraciones del modelo de onda y la calidad de los datos [23]. Estos resultados subrayan la importancia de incluir modelos de ondas excéntricas en análisis futuros, especialmente a medida que la población de BBH se vuelve cada vez más diversa con las nuevas observaciones. Tener en cuenta estos efectos es crucial para mitigar posibles sesgos en la estimación de parámetros y para maximizar el rendimiento científico de los detectores de OGs de próxima generación.

Abstract (Catalan)

La detecció d'ones gravitacionals (OGs) ha obert una nova era en l'astrofísica. Els tres primers períodes d'observació dels detectors avançats LIGO i Virgo (O1, O2 i O3) han conduït a la detecció de més de 90 esdeveniments d'OGs [1–4], tots ells provinents de sistemes binaris d'objectes compactes. Tot i que la majoria d'aquests esdeveniments han estat identificats com a fusions de forats negres binaris (BBH), també s'han observat diverses fusions de binàries d'estels de neutrons (BNS) i sistemes estel de neutrons–forat negre (NSBH) [5–9]. La part final d'aquesta tesi coincideix amb el quart període d'observació (O4), actualment en curs, que ja ha assolit una taxa de detecció significativament més alta, superant les 200 deteccions a meitat de la campanya [10]. A mesura que la sensibilitat dels detectors continua millorant, s'espera que les futures observacions per part de la col · laboració LIGO–Virgo–KAGRA (LVK), juntament amb instal · lacions en desenvolupament com el Einstein Telescope (ET) [11, 12], el Cosmic Explorer [13] i la missió espacial LISA [14–17], revelin una gamma més àmplia de propietats de les fonts. Aquestes observacions oferiran informació clau sobre el règim de camps gravitatoris intensos, la població i evolució d'objectes compactes, la formació de galàxies, la cosmologia i permetran proves fonamentals de la relativitat general [15].

Els models de formes d'ona precisos i eficients computacionalment són essencials per extreure els paràmetres físics dels senyals d'OG. A mesura que la sensibilitat dels detectors millora, la necessitat de plantilles de forma d'ona més precises i versàtils esdevé cada cop més crítica; vegeu, per exemple, les revisions sobre els reptes per a l'ET [11] i per a LISA [17]. Aquesta tesi contribueix a l'avenç en la modelització de formes d'ona en tres direccions essencials per millorar la precisió dels models i ampliar-ne la cobertura dins de l'espai de paràmetres dels sistemes BBH. Tot i que els models actuals que inclouen inspiral-merger-ringdown (IMR) descriuen amb precisió BBHs en òrbites quasi-circulars (QC) amb espins alineats, hi ha regions clau de l'espai de paràmetres que encara són poc explorades. Aquestes inclouen sistemes amb orientacions d'espí genèriques (que indueixen precessió orbital), sistemes amb raons de massa altes o extremes i sistemes amb òrbites excèntriques, tots ells motivats astrofísicament i rellevants per als observatoris d'OGs de nova generació. Aquesta tesi té com a objectiu abordar aquestes limitacions i donar suport al desenvolupament de models de forma d'ona per a BBHs genèrics, físicament robustos, que seran essencials per a l'anàlisi de dades d'OGs amb els futurs detectors terrestres de tercera generació i la missió espacial LISA.

En primer lloc, presentem un model per predir les propietats del romanent (massa i espí finals) de sistemes BBH en òrbites QC amb precessió d'espins, cobrint el complet

ventall de raons de massa [18]. Combinant coneixements de relativitat numèrica i teoria de pertorbacions de forats negres, aquest model ajuda a connectar els règims de massa comparable i de raó de massa extrema. Aquest treball estableix les bases per al desenvolupament de models de forma d'ona aplicables a tot l'espectre de raons de massa, fet especialment rellevant per a LISA, que serà sensible a inspirals amb raons de massa altes o extremes en la banda de freqüència del mil · lihertz.

En segon lloc, introduïm IMRPhenomTEHM [19], un nou model fenomenològic IMR per a BBHs amb espins alineats i òrbites excèntriques. Aquest model incorpora correccions post-newtonianes sobre la base QC del model IMRPhenomTHM i redueix significativament el cost computacional en comparació amb altres models excèntrics d'última generació [20, 21]. La seva eficiència computacional el fa especialment adequat per a estudis bayesians a gran escala i un candidat sòlid per ser utilitzat en canals estàndard d'estimació de paràmetres en xarxes de detectors actuals i futures.

Motivats pel rendiment i la precisió del model, a la darrera part d'aquesta tesi apliquem IMRPhenomTEHM a una reanàlisi d'esdeveniments seleccionats d'OGs, investigant la detectabilitat de l'excentricitat i avaluant la robustesa de les suposicions actuals de quasi-circularitat en l'estimació de paràmetres. Els nostres estudis d'estimació de paràmetres per sistemes BBH [22] identifiquen evidència d'excentricitat en dos esdeveniments de l'O3 [4], GW200129 i GW200208_22 i revelen que els esdeveniments de gran massa GW190701 i GW190929 podrien presentar característiques excèntriques. Donada l'eficiència demostrada de IMRPhenomTEHM, reanalitzem tres esdeveniments NSBH del catàleg GWTC-3 [8, 9], trobant suport per a excentricitat a GW200105 i una consistència amb una evolució quasi-circular a GW200115 i GW230529, tot destacant també l'impacte d'incerteses sistemàtiques relacionades amb la durada del senyal, les degeneracions del model de forma d'ona i la qualitat de les dades [23]. Aquests resultats posen de manifest la importància d'incloure models d'ones excèntriques en futures anàlisis, especialment a mesura que la població de BBH esdevé més diversa amb les noves observacions. Tenir en compte aquests efectes és clau per evitar possibles biaixos en l'estimació de paràmetres i per maximitzar el rendiment científic dels detectors de pròxima generació.

Acknowledgements

Encara no em puc creure que hagi arribat el moment d'escriure els agraïments de la tesi. Han estat quatre anys de molts altibaixos, i per això encara em costa més creure-m'ho. Però quina sort ser aquí ara i tenir tanta gent meravellosa amb qui compartir-ho, perquè aquesta tesi no hagués estat possible sense el suport de moltíssimes persones.

First, I would like to thank my all-time science supervisor, Sascha. It was thanks to you that I decided to start this journey, and I would not be here today without your support and trust from the very beginning. Although it took me some time to understand how science really works, I am now prouder of myself than ever – loving my thesis and everything it represents. Thank you for guiding me through this long journey. Toni, ara ja oficialment supervisor també, aquesta tesi és gràcies a tu. Gràcies per aguantar la meva part més humana aquests darrers dos anys, tant plors com xafardejos. M'has fet estimar i entendre la ciència com mai, a la vegada de fer-me entendre què és el que realment importa en el dia a dia. I tal com vaig prometre un dia, aquí tens tot el teu paràgraf d'agraïments, encara que sé que res que pugui fer o dir no seria mai suficient.

Second, thanks to all the UIB group. Gràcies Alicia per acompanyar-nos en tot el camí de la burocràcia espanyola; thanks to all the postdocs for so many pastas, drinks, and nights; gràcies als predocs per escoltar-me i aguantar-me tots aquests anys, perquè (pot ser que) (a pics) sigui un poc pesada. Aquí hauré de mencionar a en Felip, per estar allà sempre a primera hora disposat a escoltar-me (volent o no). Altres també mereixen menció especial: Jorge, hi ha poca gent tan bona i competent en el món, no tenc cap dubte que arribaràs allà on vulguis (ara que me'n vaig pots quedar-te els meus cascos); Maria, compartir tots aquests anys amb tu ha estat un plaer, i estic segura que triïs el que triïs la vida et retornarà totes les coses bones que fas pels altres. Rafel, gràcies per estar sempre a un cafè d'escoltar-me plorar o riure, per queixar-me o contar-te qualsevol tonteria, i per ser un suport fonamental en lo bo i lo dolent d'aquests anys de molta ciència i vida. Maite, no saps quant t'he enyorat aquests darrers dos anys, però d'alguna manera sempre t'he sentit allà. Crec que cap persona ha confiat tant amb jo des del principi, i no puc sentir-me més agraïda. Finalment, Joan (ja sense cognoms), no sé si mai podria haver acabat sense tu. D'alguna manera t'has convertit en un dels meus millors amics (per desgràcia teva). Ets una persona comprensiva, sincera i intel · ligent tant emocional com científicament. Si he d'agrair a la vida alguna cosa d'aquests darrers dos anys ets tu. Estic segura que la vida et retornarà totes les coses bones que desprens, i encara que ara tendràs un petit descans de jo, no pensis que t'has alliberat... et queda molta Lluc per sempre.

Now it is time to thank Amsterdam. I found in Amsterdam my home away from Mallorca – which used to be my favorite and only place on Earth (something I think many Dutch people would agree with). Maybe I realized I was not exactly who I thought I was, or maybe I simply changed. Either way, I am incredibly happy and proud that things turned out this way. But Amsterdam only felt like home because of the people who made it feel that way, and I still wonder what I did to deserve to be so lucky. Starting my round of thanks with Maria – thank you for believing in me and giving me the opportunity to visit such an amazing group and institute. I am honored to have learned from and worked with you, and I truly hope we will have more opportunities to collaborate in the future. Thanks also to the entire gravitational wave group at Nikhef for adopting me. A special mention to my data analysis team – Suzanne and Luca – for being wonderful office mates and, I am happy to say, friends now too. And to Stefano, for being the brightest person on Earth. Nikhef had much more to offer than gravitational waves, and surprised me with the coolest people ever doing extremely nerdy things such as particle physics and dark matter. I do not think I could name everyone who made this time so special, but I will mention a few. Andreas (Spanish and Italian), as I said several times before, I truly wish I were Andrea too. Thank you for making me feel at home and for letting me know that I look about as Spanish as it gets. Carlo, thank you for bringing out my most competitive side. You were always ready for anything, and somehow you brought that side out in me too. Petja, Evridiki – I am writing this and I cannot find enough words to thank you. I found home in you: comfort, love, and friendship. Thanks to you, I fell in love with this place from the very beginning, and you brought out a new side of me I did not even know existed – one that now carries your names. Finalment, Amsterdam no hagués estat el mateix sense tu, Eli. A pics em deman què feia sense tu abans. Has passat a ser família per jo, casa, un lloc segur on estar. I per molt enfora que estem, per temps que passi, sé que serà així per sempre.

Clarament aquests darrers dos anys no són els que em determinen, i sóc conscient que tota la meva vida a Mallorca m'ha fet arribar on sóc avui. Gràcies a tota la família Darder Duran per haver-me cuidat com una més durant molts d'anys; gràcies a tots els meus amics de Cala Blava (Luis i Toni inclosos) per haver-me acompanyat en tot el camí sense entendre gaire bé el que significava, amb menció especial a n'Alejandro, per haver estat allà sempre que t'he necessitat. Gràcies al Crossfit per ensenyar-me que puc més del que crec, que pot ser sí m'agrada sofrir un poquet, i donar-me una família inesperada aquests darrers dos anys. Aquí he de destacar a dues persones: Lluïsa, gràcies per passar de compi a amiga, i per tots els viatges a Berlin que t'esperen aquests pròxims anys; y Fran, gracias por confiar en mí, por ayudarme a ver las cosas bonitas que tiene la vida, por hacerme competir por primera (y quizás última) vez y por ser tan maravillosa persona. Pareix mentida agrair a l'escola en una tesi doctoral, però resulta que Sant Francesc em va donar un grup d'amics excepcional que segueix allà, molts d'ells des dels tres anys. Encara que la vida ens ha duit per molts camins distints, pareix que tots ens retornen allà mateix. Gràcies per seguir sent casa després de tant de temps, i per sempre estar tan orgullosos de jo. També agreesc els anys universitaris, perquè encara que la vida també ens ha duit a tots per camins diferents, compartim tanta història que sembla que no ha passat temps quan ens veiem. I després hi ha els que cada any ens veiem més, i no puc tenir més sort d'haver-vos trobat. Juan, gracias por estar, por ser y por acompañarme en todos los caminos elegidos. Carles, tens una forma de veure la vida que sols transmet ganes de viure-la, i molts cops m'ho has donat sense voler ni intentar-ho. Antònia, sempre he pensat que estàvem predestinades a ser amigues. Has estat indispensable per jo cada dia de la

carrera i tots els anys després, que ens han permés fer un doctorat a cada una... no saps quant t'admir! No podia acabar aquests agraïments sense ses meves nines. Adela, gracias por tu actitud positiva y contagiarla siempre a todo el mundo; Bel, gràcies per haver estat allà des dels tres anyets; Teresa, gràcies per sempre saber com treure un somriure a tothom; Irina, gràcies per aparèixer i quedar-te; Elena, gràcies per acompanyar-me tota la vida; Maria, gracias por tu corazón enorme y por ser tan buena amiga; i finalment Aina, gràcies per escoltar-me, cuidar-me, ajudar-me en tot i sobretot sempre estar allà, no crec que hagués pogut sense tu.

Finalment, agrair-ho tot a la meva família, per ser tot allò que tothom desitjaria. Eladio, gracias por enseñarme que hay otras formas de entender la vida que no implican preocupación continua. Papi, mami, gràcies per ser el meu referent en tot, per sempre haver confiat en jo i desitjar-me el millor. Gràcies per entendre'm sense dir una paraula, per acompanyar-me en totes les meves decisions i sobretot ensenyar-me què és estimar (bé). No hi haurà dia que no vos enyori.

La meva etapa a casa ha acabat, i una nova vida a Berlin comença. Però no me'n vaig tota sola, me'n vaig amb el cor ple de records de tots aquests anys aquí. Gràcies a tots per estar, aquesta tesi també és vostra.

Contents

CHAPTER 1

Preface

Gravitational waves (GWs) are ripples in spacetime that propagate outward from their sources as transverse waves, traveling at the speed of light. To emit GWs, a source must exhibit a significant, time-varying quadrupole moment, which induces perturbations in the spacetime metric that carry energy and information about the underlying astrophysical process. This requirement implies that static objects or those undergoing purely radial motion do not produce GWs. Fortunately, the Universe is filled with dynamic and energetic phenomena involving rapid accelerations, many of which generate GWs detectable by our current instruments. Among these, compact binary coalescences (CBCs) are among the loudest and best understood GW sources. Indeed, all detections reported so far by the LIGO, Virgo, and KAGRA (LVK) Collaboration fall into this category [1–4], with the majority corresponding to binary black hole (BBH) mergers – the main focus of this thesis. However, CBCs also include binary neutron star (BNS) systems – first observed on August 17, 2017 [5] – as well as neutron star–black hole (NSBH) binaries. The first NSBH merger was detected on January 5, 2020, followed by a second event just ten days later [8]. More recently, an additional NSBH detection was reported during the ongoing fourth observing run (O4), GW230529 [9].

The success of GW data analysis relies on our ability to construct waveform models that accurately capture the full complexity of signals across the parameter space of potential sources. These models serve as templates that are cross-correlated with detector data to infer the properties of the source with the methods of Bayesian inference and matched filtering. Because waveform models are evaluated of the order of millions of times during a typical analysis, they must be both computationally efficient and valid across the entire relevant parameter space to ensure accurate signal characterization. For generic BBHs, the intrinsic parameter space is defined by nine parameters: the mass ratio, the magnitudes and orientations of the individual spins, and two parameters characterizing the ellipticity of the orbit. While many waveform models have achieved remarkable accuracy in the quasi-circular (QC), aligned-spin, and near-equal-mass regimes, a comprehensive understanding of signal morphology across this high-dimensional parameter space remains incomplete. This thesis tackles three critical and interconnected challenges within this framework: (i) bridging the gap between the extreme and comparable mass ratio regimes for the remnant properties of QC spin-precessing BBHs; (ii) incorporating orbital eccentricity into a time-domain waveform model for aligned-spin BBHs; and (iii) reanalyzing publicly available LVK data using the developed eccentric model to search for signs of eccentricity, while simultaneously evaluating the impact of waveform systematics arising from missing physical effects in current models.

It is well established that insights from the extreme mass ratio (EMR) limit – particularly through the gravitational self force expansion – can inform modeling even in the comparable-mass regime [24–27]. This has fueled hope that such information can reduce the number of numerical relativity (NR) simulations required to calibrate waveform models across the mass-ratio dimension. To date, efforts to bridge the EMR and comparable-mass regimes have primarily focused on non-spinning binaries [28–30], the use of EMR waveforms to calibrate QC aligned-spin models [31–34], or on modeling final-state properties (mass and spin) in the QC case [18, 27, 35]. When the black hole spins are misaligned with respect to the orbital angular momentum, spin-orbit and spin-spin couplings induce precession of the orbital plane and of the spins themselves, increasing the dimensionality of the parameter space from three to seven (excluding orbital eccentricity). Following the strategies used in the aligned-spin case, the first part of this thesis presents a model for the remnant properties – specifically, the final mass and spin – of spin-precessing BBHs. These quantities are crucial for accurately describing the ringdown phase and for constructing complete inspiral-merger-ringdown (IMR) waveform models. This work represents a step toward unifying NR results with predictions from the EMR limit. Such an approach has the potential to significantly reduce the reliance on computationally expensive NR simulations at high mass ratios, particularly for precessing systems.

The second part of this thesis focuses on aligned-spin eccentric BBHs. Similar to the challenges encountered when modeling precessing systems, the development and validation of eccentric waveform models are hindered by the limited availability of publicly accessible NR simulations for eccentric binaries. Nonetheless, significant progress has recently been made, aided by the fact that eccentricity tends to decay rapidly [36]. As a result, BBHs are generally expected to have circularized by the time they enter the sensitivity band of ground-based detectors. Eccentric spinning binaries are often modeled using the post-Newtonian (PN) formalism [37–39], with the quasi-Keplerian parameterization commonly employed to describe their orbital motion [40–42]. A common assumption in these models is that the system circularizes before merger, allowing standard QC waveform models to be used for the late inspiral, merger, and ringdown. This assumption underlies most existing eccentric waveform models [19–21, 43, 44], which typically describe planar (non-precessing) orbits and employ a QC merger-ringdown phase calibrated to NR. Currently, only one surrogate model avoids this approximation by directly incorporating NR information, although it remains very limited in parameter space coverage [45]. Future observations by the LVK and upcoming ground-based detectors such as the ET [11, 12] and CE [13], as well as space missions like LISA [15], will significantly expand our observational capabilities. While the next-generation ground-based detectors will cover a broader frequency range and detect a larger number of events, LISA will open an entirely new low-frequency window in the millihertz band, enabling the detection of sources such as extreme-mass-ratio inspirals and the early inspiral phase of stellar-mass binaries. These advances will allow the detection of systems with non-negligible eccentricity as they enter the detector's sensitive band. As a result, developing robust methods for characterizing the orbital dynamics of eccentric binaries will be increasingly important for probing the formation and evolution of compact binary populations. To address this need, we develop IMRPhenomTEHM, a time-domain multipolar waveform model for aligned-spin BBHs in eccentric orbits. The model incorporates 3PN-accurate eccentric corrections into the eccentric dynamics of the state-of-the-art QC aligned-spin model IMRPhenomTHM, modeling the same multipoles: $(2, \pm 2), (2, \pm 1), (3, \pm 3), (4, \pm 4)$, and $(5, \pm 5)$. IMRPhenomTEHM provides a reliable description of eccentric binaries with mass ratios $q \in [1, 20]$, aligned spins

$\chi_i \in [-0.995, 0.995]$, and eccentricities up to $e = 0.4$ at 10 Hz.

Finally, the last part of this thesis focuses on parameter estimation (PE) studies using the newly developed eccentric waveform model. Neglecting eccentricity can lead to systematic biases in key parameters such as the chirp mass and effective spin. Moreover, eccentricity carries valuable information about the dynamical formation channels of binary systems, making the development of accurate waveform models for generic orbits essential. These models must be not only accurate, but also computationally efficient to allow for systematic application across large datasets. Although several previous attempts have been made to perform eccentric PE analyses, many were constrained by limitations such as sampling only over non-eccentric parameters and reweighting with eccentric models, restricting the analysis to a small number of events, or using machine learning techniques to mitigate the high computational cost associated with waveform models that include two eccentricity parameters [46–55]. Motivated by the efficiency and accuracy of our model, we reanalyze several BBH GW events previously identified in the literature as showing signs of interesting features such as spin-precession, unequal masses, or potential eccentricity. We present results obtained using both uniform and logarithmic priors on eccentricity, and compare Bayes factors between the eccentric and QC hypotheses. Our analysis identifies four events – GW190701, GW190929, GW200129, and GW200208_22 – with a preference for the eccentric hypothesis, in agreement with findings reported in the literature [47, 55]. Finally, the high computational efficiency of IMRPhenomTEHM enables us to perform PE for low total-mass events with long-duration signals. This opens the door to more detailed investigations of recent claims of eccentricity in GW200105 [56], one of the NSBH systems reported in Ref. [8], and we analyze this event using, for the first time, a fully eccentric IMR waveform model with standard stochastic sampling techniques. We find support for non-zero eccentricity in GW200105 across multiple analysis configurations. Our study also highlights the role of systematic uncertainties – including signal duration, waveform model degeneracies, and data quality – in interpreting eccentricity signatures with time-domain models. In contrast, our analyses of GW200115 and GW230529 reveal consistency with QC evolutions, reinforcing the diversity of possible formation channels within the NSBH population.

This thesis is organized as follows:

Chapter 2 introduces the foundations of GW astronomy, providing an overview of GWs and the detections made to date. It also covers the basic principles of interferometric detectors, the status of current and future detectors, and the fundamentals of data analysis, with a focus on CBCs.

Chapter 3 provides a detailed overview of BBH dynamics, parameter space, waveform morphology, and the various approximations used to model these systems across the parameter space.

Chapter 4 discusses the modeling challenges associated with generic BBH systems, focusing on the effects of spin-precession and elliptical orbits. It provides an overview of different modeling approaches and current waveform models for generic BBHs.

Chapter 5 presents the construction of a remnant model for spin-precessing binaries across the full mass-ratio range.

Chapter 6 details the construction of IMRPhenomTEHM, a time-domain multipolar waveform model for aligned-spin BBHs in eccentric orbits.

Chapter 7 & Chapter 8 present applications of the IMRPhenomTEHM model for the eccentric reanalysis of real GW events, focusing on BBH and NSBH binaries, respectively.

Chapter 9 summarizes the results presented in this thesis, discusses their implications for current and future observing runs, and outlines future directions toward the development of generic BBH waveform models across the full nine-dimensional intrinsic parameter space.

Two appendices are also included:

Appendix A provides additional material on the Fourier-domain representation, including the conventions used in this work and relevant theorems.

Appendix B contains certificates signed by the authors involved in the collaborative projects presented in this thesis, confirming their approval for inclusion.

PART I

Introductory notions

CHAPTER 2

Introduction to Gravitational waves

In this chapter, we explore the fundamental concepts of gravitational waves (GWs). First, we review the Einstein Field Equations in Section 2.1, which govern the curvature of spacetime, and the propagation of GWs. Next, we discuss the detection methods used to observe these waves in Section 2.2, highlighting the technological requirements and introducing the next generation of GW detectors. Finally, in Section 2.3 we cover the data analysis techniques employed to interpret the detected signals, including signal processing and parameter estimation.

2.1 Einstein Field Equations: Gravitational waves

General Relativity (GR) describes gravity as a geometric property of spacetime, meaning that the field responsible for gravity is the metric tensor, which encodes the curvature of spacetime itself, rather than a separate field propagating through it. The concept of gravity as the geometry of a curved manifold is motivated by the principle of equivalence. One of its forms states that, unlike other forces, unaccelerated or freely falling particles follow specific trajectories, known as *geodesics*. This idea leads to the Einstein Equivalence Principle, which asserts that "The outcome of any local non-gravitational experiment in a freely falling laboratory is independent of the velocity of the laboratory and its location in spacetime" [57].

The Einstein's Field Equations (EFE) govern how the metric responds to the distribution of energy and momentum in spacetime. These equations were developed by Albert Einstein in 1915 as part of his formulation of GR [58], serving as a generalization of the Poisson equation for the Newtonian gravitational potential. An alternative derivation of the EFE can be made through the principle of least action, or the Lagrangian formulation, which leads to the same relationship between the metric and the energy-momentum tensor:

$$R_{ab} - \frac{1}{2}Rg_{ab} = \frac{8\pi G}{c^4}T_{ab}. \tag{2.1.1}$$

Interestingly, David Hilbert independently derived the EFE from the gravitational action using variational principles, highlighting the close interplay between physics and mathematics in the development of GR. In Equation (2.1.1), R_{ab} is the Ricci curvature tensor, R the scalar curvature, g_{ab} the metric tensor, G Newton's gravitational constant, c the speed of light in vacuum and T_{ab} the stress-energy tensor. The Ricci tensor is a contraction of the Riemann tensor, which can be computed from the metric in terms of

the Christoffel symbols $\Gamma^a{}_{bc}$,

$$R_{ab} = R^c{}_{acb} = \frac{\partial \Gamma^c{}_{ab}}{\partial x^c} - \frac{\partial \Gamma^c{}_{ac}}{\partial x^b} + \Gamma^c{}_{ab}\Gamma^d{}_{cd} - \Gamma^c{}_{ad}\Gamma^d{}_{bc}, \tag{2.1.2}$$

where the quantities $\Gamma^a{}_{bc}$ are defined as

$$\Gamma^a{}_{bc} = \frac{g^{ad}}{2}\left(\frac{\partial g_{db}}{\partial x^c} + \frac{\partial g_{dc}}{\partial x^b} - \frac{\partial g_{bc}}{\partial x^d}\right). \tag{2.1.3}$$

The Ricci scalar or scalar curvature R is given by $R = g^{ab}R_{ab} = -8\pi GT/c^4$, which plugged into that same equation gives an equivalent expression for the EFE,

$$R_{ab} = \frac{8\pi G}{c^4}\left(T_{ab} - \frac{1}{2}T g_{ab}\right). \tag{2.1.4}$$

This new form provides a clearer understanding when considering the stress-energy tensor T_{ab} to be zero in the region under consideration. In Equation (2.1.4), we observe that, in this case, the right-hand side vanishes. The EFE then reduce to what are known as the vacuum field equations, or vacuum Einstein equations:

$$R_{ab} = 0. \tag{2.1.5}$$

The EFE (2.1.1) form a system of ten coupled, second-order, non-linear partial differential equations for the spacetime metric g_{ab}, relating the geometry of spacetime to the energy and momentum of matter and radiation. While compact in tensor notation, these equations are extremely complex to solve. Their non-linearity implies that solutions cannot be simply superposed, making analytical progress challenging. Consequently, it is common to impose symmetries on the metric—such as spherical or axial symmetry—to obtain exact solutions. In more general situations, solution strategies rely on approximation schemes, such as the post-Newtonian formalism or the gravitational self-force approach, which treat deviations from known solutions perturbatively. When such approximations break down, fully non-linear methods are required, and one resorts to numerical relativity. In this framework, the Einstein equations are reformulated as an initial value problem [59]. The EFE predict a variety of phenomena, including GWs, which were first proposed by Einstein in 1916 [60], but only directly detected nearly a century after their prediction in 2015 [61]. However, whether GWs represented genuine physical phenomena in full GR remained a topic of debate for several decades. It was not until the 1960s that foundational work by Pirani [62, 63], Trautman [64] and Bondi [65], followed by Robinson [66], and the Bondi–van der Burg–Metzner–Sachs (BMS) framework [67, 68] rigorously established the radiative nature of spacetime and showed that GWs carry energy and are measurable at null infinity. The standard way to rigorously define the emission and detection of GWs in GR is to work with asymptotically flat spacetimes. These are solutions to the EFE in which the geometry approaches that of flat Minkowski spacetime η_{ab} at large distances from the sources. In this setting, null infinity (denoted $\mathcal{I}^+$) represents the idealized location where outgoing radiation – traveling at the speed of light – arrives after propagating to infinite distances. The BMS formalism provided the tools to analyze the asymptotic structure of such spacetimes, showing that GWs are encoded in the behavior of the metric near $\mathcal{I}^+$, where they can be unambiguously identified and shown to carry energy.

2.1.1 Emission of gravitational waves

The simplest starting point for discussing GWs is linearized gravity. In this context, we consider the weak-field limit, which is not necessarily static, where test particles move freely. With these assumptions, we go beyond the Newtonian limit by including phenomena that are absent in Newtonian theory, yet we can still solve the EFE analytically for the ten metric coefficients g_{ab}. The weakness of the gravitational field can be expressed in terms of a metric decomposed into a flat Minkowski metric η_{ab} plus a small perturbation $h_{ab} = \epsilon m_{ab}$ with $|\epsilon| \ll 1$, so

$$g_{ab}(x) = \eta_{ab} + h_{ab}(x). \tag{2.1.6}$$

We restrict the Minkoswki metric to its canonical form $\eta_{ab} = \text{diag}(-1, 1, 1, 1)$, assuming that the coordinate system is approximately Cartesian and inertial. Furthermore, the assumption that h_{ab} is small allows to neglect terms higher than the first order in the metric perturbation. This permits to use η^{ab} and η_{ab} to raise and lower indices, as the higher-order corrections would be negligible compared to the perturbation itself. We can now study both the gravitational radiation itself, i.e. its propagation in the absence of sources ($T_{ab} = 0$), and then consider the equations coupled to energy to determine the source which generates GWs.

To obtain the linearized Einstein vacuum equations, we substitute Equation (2.1.6) into Equation (2.1.1) and expand it to first order in $h_{ab}(x)$. This expansion yields two terms: the first one is the Ricci curvature of flat spacetime, which vanishes, and the second term is the linearized equation we are looking for. By substituting Equation (2.1.6) into Equation (2.1.3), we obtain the first-order perturbation terms of the Christoffel symbols, since the zeroth-order term vanishes because the components of η_{ab} are constant:

$$\delta\Gamma^c_{ab} = \frac{1}{2}\eta^{cd}\left(\frac{\partial h_{da}}{\partial x^b} + \frac{\partial h_{db}}{\partial x^a} - \frac{\partial h_{ab}}{\partial x^d}\right). \tag{2.1.7}$$

The perturbation in the Ricci curvature is obtained by inserting Equation (2.1.7) into Equation (2.1.2), noting that the last two terms do not contribute, as they are of second order in h_{ab}. The perturbation of the Ricci tensor then becomes

$$\delta R_{ab} = \frac{\partial \delta\Gamma^c_{ab}}{\partial x^c} - \frac{\partial \delta\Gamma^c_{ac}}{\partial x^b}. \tag{2.1.8}$$

Finally, the linearized EFE in vacuum are obtained by substituting Equation (2.1.7) into Equation (2.1.8)

$$\delta R_{ab} = \frac{1}{2}[-\Box h_{ab} + \partial_a V_b + \partial_b V_a] = 0, \tag{2.1.9}$$

where $\Box = \eta^{ab}\partial_a\partial_b$ is the flat-space wave operator (d'Alembertian) and the vector V_a is defined as $V_a = \partial_c h^c_a - \frac{1}{2}\partial_a h^c_c$, and $G = c = 1$.

Equation (2.1.9) represents a set of ten linear, partial differential equations for $h_{ab}(x)$. Since coordinates are arbitrary, a specific choice can simplify the solutions, but it must leave the components of η_{ab} unchanged. Let us consider the following change:

$$x'^a = x^a + \xi^a(x), \tag{2.1.10}$$

where $\xi^a(x)$ are four arbitrary functions of the same small size as $h_{ab}(x)$. This change of coordinates implies the following metric transformation:

$$g'_{ab}(x') = \frac{\partial x^c}{\partial x'^a}\frac{\partial x^d}{\partial x'^b} g_{cd}(x) = \eta_{ab} + h'_{ab} = \eta_{ab} + (h_{ab} - \partial_a\xi_b - \partial_b\xi_a). \tag{2.1.11}$$

Adding a term $\partial_a \xi_b + \partial_b \xi_a$ to the metric perturbation thus corresponds to a coordinate transformation and is physically equivalent. This *gauge transformation* is analogous to $A_a \to A_b + \partial_a \Lambda$ for the vector potential in electromagnetism. Since $\xi^a(x)$ are arbitrary functions, they can be chosen so that $V'_a(x) = 0$, called the *harmonic gauge condition*. It can then be assumed that the initial coordinate system already satisfies $V_a(x) = 0$, simplifying the linearized Einstein equation to

$$\Box h_{ab} = 0. \tag{2.1.12}$$

Equation (2.1.12) admits a solution in the form of a superposition of plane waves, known as *gravitational waves*, which propagate at the speed of light, analogous to the situation in electromagnetism:

$$h_{ab}(x) = a_{ab} e^{i\mathbf{k}\cdot\mathbf{x}}, \tag{2.1.13}$$

where a_{ab} is a symmetric 4×4 tensor that represents the amplitudes of the components of the wave. These components are not arbitrary and can be simplified by choosing an appropriate set of coordinates. Explicit calculations show that the metric perturbation is purely spatial ($h_{ti} = 0$) and traceless ($h^a_a = 0$). Furthermore, the harmonic gauge condition implies that the spatial metric perturbation is transverse, i.e., $k^i a_{ti} = \partial_a h_{ab} = 0$, and also that $a_{tt} = 0$. This condition is referred to as the *transverse-traceless (TT) gauge*, which fixes the local gauge freedom. By orienting the z-axis along the propagation of the wave, we are left with a 2×2 symmetric and traceless matrix in the x-y subspace. This demonstrates that GWs have only two polarizations, i.e., two local degrees of freedom, denoted h_+ and $h_\times$:

$$h_{ab}(x) = \begin{bmatrix} 0 & 0 & 0 & 0 \\ 0 & h_+ & h_\times & 0 \\ 0 & h_\times & -h_+ & 0 \\ 0 & 0 & 0 & 0 \end{bmatrix} e^{i\mathbf{k}\cdot\mathbf{x}}. \tag{2.1.14}$$

One can now discuss the effects of the two polarizations separately. The effects of the two modes on a circle of test particles would distort them into ellipses oscillating in $+$ and $\times$ patterns, respectively, as seen in Figure 2.1. Alternatively, we can define the right- and left-handed circularly polarized modes as follows:

$$\begin{aligned} h_R &= \frac{1}{\sqrt{2}}(h_+ + i h_\times), \\ h_L &= \frac{1}{\sqrt{2}}(h_+ - i h_\times). \end{aligned} \tag{2.1.15}$$

The effect of these two polarizations is the rotation of the particles in either a right or left-handed sense, as seen in the h_R polarization in Figure 2.1. Thus, the degrees of freedom of the EFE (2.1.1) are reduced to two polarization states, h_+ and $h_\times$, which can be expressed as

$$\begin{aligned} h_+(t,r) &= A_+ \cos\left(\omega\left(t - \frac{r}{c}\right) + \Phi_+\right), \\ h_\times(t,r) &= A_\times \cos\left(\omega\left(t - \frac{r}{c}\right) + \Phi_\times\right), \end{aligned} \tag{2.1.16}$$

where the amplitudes $A_{+/\times}$, the frequency ω, and the phases $\Phi_{+/\times}$ contain all the relevant astrophysical information, and r is the distance to the source.

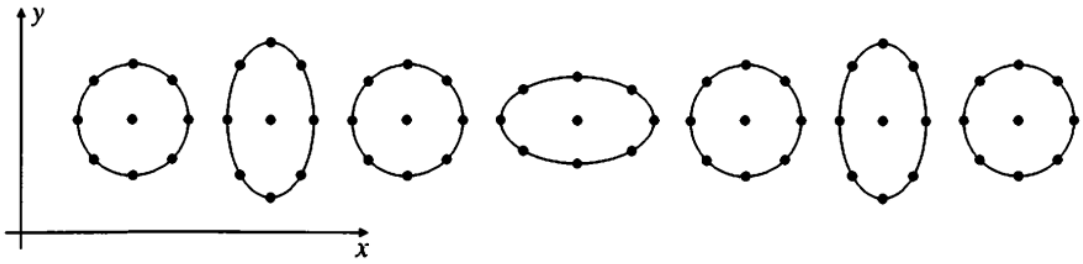

2.1.1: + polarization h_+: particles are distorted into ellipses which oscillate in a + pattern.

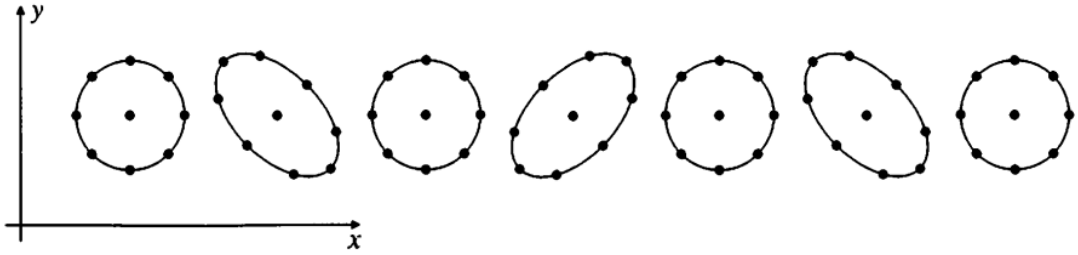

2.1.2: × polarization $h_\times$: particles are distorted into ellipses which oscillate in a × pattern.

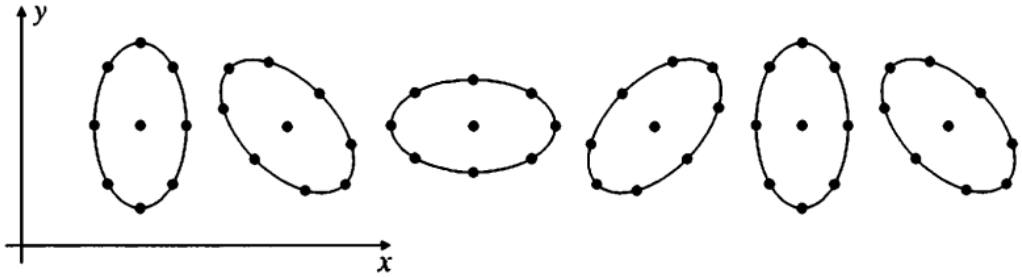

2.1.3: R polarization h_R: particles are distorted into an ellipse which rotates in a right-handed side.

Figure 2.1: Effect of a GW with different polarizations on a circle of test particles. Source: [69].

2.1.2 Generation of gravitational waves

To discuss the generation of GWs, we need to consider Equation (2.1.1) coupled to matter, which requires assuming a non-vanishing T_{ab}. This means that the transverse-traceless form derived earlier cannot be applied. However, similar to the approach for the vacuum equations, gauge transformations can be used to reduce redundant degrees of freedom on the metric perturbation. By considering the Lorentz Gauge Condition $V_a(x) = 0$, the four conditions on h_{ab} can be simplified by defining the trace-reversed amplitude as

$$\bar{h}_{ab} = h_{ab} - \frac{h}{2}\eta_{ab}, \quad \bar{h} = \eta^{ab}\bar{h}_{ab} = -h, \quad \bar{h}^{TT}_{ab} = h^{TT}_{ab}, \tag{2.1.17}$$

which ensures that the harmonic condition becomes

$$\frac{\partial \bar{h}^{ab}}{\partial x^b} = 0. \tag{2.1.18}$$

The left-hand side of the EFE (2.1.1) in the harmonic gauge takes the form $\delta R_{ab} = -\frac{1}{2}\Box h_{ab}$, as seen in Equation (2.1.12), which implies $\delta R = -\frac{1}{2}\Box h$. Setting $G = c = 1$, we obtain

$$\delta R_{ab} - \frac{1}{2}\delta R g_{ab} = 8\pi T_{ab}, \tag{2.1.19}$$

and the linearization of the EFE (2.1.1) simplifies to

$$\Box \bar{h}_{ab} = -16\pi T_{ab}. \tag{2.1.20}$$

The solution to this last equation can be obtained using a Green's function. The Green's function $G(x^d - y^d)$ for the $\Box$ operator is the solution of

$$\Box_x G(x^d - y^d) = \delta^{(4)}(x^d - y^d), \tag{2.1.21}$$

which has two possible solutions, often referred to as "retarded" or "advanced" (waves traveling forward or backward in time, respectively). We focus on the retarded solution, which gives the following general solution for the perturbation (see any textbook development e.g. [69])

$$\bar{h}_{ab}(t, \mathbf{x}) = 4 \int \frac{1}{|\mathbf{x} - \mathbf{y}|} T_{ab}(t_r, \mathbf{y}) \mathrm{d}^3 y, \tag{2.1.22}$$

where the retarded time is defined as $t_r = t - |\mathbf{x} - \mathbf{y}| = t - r$. From this last equation, we can see that the disturbance at $(t, \mathbf{x})$ is the sum of the contributions at $(t_r, \mathbf{x} - \mathbf{y})$ on the past light cone. Now, we can impose some simplifications: we consider the source isolated, far away, and slowly moving (i.e., non-relativistic motion). Working in the Fourier domain, we can find a compact form for the trace-reversed perturbation in terms of the Fourier transform of the quadrupole moment tensor of the energy density, defined as

$$I_{ij}(t) = \int \mathrm{d}^3 y T^{00}(t, \mathbf{y}) y_i y_j = \int \mathrm{d}^3 y \rho(t, \mathbf{y}) y_i y_j, \tag{2.1.23}$$

where ρ denotes the mass density. The traceless mass or reduced quadrupole moment can be thus defined as

$$Q_{ij}(t) = \int \rho(t, \mathbf{y}) \mathrm{d}^3 y \left(y_i y_j - \frac{1}{3} r^2 \delta_{ij} \right) = I_{ij} - \frac{1}{3} \delta_{ij} \delta^{kl} I_{kl}. \tag{2.1.24}$$

Transforming the perturbation expression in terms of Q_{ij} back to the time domain, we obtain the quadrupole formula, which provides the expression for the metric perturbation at points far away from the source:

$$\bar{h}_{ij}(t, \mathbf{x}) = \frac{1}{r} \frac{2G}{c^4} \frac{\mathrm{d}^2 Q_{ij}}{\mathrm{d}t^2} \left(t - \frac{r}{c} \right), \tag{2.1.25}$$

where all the c and G factors have been restored. This shows that the GWs produced by this simplified source are proportional to the second derivative of the quadrupole moment at the past light cone where the observer intersects the source.

Finally, one can consider the energy emitted via GWs. Explicit calculations lead to the following expression for the luminosity or power by the emission of these waves:

$$L = \frac{G}{5c^5} \sum_{ij} \left\langle \left(\frac{\mathrm{d}^3 Q_{ij}}{\mathrm{d}t^3}(t_r) \right)^2 \right\rangle, \tag{2.1.26}$$

This expression gives quantitatively accurate results for sources with weak gravitational fields, though the complete description (such as the numerical integration of the EFE) is necessary when considering sources with strong gravitational fields. Furthermore, it provides an intuitive understanding of the possible sources of GWs and their expected

detection rates, since the expression indicates that the rate of energy emission depends on how rapidly the quadrupole moment changes. Therefore, more violent or rapid motion leads to greater GW luminosity.

Compact binary coalescences (CBCs) are short-duration transient events and among the most efficient astrophysical sources of GWs, both because they can convert a significant fraction of their total mass into gravitational radiation and because their orbital motion provides an ideal mechanism for generating a time-varying mass quadrupole moment. In fact, all detections made by the LIGO, Virgo and KAGRA (LVK) Collaboration so far fall into this category [1–4], with the majority belonging to the subclass of binary black boles (BBHs). However, CBCs also include systems composed of two neutron stars (BNS), with the first detection occurring on August 17, 2017 [5], as well as neutron star–black hole (NSBH) binaries. The first-ever detection of an NSBH merger took place on January 5, 2020, followed by a second event of the same nature just 10 days later [8]. More recently, during the first half of the ongoing fourth observing run (O4a), another NSBH or BNS candidate has been reported [9], with the primary object lying within the BH-NS mass gap. All three groups are classified together because they share the same wave-generation mechanism: a pair of dense objects orbit each other, emitting GWs that carry away part of the system's orbital energy. This energy loss causes the objects to spiral inward, increasing their orbital speed and emitting even stronger GWs, thereby accelerating the energy loss. Eventually, this process leads to the coalescence of both objects. Since the amount of radiated energy increases as the objects get closer together, more compact and massive sources – such as black holes – produce GWs that are easier to detect.

Continuous GWs are also well understood, and those most likely to be detected by the LVK are thought to originate from a single massive spinning object, such as a neutron star [70]. A spinning neutron star emits GWs if it has any deviation from a perfect spherical shape. There are however other sources of continuous GWs (CWs): for instance, the space-based detector LISA [71] is expected to detect continuous signals from white dwarf binaries [72]. These waves are called *continuous* because if the star's spin rate remains constant, the emitted waves maintain a steady frequency and amplitude. Compared to CBC signals, CW signals are much longer but significantly simpler, resembling an almost perfect single-frequency sinusoid over short timescales (akin to "pure tones"), with only a very slow decrease in frequency (*spindown*). However, detecting CW signals poses a major computational challenge – not simply due to their long duration, but because successful detection typically requires coherent integration over long timescales and extremely dense template coverage of a vast parameter space. In particular, all-sky searches for unknown sources must scan over frequency, spindown, and sky position, which makes them especially expensive. This is the main reason why CWs have not yet been detected.

The other two sources of GWs are not as well understood as the previous ones. One of them is the stochastic GW background (SGWB), a persistent and diffuse signal composed of many unresolved GW sources overlapping in time. This background may have various origins, including early-universe processes such as inflation, phase transitions, or cosmic strings [73], but also more astrophysical sources like a superposition of distant CBCs. Although the detection of a cosmological SGWB by ground-based interferometers remains elusive, current detectors have already placed stringent upper limits on its amplitude [74], and the search methods for such signals are highly developed. In contrast, recent observations by pulsar timing arrays (PTAs) have reported evidence for a nanohertz

stochastic background [75–78], marking the first detection of a SGWB. Next-generation detectors, including the space-based LISA [15] and third-generation (3G) ground-based observatories such as the Einstein Telescope (ET) [11, 12] and Cosmic Explorer (CE) [13], will significantly enhance our sensitivity to stochastic signals. While stochastic backgrounds are not unique in their ability to probe the early Universe – other tools like primordial abundances or the cosmic microwave background (CMB) provide valuable insights – they offer a novel and complementary window into the physics of the early Universe and unresolved astrophysical populations. Finally, in contrast to the long-duration nature of stochastic waves, *burst signals* [79] are short-duration GWs expected from sources that are either unknown or not well modeled. Because their waveforms lack well-defined properties, detecting them presents a significant challenge. However, their discovery could provide groundbreaking insights into previously unknown astrophysical events.

2.1.2.1 Qualitative description of GW emission

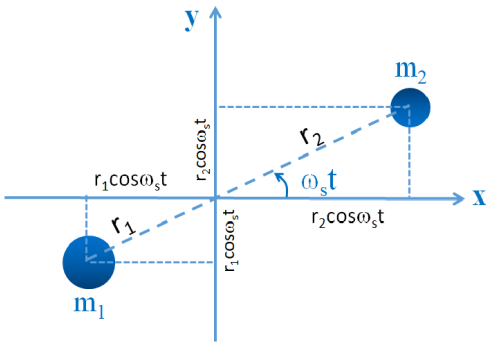

Figure 2.2: A two body system of masses m_1 and m_2 orbiting in the x-y plane. Source: [80].

During the early inspiral of a binary system, analytical approximations can provide a useful qualitative description of the emitted GW signal. A simple approximation can be derived from Kepler's third law and Einstein's quadrupole formula (2.1.25). Consider a system of two objects with masses $m_{\{1,2\}}$ orbiting in the x-y plane, as depicted in Figure 2.2. The reduced quadrupole tensor moment, defined in Equation (2.1.24), is given by

$$Q = \sum_{i\in[1,2]} \frac{m_i}{3} \begin{pmatrix} 2x_i^2 - y_i^2 & 3x_i y_i & 0 \\ 3x_i y_i & 2y_i^2 - x_i^2 & 0 \\ 0 & 0 & -r_i^2 \end{pmatrix}. \tag{2.1.27}$$

Taking into account the geometry shown in Figure 2.2, and assuming a circular orbit with separation $R = r_1 + r_2$, total mass $M = m_1 + m_2$, and orbital frequency ω (with $f_{\rm orb} = \frac{\omega}{2\pi}$), the quadrupole moment Q is given by:

$$Q(t) = \frac{1}{2}\mu R^2 \begin{pmatrix} \cos(2\omega t) + 1/3 & \sin(2\omega t) & 0 \\ \sin(2\omega t) & 1/3 - \cos(2\omega t) & 0 \\ 0 & 0 & -2/3 \end{pmatrix}, \tag{2.1.28}$$

where $\mu = \frac{m_1 m_2}{M}$ is the *reduced mass* of the system. The emitted radiation power can then be calculated using Equation (2.1.26), yielding

$$L = \frac{\mathrm{d}}{\mathrm{d}t} E_{\rm GW} = \frac{32}{5}\frac{G}{c^5}\mu^2 R^4 \omega^6. \tag{2.1.29}$$

This power comes from the orbital energy of the system, $E_{\rm orb} = -\frac{GM\mu}{2R}$, and during the inspiral, where the approximations hold, the following equality is valid:

$$L = -\dot{E}_{\rm orb} = \frac{GM\mu}{2R^2}\dot{R}. \tag{2.1.30}$$

We can now apply Kepler's third law, which establishes the relation between the orbital radius R and the orbital frequency ω, given by $R^3 = GM/\omega^2$. Taking the derivative of

this equation and substituting into Equation (2.1.30), we obtain a differential equation for the orbital frequency:

$$\dot{\omega}^3 = \left(\frac{96}{5}\right)^3 \frac{\omega^{11}}{c^{15}} G^5 \mu^3 M^2 = \left(\frac{96}{5}\right)^3 \frac{\omega^{11}}{c^{15}} (G\mathcal{M})^5, \tag{2.1.31}$$

where $\mathcal{M}$ is defined as the *chirp mass*

$$\mathcal{M} = \frac{(m_1 m_2)^{3/5}}{M^{1/5}} = \mu^{3/5} M. \tag{2.1.32}$$

Before solving this equation, which relates time and frequency, we can calculate the GW strain polarizations using the quadrupole formula (2.1.25), assuming the z-axis is orthogonal to the x-y plane (for a detailed derivation, see e.g. [81], Chapter 4.1):

$$\begin{aligned} h_+(t) &= \frac{4G\mu\omega^2 R^2}{d_L c^4} \frac{1+\cos^2(\theta)}{2} \cos(2\omega t + 2\phi), \\ h_\times(t) &= \frac{4G\mu\omega^2 R^2}{d_L c^4} \cos(\theta) \sin(2\omega t + 2\phi), \end{aligned} \tag{2.1.33}$$

where d_L is the distance to the system from the detector's frame. The polarizations reveal that the emitted waves have a frequency twice the orbital frequency, so we define the GW frequency as $\omega_{\mathrm{GW}} = 2\omega$. Substituting this into Equation (2.1.31) and solving the differential equation for $f_{\mathrm{GW}} = \frac{\omega_{\mathrm{GW}}}{2\pi}$ gives the time evolution of the GW frequency:

$$\begin{aligned} f_{\mathrm{GW}}(t) &= \frac{1}{\pi} \left(\frac{5}{256(t_{\mathrm{coal}} - t)}\right)^{3/8} \left(\frac{G\mathcal{M}}{c^3}\right)^{-5/8}, \\ \tau(f) &= \frac{5}{256} (\pi f_{\mathrm{GW}})^{-8/3} \left(\frac{G\mathcal{M}}{c^3}\right)^{-5/3}, \end{aligned} \tag{2.1.34}$$

where t_{coal} is the coalescence time, and τ is the remaining time until coalescence for a given frequency ($\tau = t_{\mathrm{coal}} - t$). These expressions indicate that the duration of detectable GW emission depends on the masses of the objects involved. For instance, consider two equal mass systems – a BNS with $M_{\mathrm{NS}} = 3M_\odot$, and a BBH with $M_{\mathrm{BH}} = 50M_\odot$. Assuming a starting frequency of 10 Hz, we find $\tau_{\mathrm{BNS}} \approx 15$ minutes for the BNS, and $\tau_{\mathrm{BBH}} \approx 8$ seconds for the BBH system.

These approximations provide a rough but realistic estimate of the expected duration of GW signals: while BBH GWs might only last for a few seconds, signals from BNS systems can persist for hundreds of seconds. For a more quantitative description of the inspiral phase, more refined approximations – such as post-Newtonian expansions [82] or other perturbative methods used to solve the EFE – are required. However, these approximations generally break down in the late stages of the evolution, when the two compact objects are sufficiently close to merge, as well as during the post-merger phase. In such regimes, fully numerical solutions of the EFE become necessary. We refer the reader to Section 3.2.1 for a detailed discussion of the available methods and approximations used to describe the complete GW signal from a CBC, and to Section 4.3 for an overview of current BBH waveform models.

2.2 Gravitational wave detections

The emission of GWs is associated with energy loss, which, under the conditions described above, is governed by Equation (2.1.26). This phenomenon enabled the first indirect

confirmation of GWs through pulsars — rapidly rotating neutron stars that emit radio waves. The discovery of the relativistic binary pulsar PSR B1913+16 in 1974 by Russell A. Hulse and Joseph H. Taylor provided crucial evidence, as the observed changes in the binary's orbital motion (inferred from pulsar emissions) closely matched the predictions of the quadrupole formula [83]. This discovery served as the first-ever proof of GWs and was recognized with the 1993 Nobel Prize in Physics. After decades of efforts to detect GWs directly – beginning with resonant mass detectors and later advancing to laser interferometry – the first direct detection was finally achieved on September 14, 2015, by the Advanced Laser Interferometer GW Observatory (LIGO) [61]. The signal originated from a BBH with initial masses of $36^{+5}_{-4}M_{\odot}$ and $29^{+4}_{-4}M_{\odot}$. Since then, three observational runs (O1, O2, and O3) have led to the detection of over 90 GW events [1–4], all originating from compact object binaries. The majority of these events have been identified as BBH mergers, although several BNS and NSBH mergers have also been observed. LIGO [84] has played a role in all detections to date, with the Virgo detector [85] joining during the second observing run. The GEO600 detector [86] began taking data simultaneously with Advanced LIGO on September 18, 2015. More recently, the KAGRA detector [87] in Japan became operational during the third observing run (O3), further enhancing the global network of GW detectors. Together, these detectors form the current operational network for GW observations. The fourth observing run (O4) began in May 2023 and is scheduled to continue until October 7, 2025. This run marks a significant improvement in detection capabilities, with over 200 events detected in just the first half [10].

Between observational runs, the detectors are upgraded, additional detectors become operational, and overall sensitivity improves. These advances have been driven by the advancement of laser interferometers, which provide the required sensitivity to measure the distortions caused by passing GWs. In the following, we introduce in Section 2.2.1 the operating principles of these interferometric detectors. We then explore the network of existing observatories and the planned next-generation detectors in Section 2.2.2, along with a summary of the most significant events detected to date. Finally, in Section 2.2.3 we revisit the basics of the response of an interferometric detector.

2.2.1 Interferometric detectors

Interferometers, first invented by Albert Michelson in the 19^{th} century, are now widely used in many fields due to their ability to measure small distances. In the particular case of GWs, they can measure changes in distance as small as one ten-thousandth of the size of a proton.

These interferometers operate on the principle of Michelson interferometers, in which two laser beams are combined to produce an interference pattern that encodes information about the observed phenomenon. As GWs propagate, they distort space-time by stretching it in one direction while compressing it in the perpendicular one, as illustrated in Figure 2.1. Current GW detectors typically feature orthogonal arms, as shown in Figure 2.3. When a passing GW alters the relative arm lenghts – a motion known as *differential arm motion* – the laser beams travel different distances, shifting their interference phase. This results in an optical signal proportional to the wave's strain. Alternative configurations are also possible. For instance, future detectors like LISA and ET are designed with three arms. This triangular configuration allows the construction of a null stream, which can be used for noise characterization and vetoing of spurious events, and it allows a local disentangling

of the GW polarizations.

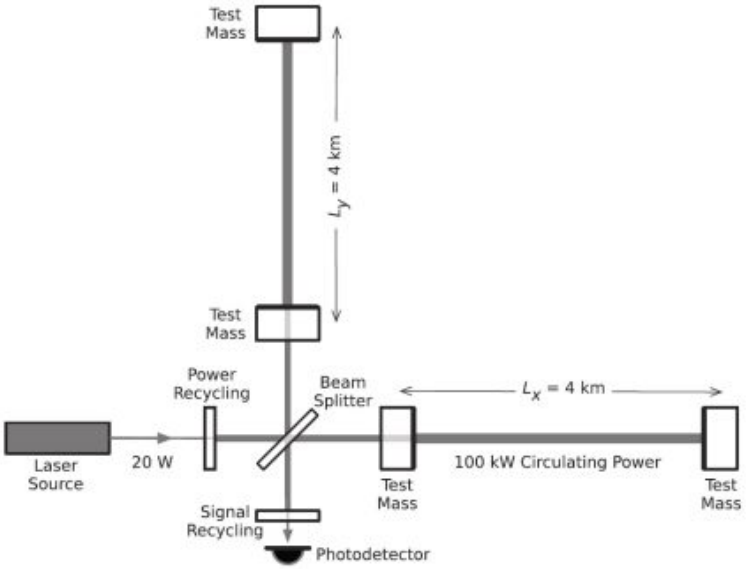

Figure 2.3: Simplified diagram of a LIGO interferometer. The interferometer consists of two orthogonal arms, each of which is several kilometers long. A laser beam is split into two separate beams that travel along each arm, and are reflected back by mirrors at the ends of the arms. When a GW passes through, it causes a distortion in space-time, stretching one arm while compressing the other. This change in the arm lengths leads to a shift in the interference pattern of the laser beams, allowing the strain caused by the GW to be measured. Source: [61].

Although the concept of an interferometer is straightforward, its practical implementation is quite challenging. The physical effect of a GW is to perturb the relative positions of the test particles at the ends of the interferometer arms. If the two masses are separated by a distance L and the strain of the wave is h, the resulting change in their distance can be approximated by

$$\frac{\delta L}{L} \sim h. \tag{2.2.1}$$

For example, the strain of the first-ever detection of a GW [61] was on the order of 10^{-21}. Using Equation (2.2.1), this implies that the interferometer sensitivity must reach

$$\delta L \sim 10^{-16} \left(\frac{h}{10^{-21}}\right) \left(\frac{L}{\text{km}}\right) \text{cm}. \tag{2.2.2}$$

This illustrates the extreme sensitivity required to detect the incredibly small distortions caused by passing GWs.

Achieving such sensitivity requires suppressing multiple sources of noise that can affect the detector's measurements. At low frequencies (below approximately 10 Hz), seismic noise becomes one of the dominant contributors, caused by ground vibrations from both natural and human-induced sources. Gravity gradient noise, resulting from fluctuations in the Earth (e.g. clouds or rain), as well as the thermal noise in the suspension systems and mirrors of the interferometer contribute to the overall noise at these low frequencies, as temperature variations lead to microscopic movements of the detector components. At higher frequencies (above 100 Hz), the main source of noise is shot noise, which comes

from quantum fluctuations in the number of photons arriving at the detector. This limits how precisely we can measure changes in the light's amplitude and, therefore, the distance between the mirrors. Optical imperfections like mirror roughness or misalignment also affect performance in this frequency range. Furthermore, external radio-frequency interference from electronic devices can also contaminate the signals in this range. The total sensitivity curve of the detector is then determined by the sum of all these noise contributions, as shown in Figure 2.4 for the LIGO and Virgo detectors during O3. The sharp spectral lines visible in the amplitude spectral density correspond to calibration signals, mechanical resonances, or electrical interference.

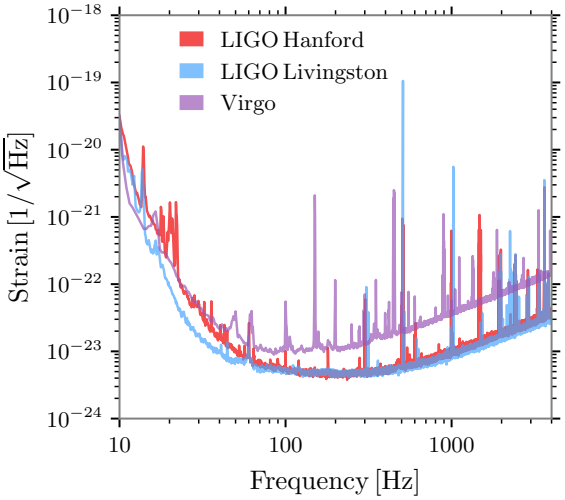

Figure 2.4: Representative amplitude spectral density of the strain sensitivity for the three interferometers operative during O3: LIGO Livingston on January 4, 2020, at 02:53:42 UTC; LIGO Hanford on January 4, 2020, at 18:20:42 UTC; and Virgo on February 9, 2020, at 01:16:00 UTC. Source: [4].

2.2.2 Current observations and future prospects

During O1 and O2, the LIGO-Virgo collaboration detected 11 GW events [46], including the first ever detection of a BBH merger [61] and the observation of a BNS on August 17, 2017 [5]. The latter provided the first direct multi-messenger observation of GWs and electromagnetic counterparts. The third observing run (O3), which began in April 2019, was suspended on March 26 2020 [88], roughly a month before the planned end, due to the COVID-19 pandemic. On 25 February 2020, during this last observational run, the Kamioka GW Detector KAGRA [87] in Japan became operational, joining LIGO and Virgo during the second part of O3.

Despite the premature end, O3 significantly expanded the catalog of detected events, including the first observations of asymmetric mass ratio binaries and NSBH mergers. The latest public catalog, GWTC3, includes over 90 GW detections [4]. Among them, the first two confidently identified NSBH mergers, GW200105 and GW200115, were observed [8]. The component masses of GW200105 were $8.9^{+1.2}_{-1.5}M\odot$ and $1.9^{+0.3}_{-0.2}M\odot$, while those of GW200115 were $5.7^{+1.8}_{-2.1}M\odot$ and $1.5^{+0.7}_{-0.3}M\odot$. Another notable event, GW190814, involved a compact binary coalescence between a $22.2 - 24.3M_\odot$ BH and a compact object with a mass of $2.50 - 2.67M_\odot$ [7], making it a possible NSBH system or a highly unusual

low-mass black hole. Another landmark discovery from O3 was GW190521, the first observational evidence of an intermediate-mass black hole (IMBH), with a remnant mass of approximately $142M_\odot$ [89, 90]. This detection provided the first direct confirmation of BHs in the elusive *pair-instability mass gap* and reinforced the existence of a previously unconfirmed population of IMBHs.

The fourth observing run (O4) of GW observatories began in May 2023, marking a significant advancement in the detection capabilities of these instruments. LIGO's detectors achieved an improved sensitivity of 130-150 Mpc, later enhancing to nearly 160 Mpc for both detectors by late 2023. Virgo, after addressing technical challenges, joined the O4 run during its second part (O4b), which began on 10 April 2024, with a sensitivity of 50 to 55 Mpc. KAGRA met its planned 1 Mpc sensitivity before the start of O4 and aims to reach 10 Mpc by the end of the run. During O4, hundreds of candidate GW events have been been publicly announced on `gracedb.ligo.org`, underscoring the enhanced capabilities of the observatories. One particularly notable event is GW230529 [9], a CBC involving component masses of 2.5–4.5 $M_\odot$ and 1.2–2.0 $M_\odot$. The primary object is most likely a black hole, suggesting a potentially higher rate of NSBH mergers with electromagnetic counterparts and offering further evidence for compact objects populating the so-called lower mass gap. The O4 run is scheduled to continue until 7 October 2025, with planned commissioning breaks to further enhance detector performance. These improvements are anticipated to increase the sensitivity of the detectors, thereby expanding the observable volume of the universe and potentially leading to more frequent detections of GW events.

Looking ahead, several new observatories are expected to join the global network of GW detectors. The Indian Initiative in GW Observations, LIGO-India [91] is anticipated to become operational in the coming years, contributing to the global effort in GW astronomy. The 3G ground-based detectors: the Cosmic Explorer [13] and the Einstein Telescope (ET) [11, 12], a proposed underground observatory in Europe, as well as the Laser Interferometer Space Antenna (LISA) [15], the first space-based detector, are both expected to become operational during the 2030s. These advancements will enable the detection of more massive phenomena, such as mergers of supermassive black holes typically found at the centers of galaxies, and will also allow for the observation of lower-frequency GWs from different sources, also beyond CBCs.

Figure 2.5 shows the broad range of astrophysical sources across different frequency bands that GW detectors are expected to characterize. Current ground-based interferometers, such as LIGO, Virgo, KAGRA, and GEO600, operate in the 10-10^3 Hz range, primarily detecting CBCs of stellar-mass BHs and NSs. This includes landmark events like GW150914, the first observed BBH [61]. In addition to CBCs, these detectors aim to capture core-collapse supernovae, CWs from spinning neutron stars, and a potential stochastic GW background from unresolved astrophysical or cosmological sources. While GEO600 contributes mainly to detector R&D, KAGRA, which features underground operation and cryogenic cooling, enhances global sky coverage. The design sensitivity of LIGO and Virgo, also shown in Figure 2.5, will improve detection rates and expand the accessible astrophysical population.

Future detectors will extend sensitivity toward lower frequencies, enabling the observation of new types of sources. ET and CE are expected to reach down to 1 Hz, enabling the detection of IMBHs and high-redshift mergers with improved signal fidelity. At the same time, their enhanced high-frequency sensitivity will allow for more

detailed characterization of BNS merger and post-merger phases [11, 13]. Meanwhile, LISA, operating in the mHz range, will be sensitive to galactic binaries, extreme mass-ratio inspirals (EMRIs), and supermassive binary black hole (SMBBH) mergers [15, 16]. Additionally, as previously mentioned, PTAs have recently provided evidence of a nanohertz stochastic background, likely originating from inspiraling SMBBHs [75–78]. As shown in Figure 2.5, the combined frequency coverage of these detectors enables multi-band GW astronomy, bridging observational gaps and allowing a comprehensive study of compact objects and cosmic evolution.

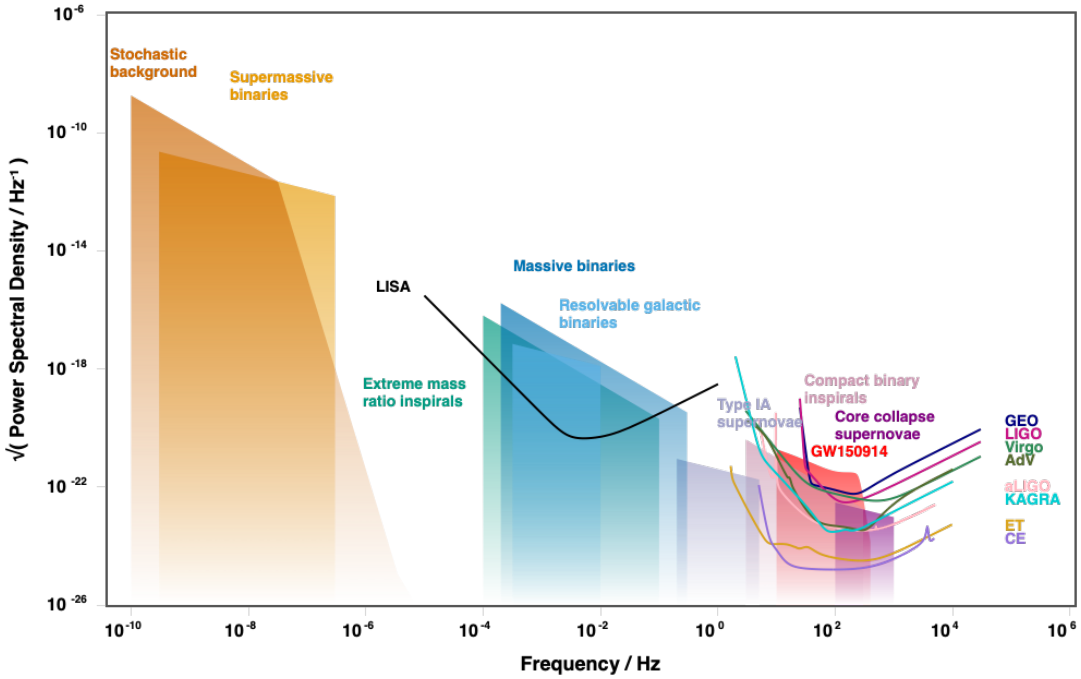

Figure 2.5: Sensitivity curves of current and future GW detectors, along with representative astrophysical sources. The curves show the amplitude spectral density of the strain sensitivity for ground-based detectors, including LIGO (for O1 and design), Virgo (O1 and design), GEO, KAGRA, and next-generation observatories such as ET and CE. The expected sensitivity of the space-based LISA mission is also shown. Overlaid are characteristic strain amplitudes for various GW sources, including the stochastic background, supermassive binary black holes, extreme mass ratio inspirals, massive and galactic binaries, Type Ia supernovae, compact binary inspirals, core-collapse supernovae, and the first detected event, GW150914. The placement of these sources illustrates their detectability across different frequency bands. Figure generated using gwplotter, based on Ref. [92].

2.2.3 Detector's response

Following Ref. [92], the response of a GW interferometer to an incoming signal depends on the relative orientation of the detector and the wave. In the absence of noise, the measured strain is given by the difference in deformation between the two arms [93]

$$h(t) = \frac{1}{2} h_{ij}\ (l_1^i l_1^j - l_2^i l_2^j), \tag{2.2.3}$$

where $l_{1,2}^i$ are unit vectors describing the directions of the interferometer arms, originating from the beam splitter (which we take as the origin of our coordinate system), as shown

in Figure 2.3. To describe the GW signal in a convenient reference frame, we introduce an orthonormal basis $(p^i, q^i, \hat{r}^i)$, where $\hat{r}^i$ is the unit vector pointing from the detector to the source at sky location (d_L, α, δ). The polarization basis tensors can then be expressed in terms of p^i and q^i, which describe the two independent polarization states of the wave:

$$H^+_{ij} = p_i p_j - q_i q_j, \tag{2.2.4}$$
$$H^\times_{ij} = p_i q_j + q_i p_j. \tag{2.2.5}$$

There remains a freedom in the choice of the polarization basis, corresponding to a rotation of p^i and q^i by an angle Ψ around $\hat{r}^i$. This angle, known as the *polarization angle* determines the orientation of the wave's polarizations relative to the detector. By combining Equation (2.2.3) and Equation (2.2.5), with Equation (2.1.15), the detector's output can be rewritten as

$$h(t) = F_+(\alpha, \delta, \Psi) h_+(\Pi; t) + F_\times(\alpha, \delta, \Psi) h_\times(\Pi; t), \tag{2.2.6}$$

where Π encapsulates all the astrophysical parameters of the source. The functions $F_+(\alpha, \delta, \Psi)$ and $F_\times(\alpha, \delta, \Psi)$, known as *detector response functions* or *antenna-pattern functions*, characterize the sensitivity of the interferometer to each polarization mode as a function of the source's sky location and wave polarization. These response functions inherit their angular dependence from the detector geometry:

$$F_+(\alpha, \delta, \Psi) = \frac{1}{2} H^+_{ij} (l^1_1 l^j_1 - l^i_2 l^j_2), \tag{2.2.7}$$
$$F_\times(\alpha, \delta, \Psi) = \frac{1}{2} H^\times_{ij} (l^1_1 l^j_1 - l^i_2 l^j_2). \tag{2.2.8}$$

Assuming the detector consists of orthogonal arms aligned with the x and y axes, and defining l^i_1 and l^i_2 as the corresponding unit vectors, one can derive the explicit angular dependence of the antenna pattern functions [94]:

$$F_+(\alpha, \delta, \Psi) = \frac{1}{2} \left(1 + \cos^2 \alpha\right) \cos 2\beta \cos 2\Psi - \cos \alpha \sin 2\beta \sin 2\Psi, \tag{2.2.9}$$
$$F_\times(\alpha, \delta, \Psi) = \frac{1}{2} \left(1 + \cos^2 \alpha\right) \cos 2\beta \sin 2\Psi - \cos \alpha \sin 2\beta \cos 2\Psi. \tag{2.2.10}$$

In principle, an interferometric detector is sensitive to signals arriving from any direction. However, due to the angular dependence of the antenna pattern functions in Equation (2.2.10), certain directions – known as *blind spots* – lead to a vanishing response, limiting the detector's sensitivity to waves from those regions. The *antenna power pattern* of a detector can be defined as [94]

$$\begin{aligned} P(\alpha, \delta) &= F_+(\alpha, \delta, \Psi)^2 + F_\times(\alpha, \delta, \Psi)^2 = \\ &= \frac{1}{4} \left(1 + \cos^2 \alpha\right)^2 \cos^2 2\beta + \cos^2 \alpha \sin^2 2\beta. \end{aligned} \tag{2.2.11}$$

Notably, this function is independent of the polarization angle, as expected, and it highlights the presence of "blind spots" where a single detector has reduced sensitivity.

Increasing the number of detectors mitigates this issue, as blind spots arise due to the relative orientation between the wave and a given detector. Moreover, multiple detectors

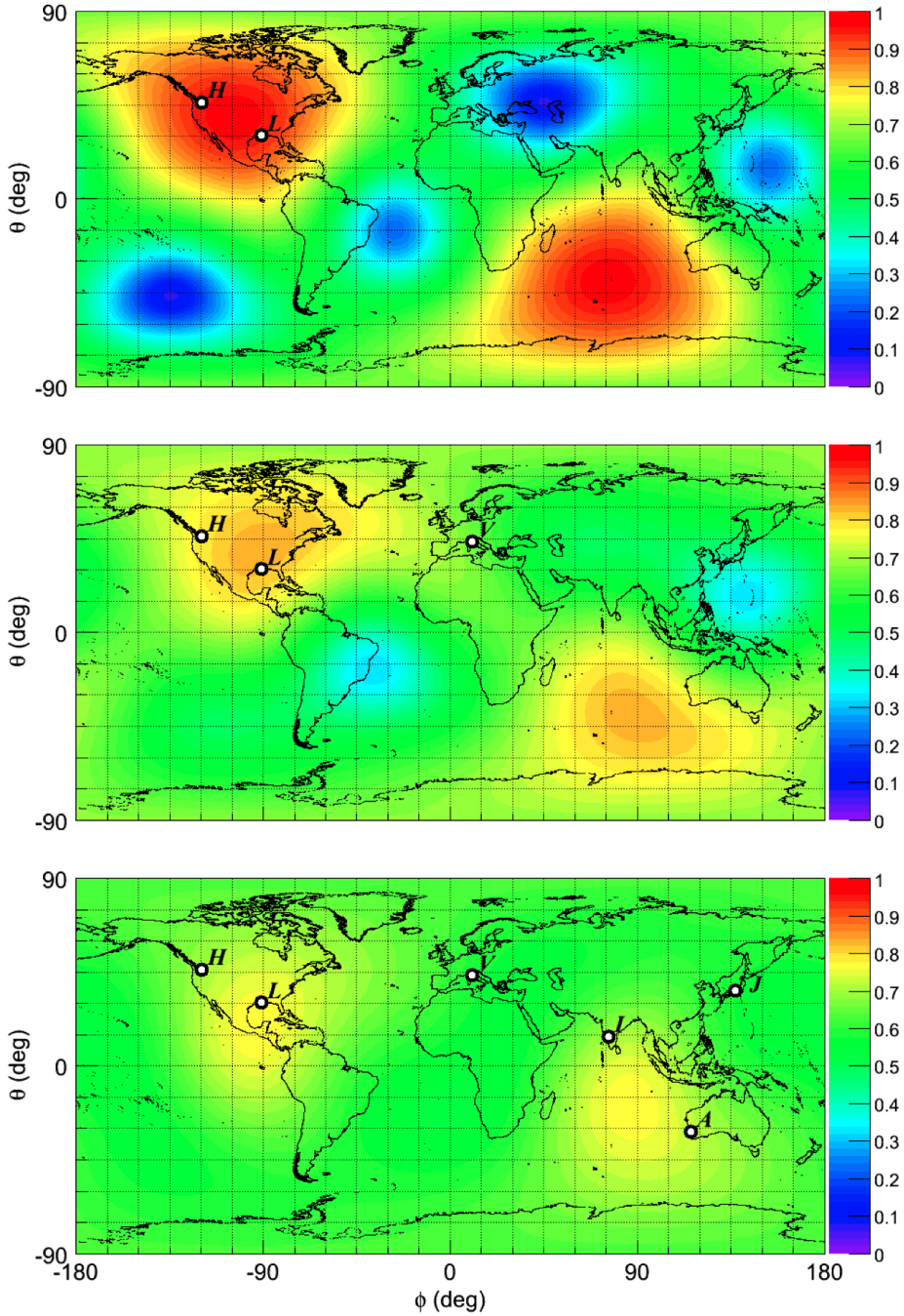

Figure 2.6: Distributions of the network antenna factor as a function of latitude and longitude (λ, ϕ) for different GW detector networks. The plots show the sensitivity of the Hanford-Livingston network (top), the Hanford-Livingston-Virgo network (middle), and a six-detector network (bottom), highlighting how additional detectors improve sky coverage. Source: [95].

are crucial for signal characterization: A detected waveform h depends on five unknowns: the two GW polarizations and three angular parameters (sky location and polarization angle). A single detector provides only two equations, leaving the system under-determined. Additional detectors increase the number of constraints, improving source localization and parameter estimation. To quantify the response of a detector network, one can define the *network antenna power pattern* P_N as the sum of the individual antenna power patterns P_k of each detector:

$$P_N(\lambda, \phi) = \sum_k (F^2_{+,k} + F^2_{\times,k}), \tag{2.2.12}$$

where (λ, ϕ) are the Earth-based longitude and latitude coordinates. The functions $F_{+/\times,k}$ describe each detector's response, requiring an appropriate transformation from the chosen celestial reference frame. Figure 2.6 illustrates the distribution of the network antenna power patterns from Equation (2.2.12) for different detector networks [95]. As the number of detectors increases, blind spots diminish, and the ability to localize sources improves. The figure compares the sensitivity of different detector networks, demonstrating how additional detectors enhance sky coverage.

2.3 Data analysis

The ability of a GW detector to measure an incoming signal depends on its antenna pattern, as shown in Section 2.2.3, which determines the strength of the response based on the wave's direction and polarization. However, real observations are affected by noise, meaning that the detector output is not just the GW signal but also unwanted fluctuations.

The output of the detector is a time series $x(t)$, which includes all the noise contributions briefly introduced in Section 2.2.1, $n(t)$, and also a possible GW signal $s(t)$, so $x(t) = s(t) + n(t)$. The detector records data at discrete time steps Δt with a sampling frequency $f = 1/\Delta t$ over a finite duration, such that

$$t_j = t_0 + j\Delta t \;\rightarrow\; x(t_j) = x_j = s_j + n_j \;,\; j = 0, 1, ..., N-1. \tag{2.3.1}$$

To analyze GW signals efficiently, it is often advantageous to work in the frequency domain. For short-duration signals, such as those from CBCs, the detector's response can be considered time-independent to a good approximation, depending primarily on the frequency. This simplification holds because the signal duration is short compared to the timescale over which the detector's orientation and sensitivity change significantly due to Earth's rotation or orbital motion. However, for longer signals – such as CWs or the extended inspirals observable with 3G ground-based detectors such as ET and CE, or space-based observatories like LISA – the time dependence of the detector's motion and response becomes non-negligible. In these cases, a more general treatment in the time-frequency domain or fully time-dependent modeling is required to accurately capture the signal and extract physical information.

In the following, we characterize the noise properties of GW detectors in Section 2.3.1. We then introduce the fundamentals of matched filtering, the primary method used for signal detection, in Section 2.3.2. Finally, in Section 2.3.3, we present the basic concepts of Bayesian inference, which serves as the standard statistical framework for GW astronomy and parameter estimation studies. Appendix A provides details on the Fourier conventions used in this project, along with key theorems and definitions relevant to signal processing in GW data analysis.

2.3.1 Noise characterization

The overall effect of noise is often well described as a random process, typically assumed to follow a Gaussian distribution. This assumption stems from the *Central Limit Theorem* [96], which states that a process composed of many independent subprocesses tends to be Gaussian, regardless of the individual distributions of its components. Noise is classified as *white* when its power is evenly distributed across all frequencies, while *coloured* noise exhibits frequency-dependent variations. A random process is considered *stationary* if its statistical properties remain constant over time. In this case, the *Ergodic Theorem* [97] ensures that time averages over a single realization, $n(t)$, are equivalent to ensemble averages over multiple realizations. When considering a sufficiently small frequency band or a short time, detector noise can be approximated as white, stationary, and Gaussian. Moreover, without loss of generality, we assume that $\langle n(t)\rangle = 0$, where the angle brackets denote an ensemble average. For a stationary random process $n(t)$, the *Ergodic theorem* allows us to express the autocorrelation function $C_n(t)$ (A.C.3) as

$$C_n(t) = \lim_{T\to\infty} \int_{-T/2}^{T/2} \mathrm{d}t' n(t')n(t+t') = \langle n(t')n(t+t')\rangle. \tag{2.3.2}$$

Here, $C_n(0)$ corresponds to the second moment $\langle n^2\rangle$ of the random process, which, for zero mean noise, is also its variance σ_n^2. In the case of white noise, where values at different times are statistically independent, $C_n(t)$ is proportional to a Dirac delta function $\delta(t)$. Using Equation (A.C.4), we see that white noise has a flat power spectrum, meaning that its total power is uniformly distributed across all frequencies. By combining the autocorrelation function from Equation (2.3.2) with the definition of the Power Spectral Density (PSD) in Equation (A.C.4), we arrive at the standard expression for the *one-sided PSD* in the case of stationary Gaussian noise:

$$S_n(f) = 2\int_{-\infty}^{\infty} \mathrm{d}t \langle n(t')n(t+t')\rangle e^{-2i\pi ft}, \tag{2.3.3}$$

The *two-sided PSD* is half of this value. From this, it follows that noise components in the frequency domain are statistically independent for different frequencies $f \neq f'$:

$$\langle \tilde{n}(f)\tilde{n}^*(f')\rangle = \delta(f-f')\frac{S_n(f)}{2}. \tag{2.3.4}$$

If $n(t)$ is dimensionless, $S_n(f)$ has units of Hz^{-1}. The detector noise is often characterized by $\sqrt{S_n(f)}$, known as the *spectral amplitude* (see Figure 2.4 and Figure 2.5). Each noise curve exhibits a distinct frequency dependence, indicating that GW detector noise is colored.

In reality, noise is not perfectly Gaussian. Instead, it is typically modeled as a combination of Gaussian noise and non-Gaussian artifacts, such as spectral "lines" and "glitches". Spectral lines are narrow-band features caused by periodic processes in the detector and its environment, such as electrical power lines. "Glitches" are short, transient noise bursts of instrumental or environmental origin that can mimic GW signals.

2.3.2 Matched filtering: GW detections

Detecting a signal $s(t)$ that is much weaker than the detector noise $n(t)$ requires an optimal detection strategy. For stationary Gaussian noise, the most effective method when the

expected signals are theoretically known is *matched filtering* [98]. In the following, we provide a brief introduction, following the discussion in Ref. [81], Chapter 7.

The core idea of this method is to compute the inner product between the detector output $x(t)$ and a filter function $h(t)$, chosen to maximize the signal-to-noise ratio (SNR). The SNR is defined as the ratio between S, the expected filtered output when the signal is present, and N, the root-mean-squared value of the filtered data when the signal is absent. Using the definition of $S_n(f)$ in Equation (2.3.3), and noting that $\langle n(t) \rangle = 0$, one can derive [92]

$$\mathrm{SNR} = \frac{S}{N} = \frac{\int_{-\infty}^{\infty} \mathrm{d}f \tilde{x}(f)\tilde{h}^*(f)}{\left(\int_{-\infty}^{\infty} \mathrm{d}f \frac{S_n(f)}{2}|\tilde{h}(f)|^2\right)^{1/2}}. \tag{2.3.5}$$

We now define the inner product between two real functions in terms of $S_n(f)$ as

$$(A(t)|B(t)) = 4 \cdot \mathrm{Re} \int_0^{\infty} \mathrm{d}f \frac{\tilde{A}^*(f)\tilde{B}(f)}{S_n(f)}, \tag{2.3.6}$$

which leads to the SNR expression:

$$\mathrm{SNR} = \frac{(s|u)}{(u|u)^{1/2}}, \text{ with } \tilde{u}(f) = \frac{S_n(f)}{2}\tilde{h}(f). \tag{2.3.7}$$

To maximize the SNR (2.3.7), the template h must be chosen such that its scalar product with s is maximized, i.e., u is parallel to h, leading to

$$\tilde{h}(f) \propto \frac{\tilde{s}(f)}{S_n(f)}. \tag{2.3.8}$$

Substituting this optimal filter into Equation (2.3.7), we obtain the optimal SNR:

$$\mathrm{SNR}^2_{\mathrm{opt}} = (s|s) = 4 \int_0^{\infty} \mathrm{d}f \frac{|\tilde{s}(f)|^2}{S_n(f)}. \tag{2.3.9}$$

GW detections correspond to statistically significant SNR peaks relative to a background noise estimate. This means that detections are not based solely on the SNR of a signal, but rather on how likely such an SNR could arise from instrumental noise or glitches. The background distribution is typically estimated using time-shifted analyses, which remove any coincident astrophysical signals while preserving the noise statistics. Additional discriminators, such as the χ^2 test [61, 99, 100], are used to further distinguish astrophysical signals from transient noise artifacts. This detection process – known as the *search* stage (see e.g. [100] or [101] for an alternative approach with the GstLAL pipeline) – aims to identify statistically significant candidate events by maximizing sensitivity while controlling the false alarm rate. Once candidate events are identified and their significance estimated, a more computationally intensive parameter estimation (PE) stage follows to infer the physical properties of the sources. While the search determines whether an event is likely astrophysical, the PE step assumes the presence of such signal and explores the posterior distributions of its parameters.

To efficiently cover the parameter space in search pipelines, especially for CBCs, a *template bank* is constructed – a discrete set of waveform templates spanning various physical parameters. For instance, Ref. [102] introduces a geometric approach to template

placement, using a *mismatch* metric in parameter space to guide the efficient and uniform distribution of templates. Search strategies vary depending on the expected properties of the GW sources. Modeled searches, such as those targeting CBCs, use *matched filtering* to scan the data with template waveforms and identify peaks in the matched-filter SNR. These pipelines are highly sensitive to weak signals with known morphology. In contrast, unmodeled or burst searches rely on excess power in the time-frequency representation of the data and are designed to capture generic transient signals, including those from sources not well described by existing models. Template banks are designed for computational efficiency, which limits their resolution in parameter space. As a result, matched-filter searches only yield approximate estimates of the source parameters. A more accurate and detailed analysis is performed in the PE phase. This step typically involves Bayesian inference techniques and requires evaluating waveform models millions to billions of times – orders of magnitude more than the number of templates used in the search phase. In Section 2.3.3, we introduce the basics of Bayesian inference as applied to PE, highlighting how these methods allow us to extract astrophysical information from detected signals with quantified uncertainties.

For future detectors such as LISA, the separation between the search and parameter estimation stages is less clear-cut. Due to the long-duration nature of the signals and the possibility of multiple overlapping sources, more general and global inference strategies may be required. In such cases, disentangling signals and inferring source properties becomes a tightly coupled problem, representing one of the key challenges in the data analysis of next-generation observatories.

2.3.3 Parameter estimation: Bayesian inference

Bayesian inference provides the fundamental statistical framework for GW astronomy, enabling the characterization of detected signals through parameter estimation. This approach leverages Bayes' theorem to derive the probability distribution of the source parameters, Π, given an observed GW signal in the detector data, d, and assuming a theoretical signal model, $h_M(t;\Pi)$. According to Bayes' theorem, the posterior probability distribution for Π given the model h_M, is expressed as

$$P(\Pi|d,h_M) = \frac{P(d|\Pi,h_M)\cdot P(\Pi,h_M)}{P(d,h_M)}, \tag{2.3.10}$$

where $P(d|\Pi,h_M)$ is the likelihood function, quantifying the probability of observing d given specific parameters Π. The term $P(\Pi,h_M)$ represents the prior probability distribution, encapsulating prior knowledge or assumptions about the parameters before considering the data. The denominator, $P(d|h_M)$, known as the *evidence* of the model hypothesis h_M, normally represented by $\mathcal{Z}$, is given by

$$\mathcal{Z} = P(d|h_M) = \int \mathrm{d}\Pi P(d|\Pi,h_M)P(\Pi,h_M). \tag{2.3.11}$$

This quantity serves as a normalization factor and is crucial in Bayesian model selection, allowing comparison between competing models. In the context of GW astronomy, Bayesian inference is employed not only to estimate source parameters but also to assess the relative likelihood of different waveform models or astrophysical scenarios. Given two competing models, A and B, one can compare their relative probabilities given the observed detector

data through the odds ratio $\mathcal{O}_{\mathrm{A/B}}$:

$$\mathcal{O}_{\mathrm{A/B}} = \frac{P(h_{\mathrm{A}}|d)}{P(h_{\mathrm{B}}|d)} = \frac{P(h_{\mathrm{A}})P(d|h_{\mathrm{A}})}{P(h_{\mathrm{B}})P(d|h_{\mathrm{B}})} = \tag{2.3.12}$$

$$= \frac{P(h_{\mathrm{A}})}{P(h_{\mathrm{B}})}\frac{\mathcal{Z}_{\mathrm{A}}}{\mathcal{Z}_{\mathrm{B}}} = \frac{P(h_{\mathrm{A}})}{P(h_{\mathrm{B}})}\mathcal{B}_{\mathrm{A/B}}. \tag{2.3.13}$$

The first term, $P(h_{\mathrm{A}})/P(h_{\mathrm{B}})$, represents our prior belief about the relative likelihood of A versus B events occurring in the universe. This prior can be informed by astrophysical expectations or inferred from previous GW detections, which provide empirical rate estimates for different source populations. The second term, $\mathcal{B}_{\mathrm{A/B}} = \mathcal{Z}_{\mathrm{A}}/\mathcal{Z}_{\mathrm{B}}$, is the *Bayes factor*, which quantifies how well the observed data supports one model over the other. In GW data analysis, the logarithm of the Bayes factor, $\log_{10} B_{\mathrm{A/B}}$, is commonly used to compare different models or assess distinct source features within the same dataset. A positive value of $\log_{10} B_{\mathrm{A/B}}$ favors model A over model B, and a threshold of $\log_{10} B_{\mathrm{A/B}} > 1$ is typically considered strong evidence in support of A [103].

For a detector with stationary, Gaussian noise, the likelihood function takes the form

$$P(d|\Pi, h_M) \propto \exp\left[-\frac{1}{2}\langle d - h_M(\Pi)|d - h_M(\Pi)\rangle\right], \tag{2.3.14}$$

where the noise-weighted inner product is defined as

$$\langle A|B\rangle = 2\int_{f_{\mathrm{low}}}^{f_{\mathrm{high}}} \mathrm{d}f \frac{\tilde{A}^*(f)\tilde{B}(f) + \tilde{A}(f)\tilde{B}^*(f)}{S_n(f)}. \tag{2.3.15}$$

Here, tildes denote Fourier transforms, asterisks indicate complex conjugation, and $S_n(f)$ represents the one-sided PSD of the detector (2.3.3). The integration limits $[f_{\mathrm{low}}, f_{\mathrm{high}}]$ define the relevant frequency range for the analysis, which depends on the detector's sensitivity across different frequencies. For a network of detectors, assuming uncorrelated noise, the total likelihood function is obtained as the product of individual detector likelihoods. It is worth noting that Equation (2.3.15) generalizes Equation (2.3.6) to complex functions while incorporating the detector's sensitive frequency range.

Although Π generally represents a set of astrophysical parameters which characterize the GW source, we are typically interested in analyzing one parameter at a time. In that case, we need to *marginalize* or integrate over all the other parameters we are not interested in, often referred to as "nuisance parameters". The marginalized posterior for the parameter of interest, Π_i, is then given by

$$P(\Pi_i|d, h_M) = \int \left(\prod_{k\neq i} \mathrm{d}\Pi_k\right) P(\Pi|d, h_M). \tag{2.3.16}$$

2.3.3.1 Sampling methods for compact binary coalescences

Compact binaries are the main topic of this thesis, and further details on these sources can be found in Chapter 3 and Chapter 4. These are currently the only sources detected by GWs so far, primarily because their waveform anatomy is well understood and modeled across the parameter space (for a deeper dive into the fascinating world of waveform models, the reader will need to wait). Due to the development of these models, known as

waveform approximants, predicting the data morphology d given certain parameters Π becomes straightforward. Thus, computing the posterior as given in Equation (2.3.10) is an inverse problem, which is computationally more challenging than forward problems. One might naively attempt to compute the posterior by discretizing each parameter dimension into, say, 10 bins. However, a generic compact binary system is described by as many as 18 intrinsic and extrinsic parameters. This would require evaluating the likelihood function 10^{18} times. To overcome this challenge, PE in CBC studies relies on stochastic sampling techniques, which are far more efficient at exploring high-dimensional and complex parameter spaces. These methods can reduce the number of required likelihood evaluations to a practical range, typically between 10^5 and 10^8. Two main techniques, Markov Chain Monte Carlo (MCMC) [104, 105] and nested sampling [106], are widely used for this purpose. We point to Ref. [107] for an introduction to Bayesian inference in GW astronomy, including a detailed description on these samplers, and in the following we just provide the basics of each technique.

MCMC sampling was first introduced in Ref. [104] and later extended in Ref. [105]. A recent overview on current MCMC methods used in astronomy can be found in Ref. [108]. These methods generate processes, typically referred to as *walkers*, which undergo a random walk through the posterior distribution. The probability of moving to any given point is determined by the transition probability of the Markov chain. This approach allows for estimating the posterior probability distribution by tracking the positions of the walkers. However, the MCMC sampling is highly sensitive to the initial positions of the walkers, requiring a "burn-in" phase to ensure that the walkers reach a steady state before they start sampling the posterior distribution. Additionally, the user must define a termination condition, which involves understanding how many samples are needed to accurately describe the posterior. Walkers can also struggle to find multimodalities in the posterior distribution, particularly if the regions between modes have low probability. This issue can only be mitigated by generating a large number of walkers. Consequently, MCMC methods can be computationally expensive, especially in high-dimensional spaces, and many variants of this sampling have been proposed in the literature to improve its performance.

Nested sampling was the first widely used alternative to MCMC in GW astronomy. Unlike a MCMC sampler, which are primarily designed to draw samples from the posterior distribution, nested sampling was developed with the goal of efficiently computing the Bayesian evidence $\mathcal{Z}$ (or marginal likelihood). This quantity plays a central role in model selection, enabling comparisons between different waveform models or hypotheses (e.g., BNS vs NSBH vs BBH systems, or eccentric vs QC). The method begins by populating the parameter space with a set of "live points" sampled from the prior distribution. At each iteration, the live point with the lowest likelihood is removed and replaced by a new point with a higher likelihood, thereby iteratively exploring nested contours of increasing likelihood. To obtain posterior samples, each removed point is assigned a weight proportional to its posterior probability. The evidence is computed by summing the product of the likelihood and the prior volume associated with each removed point. Because the algorithm systematically moves toward regions of higher likelihood, it becomes possible to estimate an upper bound on the remaining contribution to the evidence. This is done by assuming the remaining prior volume is uniformly populated by the current highest-likelihood live point. The algorithm terminates once the current estimate of the log-evidence is sufficiently close to this upper bound. In practice, this condition is expressed

as the difference between the computed log-evidence and its estimated upper limit, and the sampling is stopped when this difference satisfies dlogz < 0.1. Unlike MCMC algorithms, nested sampling is not trivially parallelizable, and posterior samples do not accumulate linearly with runtime. However, it can outperform MCMC in certain settings, particularly when evaluating the evidence or navigating multi-modal or degenerate posteriors, which frequently arise in GW analyses. As a result, nested sampling has become the standard approach within the LVK Collaboration, particularly in PE studies involving CBCs. It is also the method used for the results presented in this thesis in Chapter 6, Chapter 7, and Chapter 8.

To ensure the reliability of a PE run, it is essential to monitor convergence diagnostics throughout the sampling process, regardless of the sampler used. In nested sampling, one of the key indicators is the evolution of the log-evidence estimate, particularly the value of dlogz, which quantifies the estimated remaining contribution to the evidence. Setting a sufficiently low threshold, such as dlogz < 0.1, ensures that additional samples are unlikely to significantly change the result. For MCMC-based methods, convergence is commonly assessed using metrics such as the Gelman-Rubin statistic [109] and autocorrelation lengths [110]. A standard practice across any sampling method is to inspect the stability of posterior distributions as more samples are accumulated, often by comparing independent runs or *chains* initialized with different random seeds. This helps confirm robustness, assess the number of effective posterior samples and sampling efficiency, and enables a visual inspection of trace plots across chains to identify potential issues with convergence.

Currently, all these sampling algorithms are implemented in public codes that are widely used within the GW community. Specifically, the two main GW PE codes that implement stochastic sampling techniques are `LalInference` [111, 112] and `Bilby` [113], implemented in `C` and `python`, respectively. Both codes feature implementations of MCMC samplers: `LALInferenceMCMC` and `bilby-MCMC` [114], as well as nested sampling implementations: `LALInferenceNest` and `bilby-dynesty` [115, 116]. In this work, we primarily rely on the `dynesty` implementation [116], both through the `bilby_pipe` [117] package, a python tool for automating the process of running `bilby` on computing clusters, and through `parallel_bilby` [118], which implements a parallelizable version of nested sampling across nodes. Other codes are also available, such as `pycbc-inference` [119], `Eryn` [120], and `bajes` [121].

CHAPTER 3

Gravitational waves from binary black holes

As discussed in the previous chapter, CBCs are among the most efficient astrophysical processes for generating GWs. In these systems, a pair of dense objects orbit one another, emitting gravitational radiation that carries away orbital energy. This energy loss causes the objects to spiral closer together, increasing their orbital velocity and enhancing the GW emission in a runaway process that ultimately leads to their merger. Because black holes (BHs) are the most compact known objects, they are also the most efficient sources of detectable GWs, as discussed in relation to Equation (2.1.25) and Equation (2.1.26). Indeed, events identified as binary BH (BBH) mergers account for the majority of GW detections currently reported by the LVK Collaboration [1–4].

This chapter provides an overview of GWs emitted by BBHs. In Section 3.1, we introduce fundamental aspects of BHs in GR and define the parameter space of BBH systems. In Section 3.2, we examine the morphology of GW signals across the inspiral-merger-ringdown (IMR) phases, reviewing the different techniques used to model BBH systems across its parameter space. Finally, in Section 3.3, we discuss the decomposition of the GW signal into spherical harmonic modes – a common and fruitful approach for representing the angular dependence of the waveform.

3.1 Introduction to black holes

A BH is a region of spacetime from which neither matter nor radiation can escape to the distant universe, due to the presence of the *event horizon*: the boundary of a causally disconnected region of spacetime with respect to null infinity. In classical GR, the BH region typically contains "trapped surfaces" (see e.g. [122]), which can be interpreted as local analogs of the event horizon. Assuming the validity of GR, as well as other conditions on causality and the behavior of matter, the singularity theorems [123] then predict the development of a singularity in the BH region of spacetime. These extreme objects are direct prediction of GR and arise as solutions to the EFE (2.1.1). The first exact BH solution was found by Karl Schwarzschild in 1916 [124], shortly after Einstein formulated GR. In Schwarzschild coordinates (t, r, θ, ϕ), the Schwarzschild metric takes the form

$$\mathrm{d}s^2 = -\left(1 - \frac{R_s}{r}\right) c^2 \mathrm{d}t^2 + \left(1 - \frac{R_s}{r}\right)^{-1} \mathrm{d}r^2 + r^2(\mathrm{d}\theta^2 + \sin^2\theta \mathrm{d}\phi^2), \tag{3.1.1}$$

where R_s is the Schwarzschild radius, given by $R_s = \frac{2GM}{c^2}$. This solution describes the gravitational field of a spherically symmetric, non-rotating, and uncharged BH with mass M in vacuum. The Schwarzschild metric is asymptotically flat, and at sufficiently large distances from the central mass (i.e., for $r \gg r_s$), slowly moving particles follow trajectories that closely resemble those predicted by Newtonian gravity. The Schwarzschild solution exhibits two singularities: one at $r = 0$, which is an intrinsic curvature singularity, and another at the Schwarzschild radius r_s. The nature of this second singularity was not fully understood at the time, but it is now recognized as the *event horizon*, a surface beyond which causal influences can only move inwards. Importantly, this singularity can be avoided by using appropriate coordinates. A complete description of the Schwarzschild metric was later provided by Martin Kruskal [125], who introduced the Kruskal-Szekeres coordinates, covering the entire spacetime manifold.

This breakthrough occurred during the early years of the golden age of GR, which further fueled interest in the study of compact objects. During this period, more general solutions for BHs were discovered. In 1963, Roy Kerr found the equilibrium solution for rotating BHs [126], and in 1965, Ezra Newman solved the EFE for a point mass that is both rotating and charged [127]. The no-hair theorem [128, 129] also emerged during the golden era. It states that a stationary BH solution is completely characterized by only three parameters: mass M, charge Q, and angular momentum $\vec{S}$, as described by the Newman solution. Furthermore, while the mass of a BH can take any positive value, the other two quantities must satisfy the following constraint (in geometric units $G = c = 1$) [130]:

$$Q^2 + \frac{|\vec{S}|^2}{M^2} \leq M^2. \tag{3.1.2}$$

A well-established pathway for BH formation is the gravitational collapse of massive stars. This occurs when a star's internal pressure can no longer resist its own gravitational pull – typically because there is insufficient nuclear fuel to sustain stellar nucleosynthesis. As a result, the core temperature drops below the threshold needed to counteract collapse. If the mass of the remnant – i.e., the compact object left behind after the explosion – exceeds the Tolman–Oppenheimer–Volkoff (TOV) limit [131], no known form of degeneracy pressure can halt the collapse, and the star inevitably forms a black hole. While the exact value of the TOV limit remains uncertain, theoretical work places the limit at approximately $(1.5 - 3.0)\ \mathrm{M}_\odot$ [132, 133]. Given the strength of the electromagnetic force, these BHs are expected to be electrically neutral, just as the predecessor star was. If a net charge were to exist on an astrophysical body, it would repel and attract particles, eventually neutralizing itself. Rotation is, however, an expected property of general BHs. According to Equation (3.1.2), the angular momentum must satisfy

$$|\vec{S}| \leq \frac{GM^2}{c}. \tag{3.1.3}$$

We can define a dimensionless spin parameter $\vec{\chi} = \frac{c\vec{S}}{GM^2}$, such that

$$0 \leq |\vec{\chi}| \leq 1. \tag{3.1.4}$$

Thus, general BHs are characterized by their mass M and angular momentum or *spin* χ, and are referred to as *Kerr BHs*, after Roy Kerr, who found their equilibrium solution.

3.1.1 Black hole mass spectrum: Insights from GW observations

The detection of GWs from BBHs has significantly contributed to understanding the possible mass range of BHs, which is one of the key characteristics used by astronomers to classify them. Black holes are generally divided into three categories based on their mass: stellar-mass, intermediate-mass, and supermassive BHs. Additionally, cosmologists hypothesize the existence of a fourth type – primordial BHs (PBHs), which may have been created in the early universe but remain undetected (we point the reader to Ref. [134] for a review on these objects).

Supermassive black holes (SBHs) are typically defined as those with masses exceeding $10^5\ M_\odot$. Observations suggest that nearly every large galaxy, including the Milky Way, hosts a SBH at its center. The origins of these objects remain an active area of research, with several hypotheses proposed for their formation. Some evidence suggests that the earliest SBHs formed within the first billion years after the Big Bang. One possibility is that they originated from the collapse of supermassive stars, providing them with an initial mass advantage. While their formation mechanisms remain uncertain, it is well understood that SBHs can grow by accreting matter from their surroundings or by merging with other BHs – either stellar-mass BHs or other SBHs during galaxy collisions.

On the other hand, stellar-mass BHs (SMBHs) arise from the gravitational collapse of massive stars. As discussed previously, the fate of a collapsing star depends on the mass of its remnant after the explosion. If the remnant mass exceeds the TOV limit ($\sim 3\ M_\odot$) [132, 133], neutron degeneracy pressure is insufficient to prevent further collapse, and the object becomes a BH. However, the exact mass limits of SMBHs remain uncertain. Historically, BHs with masses below $5M_\odot$ had rarely been observed, suggesting the existence of a mass gap where compact objects could not be unambiguously classified as neutron stars or BHs. On the other hand, the masses of SMBHs can range from a few solar masses up to about $100M_\odot$, depending on the progenitor star's properties and its evolution. The upper limit for SMBH formation is constrained by the *pair-instability supernovae* (PISNe), a phenomenon caused by pair production inside very massive stars. In stars with helium core masses between $\sim 130 - 250\ M_\odot$,this process leads to a complete disruption of the star, preventing BH formation [135]. As a result, BHs more massive than $\sim 100\ M_\odot$ cannot form directly from single-star collapse.

The observed mass gap between stellar-mass and supermassive BHs led to the hypothesis of intermediate-mass BHs (IMBHs), which are thought to have masses in the range $100 - 10^5\ M_\odot$. These objects cannot form via the collapse of a single star due to the PISNe mass gap ($130 - 250\ M_\odot$). Similarly, they are unlikely to form through the same mechanisms as SMBHs, as the conditions necessary for their growth are not typically found outside the dense environments of galactic centers. However, over cosmic time, hierarchical mergers –in which smaller BHs merge to form increasingly massive ones– are thought to contribute to the growth of IMBHs. SMBHs, through repeated mergers and accretion, can gradually build up to form these intermediate-mass objects. Additionally, very massive stars exceeding $\sim 250\ M_\odot$ may undergo direct collapse into IMBHs without an explosive event.

The detection of GWs has significantly advanced our understanding of BHs across all mass scales. Observations from the LVK have provided direct evidence of BH mergers, revealing the presence of BHs in previously unexplored mass ranges. Figure 3.1 shows the

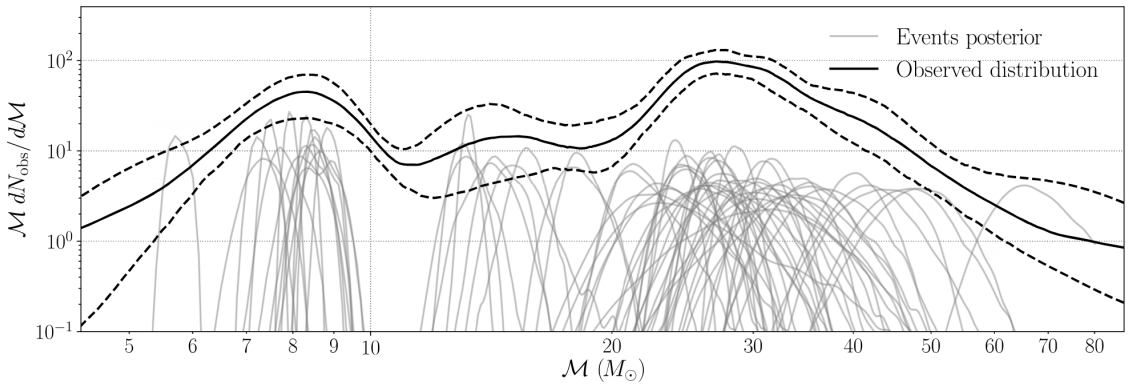

Figure 3.1: Substructure in the source chirp-mass distribution for the BBH mergers in GWTC3 [4] with a false alarm rate (FAR) of $< 1\ \mathrm{yr}^{-1}$. The plot shows the individual event observations (gray) and an inferred chirp-mass distribution (black solid) using an adaptive kernel density estimator. A 90% confidence interval is represented by the black dashed line, obtained through bootstrapping. The kernel bandwidth is optimized for local event density. Source: [136].

source chirp-mass distribution for BBHs observed during the first three observing runs by the LVK Collaboration [4]. The first (and so far only) observational evidence of an IMBH within the PISNe mass gap came from the GW event GW190521 [89, 90], with a source chirp mass $\sim 69 M_\odot$. This event, corresponding to the merger of two SMBHs ($65\mathrm{M}_\odot$ and $85\mathrm{M}_\odot$), resulted in the formation of a 142 $M_\odot$ black hole – placing it within the IMBH pair-instability mass gap range. An extended reanalysis of this event was carried out by the UIB group [137], along with other independent studies [49, 138–141]. Among the more than 90 CBC detections in GWTC-3 [4], notable events which are not BBHs include GW170817 [5] and GW190425 [6], both consistent with BNS mergers with total masses of approximately 3.4 $M_\odot$. Their remnants fall within the previously observed low-mass gap between neutron stars and BHs. The detection of such objects provides valuable insights into the nature of compact objects in this lower mass gap range, where previous electromagnetic observations did not find evidence for these objects.

These discoveries further underscore the transformative role of GW astronomy, opening a new observational window that enables us to explore astrophysical phenomena that are otherwise inaccessible through traditional electromagnetic observations.

3.1.2 The binary black hole parameter space

We now consider binaries of general Kerr BHs, which are fully described by their masses m_1 and m_2, and their spin angular momenta $\vec{S}_1$ and $\vec{S}_2$. It is common to use dimensionless spin parameters, defined as $\vec{\chi}_i = \vec{S}_i/m_i^2$. The intrinsic BBH parameter space is thus eight-dimensional for circular orbits. For eccentric binaries, two more parameters are needed. While there are various ways to define these eccentricity parameters, in this work we specifically use the eccentricity e and the position of the binary in the ellipse at a reference time, defined by the *mean anomaly* l. Alternative definitions and options are discussed in more detail in Section 4.2. While this set of 10 parameters fully describes a BBH system, additional extrinsic parameters are required to characterize the GW signal as detected by an interferometric observatory. As introduced in Chapter 2, these parameters establish the connection between the source and detector frames. The extrinsic parameters,

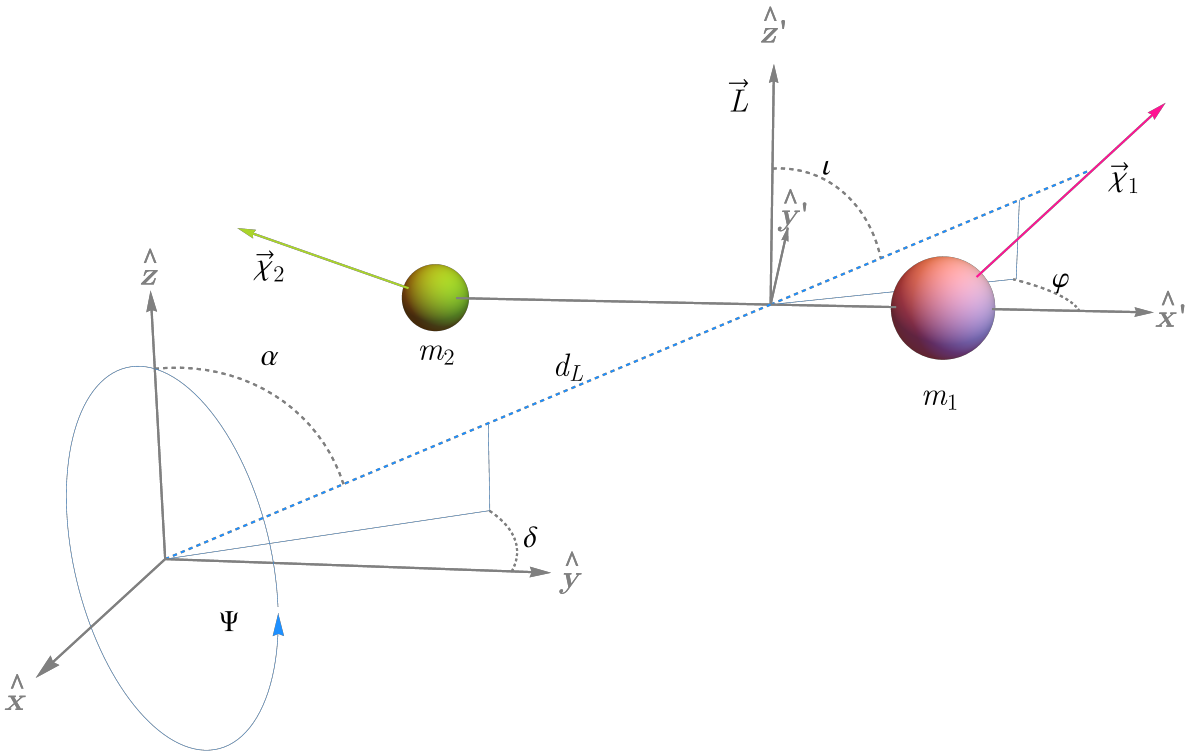

Figure 3.2: Schematic representation of the intrinsic and extrinsic parameters defining a BBH system of masses $m_{\{1,2\}}$ and dimensionless spins $\vec{\chi}_{\{1,2\}}$, alongside the coordinate frame definitions. The detector's inertial frame is denoted by $\{\hat{x}, \hat{y}, \hat{z}\}$, while the source frame is represented by primed coordinates, with the $\hat{z}'$-axis aligned with the orbital angular momentum $\vec{L}$. The frames are connected by the luminosity distance d_L, right ascension α, declination δ, and the polarization angle Ψ. The inclination ι and phase φ angles characterize the orientation of the binary's orbit as seen from the detector's frame. The eccentricity and mean anomaly, describing elliptical orbits, are not shown in this schematic.

as described in Section 2.2.3, include the luminosity distance d_L, right ascension α and declination δ, which specify the source's position in the sky. The polarization angle Ψ determines the orientation of the wave's polarization relative to the detector. Finally, the inclination angle ι and phase φ define the orientation of the binary's orbit as seen from the detector's frame. The source reference frame is typically defined by pointing the z'-axis in the direction of the orbital angular momentum $\vec{L}$ of the binary, which is approximately orthogonal to the plane defined by the two BHs. The orientation of the x'- and y'- axes is however not uniquely fixed. A common convention within the LVK Collaboration is to align the x'-axis along the direction from the lighter to the heavier BH, with the y'-axis completing the right-handed coordinate system [111, 142]. This is typically referred to as the L_0-frame. Figure 3.2 provides a representation of intrinsic and extrinsic parameters which define a BBH system, as well as the frame definitions used in this work.

Although the intrinsic parameters defined above fully characterize the binary system, it is common to introduce additional derived quantities that are especially useful for modeling and interpretation. First, to further reduce the dimensionality of the problem, it is common to adopt geometric units, setting $G = c = 1$. In vacuum GR, where no other fundamental constants are present, this choice implies that the total mass of the system $M = m_1 + m_2$ sets the overall scale. Consequently, the BBH parameter space can often be expressed in terms of dimensionless quantities rather than the individual masses. However,

this simplification breaks down in systems with matter, such as BNS, or in alternative theories of gravity, where additional physical scales and interactions must be considered. To characterize the binary mass properties, we thus define the mass ratio $q = m_1/m_2 \geq 1$, the symmetric mass ratio $\eta = m_1 m_2/(m_1 + m_2)^2$, and the chirp mass, as defined in Equation (2.1.32) The chirp mass is a key parameter in GW analysis, as it governs the leading-order frequency evolution of a binary system as seen in Equation (2.1.34), making it typically the best-measured mass parameter from GW signals.

Since GWs are affected by cosmic expansion, one needs to distinguish between *source-frame masses*, which refer to the intrinsic masses in the binary rest frame, and *detector-frame masses* (or *redshifted masses*), which are observed in our frame and affected by the cosmological redshift z:

$$M_{\text{detector}} = (1 + z) M_{\text{source}} \tag{3.1.5}$$

Observed GW frequencies are redshifted, making source-frame masses appear larger. Consequently, in parameter estimation, detector-frame masses are directly inferred, while source-frame masses require an independent redshift measurement.

In GW astronomy, it is useful to define two effective spin parameters that summarize the dominant spin effects in the binary's dynamics: the *effective inspiral spin parameter* χ_{eff} [143–145], and the *effective spin precession parameter* χ_{p} [146]. A detailed explanation of the impact of BH spins on binary dynamics can be found in Section 4.1. χ_{eff} captures the leading-order spin contributions aligned with the orbital angular momentum and is conserved throughout inspiral [143–145]:

$$\chi_{\text{eff}} = \frac{m_1 \chi_1 + m_2 \chi_2}{M}. \tag{3.1.6}$$

On the other hand, χ_{p} quantifies the in-plane spin effects, representing an average measure of spin precession over multiple cycles [146]:

$$\chi_{\text{p}} = \frac{S_{\text{p}}}{A_1 m_1^2}, \tag{3.1.7}$$

where S_{p} is the maximal projected in-plane spin,

$$S_{\text{p}} = \max(A_1 S_{1\perp}, A_2 S_{2\perp}), \tag{3.1.8}$$

with the coefficients $A_1 = 2 + 3/2q$ and $A_2 = 2 + 3q/2$.

3.2 Gravitational wave morphology

Regardless of the specific properties of a BBH, its GW-driven evolution follows three distinct phases. This general structure also applies to other compact binary systems, such as BNS and NSBH mergers. Figure 3.3 illustrates this evolution using the first detected GW signal, GW150914 [61]. This event originated from a compact binary coalescence with component BH masses of $36^{+5}_{-4} M\odot$ and $29^{+4}_{-4} M\odot$. The merger resulted in a final BH of mass $62^{+4}_{-4} M\odot$, with $3.0^{+0.5}_{-0.5} M\odot$ radiated away as GWs. The underlying mechanism is, however, universal for any compact binary. The *inspiral* is the longest phase, where the two objects orbit each other while gradually losing energy through GW emission. This energy loss causes the orbit to shrink, leading to an increase in both orbital frequency and

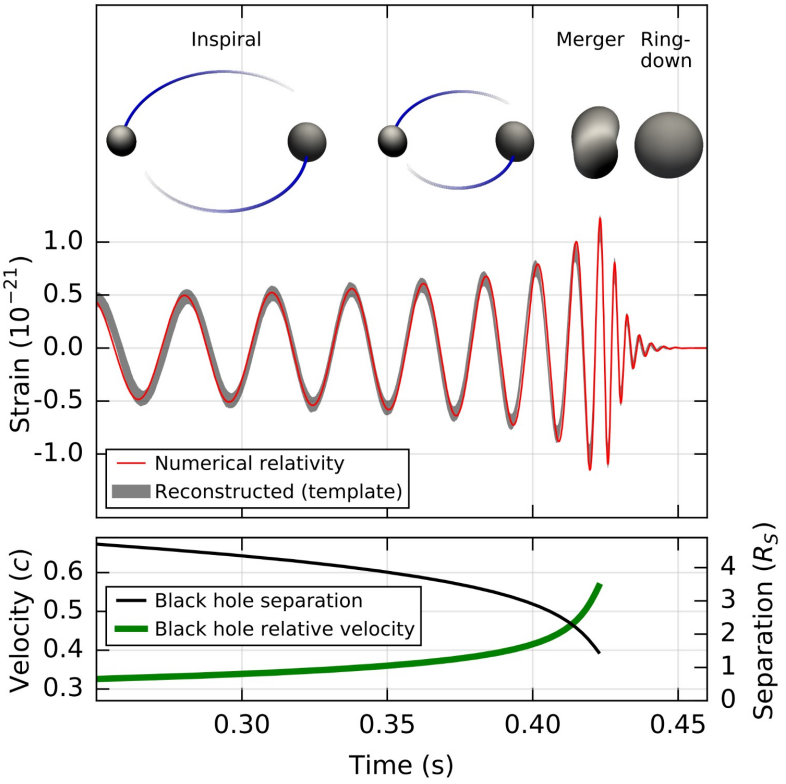

Figure 3.3: Evolution of the GW signal from GW150914, the first detection of a BBH merger. The signal consists of three main phases: the inspiral, during which the BHs gradually spiral toward each other; the merger, where they coalesce into a single BH; and the ringdown, as the remnant settles into a final stable state, typically described by a Kerr BH. *Top*: GW strain amplitude, highlighting the different phases of the binary's evolution. The solid red line corresponds to a numerical relativity (NR) waveform for a system with parameters consistent with those inferred from GW150914 (`SXS:BBH:0305` [147]), while the shaded gray region shows the 90% credible interval of the observed signal, modeled using BBH template waveforms [148]. *Bottom*: Evolution of the binary's effective Keplerian separation in units of the Schwarzschild radius (R_s) and the relative velocity, expressed via the post-Newtonian parameter v/c. Source: [61].

Keplerian velocity, given $v = (GM\pi f)^{1/3}$ (see bottom panel of Figure 3.3). The emission of stronger GWs further accelerates the inspiral, bringing the objects closer together. This process culminates in the *merger*, the moment of coalescence, where the GW amplitude reaches its peak. The final phase, the *ringdown*, follows as the remnant BH radiates away distortions and settles into a stationary Kerr black hole. The amplitude of the GWs emitted reflects this evolution (see the top panel of Figure 3.3). During the inspiral, the amplitude increases as the objects spiral inward. The merger corresponds to the peak amplitude, after which the ringdown phase exhibits an exponential decay, quickly making the signal undetectable. While this describes the general evolution in BBH coalescences, the BH spins and the binary's ellipticity affect the waveform's morphology. Specifically, spins misaligned with the binary's orbital angular momentum (roughly orthogonal to the orbital plane) cause a modulation of the signal, known as *precession*. This occurs because the orbital plane no longer remains fixed, causing the direction of GW emission to change over time. In the case of elliptical orbits, the frequency evolution is influenced

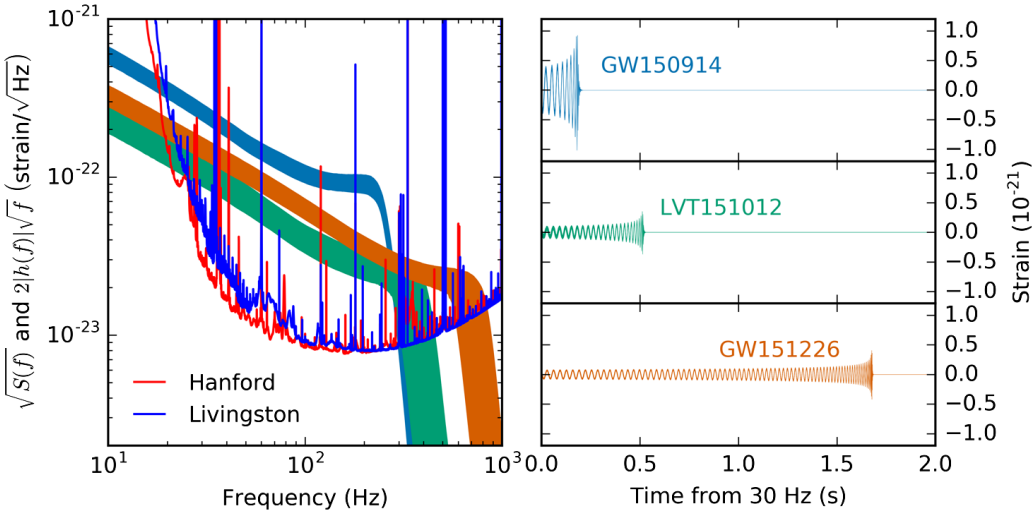

Figure 3.4: Representation of the three BBH events detected during GWTC-1: GW150914, GW151226, and LVT151012. *Left panel*: Amplitude spectral density of the total strain noise in the H1 and L1 detectors, overlaid with the recovered signals, scaled to illustrate their relative SNR. *Right panel*: Time evolution of the reconstructed signals as they enter the detectors' sensitive band at 30 Hz. The shaded regions indicate the 90% credible intervals from a Bayesian analysis using a nonprecessing spin waveform model. Source: [149].

by the varying distance between the objects at different points in the orbit, leading to additional modulations. A detailed description of these dynamic effects from precession and eccentricity in BBH systems is provided in Chapter 4.

GW detections are most naturally described in the frequency domain, as discussed in Section 2.3. The ability to detect a signal depends on the detector's sensitivity during each observing run, characterized by the noise PSD curves defined in Equation (A.A.3). When the GW signal's frequency sweeps through the detector's sensitive band, it may rise above the noise floor and become detectable. Figure 3.4 illustrates the three BBH events detected during GWTC-1 [1, 149], showing both their time domain and frequency domain representations. The left panel presents the recovered signals relative to the detector noise, demonstrating how the SNR varies across different frequencies. The right panel shows the time evolution of these signals as they enter the detector's sensitive band at 30 Hz. This figure provides a complementary view to the time-domain morphology discussed earlier. In the frequency domain, the GW amplitude initially decreases with frequency during the inspiral, reflecting the accumulation of many cycles at lower frequencies. The merger phase follows with a slower falloff of the amplitude. Finally, the ringdown appears as a sharp, exponential decay at high frequencies. Notably, while the ringdown corresponds to an exponential decay in the time domain due to the damped oscillations of the final BH (see Section 3.3), its steep falloff in the frequency domain results from the Lorentzian-like shape of the quasinormal mode (QNM) spectrum. This falloff also receives residual contributions from the inspiral and merger phases, whose spectral content can extend beyond the ringdown peak and influence the overall shape of the signal at high frequencies.

The waveform duration and structure depend on the binary's mass and spin. For instance, GW150914, the most massive event in this set, lasted only a few cycles but exhibited the largest amplitude, with the merger signal well above the noise floor. In contrast, GW151226, a lower-mass event, had a weaker amplitude but spanned a much

broader frequency range, reaching nearly 800 Hz and displaying many more cycles in the detector's band.

3.2.1 IMR signal: Approximation methods

Several techniques have been developed to provide an accurate description of the full IMR evolution of CBCs. In Section 2.1.2.1, we provided a qualitative description of the GWs emitted by a compact binary system, and while the estimates derived from these simple approximations offer valuable insights, more sophisticated methods are needed for GW data analysis.

During the early stages of the inspiral, the system can be accurately described using the *post-Newtonian* (PN) *approximation*, which expands the dynamics in powers of the PN velocity parameter v/c, where v is the characteristic orbital velocity. PN expansions [82] of Equation (2.1.33) and Equation (2.1.29) improve the accuracy of the description by incorporating corrections in powers of $(v/c)^2$. However, as the binary components approach relativistic speeds, particularly during the last orbits and the merger, these approximations begin to break down. In this regime, PN methods become inadequate and the EFE must be solved numerically. Hence, the complete description of the GW signal from compact binaries became feasible only after breakthroughs in NR simulations in 2005 [150–152].

For general sources it is however hopeless to solve the problem via a rigorous deduction within the exact theory of GR, and we have to rely to approximation methods. In some regions of the parameter space, alternative methods such as BH perturbation theory and gravitational self force remain valid even at small separations. Figure 3.5 provides a schematic overview of the different modeling approaches applied across the BBH parameter space. In the following, we will explore these methods in more detail, discussing their applicability and limitations.

3.2.1.1 Numerical relativity

Numerical relativity (NR) is a branch of computational physics dedicated to solving the EFE in the strong-field regime, where spacetime curvature is highly nonlinear and analytical solutions are not feasible. This regime governs extreme astrophysical phenomena, such as the merger of BBHs, the formation and evolution of dynamical horizons [153], and the properties of the remnant BH [154]. Additionally, NR provides a powerful tool for testing GR, enabling constraints on possible deviations or uncovering new physics [155–158].

In this highly nonlinear regime, solving the EFE requires NR, which involves direct integration of the full dynamical field equations using high-performance computing. This became feasible only in 2005, with breakthroughs by Pretorius [150], Campanelli et al. [151], and Baker et al. [152]. A well-posed mathematical model ensures a unique, bounded solution that continuously depends on initial data – an essential property for reliable numerical simulations. However, establishing the well-posedness of the EFE is not straightforward; it depends both on the choice of gauge and on how the equations are split between evolution equations and constraints when formulating the EFE as an initial value problem. To facilitate numerical evolution, different formulations of the EFE have been developed, including the Arnowitt-Deser-Misner (ADM) formalism [159, 160], the Baumgarte-Shapiro-Shibata-Nakamura (BSSN) formulation [161, 162], and the Generalized Harmonic Gauge (GHG) approach [163]. Since the NR breakthrough in

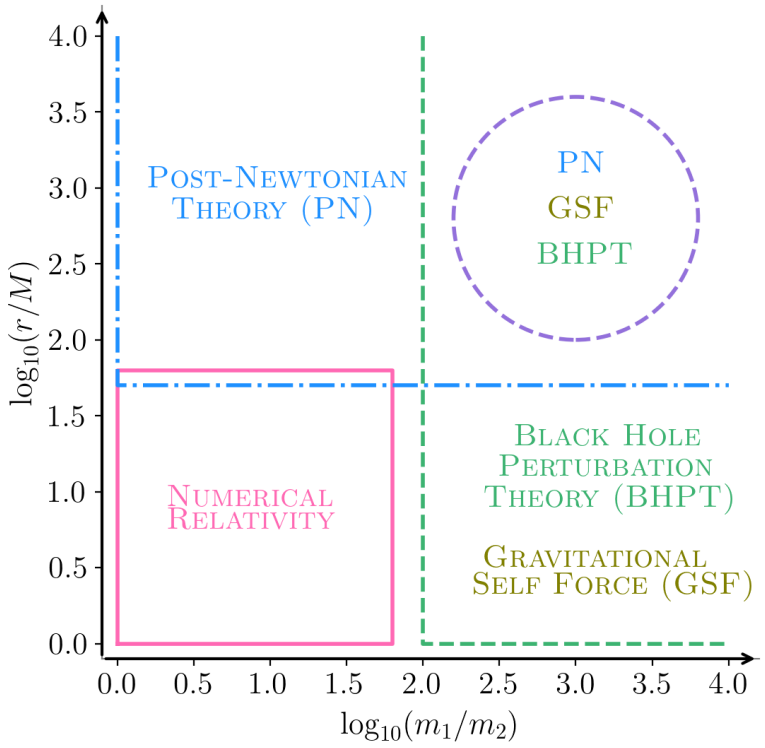

Figure 3.5: Overview of different methods used to model the IMR evolution of BBH systems across the parameter space. The x-axis represents the mass ratio, m_1/m_2, while the y-axis shows the binary's orbital separation in terms of the Schwarzschild radius, r/M. The figure illustrates the applicability of Post-Newtonian (PN) expansions, Numerical Relativity (NR), Gravitational self force (GSF), and Black Hole Perturbation Theory (BHPT) methods across this space.

2005, significant progress has been made in developing numerical methods for solving the EFE. We refer to review articles for a comprehensive overview of NR techniques and advancements [164–168].

Numerical simulations are crucial for studying the nonlinear dynamics of spacetime curvature and serve numerous applications, including benchmarking against analytic PN and GSF approximations [24, 169, 170] and assessing their validity limits, but in the following we focus on BBH simulations. A key application of BBH simulations is modeling the GWs emitted during the late inspiral, merger, and ringdown – the focus of this chapter. These waveforms are essential for analyzing observed signals from BBHs and, as discussed in Section 4.3, are integral to the construction and validation of current waveform models [20, 21, 28, 31–34, 171–191]. NR simulations can also be used to validate GW searches [192–194], perform direct parameter estimation [195, 196], construct template banks [197], and develop waveform families without intermediate analytical models through techniques such as reduced order modeling [182, 183, 198, 199]. To ensure all these applications, NR simulations must be sufficiently long to cover the detector's sensitive frequency band or enable reliable hybridization [200–202]. They must also achieve high accuracy, especially when computing higher-order spherical harmonic modes. Additionally, simulations must map the full nine-dimensional parameter space of BBHs. Despite significant progress,

much of the high-mass-ratio, high-spin parameter space remains unexplored, and only a few simulations include eccentricity, with even fewer also incorporating precession.

To meet these demands, several NR codes have been developed, including BAM [203, 204], LAZEV [151, 205–207], LEAN [208, 209], MayaKranc [210, 211], the Princeton University code [150, 212–214], Dendro-GR [215], GRChombo [216], the University of Illinois code [217], SpEC [218], and SpECTRE [219]; and there exist public NR catalogs providing BBH simulations. The Georgia Tech group released a catalog [220] in May 2016, featuring 452 distinct simulations (from over 600 [221]), covering precessing-spins and mass ratios up to 15. The Rochester Institute of Technology (RIT) group published an initial catalog [222] in 2017, later updated in 2019 to include 320 simulations [223, 224], with precessing binaries up to mass ratio 6, and another one in 2022 [225]. In 2021, the Cardiff group released 80 simulations [226], spanning the single-spin precessing parameter space up to mass ratio 8 using the BAM code. The largest public catalog is maintained by the SXS collaboration [227–229]. As of March 20, 2025, it includes 3839 BBH simulations, covering elliptical, precessing spins, and mass ratios up to 20, available at `www.black-holes.org/waveforms`.

3.2.1.2 Post-Newtonian formalism

Despite significant advances is NR, the PN approximation remains indispensable for accurately describing the inspiral phase of compact binaries and serves as a benchmark for validating numerical simulations. It was first developed in the early days of GR by Droste in 1917 [230] and later by Lorentz and Droste in 1937 [231], and it is particularly effective when the binary components are far apart. In these weak-field and low-velocity conditions, the PN framework can accurately describe the binary dynamics by numerically solving the PN equations of motion or using the adiabatic approximation to arrive at the balance equations (see, e.g., Ref. [232]):

$$\frac{\mathrm{d}\phi}{dt} - \frac{v^3}{M} = 0, \tag{3.2.1}$$

$$\frac{\mathrm{d}v}{\mathrm{d}t} + \frac{F(v)}{ME'(v)} = 0, \tag{3.2.2}$$

where $\omega = \mathrm{d}\phi/\mathrm{d}t$ is the orbital frequency, $v = \omega^{1/3}$, $F(v)$ is the GW luminosity, and $E(v)$ is the system's binding energy. Radiation-reaction (RR) effects first appear in the equations of motion at 2.5PN order [233–236], modifying the orbital dynamics through the emission of gravitational radiation. The amplitude of the associated RR force is calculated using higher-order PN expansions of the quadrupole formula, and was experimentally confirmed through the observed secular acceleration in the orbital motion of systems such as the Hulse–Taylor binary pulsar [83].

As the velocity of the binary increases, the higher is the desirable order of the expansion, and current PN expressions are available at different PN orders, i.e. $(v/c)^{2n}$. For instance, the equations of motion and energy for QC orbits are given in Ref. [237] up to 4.5PN. However, for more general systems, the achieved PN order is typically lower. In particular, the gravitational multipoles emitted by spinning BBHs in planar eccentric orbits have only recently been derived up to 3PN order for nonprecessing-spin binaries [39]. It remains unclear, however, what PN order is required for improved agreement with NR, as convergence of the PN expansion does not necessarily guarantee convergence to the true NR result.

One limitation arises from the fact that the orbital evolution cannot be specified uniquely due to the inherent freedom in the choice of parameter used in the PN expansion as well as the method pursued in solving the relevant differential equations. Hence, different PN families arise because one can choose to treat the ratio $F/E'(v)$ differently while being equivalent with the same PN order [238]: `TaylorT1`, `TaylorT2`, `TaylorT3`, `TaylorT4` in the time domain, and `TaylorF2` in the Fourier domain, which is the most commonly used form of the approximant, obtained using the *stationary phase approximation* (SPA). For a comparison of the different approximants, we point the reader to Ref. [232]. Although PN results are good up to mildly relativistic velocities, these PN approximants become less and less accurate in the strongly relativistic regime, and more differences arise among them. Thus, there have been efforts to extend the evolution of a binary beyond what is naturally prescribed by the PN formalism by applying resummation methods [239]. In particular, the effective-one-body (EOB) [240, 241] extensions of the PN approximants are needed for analytical treatments close to and beyond the applicability limit of PN expressions. We refer to Section 4.3 for a detailed explanation on the EOB formalism, as one of the main waveform model families for BBHs.

Another layer of ambiguity in PN theory arises from the choice of gauge, i.e., the coordinate system used to express the equations of motion and gravitational waveform. While physical observables are gauge invariant, truncated PN expressions do depend on the gauge, leading to potentially different results at a given PN order. Common choices include the harmonic gauge, in which the PN equations are traditionally derived, and the ADM (Arnowitt-Deser-Misner) gauge, often used in Hamiltonian formulations. Additionally, the EOB formalism defines its own gauge (EOB gauge) to improve the analytical description of the binary's dynamics, particularly near merger. Each gauge offers different benefits – for instance, the harmonic gauge leads to more compact expressions for radiation-reaction terms, while the ADM gauge is better suited for canonical Hamiltonian treatments. Therefore, differences may also arise from gauge artifacts rather than physical discrepancies.

Even though NR computations take over to accurately describe the merger phase [150–152], the PN approximation remains indispensable in current CBC GW inspiral modeling. The equations of motion and radiation field must be known to very high PN orders for accurate predictions of GW signals, especially when modeling systems like BNSs or BBHs. However, it is important to note that the convergence of the PN series is not guaranteed, and higher PN orders do not necessarily lead to improved agreement with NR results. For the most comprehensive updates on PN theory for GWs, the review by Blanchet [82] provides a detailed summary.

3.2.1.3 Black hole perturbation theory & gravitational self force

Much of the success of GW astronomy relies on perturbation theory. PN theory provides a crucial framework for modeling the early inspiral phase of binaries – that is, the weak-field regime – while strong-field perturbation theory can also provide crucial information. In particular, *black hole perturbation theory* (BHPT) plays a fundamental role in understanding QNM ringdown following a merger, tidal interactions in compact objects, and extreme-mass-ratio inspirals (EMRIs) through *gravitational self force* (GSF) calculations. For an updated review of BHPT and GSF, we point the reader to Ref. [242] and the references therein.

BHPT assumes that the metric describing a concrete source can be expressed as a small perturbation around a known background metric $g^{(0)}_{\alpha\beta}$. The metric is then written as:

$$g_{\alpha\beta} = g^{(0)}_{\alpha\beta} + \epsilon h^{(1)}_{\alpha\beta} + \epsilon^2 h^{(2)}_{\alpha\beta} + ... \tag{3.2.3}$$

where $\epsilon \ll 1$, leading to a linear system of equations for solving the perturbations. BHPT originated from Regge and Wheeler's study of odd-parity perturbations of Schwarzschild spacetime in the late 1950s [243], later extended by Zerilli's work on even-parity perturbations [244, 245]. Vishveshwara [246] then identified QNMs, with Press [247] and Chandrasekhar & Detweiler [248] further analyzing their frequencies. This foundational work improved our understanding of the ringdown emission, as further discussed in Section 3.3. A major breakthrough came with Teukolsky's derivation of decoupled and separable equations for Kerr perturbations [249, 250], reducing the problem to solving uncoupled ordinary differential equations. The most commonly used metric reconstruction gauges include the radiation gauges, Regge-Wheeler-Zerilli gauges, and the Lorenz gauge.

BHPT can be formulated with a general source term, while GSF theory arises when describing the motion of a small object in curved spacetime. Unlike in electromagnetism, where a point-particle approximation works at all orders, in gravity, non-linear effects require directly accounting for the small body's finite size. GSF theory aims to extend the point-particle approximation by reducing the object to a few bulk properties (such as mass and spin) supported on a worldline. This approach leads to a skeletonization of the small body, reducing it to a singularity endowed with its multipole moments, alongside an equation governing its trajectory. The framework is crucial for modeling EMRIs, where a stellar-mass compact object orbits a supermassive black hole.

The foundations of GSF theory were laid by De Witt and Brehme [251], followed by posterior efforts [252–255]. The state-of-the-art is currently the second order in the mass ratio, for both the binding energy [256] and the energy flux and waveform [26, 257]. A key challenge remains the comparison between PN and GSF methods in their overlapping regime – the slow-motion, weak-field limit of an EMRI. Notably, leading-order mass-ratio expansions have achieved remarkable PN precision, with results reaching high PN-equivalent orders [258–260].

Over the past two decades, the study of GSF in BHPT has gained significant attention, largely driven by the upcoming LISA mission. LISA will detect GWs in the millihertz range (see Figure 2.5), where EMRIs are expected to be a key source. In this frequency band, SBHs with masses between $\sim 10^5$ and 10^7 $M_\odot$ dominate, while the smaller companions are expected to have stellar masses, leading to extreme mass ratios of order 10^{-4} to 10^{-7}. Given this mass hierarchy, BHPT provides an ideal framework for accurately modeling their waveforms. Over LISA's operational timescale of several years, the smaller body in an EMRI will complete $10^4 - 10^5$ highly intricate orbits in the strong-field region around the central black hole. This will allow for precise measurements of the black hole's parameters, tests of the Kerr hypothesis, and potential deviations from GR. Radiation reaction will drive the orbit's evolution, leading to a plunge into the black hole, making self force effects crucial for accurate waveform modeling. It is well established that extracting maximal information from EMRI observations will require second-order GSF calculations [261–263]. Beyond EMRIs, GSF techniques also hold promise for IMRIs [264], where the mass ratio may be as large as 10^{-2}. This extends the relevance of BHPT and GSF to current ground-

based GW detectors, enabling improved models for detecting and interpreting signals from IMRIs.

The `Black Hole Perturbation Toolkit` [265] provides open-source implementations of state-of-the-art numerical algorithms for solving equations in BHPT and GSF calculations. It also serves as a centralized repository for numerical data and analytical PN series expansions produced by the research community.

3.3 Spherical harmonic decomposition

The GW strain h encodes the emitted radiation from a BBH system. As discussed in Section 3.1.2, the BBH parameter space is defined by intrinsic properties – the mass ratio q, BH spins $\vec{\chi}_i$, and eccentricity parameters (e, l) – along with extrinsic parameters that determine the binary's orientation and position relative to the detector.

Since the observed waveform depends on both intrinsic parameters $\vec{\lambda}$ and extrinsic ones, it is useful to decompose the strain into spin-weighted spherical harmonics (SWSH), a standard technique in GW analysis. As illustrated in Figure 3.2, the binary's sky location $\vec{d_L}$ is specified by the angles ι and φ, which correspond to standard polar coordinates on the unit sphere, and the luminosity distance d_L. At sufficiently large distances – appropriate for astrophysical sources – the strain scales inversely with d_L, i.e.,

$$h(t, \vec{d_L}, \boldsymbol{\lambda}) = \frac{h_0(t, \vec{\hat{d}_L}, \boldsymbol{\lambda})}{d_L} + O(d_L^{-2}), \tag{3.3.1}$$

where h_0 captures the leading order angular dependence of the waveform, and $\boldsymbol{\lambda}$ includes the intrinsic parameters of the source. Furthermore, the strain can be expressed in terms of the TT polarizations introduced in Section 2.1, Equation (2.1.14),

$$h(t, \vec{r}, \boldsymbol{\lambda}) = h_+(t, \vec{r}, \boldsymbol{\lambda}) - i h_\times(t, \vec{r}, \boldsymbol{\lambda}), \tag{3.3.2}$$

allowing the GW signal to be represented as a single complex quantity.

The angular dependence of the GW strain can be described using SWSHs. The strain is a tensorial quantity and is naturally expanded in terms of SWSHs with spin weight $s = -2$ [266, 267],

$$h(t, \vec{r}, \boldsymbol{\lambda}) = \frac{1}{r} \sum_{l \geq 2, m=-l}^{m=l} h_{lm}(t, \boldsymbol{\lambda}) Y^{-2}_{lm}(\vec{\hat{d}_L}) = \frac{1}{r} \sum_{l,m} h_{lm}(t, \boldsymbol{\lambda}) Y^{-2}_{lm}(\iota, \varphi). \tag{3.3.3}$$

Higher order terms are strongly suppressed, and for comparable mass systems, only a handful of terms contribute significantly in current GW data analysis applications [188].

Describing the waveform in terms of individual modes $h_{lm}(t, \boldsymbol{\lambda})$ rather than the strain in a particular direction simplifies the analysis, as each mode depends only on time and the intrinsic properties of the binary. Each mode, a complex function, is conveniently expressed in terms of its amplitude $A(t, \boldsymbol{\lambda})$ and phase $\Psi(t, \boldsymbol{\lambda})$,

$$h_{lm}(t, \boldsymbol{\lambda}) = A_{lm}(t, \boldsymbol{\lambda}) e^{-i\Psi_{lm}(t, \boldsymbol{\lambda})}, \tag{3.3.4}$$

which is particularly useful in data analysis and modeling purposes. First, PN theory provides expressions for these modes that are valid during the early inspiral phase. These

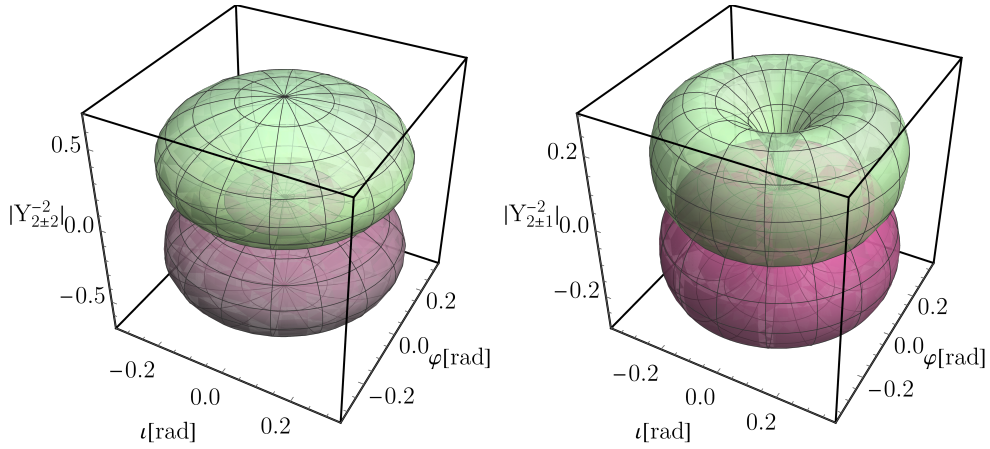

Figure 3.6: Absolute value of the spherical harmonics of spin-weight $s = -2$ for the $(l, m) = (2, \pm 2)$ (*left*) and $(l, m) = (2, \pm 1)$ (*right*) as a function of the angular coordinates ι and φ (see Equation (3.3.5)). The positive m-modes are shown in green, and the negative m-modes are shown in pink, illustrating the angular dependence of the GW strain h for these modes.

expressions depend on the intrinsic parameters of the system, and even at leading PN order, the asymmetry in mass ratio favors the emission of higher order modes (HMs). Notably, the larger the mass ratio, the greater the contribution of HMs compared to the quadrupole emission. Additionally, this decomposition reveals the impact of the binary's orientation. The angular dependence is encoded in the spherical harmonics $Y^{-2}_{l,m}$, which influence which modes are observable in the detector's frame. For example, consider the quadrupole modes $(l, m) = (2, \pm 2)$, and $(2, \pm 1)$. The angular dependence of these modes is given by

$$\begin{aligned} Y^{-2}_{2,\pm2} &= \sqrt{\frac{5}{64\pi}}\ (1 \pm \cos\iota)^2\ e^{\pm 2i\varphi}, \\ Y^{-2}_{2,\pm1} &= \sqrt{\frac{5}{64\pi}}\ \sqrt{1 \mp \cos\iota}\ (1 \pm \cos\iota)^{3/2}\ e^{\pm i\varphi}, \end{aligned} \tag{3.3.5}$$

as shown in Figure 3.6, where positive m-modes are in green and negative m-modes are in pink. The figure clearly shows the preferred directions in which each mode exhibits stronger emission, or in some cases, is suppressed. From the left plot of Figure 3.6, we see that the quadrupole modes are maximized at *face-on* orientations, i.e. $\iota = \{0, \pi\}$ radians, while the $(2, \pm 1)$ modes vanish for *face-on* binaries. Different modes peak at different values of ι, and the dominant modes vanish at *edge-on* orientations, implying that for $\iota = \pi/2$ radians, subdominant modes will exclusively contribute to the detected GW.

The simpler the system, the fewer HMs are needed for an accurate description. For example, in equal-mass, non-spinning binaries, the GW emission is predominantly concentrated along the axis orthogonal to the orbital plane, and the signal is well captured by only the leading quadrupole modes. However, in systems with asymmetric mass ratios or precessing spins, HMs become much more important, and including them significantly improves PE results for systems with asymmetric mass ratios or precessing features, leading to notable improvements for events like GW190412 or GW190814 [7, 268, 269]. Finally, using only the dominant harmonics for PE purposes leads to a degeneracy between luminosity distance and inclination angle, as they both appear as multiplicative factors in the oscillatory part of the waveform. Subdominant modes help break this degeneracy,

improving the inference of these parameters.

The spherical harmonic decomposition in Equation (3.3.3) is useful during the inspiral and merger, but it is not the most natural choice for describing the entire binary evolution. Once the final BH settles into a stationary Kerr configuration during the ringdown, the emitted GWs are dominated by a superposition of QNMs. These modes emit GWs at characteristic complex frequencies, which can be derived from BHPT [270]. In this regime, the strain can be written as

$$h(t, \boldsymbol{\lambda}, \iota, \varphi) \approx \sum_{l,m,n} a_{lmn}(t, \boldsymbol{\lambda}) \mathcal{Y}^{-2}_{lm}(\iota, \varphi) e^{i(\omega_{lmn} t + \Phi_{lmn}(t, \boldsymbol{\lambda}))}, \tag{3.3.6}$$

where $\mathcal{Y}^{-2}_{lm}(\iota, \varphi)$ are the *spheroidal harmonics of spin weight* $s = -2$ [249, 271], and $a_{lmn}(t, \boldsymbol{\lambda})$ and $\Phi_{lmn}(t, \boldsymbol{\lambda})$ are the amplitude and phase of the QNMs, which depend on the intrinsic properties of the source and are not determined by BHPT. The complex frequencies ω_{lmn} only depend on the remnant BH's mass M_f and spin χ_f, so $\omega_{lmn}(M_f, \chi_f)$, and are characterized by the integers numbers l, m, and n (with $n \geq 0$ indicating different overtones). These frequencies are typically computed in a frame defined by the remnant BH's final spin, $\vec{\chi}_f$, which points in the $\hat{z}$-direction. The real and imaginary parts of ω_{lmn} correspond to the *ringdown frequency* and *damping rate*, respectively:

$$\begin{aligned} f^{\mathrm{ring}}_{lm}(M_\mathrm{f}, \chi_\mathrm{f}) &= \frac{\mathrm{Re}(\omega_{lm})}{2\pi}, \\ f^{\mathrm{damp}}_{lm}(M_\mathrm{f}, \chi_\mathrm{f}) &= \frac{\mathrm{Im}(\omega_{lm})}{2\pi}. \end{aligned} \tag{3.3.7}$$

Perturbation theory predicts two possible values for the ringdown frequency of a perturbed black hole: a *prograde* ($m > 0$) and a *retrograde* ($m < 0$) frequency [272]. The prograde frequency dominates when the final spin aligns with the direction of the GW emission prior to merger, which occurs in systems with spins aligned orthogonally to the orbital plane. Conversely, the retrograde frequency dominates for anti-aligned systems. For systems with misaligned spins (*precessing systems*, see Section 4.1 for details), the orbital plane precession excites both prograde and retrograde modes. Based on the non-precessing case, we expect the prograde modes to dominate for "positive" final spins and the retrograde modes for "negative" final spins. These findings, originally published in my master's thesis [273], were later confirmed by posterior independent studies [274]. For a more detailed explanation of this effect and a simple fit to model the *beating effect* between prograde and retrograde contributions in the spheroidal basis, we refer the reader to Ref. [274].

Consequently, during the ringdown phase, spheroidal harmonics offer a more natural basis, as they directly describe the QNM structure of the remnant black hole. However, for convenience, current waveform models maintain the spherical harmonic decomposition throughout the entire IMR evolution. Spheroidal harmonics can be expressed as a linear combination of spherical harmonics:

$$\mathcal{Y}^{-2}_{lm}(\iota, \varphi) = \sum_{l'} \alpha_{ll'm} Y^{-2^*}_{lm}(\iota, \varphi), \tag{3.3.8}$$

where $\alpha_{ll'm}$ are the mixing coefficients [275, 276]. This relationship allows for converting spherical harmonic multipoles to spheroidal harmonic multipoles, and vice versa. However,

since spherical harmonics encompass a superposition of several spheroidal harmonics [277–279], QNM mixing arises. This effect, known as *mode mixing* [275, 280, 281], becomes particularly significant in cases where different modes have similar real parts of their ringdown frequencies – for example, the $(l = 3, m = 2)$ spherical harmonic mode contains contributions from both the ω_{320} and ω_{220} spheroidal modes [186, 282–286]. In such situations, it is advantageous to first model the spheroidal harmonic modes, which are free from mixing, and then transform the results into the standard spherical decomposition typically used for waveform modeling. This strategy is implemented, for instance, in the IMRPhenomXHM model [33] (see also Section 7.2.2 for further discussion on waveform models).

CHAPTER 4

Modeling the dynamics of black hole binaries

In the previous chapter, we introduced the fundamental concepts needed to understand GW emission from BBH systems. The evolution of a generic binary follows a characteristic morphology consisting of an inspiral, merger, and ringdown phase, and the methods discussed can be applied for modeling purposes. However, a general BBH system spans a nine-dimensional parameter space: the mass ratio q, the two BH spin vectors $\vec{\chi}_{1,2}$, and two parameters related to elliptical orbits, the orbital eccentricity e and mean anomaly l. Some of these parameters have a more pronounced impact on the waveform morphology, as previously mentioned in Chapter 3. This chapter focuses on these effects, particularly on the approaches used for waveform modeling.

Specifically, we analyze the role of BH spins, which, depending on their orientation, may lead to the phenomenon of *spin-precession*, as well as the effect of eccentric orbits. Due to the high dimensionality of generic BBH systems, these two effects have so far been mostly studied – and modeled – separately for the IMR signal. We follow the same approach here: Section 4.1 explores spin effects, discussing precession within the PN formalism and its main modeling approach, while Section 4.2 examines eccentric orbits, their parameterization, and their PN-based modeling. Finally, Section 4.3 provides an overview of waveform model development for BBH systems, and discuss the different modeling approaches and current state of generic BBH modeling.

4.1 Spin effects

For binaries composed of rotating Kerr black holes, the orientation of the spin vectors $\vec{S}_1$ and $\vec{S}_2$ significantly influences the binary evolution, and hence the waveform. When the spins are aligned with the orbital angular momentum $\vec{L}$, which is approximately orthogonal to the orbital plane defined by the two BHs, the system is referred to as *aligned-spinning*, and retains equatorial symmetry. The orbital plane and spin directions remain unchanged over time, and the system's parameter space is effectively three-dimensional: q, S_{1z}, and S_{2z}. The loss of $\vec{L}$ is entirely due to GW emission, varying over the inspiral timescale, while the total angular momentum

$$\vec{J} = \vec{L} + \vec{S} = \vec{L} + \vec{S}_1 + \vec{S}_2 \tag{4.1.1}$$

evolves due to the radiation of $\vec{L}$.

For *non-precessing* binaries – aligned- or non-spinning –, GW emission is primarily along $\vec{L}$, leading to a natural hierarchy in mode amplitudes when choosing $\vec{L}$ as the $\hat{z}$-axis. The dominant modes are $(l, m) = (2, \pm 2)$ as mentioned in Section 3.3, and is some cases will be enough to accurately characterize a GW signal. Additionally, reflection symmetry across the orbital plane imposes the relation [287]

$$h_{lm} = (-1)^l (h_{l-m})^*, \tag{4.1.2}$$

where h^* the complex conjugate. This allows focusing on modeling the modes with positive m, as $(l, \pm m)$ differ only by a phase shift of π for odd l. In non-precessing systems, symmetries further simplify the individual mode analysis. Odd m-modes vanish in symmetric binaries, and the $m = 0$ mode is associated with memory effects, with its non-oscillatory phase allowing analytical expressions in terms of integrals of other modes [288].

In contrast, *precessing* binaries – where at least one spin is misaligned with $\vec{L}$ – exhibit time-dependent variations in both $\vec{S}(t)$ and $\vec{L}(t)$, causing the orbital plane to precess. This increases the number of parameters to seven (six for spins, one for mass ratio) and breaks all the symmetries of non-precessing systems. As a result, mode mixing occurs for fixed l, the natural amplitude hierarchy is lost, and the symmetry of Equation (4.1.2) no longer holds in any frame.

The structure of this section is as follows: First, in Section 4.1.1, we summarize the effects of BH spins on the binary evolution as described by PN theory. In Section 4.1.2, we introduce the *twisting up procedure*, which defines a non-inertial frame tracking the direction of maximum emission, $\vec{L}$, approximately orthogonal to the orbital plane – since GWs are primarily emitted in this direction, the so-called *quadrupole-aligned* frame eliminates the amplitude modulations on the waveform caused by precession. Finally, in Section 4.1.3 we describe the standard approach to modeling precession in the Fourier domain.

4.1.1 Post-Newtonian description of precession

The PN approximation (see Section 3.2.1.2 for details and references) permits to describe the evolution of binary systems in terms of a point particle Hamiltonian. The leading order spin effects in PN are split into two contributions: the spin-orbit (SO), which is the dominant effect, and the spin-spin (SS) interaction (see e.g. [278, 289] for further discussion of these two terms). For a qualitative description of precession, we focus on the leading order spin-orbit Hamiltonian:

$$H_{\rm SO} = 2\frac{\vec{S}_{\rm eff} \cdot L}{R^3}, \tag{4.1.3}$$

where R is the separation between the two BHs and the effective spin $\vec{S}_{\rm eff}$ is defined as

$$\vec{S}_{\rm eff} = \left(1 + \frac{3}{4}\frac{m_2}{m_1}\vec{S}_1\right) + \left(1 + \frac{3}{4}\frac{m_1}{m_2}\vec{S}_2\right). \tag{4.1.4}$$

Equation (4.1.3) shows that the potential energy depends on the aligned spin components, i.e., those parallel to the orbital angular momentum. The sign of the scalar product determines the type of interaction: it is *attractive* if $\vec{S}_{\rm eff}$ and $\vec{L}$ are anti-aligned ($\vec{S}_{\rm eff} \cdot L < 0$) or *repulsive* if they are aligned ($\vec{S}_{\rm eff} \cdot L > 0$). In the case of an attractive interaction,

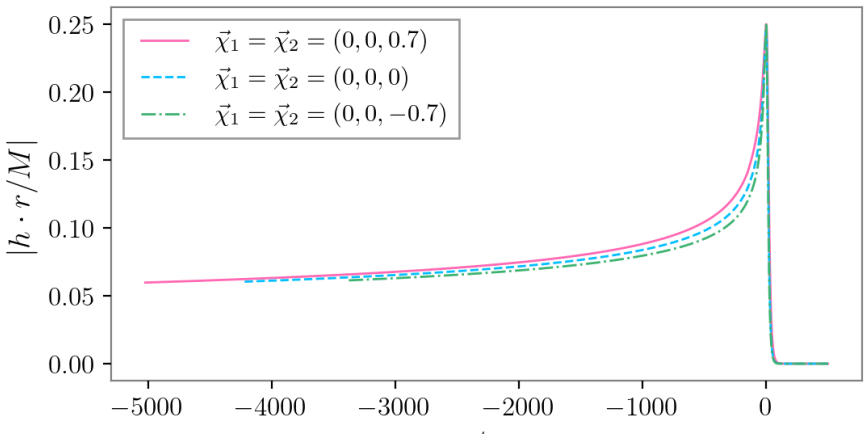

Figure 4.1: GW amplitude for a BBH system with mass ratio $q = 1$, inclination $\iota = 0°$, and reference phase $\varphi = 0°$ at $Mf_{\rm ref} = Mf_{\rm min} = 0.0049$, computed using the IMRPhenomTHM model (see Section 4.3 for details). We compare three spin configurations: non-spinning (dashed blue), aligned spins (solid pink), and anti-aligned spins (dot-dashed green).

the objects inspiral faster, emitting less gravitational radiation. Conversely, if the spins are aligned, the objects will orbit for a longer period, emitting more GWs. This effect is illustrated in Figure 4.1, where we show the waveform evolution for three different systems: non-spinning (dashed blue), spins aligned with the orbital angular momentum (solid pink), and anti-aligned (dot-dashed green). We observe that, for the same binary parameters, the more aligned the spin components are with the orbital angular momentum, the longer the waveform lasts, as the system emits stronger gravitational waves over an extended period. In contrast, anti-aligned spin configurations inspiral more rapidly, resulting in shorter and weaker GW signals.

From the SO interaction, one can also derive the time evolution of the total spin $\vec{S}$ [278]

$$\dot{\vec{S}}_{\rm SO} = -\frac{2}{R^3}\vec{S}_{\rm eff} \times \vec{L}. \tag{4.1.5}$$

This equation illustrates the behavior in both non-precessing and precessing systems. If the BH spins (and hence $\vec{S}$) are aligned with the orbital angular momentum $\vec{L}$, the time evolution of the total spin $\vec{S}$ vanishes, indicating that $\vec{S}$ is conserved (up to 1.5PN order [146]). However, in precessing systems, the orthogonal components of $\vec{S}$ lead to a non-zero cross product with $\vec{L}$, causing the total spin to vary over time. The magnitude of the precession depends on both the magnitude of the total spin, and its relative orientation with respect to the orbital angular momentum. If either of these is small relative to $\vec{L}$, then precession modulations can be neglected.

So far, we have stated that for spinning binary systems – whether aligned or precessing – the orbital angular momentum $\vec{L}$ is only approximately orthogonal to the orbital plane. This can also be seen at leading order in SO interactions (following Equation (4.1.3)). According to Hamilton's equations, the momentum vector $\vec{p}$ evolves as

$$\frac{\mathrm{d}\vec{p}}{\mathrm{d}t} = -\frac{\partial H}{\partial \vec{R}}. \tag{4.1.6}$$

Since the Hamiltonian H depends on the spins, the momentum acquires a spin-dependent contribution, meaning that the velocity vector $\vec{v} = \dot{\vec{R}}$ is generally not parallel to the

momentum $\vec{p}$. Consequently, the orbital frequency vector $\vec{\omega}$, which is orthogonal to the orbital plane and defined as

$$\vec{\omega} = \frac{\vec{R} \times \vec{v}}{R^2}, \tag{4.1.7}$$

is not necessarily aligned with the orbital angular momentum $\vec{L}$, given by

$$\vec{L} = \vec{R} \times \vec{p} = \vec{L}_{\rm NS} + \vec{L}_{\rm S} = \vec{L}_{\rm NS} + \vec{L}_{\rm SO} + \vec{L}_{\rm SS}. \tag{4.1.8}$$

From the SO interaction term in the Hamiltonian (Equation (4.1.3)), the contributions to $\vec{L}$ at leading order are given by [278]

$$\begin{aligned}
\vec{L}_{\rm NS} &= \mu(\vec{r} \times \vec{v}) \left[1 + \frac{1}{2}v^2(1-3\eta) + (3+\eta)\frac{M}{R}\right], \\
\vec{L}_{\rm SO} &= \frac{\mu}{M}\left[\frac{M}{r}\vec{n} \times \left(\vec{n} \times \left(3\vec{S} + \delta M\left(\frac{\vec{S}_1}{M_2} - \frac{\vec{S}_2}{M_1}\right)\right)\right) - \frac{1}{2}\vec{v} \times \left(\vec{S} + \delta M\left(\frac{\vec{S}_1}{M_2} - \frac{\vec{S}_2}{M_1}\right)\right)\right],
\end{aligned} \tag{4.1.9}$$

where $\delta M = m_1 - m_2$, μ is the reduced mass, η is the symmetric mass ratio, and $\vec{n}$ is the unit vector along $\vec{r}$.

The magnitude of precessional modulations can also be analyzed within PN theory. The total angular momentum $\vec{J}$ is conserved at 2PN order when the loss of energy due to gravitational radiation is neglected [278], so

$$\dot{\vec{S}} = -\dot{\vec{L}}. \tag{4.1.10}$$

Increasing the mass ratio reduces the magnitude of L at a given separation (Equation (4.1.9)), while the spin magnitude S remains unchanged. Consequently, the relative variation in $\vec{L}$ due to spin precession increases, implying that spin precession effects are more pronounced in asymmetric systems with larger mass ratios.

Modeling precessing waveforms has thus proven challenging. The introduction of misaligned spins introduces additional terms in the PN equations at high orders, complicating their analytical solution and limiting the development of phenomenological descriptions. Additionally, the large parameter space makes it difficult to cover all configurations with NR simulations. However, the PN framework provides key insights: the spin components orthogonal to the orbital plane do not affect the system's energy (at least at low PN orders) but instead contribute to the precession of the total spin and the orbital angular momentum. Furthermore, the acceleration due to orbital motion dominates over the precessional motion, meaning that the power radiated due to precession is negligible during the inspiral. These features can be leveraged to construct more efficient precessing waveform models. One approach is to work in a coordinate frame that follows the precessing motion and rotates relative to a fixed inertial frame. In this *co-precessing frame*, the waveform resembles that of an aligned-spin system [290], significantly simplifying its description. We detail this procedure in the following section.

4.1.2 Twisting up procedure

In non-precessing systems, the dynamics are dominated by two distinct time scales: the fast *orbital time scale* associated with the nearly circular motion, and the slower *inspiral*

time scale due to GW emission. Gravitational radiation in such systems is primarily driven by the orbital motion. When considering systems with misaligned spins, a third time scale appears – *spin-precession time scale*, which lies between the orbital and inspiral scales. Though it introduces rich dynamics, during the inspiral, precession evolves more slowly than the orbital motion during the inspiral, and thus contributes little to the total energy loss. As a result, the inspiral rate of precessing binaries can be well approximated by that of non-precessing systems with similar parameters.

The key effect of precession is instead seen in amplitude and phase modulations of the gravitational waveform. These modulations can be captured by mapping a non-precessing waveform into a co-rotating frame – a procedure commonly referred to as "twisting up" the waveform [279], first formalized in Ref. [290]. In this appropriately chosen *co-precessing frame*, the waveform resembles that of a non-precessing binary, especially in its dominant features, such as the symmetry of the $\pm m$ modes across the orbital plane. To define the co-precessing frame, the standard approach is to maximize the amplitude of the quadrupole modes (i.e., $(l, m) = (2, \pm 2)$), leading to what is known as the *quadrupole-aligned frame*. This frame tracks the dominant radiation direction, which is approximately perpendicular to the orbital plane – a direction that closely aligns with the orbital angular momentum, as seen in Section 4.1.1. This frame has the advantage that the spin components parallel and orthogonal to $\vec{L}$ are approximately preserved (see discussion in e.g. Ref. [146]), which implies that the co-precessing waveform will exhibit the same features as the one produced by a system with the same parallel components of $\vec{S}$. The full twisting up procedure thus involves applying the rotation between the inertial and the co-precessing frame to the waveform SWSH decomposition:

$$\begin{aligned} h^{\mathrm{I}}_{lm}(t, \boldsymbol{\lambda}) &= \sum_{m'=-l}^{l} h^{\mathrm{cop}}_{lm'}(t, \boldsymbol{\lambda}) \mathcal{D}^{l*}_{mm'}(\vec{R}(t)), \\ h^{\mathrm{cop}}_{lm'}(t, \boldsymbol{\lambda}) &= \sum_{m=-l}^{l} h^{\mathrm{I}}_{lm}(t, \boldsymbol{\lambda}) \mathcal{D}^{l}_{mm'}(\vec{R}(t)), \end{aligned} \tag{4.1.11}$$

where $\mathcal{D}^{l}_{mm'}$ are Wigner matrices corresponding to the rotation $\vec{R}(t)$ between frames.

This procedure has enabled the development of several waveform models for precessing systems, starting with Ref. [279], and has become standard in GW astronomy (see Section 4.3 for a summary of precessing models). In the following, we discuss the key ingredients of this construction in more detail. In Section 4.1.2.1, we explore the structure of co-precessing modes and their relation to aligned-spin waveforms. Section 4.1.2.2 introduces the Euler angles as the main description used to perform the rotation in Equation (4.1.11), and Section 4.1.2.3 addresses the choice of frames used to represent the waveform.

4.1.2.1 Co-precessing modes

The twisting-up procedure relies on the separation of timescales between the rapid orbital motion and the slower precession dynamics. Since the orbital motion dominates the GW emission, it is reasonable to assume that the radiated energy and angular momentum are largely unaffected by precession. This is supported by NR simulations, which show that the final mass of the remnant depends only weakly on precession (see e.g. Ref. [286]). Hence, the spherical harmonic modes of the precessing waveform in the co-precessing

frame, $h^{\rm cop}_{lm}$, are approximately given by the aligned-spin modes, $h^{\rm AS}_{lm}$, computed in the L_0-frame (aligned with the initial orbital angular momentum, see Figure 3.2 for visual definition). These modes can be seen in the top panel of Figure 4.2.

However, there are two main *limitations* to this approach. First, the symmetry relation across the orbital plane, which is valid for aligned-spin systems, no longer holds for the co-precessing modes. This symmetry violation, its connection to the recoil, as well as its impact on the SNR, was first discussed in Ref. [291]. This breakdown was largely ignored in waveform models until recent work began to explicitly incorporate it [292–294]. A more detailed discussion of this and other approximations in the twisting-up method is given in Ref. [295]. Second, the aligned-spin and co-precessing systems do not lead to the same remnant spin, and therefore differ in the ringdown frequency. While the final mass is largely unaffected, the final spin depends on the full angular momentum content at merger, including spin components orthogonal to the orbital plane [296]. Hence, to correctly describe the ringdown (see Section 3.3 for more details on QNM emission), the final spin of the precessing system must be estimated. Surrogate models trained on NR simulations exist for this purpose [35, 286], but they are typically computationally expensive. A more broadly applicable but less accurate estimate is provided in Sec. IV.D of Ref. [189], which we summarize in the following.

Most of the orbital angular momentum is only radiated away near merger, so the pre-merger values of $(\vec{S}_1, \vec{S}_2, \vec{L})$ determine the final state (which corresponds to the total orbital angular momentum $\vec{J}$. The spin vectors can be decomposed into components *parallel* and *perpendicular* to $\vec{L}$:

$$S_\parallel = \vec{S}_1 \cdot \hat{L} + \vec{S}_2 \cdot \hat{L}, \tag{4.1.12}$$

$$\vec{S}_\perp = \vec{S}_1 - (\vec{S}_1 \cdot \hat{L})\hat{L} + \vec{S}_2 - (\vec{S}_2 \cdot \hat{L})\hat{L}, \tag{4.1.13}$$

so the final spin magnitude is then given by

$$S_f = M_f^2 \chi_f = \sqrt{|\vec{S}_\perp|^2 + (S_\parallel + L_f)^2}, \tag{4.1.14}$$

where χ_f is the dimensionless final spin, and L_f is determined from a non-precessing system via:

$$S_\parallel + L_f = M_f^2 \chi_f^\parallel. \tag{4.1.15}$$

To use this in a twisting-up model, one assumes that the total spin magnitude S and its projection along $\vec{L}$ are conserved during the evolution. This allows $S_\parallel$ to be approximated using the non-precessing configuration. The quantities M_f and $\chi_f^\parallel$ can be accurately described by NR-based fits for aligned-spin binaries (e.g., [27]), as functions of the symmetric mass ratio and aligned spin components. The perpendicular spin magnitude can be related to the effective precession parameter χ_p (as defined in Equation (3.1.7)), yielding the final estimate:

$$\chi_f = \sqrt{\left(\chi_p \frac{m_1^2}{M_f^2}\right)^2 + {\chi_f^\parallel}^2}. \tag{4.1.16}$$

Although these approximations are quite simplistic, they are surprisingly accurate and are currently used in state-of-the-art models. Nonetheless, Chapter 5 introduces a new methodology and improved fits to more accurately describe the final mass and spin of precessing systems across the full mass ratio range [18].

So far, we have discussed the magnitude of the final spin. However, the direction also plays an important role. In systems with modest precession, the final spin typically aligns with the total angular momentum $\vec{J}$. This assumption, however, breaks down for configurations exhibiting *transitional precession* [277, 278, 297]. This phenomenon arises when the orbital angular momentum $\vec{L}$ and the total spin vector $\vec{S}$ have comparable magnitudes but point in opposite directions, causing the total angular momentum $\vec{J}$ to become small. At sufficiently large separations, $\vec{L}$ dominates over $\vec{S}$; however, as the binary inspirals, $\vec{L}$ shrinks while the spins remain approximately constant. In systems with high mass ratios, $\vec{L}$ can eventually become smaller than $\vec{S}$, allowing the direction of $\vec{J}$ to flip from being $\vec{L}$-dominated to $\vec{S}$-dominated. As a result, the final spin direction can reverse relative to its initial orientation. Such behavior highlights challenges for waveform modeling, particularly in systems where spins nearly anti-aligned with the orbital angular momentum lead to instabilities in the spin components parallel and orthogonal to $\vec{L}$, which are no longer approximately conserved. In these cases, the assumptions underlying specific implementations of the twisting-up approach may break down, and more generally, modeling approaches must always be carefully tested and validated against NR to ensure their robustness.

4.1.2.2 Euler angle description

The transformation between the co-precessing and inertial frames is described by a time-dependent rotation, typically encoded in three Euler angles that track the direction of maximum emission $\vec{L}$. By construction, the Euler angles α and β are defined in the inertial frame $\{x, y, z\}$ as

$$\begin{aligned} \alpha &= \arctan(L_y, L_x) = \arctan \frac{L_x}{L_y}, \\ \cos\beta &= \vec{z} \cdot \vec{L} = L_z. \end{aligned} \tag{4.1.17}$$

However, specifying the orientation of $\vec{L}$ still leaves an ambiguity in rotations about that axis. To resolve this, Ref. [298] proposed the *minimal rotation condition*, which ensures that the co-precessing frame evolves smoothly and remains invariant under fixed inertial frame rotations. This is crucial for meaningful comparisons between NR and analytical waveforms, and yields higher-mode amplitudes consistent with those of non-precessing binaries. The condition is given by

$$\dot{\gamma} = -\dot{\alpha}\cos\beta. \tag{4.1.18}$$

Since Equation (4.1.18) only determines the time derivative of γ, its integration introduces an arbitrary constant. A common convention is to set $\gamma = 0$ at some reference time or frequency during the inspiral.

The rotation from the co-precessing to the inertial frame, which is needed to compute the inertial-frame modes via Equation (4.1.11), is expressed in terms of Wigner matrices [299]. These matrices are functions of the Euler angles and provide a convenient coordinate basis for implementing the rotation. Explicit expressions and derivations can be found in Ref. [299]. Several approaches exist to compute the Euler angles within PN theory. These include direct numerical integration of the spin precession equations [300], analytical approximations assuming a single-spin system with orbital averaging [301], and multiscale analysis methods [302] that exploit timescale separations during the inspiral. These methods are primarily used to track the evolution of the binary's orientation.

Although Euler angles have historically been the most common description for modeling precession, quaternions have been proposed as a more efficient and robust alternative [303]. In fact, quaternions are the standard tool for performing rotations in fields such as computer graphics, whereas Euler angles were initially used in GW modeling largely because they are more intuitive. Quaternions offer a compact representation, are computationally faster than matrix or trigonometric operations, and avoid coordinate singularities such as *gimbal lock*. This singularity occurs when two of the rotation axes become aligned, effectively reducing the dimensionality of the rotation space. However, when the reference axis is chosen to be the total angular momentum $\vec{J}$, the region of parameter space where gimbal lock becomes problematic is relatively small (see also [304]). Beyond their numerical advantages, quaternions simplify the composition of successive rotations, which can be performed via vector multiplication rather than matrix multiplication. While phenomenological models typically rely on Euler angles, both the SEOB family [31, 173] and surrogate models [184] employ quaternions for these reasons. For a detailed description of these models, see Section 4.3.

4.1.2.3 Frame definitions

So far, we have established that the co-precessing frame is the most natural for precessing systems, as it simplifies waveform morphology by eliminating oscillations. However, while this frame is useful for modeling, waveforms must ultimately be expressed in an inertial frame. Unlike non-precessing systems, precessing binaries do not have a uniquely preferred inertial frame, and the choice of frame significantly impacts the complexity of the waveform.

One commonly used frame with advantageous properties is defined by the total angular momentum $\vec{J}$ at a reference time, such that $\hat{z} = \hat{\vec{J}}(t_{\rm ref})$. This is known as the J-frame, in which the waveform takes a relatively simple form because, as discussed in Equation (4.1.10), $\vec{J}$ remains approximately constant during the binary evolution. However, for highly precessing systems, this frame can undergo a flip due to the *transitional precession* mentioned in Section 4.1.2.1 [277, 278, 297], requiring extra caution.

Another widely adopted frame is based on the orbital angular momentum $\vec{L}$, where the z-axis is aligned with $\vec{L}(t_{\rm ref})$. This choice is consistent with the natural frame for aligned-spin and non-spinning systems. In practice, it is common to approximate $\vec{L}$ using the Newtonian angular momentum $\vec{L}_N$, which aligns with the instantaneous orbital frequency vector. Since the difference between $\vec{L}_N$ and $\vec{L}$ is small in the comparable mass regime, using $\vec{L}_N$ simplifies computations while maintaining accuracy. This frame is referred to as the L_0-frame (already introduced in Section 3.1.2), which coincides with the quadrupole frame at $t_{\rm ref}$. As discussed in Section 4.1.2.1, one key advantage of this frame is that spin components parallel and perpendicular to $\vec{L}$ remain approximately conserved. Consequently, this frame is often used to define spin vectors in NR initial data, as it ensures minimal evolution of the spin components. However, this simplicity comes at the cost of a more complex representation of the spherical harmonic modes.

Both the L_0-frame and J-frame are related by a time-independent global rotation, allowing spherical harmonic modes to be transformed between them via the Euler angles:

$$h^{\vec{L}_0}_{lm}(t, \boldsymbol{\lambda}) = \sum_{m'=-l}^{l} \mathcal{D}^{l*}_{mm'}(-\gamma_{\rm ref}, -\beta_{\rm ref}, -\alpha_{\rm ref}) h^{\vec{J}}_{lm'}(t, \boldsymbol{\lambda}). \tag{4.1.19}$$

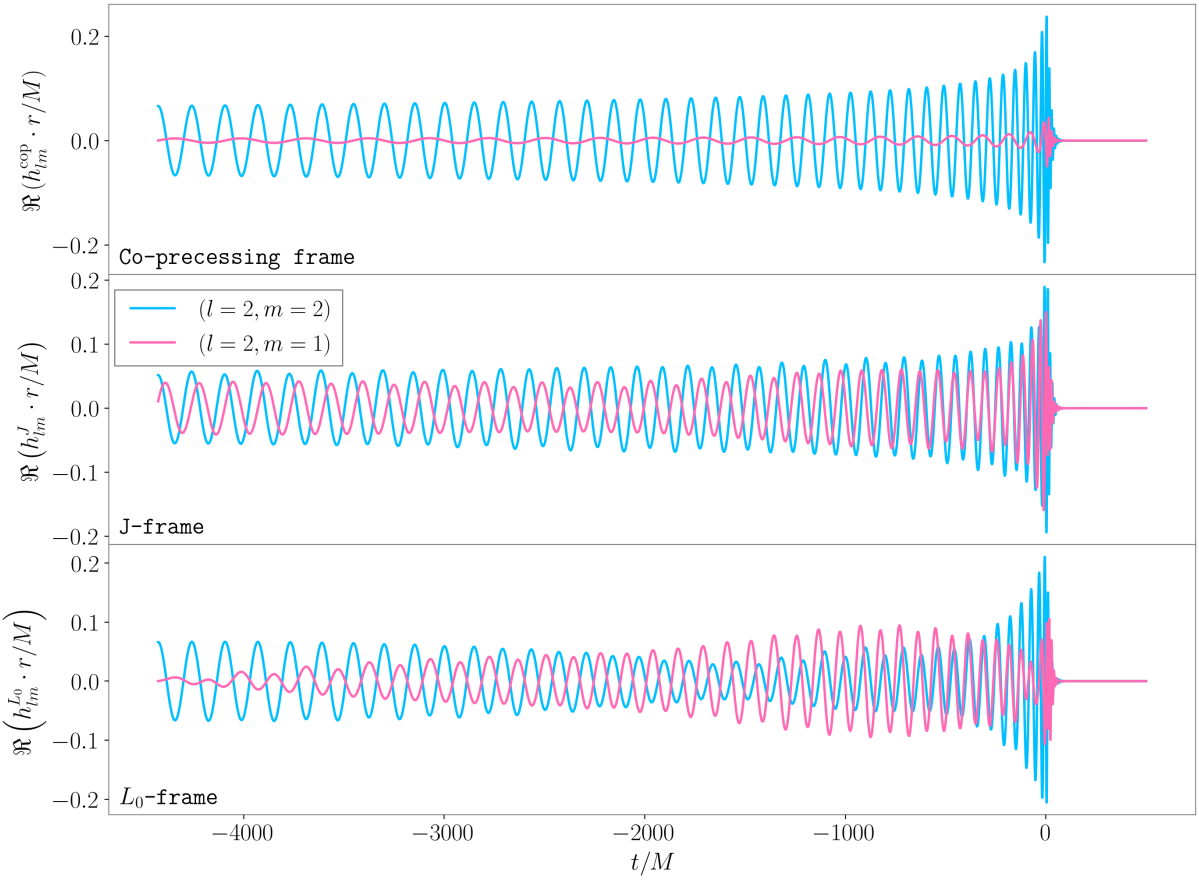

Figure 4.2: Real part of the $(\ell = 2, m = 2)$ (blue) and $(\ell = 2, m = 1)$ (magenta) GW modes for a precessing BBH system with mass ratio $q = 4$, computed using the IMRPhenomTPHM model. The spins are given by $\vec{\chi}_1 = (-0.2, -0.8, 0)$ and $\vec{\chi}_2 = (0, 0, 0.8)$ at a reference frequency $f_{\rm ref} = f_{\rm min} = 15$ Hz. We show the waveform in three different frames: the co-precessing frame (top), the J-frame (middle), and the L_0-frame (bottom).

Once the z-axis is aligned with either $\vec{L}(t_{\rm ref})$ or $\vec{J}(t_{\rm ref})$, the choice of the remaining axes is arbitrary. A common convention in the LVK is to define the x-axis along the separation vector between the larger and smaller black holes at $t_{\rm ref}$, i.e. $\hat{x} = \vec{r}_1(t_{\rm ref}) - \vec{r}_2(t_{\rm ref})$ [111, 142]. The y-axis is then determined by orthogonality, following the right-hand rule (see Figure 3.2 for a visual representation).

Here, the reference time $t_{\rm ref}$ is typically chosen with respect to the merger time (often set as $t_{\rm merger} = 0$) and corresponds to a specific moment in which all time-dependent quantities of the system are defined. This reference time is associated with a concrete frequency, denoted as $f_{\rm freq}$, which can be obtained from the time evolution of the $(2, 2)$-mode frequency. The choice of reference time for waveform decomposition depends on the region of interest: for instance, if one is interested in the final state, a reference time close to merger will be more optimal (as done in Chapter 5). In general, for waveform modeling, this time is typically chosen further from the merger, as the evolution in that region is simpler, and hence the evolution of $\vec{L}$ and $\vec{J}$ are more stable.

Figure 4.2 shows the real part of the $(2, 2)$ and $(2, 1)$ modes of a precessing BBH system, decomposed in the frames introduced above. In the co-precessing frame, the modes remain nearly circularly polarized, exhibiting a morphology similar to that of an

aligned-spin system, and preserving the typical mode hierarchy, with the $(2,2)$ mode dominant. However, in the inertial frames, precession introduces amplitude and phase modulations. These effects are particularly evident in the L_0 frame, where the orbital angular momentum exhibits a complex precessional motion. Since the total angular momentum $\vec{J}$ remains approximately constant throughout the evolution, the waveform in the J-frame appears smoother. In contrast, the L_0 frame captures the full impact of precession, resulting in a more intricate waveform morphology and even a reversal of the mode hierarchy, with the $(2,1)$ mode exhibiting more power than the $(2,2)$ mode during part of the inspiral.

4.1.3 Fourier domain description of precession

The time-dependent modulation of the GW signal induced by misaligned spins naturally motivates the use of a time-domain "twisting-up" approximation to account for these effects in waveform models. This provides a simple and intuitive description of precession. However, as discussed in Section 2.3, frequency-domain templates are typically preferred for data analysis in current ground-based detectors, as they allow for a fast evaluation of likelihoods through direct computation of inner products with detector data.

The twisting up procedure used to incorporate precessing effects introduces challenges in the frequency-domain waveform modeling. These models typically rely on closed-form expressions for the waveform modes, which are derived using the Stationary Phase Approximation (SPA) [305]. The SPA estimates integrals of oscillatory functions by identifying regions where the phase varies slowly – i.e., near stationary points. For a general oscillatory integral

$$I(k) = \int_{\mathbb{R}} g(x) e^{ik\mu(x)} \mathrm{d}x, \tag{4.1.20}$$

with real-valued $g(x), \mu(x)$, and large real k, the dominant contributions come from the stationary points x_0, where the exponential term oscillates slowly: $\frac{d\mu(x)}{dx} \approx 0$. Under suitable conditions, the SPA yields

$$\int_{\mathbb{R}} g(x) e^{ik\mu(x)} \mathrm{d}x = \sum_{x_0 \in \Sigma} g(x_0) e^{ik\mu(x_0) + \mathrm{sign}(\mu''(x_0))i\pi/4} \left(\frac{2\pi}{k|\mu''(x_0)|} \right)^{1/2} + O(k^{-1/2}). \tag{4.1.21}$$

In GW analysis, the SPA is applied to compute the Fourier transform of the strain $h(t)$ as

$$\tilde{h}(f) = \int_{\mathbb{R}} |h(t)| e^{i\Phi(t)} e^{-2i\pi f t} \mathrm{d}t = \int_{\mathbb{R}} |h(t)| e^{i(\Phi(t) - 2\pi f t)} \mathrm{d}t. \tag{4.1.22}$$

Defining $\mu(t) = \frac{1}{f}\Phi(t) - 2\pi t$, we obtain:

$$\tilde{h}(f) = \int_{\mathbb{R}} |h(t)| e^{if\mu(t)} \mathrm{d}t, \tag{4.1.23}$$

so stationary points occur at times when $\frac{\mathrm{d}\Phi}{\mathrm{d}t}\frac{1}{f} = 2\pi$. Then, the SPA is valid when the oscillation rate of the amplitude $|h(t)|$ is lower than the oscillation of the phase.

In aligned-spin systems, this condition typically holds throughout the binary evolution. However, for precessing systems, SPA remains valid only during the inspiral, as precession becomes significant near merger and ringdown, and amplitude modulations are comparable to the phase ones. Additionally, precessing signals exhibit power at both positive and

negative frequencies. Due to the conventions used in GW data analysis (see e.g. [189]), for aligned-spin systems, the $m < 0$ modes have support in the positive frequency range, while modes with $m > 0$ dominate the negative frequency range. In a co-precessing frame, the same convention applies, with the modes reflecting the same frequency behavior, although this will in general not be true for any inertial frame. Moreover, purely SPA-based precessing models are not entirely reliable in regions where the SPA is expected to fail, such as for short signals where amplitude modulations become significant, particularly near merger. In high-mass events, like GW190521 [89], only the late merger-ringdown phase is observed, and models like IMRPhenomXPHM [189] may not fully capture the dynamics of these final stages due to the SPA limitations. In contrast, time-domain models, which do not rely on the SPA, can more accurately capture the dynamics during these final stages, though they come with higher computational costs. Although alternative approaches, such as the Shifted Uniform Asymptotics (SUA) formalism [306, 307], have been proposed to extend beyond the SPA, they still depend on it during the inspiral phase. Another limitation of frequency-domain precession models is their incomplete description of the ringdown emission. While in the time domain, the ringdown frequencies directly influence the morphology of the signal (see Section 3.3), this relationship is less straightforward in the frequency domain. The Fourier transform does not separate the inspiral from the merger/ringdown phases, meaning that the exponential decay of the amplitude is not directly tied to the imaginary part of the ringdown frequency.

Despite these limitations, IMRPhenomXPHM [189] – a purely SPA-based precessing frequency-domain model constructed on top of IMRPhenomXHM [33, 308] – has been regularly employed in LVK data analysis [2, 3, 309] due to its robustness and surprising accuracy. The SPA serves as an excellent starting point for generating closed-form precessing models, and by calibrating these models to NR simulations, it is possible to obtain accurate models with corrections that allow for broader applicability. This approach was initially applied to aligned-spin models (see e.g., [33, 308]), which was more straightforward due to the lower-dimensional parameter space and the higher density of NR simulations in that space. Only in recent years the first attempts have been made to calibrate precessing models in the frequency domain, leading to a new family of NR-calibrated precessing models [293, 294, 310]. A review of these models can be found in Section 4.3.

Finally, it is important to note that current data analysis techniques assume the detector's motion can be neglected during the event, and hence the frequency domain turns out to be the most efficient to describe both the signal and noise. This assumption is valid for transient signals in ground-based detectors. However, for longer-duration signals, such as CWs or signals detectable by 3G ground-based detectors or LISA, the detector's motion during the signal duration must be considered. In these cases, the time dependence of the detector response becomes significant, necessitating the development of time-frequency methods [311, 312].

4.2 Eccentric effects

As seen in Section 4.1, spin effects influence the entire evolution of the gravitational waveform, becoming especially pronounced near merger. This can be seen in Equation (4.1.3), where the spin term decays faster than the Newtonian term with increasing separation.

Moreover, spin effects also impact the remnant BH, particularly the final spin, due to the addition of the in-plane spins to the orbital angular momentum. As a result, precessing waveform models have been developed and widely adopted since the first GW detections, as spin-induced precession may already be observable with current detectors. For instance, spin-precession was claimed in the case of GW200129 [313], an event that also shows other intriguing features compatible with possible dynamical formation channel, evidenced by a significant kick velocity [314], and signs of orbital eccentricity [22, 55, 315] (see Chapter 7 for an analysis of this event with IMRPhenomTEHM [19]). Additionally, there have been claims of false violations of GR due to waveform systematics [316]. However, it is important to note that this event also exhibits a glitch in the LIGO Livingston data within the 20–50 Hz frequency range. While various glitch mitigation techniques have been applied to assess the impact of the glitch on both the precession and eccentricity [22, 55, 317, 318], making definitive conclusions for this event remains challenging.

Detecting precession in GWs would provide valuable insight into binary formation (see Ref. [319, 320] for reviews): aligned spins suggest *isolated binary evolution*, where interactions like mass transfer or common-envelope phases tend to align the spins, while misaligned or isotropic spin distributions point toward *dynamical formation* in dense stellar environments such as globular clusters. That said, spin directions may become randomized over time – e.g., due to supernova kicks – reducing their effectiveness as formation channel indicators. In addition to spin, the binary's formation history is also imprinted in its component masses and orbital eccentricity. The presence or absence of eccentricity and spin precession thus serves as a potential discriminator between isolated and dynamical formation channels, although disentangling these effects remains challenging due to parameter degeneracies and limited detector sensitivity. Identifying such imprints in GW observations is crucial to distinguishing between different formation scenarios, though this task remains difficult due to the high dimensionality of the BBH parameter space and the sensitivity limitations of current detectors. Moreover, multiple formation channels may be at play simultaneously, further complicating source classification.

One robust theoretical expectation is that binaries formed through isolated evolution circularize well before entering the sensitive frequency band of the LVK detectors, due to the efficient loss of angular momentum via gravitational radiation [36]. Orbital eccentricity in BBH mergers is therefore considered a smoking gun of dynamical formation: its detection would strongly suggest a dynamical origin, such as interactions in globular clusters or galactic nuclei [321, 322], or hierarchical mergers through the Kozai-Lidov mechanism in triple systems [323, 324]. By studying the effects of eccentricity on GW signals, we can help quantify the fraction of BBH mergers arising from dynamical interactions.

Given the current sensitivity of ground-based detectors, many waveform models for BBH mergers assume quasi-circular (QC) orbits [31, 171–174, 183, 186, 190]. Observationally, the LVK Collaboration [1–4] and independent studies[325–330] have found that most detected signals are consistent with circular binaries. Several formation mechanisms support this scenario, including common envelope evolution [331–335], chemically homogeneous evolution [336–338], stable mass accretion from a stellar companion [339, 340], or fallback driven by ambient gas [341].

In contrast, dynamically formed BBHs can also merge within a Hubble time, but follow a different evolutionary pathway. Here, the progenitor BHs do not originate from a single stellar binary but instead form binaries through gravitational interactions in dense

stellar environments like young clusters, globular clusters, or galactic nuclei [342–344]. In such environments, frequent interactions can result in black holes exchanging partners in multiple binary configurations before eventually merging. In particular, three-body interactions can harden binaries by transferring binding energy to a third object, thereby increasing the likelihood of merger.

Future observations with LVK and next-generation detectors such as ET [11, 12], CE [13], and space-based observatories like LISA [15, 345] will access a broader frequency range and detect a larger population of sources. This will significantly enhance our ability to infer binary properties and evolutionary pathways, making the development of robust techniques to model and interpret eccentric systems an urgent priority. Several eccentric BBH models have therefore been proposed in recent years [19–21, 43, 175, 176, 346–358] (see Chapter 6 for a detailed description on IMRPhenomTEHM, a time-domain phenomenological multipolar model for aligned-spin binaries [19]), and here we focus on the fundamental principles underlying their construction. In the following we exclude the surrogate model [45], which does not rely on these approximations but at the same time is restricted to comparable-mass, non-spinning binaries due to the limited number of NR simulations.

The rest of the section is organized as follows: We first discuss eccentricity within PN theory in Section 4.2.1, providing an overview of the common modeling approach for eccentric orbits. Finally, in Section 4.2.2, we summarize the different definitions of eccentricity found in the literature and present the specific parameterization used in this work.

4.2.1 Post-Newtonian description of eccentricity

Eccentricity quantifies the deviation of an orbit from circularity and it is most easily understood in the Newtonian regime. In the Keplerian framework, the eccentricity e appears in the radial orbital equation,

$$r(t) = \frac{a(1-e^2)}{1 + e\cos v(t)}, \tag{4.2.1}$$

where r is the radial separation from the focus of the ellipse, a the semimajor axis, and v the true anomaly. This definition leads to the standard classification: circular orbits for $e = 0$, elliptic for $0 < e < 1$, and unbound (parabolic or hyperbolic) for $e \geq 1$. In a BBH system with total mass M, Kepler's third law relates the semi-major axes $a_{1,2}$ of the two components and the *Keplerian angular frequency* $\bar{\omega}$ via

$$\bar{\omega}^2 (a_1 + a_2)^3 = GM. \tag{4.2.2}$$

The *instantaneous orbital frequency* varies over the orbit as

$$\omega(t) = \frac{\bar{\omega}\sqrt{1-e^2}}{[1 - e\cos u(t)]^2} \approx \bar{\omega}[1 + 2e\cos(\bar{\omega}t)] + \mathcal{O}(e^2), \tag{4.2.3}$$

where $u(t)$ is the eccentric anomaly, and the approximation holds for small eccentricities. Eccentric binaries thus exhibit frequency modulations around the mean orbital value, with amplitude scaling as $2e\bar{\omega}$, which vanish in the QC limit. These modulations are also reflected in the GW signal, which, for eccentric binaries, contains power distributed across

multiple harmonics of the orbital frequency, in contrast to QC systems, where most power is concentrated in the second harmonic [359]. Moreover, GW emission is asymmetric, with stronger radiation emitted near periastron than apastron.

The Keplerian notion of eccentricity however becomes inadequate in the presence of radiation-reaction effects, for two principal reasons. First, in GR orbits are no longer closed: both the semi-major axis and the eccentricity decay over time due to the emission of gravitational radiation. At leading PN order, their orbit-averaged evolution (denoted by $\langle\rangle$) is governed by the Peters–Mathews equations [36]:

$$\left\langle \frac{\mathrm{d}a}{\mathrm{d}t} \right\rangle = -\frac{64}{5} \frac{G^3 m_1 m_2 M}{c^5 a^3 (1-e^2)^{7/2}} \left(1 + \frac{73}{24} e^2 + \frac{37}{96} e^3\right), \tag{4.2.4}$$

$$\left\langle \frac{\mathrm{d}e}{\mathrm{d}t} \right\rangle = -\frac{304}{15} \frac{G^3 m_1 m_2 M}{c^5 a^4 (1-e^2)^{5/2}} \left(1 + \frac{121}{304} e^2\right). \tag{4.2.5}$$

Second, eccentricity is a gauge-dependent quantity, which complicates its interpretation in relativistic frameworks and contributes to inconsistencies across theoretical descriptions (see Section 4.2.2 for a detailed discussion). Even within the PN formalism, different approaches to eccentricity lead to distinct physical interpretations. The Lincoln–Will approach [360] employs a Newtonian-like framework, describing radiation reaction via multiscale analysis and using a single eccentricity parameter. However, this eccentricity does not directly correspond to circular ($e = 0$) or unbound ($e = 1$) limits and may even exhibit secular growth in the late inspiral [355], similar to behavior seen in SF calculations. In contrast, the quasi-Keplerian (QK) formalism [40, 361] introduces three eccentricity parameters to more accurately represent relativistic motion. These parameters are derived from a PN-order-by-order solution of the equations of motion and exhibit the correct limits in both circular and unbound regimes. Additionally, the QK formalism averages the GW fluxes of energy and angular momentum over an orbit, resulting in a monotonic decrease in eccentricity consistent with NR predictions. For these reasons, we adopt the QK formalism in this work.

The QK parametrization is a generalization of the classical Keplerian formalism [40, 361–364], incorporating periastron advance and relativistic corrections due to radiation reaction. It is constructed by solving for the conserved energy E and total angular momentum J, under the assumption that orbits are bounded between a minimum and a maximum separation. This leads to the generalized radial equation [365]:

$$r = a_r(1 - e_r \cos u), \tag{4.2.6}$$

where a_r is the semi-major axis and e_r is the radial eccentricity. The full QK parametrization, valid in any chosen coordinate gauge, is given by (along with Equation (4.2.6)):

$$l = u - e_t \sin u + f_{v-u}(v - u) + f_v \sin v, \tag{4.2.7}$$

$$\frac{2\pi}{\Pi}(\phi - \phi_0) = v + g_{2v} \sin(2v) + g_{3v} \sin(3v), \tag{4.2.8}$$

$$v = 2 \arctan\left[\sqrt{\frac{1+e_\phi}{1-e_\phi}} \tan\frac{u}{2}\right], \tag{4.2.9}$$

where ϕ is the orbital phase, l the mean anomaly, Φ is the azimuthal angle swept between two successive periastron passages, and $f_{v-u/v}$ and $g_{2v/3v}$ are expressions in terms of

$\{u, e_t, l\}$ which depend on the gauge and coordinates used. The two additional eccentricities introduced in Equation (4.2.9), the time eccentricity e_t and phase eccentricity e_ϕ, complete the QK framework. e_ϕ is defined such that no term proportional to $\sin v$ appears in the expression for ϕ. To express the binary dynamics in a gauge-invariant way, it is usual to introduce

$$x = \left(\frac{GM\omega}{c^3}\right)^{2/3}, \tag{4.2.10}$$

where ω is the orbital angular frequency. The QK parametrization then expresses all dynamical quantities as functions of $(x, e_t \equiv e, u)$. These expressions are exact at each PN order, provided the orbits remain planar, as in non-precessing binaries. In the presence of spin-induced precession, they can still be applied approximately in a co-precessing frame as done for QC binaries [279], which is useful in waveform modeling.

It is important to note that the dependence of the QK parameters on E and J varies with the choice of coordinate gauge. For example, Ref. [365] provides expressions for non-spinning binaries up to 3PN order in modified harmonic coordinates; Refs. [362, 363] extend the results to include SO and SS terms up to 3.5PN in ADM coordinates using the Newton–Wigner spin-supplementary condition (SSC); and Ref. [39] uses harmonic coordinates and a covariant SSC to derive spinning corrections up to 3PN.

The results above describe the conservative part of the binary dynamics and are exact in eccentricity (i.e., no small-eccentricity expansion is needed). However, when incorporating GW emission, it is often necessary to expand quantities in small eccentricity to obtain closed-form expressions at a given PN order. This is particularly true in the calculation of GW multipoles, as the integrals involved in the tail terms cannot be solved analytically unless an eccentricity expansion is performed. In such contexts, it is convenient to use the parameter set (x, e, l). For example, Ref. [38] computes GW modes up to 3PN for non-spinning eccentric binaries, expanded in eccentricity up to e^6, while Ref. [39] provides spinning contributions at 3PN, also expanded up to e^6. Hence, in the context of waveform modeling, we are typically interested in the variables (x, e, l), which parameterize the orbit and hence the GW emission. The secular evolution of these quantities is described by orbit-averaged PN equations, yielding a system of coupled differential equations:

$$\langle \dot{x} \rangle = f(x, e), \tag{4.2.11}$$

$$\langle \dot{e} \rangle = g(x, e), \tag{4.2.12}$$

$$\langle \dot{l} \rangle = m(x, e). \tag{4.2.13}$$

Expressions for these equations are available in the literature across different coordinate gauges. For example, Refs.[37, 38] provide the 3PN non-spinning contributions in ADM and modified harmonic coordinates, while Ref. [39] presents the 3PN spinning contributions in harmonic coordinates.

By solving the equations for $\langle x \rangle$ and $\langle e \rangle$, one finds that eccentricity decays rapidly – even for systems with initial eccentricities close to unity. This supports the statement made earlier in this section: we expect most BBHs to have circularized by the time they enter the sensitivity band of ground-based detectors (we point the reader to Chapter 7 and Chapter 8 for eccentric reanalysis of GWTC3 events). Indeed, the estimated BBH population is not expected to exhibit significant eccentricity during the late inspiral and merger [36]. For instance, Figure 4.3 shows the evolution of the orbital eccentricity as a function of the GW frequency of the $(2, 2)$-mode obtained by solving the set of coupled

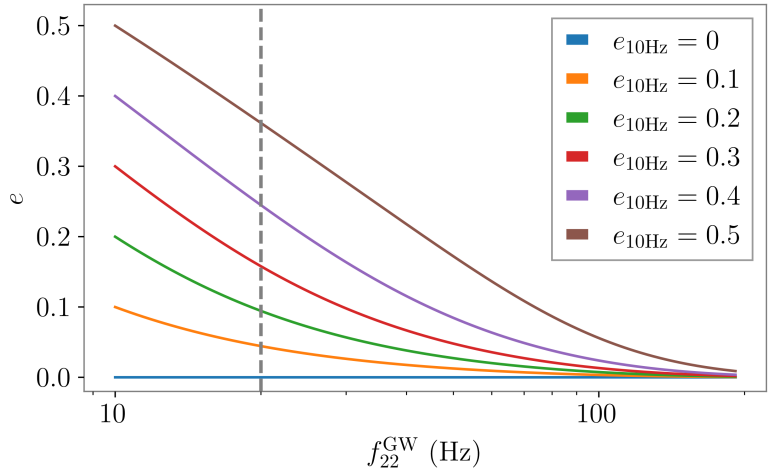

Figure 4.3: Evolution of the orbital eccentricity as a function of the GW frequency of the $(2,2)$-mode $f_{22}^{\rm GW}$ for a binary with total mass $M = 70M_\odot$, mass ratio $q = 1$, and aligned spins $\chi_{1z} = 0.7, \chi_{2z} = 0.5$. Each curve corresponds to a different initial eccentricity defined at a reference frequency of 10 Hz. The vertical dashed line at 20 Hz marks the typical lower frequency sensitivity of current ground-based detectors, illustrating that a significant amount of circularization occurs before the binary enters the detector band.

differential equations in Equation (4.2.13) for the 3PN spinning and 2PN non-spinning equations in the QK parametrization and MH gauge [39]. The eccentricity decays rapidly due to gravitational RR, with all cases approaching circularization by the time the system reaches merger.

These results motivate the fact that PN may be sufficient for now to model IMR eccentric binaries, since it is expected that eccentricity only impacts the early inspiral. One can assume that the system circularizes by merger and use standard QC models – aligned-spin for now – typically calibrated to NR. This assumption forms the foundation of most existing IMR eccentric waveform models [19–21, 43, 175, 176, 346–358] (except for the surrogate [45]). Furthermore, these models have been developed in the time domain, as eccentricity introduces strong time-dependent features in the waveform. Building on progress in modeling spin precession, recent efforts have started to apply the SPA to derive closed-form expressions for eccentric waveform modes in the Fourier domain. While fully general Fourier-domain models for eccentric binaries are still under development, initial inspiral models that incorporate both eccentricity and spin precession have already appeared in the literature [366, 367].

The assumption of circularization at merger breaks down for high-mass binaries formed through dynamical interactions, such as in globular clusters, where eccentricity may persist until merger (see e.g. [321]). In such cases, waveform models must be calibrated to NR simulations. Yet, due to the computational challenges in producing accurate NR waveforms in the eccentric regime and hence the lack of these, no generic model has yet been constructed following this approach. There has been some development within the surrogate family; however, due to the limited number of NR eccentric simulations, the only available surrogate model is restricted to comparable-mass, non-spinning binaries [45]. Nonetheless, current eccentric models assuming a QC merger – despite these limitations – have shown good agreement with NR simulations and have even succeeded in identifying potential eccentric features in public GW events [22, 47, 49, 53, 55, 315]. We refer the

reader to Chapter 6 for the construction of a time-domain, aligned-spin waveform model for eccentric binaries, and to Chapter 7 and Chapter 8 for a reanalysis of selected GWTC-3 events aimed at finding signatures of eccentricity.

4.2.2 Eccentricity parametrization

A key challenge in modeling eccentric systems is that eccentricity is not a well-defined or gauge-invariant quantity in GR, as discussed in Section 4.2.1. Unlike Newtonian orbits, relativistic binaries exhibit *periastron precession* and energy loss through GW emission, preventing closed orbits and complicating its definition.

Different frameworks approximate eccentricity in GR in various ways, and for a detailed overview we point the reader to Ref. [368]. The PN formalism includes the Lincoln–Will [360, 369, 370] and QK [40, 42, 361, 365, 371–373] approaches – respectively using a single parameter or multiple eccentricities to capture relativistic effects (see Section 4.2.1 for details). In the SF approach, eccentricity is derived from geodesic motion and can grow near the separatrix in the adiabatic limit [374]. NR simulations of BBHs have been routinely performed over two decades. Historically, however, eccentricity was considered an undesirable feature in NR simulations for two main reasons. First, motivated by the expectation that most GW signals in the frequency band of ground-based detectors would have negligible eccentricity [36], NR efforts primarily focused on QC BBH mergers [222–224, 226–228], to meet the demands of waveform model development. Second, eccentric systems introduce an additional timescale – the periastron timescale – which can become much shorter than the orbital period for near-parabolic orbits. Resolving such short timescales requires significantly higher resolution, increasing computational cost and complexity. At the same time, generating genuinely QC initial data proved non-trivial: generic initial configurations often contained a small radial velocity component that induced residual oscillations, indicative of non-zero eccentricity. This led to the development of eccentricity reduction techniques [375–379], which typically define eccentricity via the motion of the compact objects, using fits to analytical PN or Newtonian expressions [147, 378, 379]. Nevertheless, even in the early days of NR, a limited number of studies addressed eccentric BBH coalescences, including head-on collisions, which were among the first simulations performed [380]. Significant attention was also given to zoom whirl orbits, which describe high-eccentricity inspirals around rapidly spinning Kerr black holes (see, e.g., [381, 382]). Today, growing interest in eccentric CBCs has renewed efforts in this direction. Thanks to improvements in algorithms and computing power, NR simulations of BBHs with moderate eccentricities have become increasingly feasible (see, e.g., [225, 229, 346, 347, 383, 384])

Despite the varying definitions, all methods should agree in overlapping regimes – to avoid ambiguities in interpreting GW signals from eccentric systems, consistent definitions of eccentricity across waveform models are essential for robust comparison and physical interpretation. First, describing an eccentric orbit generally requires two parameters. In the context of bound BBH systems, it is standard to use *eccentricity* e and *mean anomaly* l, which are also adopted in current waveform models and will be the focus of this work. Other parameter choices are possible and more appropriate in different regimes: for instance, *energy* and *angular momentum* at infinity are conserved quantities in Newtonian mechanics and in certain limits of GR, and are frequently used in GSF [242]. In the EOB formalism, initial conditions for the dynamics are prescribed in terms of eccentricity parameters defined within the QK parameterization (typically the *Keplerian*

eccentricity and the *relativistic mean anomaly*) [20, 21, 43, 44, 356]. In the case of unbound or scattering encounters, eccentricity is often paired with the *impact parameter* [382].

A robust definition of eccentricity and mean anomaly should fulfill several requirements [385]. First, to avoid gauge ambiguities, these quantities should be defined using observables accessible at future null infinity, such as the gravitational waveform. Second, in the limit of large binary separation, the definition should reduce to the uniquely defined Newtonian eccentricity:

$$e_{\rm Newt} = \frac{r^{\rm a} - r^{\rm p}}{r^{\rm a} + r^{\rm p}}, \tag{4.2.14}$$

where $r^{\rm a}$ and $r^{\rm p}$ are the separations at apocenter (point of furthest approach) and pericenter (point of closest approach), respectively. It should also be valid across the entire eccentricity range for bound systems, returning zero for QC inspirals and approaching unity for parabolic trajectories. Similarly to other BBH parameters such as component spin directions, orientation with respect to the observer, both eccentricity and mean anomaly evolve over time, and hence it is necessary to specify the point at which they are to be evaluated. This is typically chosen to be the moment when the GW frequency reaches a reference value $f_{\rm ref}$. For QC binaries without spin precession, the GW frequency increases monotonically, allowing $f_{\rm ref}$ to be uniquely associated with a reference time $t_{\rm ref}$. In spin-precessing QC binaries, although the inertial frame frequency $f_{\rm ref} = \omega_{22}/(2\pi)$ can become non-monotonic due to precession (see Section 4.1.2.3 for frame definitions), it remains monotonic in a co-precessing frame [298]. However, no analogous frame exists for eccentric binaries. In general, $\omega_{22} \sim 2\omega$ becomes a highly oscillatory function, as do all orbital elements, making the choice of reference frequency more ambiguous, since a given reference frequency may occur at multiple points during the evolution. Therefore, a good eccentricity definition for modeling should also prescribe a unique and physically meaningful reference point. It is common to define the reference time $t_{\rm ref}$ as the time in which some *orbit averaged frequency* $\langle f_{\rm ref} \rangle$ is reached, and this is indeed the choice made in the eccentric model presented in Chapter 6. Finally, in the limit of large mass ratio, the eccentricity should converge to the test-particle eccentricity defined along Kerr geodesics.

Several efforts have been made to standardize the definition of eccentricity [45, 346, 356, 385–389], or to establish mappings between different formalisms [390]. However, these approaches often neglect the mean anomaly or fail to reproduce the correct behavior in the limit of large separations or high mass ratios. In this work, we follow the framework introduced in Ref. [386], implemented in the `gw_eccentricity` package [385] in `python`, which has been validated across the full range of eccentricities and formalisms – including PN theory, NR, EOB, and EMRIs – as shown in Ref. [385]. This definition of eccentricity is constructed from the instantaneous angular GW frequency of the dominant $(2, 2)$ mode, ω_{22}, measured at successive periastron and apastron passages. Specifically, one defines an auxiliary parameter,

$$e_{\omega_{22}} = \frac{\omega_{22,\rm p}^{1/2} - \omega_{22,\rm a}^{1/2}}{\omega_{22,\rm p}^{1/2} + \omega_{22,\rm a}^{1/2}}, \tag{4.2.15}$$

where $\omega_{22,\rm p}$ and $\omega_{22,\rm a}$ denote the GW frequencies at periastron and apastron, respectively. This quantity is then mapped to a gauge-minimized eccentricity estimate via

$$\psi = \arctan\left(\frac{1 - e_{\omega_{22}}^2}{2 e_{\omega_{22}}}\right), \tag{4.2.16}$$

$$e^{\rm GW} = \cos(\psi/3) - \sqrt{3}\sin(\psi/3). \tag{4.2.17}$$

The eccentricity measure $e^{\rm GW}$ builds on earlier definitions proposed in the literature [45, 346, 356, 387, 391], improving them in two key aspects. First, it is constructed directly from the GW strain h_{22}, evaluated at future null infinity, thereby ensuring gauge independence – unlike earlier approaches that relied on the orbital frequency, which is gauge-dependent. Second, $e^{\rm GW}$ recovers the correct Newtonian limit in the regime of large separations, a property not satisfied by intermediate quantities such as $e_{\omega_{22}}$.

To fully characterize an eccentric orbit at a given reference frequency, an additional parameter is required. We adopt the mean anomaly, $l^{\rm GW}(t)$, which quantifies the fraction of an orbital cycle (expressed as an angle) elapsed since the most recent periastron passage. Generalizing the Newtonian definition, it is given by [45, 142, 346, 386]:

$$l^{\rm GW}(t) = 2\pi \frac{t - t_i^{\rm p}}{t_{i+1}^{\rm p} - t_i^{\rm p}}, \tag{4.2.18}$$

where $t_i^{\rm p}$ and $t_{i+1}^{\rm p}$ denote consecutive periastron times identified via ω_{22}. It is important to emphasize that the mean anomaly is an intrinsic physical parameter of the system – similar to the orbital eccentricity $e^{\rm GW}$ – and cannot be absorbed by a simple time or phase shift [45]. Varying the mean anomaly at fixed time before merger necessitates a change in frequency, thereby altering the physical configuration. Neglecting this parameter in waveform modeling or PE has been shown to induce systematic biases in the recovered source properties [45, 54, 392].

4.3 Overview of BBH modeling

The detection and characterization of GWs rely on accurate waveform templates [1–4], which are used in matched filtering procedures, as explained in Section 2.3.3. NR simulations provide the most accurate waveforms for BBH binaries, but they are computationally expensive and cannot span the full nine-dimensional parameter space of generic binaries. To overcome this limitation, NR results are combined with analytical insights to construct waveform models that cover broader regions of the parameter space.

Two major waveform model families have been developed following this hybrid approach. Effective-One-Body (EOB) models [32, 171–173, 178, 240, 393–407] reformulate the two-body problem into that of a test particle moving in a deformed spacetime, capturing strong-field dynamics in the time domain. Phenomenological models use closed-form expressions calibrated to NR and EOB waveforms, leading to the development of the IMRPhenom family [19, 33, 34, 186–191, 279, 408–412]. Originally formulated in the frequency domain, these models – particularly the IMRPhenomX family, mainly developed at UIB – gained popularity in Bayesian inference due to its computational speed [1–4]. However, as discussed in Section 4.1 and Section 4.2, time domain models offer a more faithful representation of the source dynamics, motivating the development of the IMRPhenomT family – the first time-domain phenomenological models [19, 34, 190, 191, 412].

In parallel, the NRSurrogate family [28, 45, 182–184, 198, 199, 413, 414] uses interpolation among densely sampled NR simulations to produce fast waveforms with NR-level accuracy within their training domain. While these models are often more

accurate, they are typically constrained by the limited parameter space covered by NR simulations compared to the other two approaches.

These models are now standard tools in GW astronomy and are traditionally implemented in the LIGO Algorithm Library (LAL) [111] using `C` . Recently, `python`-based alternatives have emerged, including `pyseobnr` [415] for SEOB models, `phenomxpy` [416] for IMRPhenom, and `gwsurrogate` [417] for NRSurrogate models. The following sections summarize each family and review the available models.

4.3.1 Effective-one-body formalism

The EOB formalism arises from resummation techniques applied to the PN series to extrapolate results to high-velocity regimes, enabling the modeling of two key ingredients of GW signals: the two-body energy and the GW energy flux. It maps the real conservative two-body dynamics – computed up to the highest PN order available – onto an effective one-body problem, where a test particle of mass $\mu = m_1 m_2/M$ moves in an effective background metric $g_{\rm eff}$. It was originally assumed – and later confirmed [240, 241] – that the resummed quantities provide a more accurate description of the comparable-mass regime, viewed as a smooth deformation of the test-mass case. The formalism becomes increasingly natural in the large mass-ratio limit, where it smoothly connects with GSF (see e.g. [418]). For BBH systems, it is typically assumed a deformed Schwarzschild or Kerr metric, with the deformation parametrized by the symmetric mass ratio $\eta = \mu/M$. This mapping is constructed within the Hamilton-Jacobi formalism, with the energy relation between the effective and real dynamics given by

$$H_{\rm EOB} = M\sqrt{1 + 2\eta\left(\frac{H_{\rm eff}}{\mu} - 1\right)}. \tag{4.3.1}$$

A final crucial ingredient in the EOB model is the treatment of the merger-ringdown phase. After merger, the system settles into a Kerr black hole and emits QNMs, as discussed in the previous chapter. In the EMRI limit, Refs. [247, 419] observed that when a test particle falls radially below $r = 3M$ – the light ring of Schwarzschild – it promptly excites QNMs, producing a universal merger signal. This occurs because direct gravitational radiation from the particle is filtered by the curvature potential barrier surrounding the light ring. In the comparable-mass case, Ref. [420] introduced the *close-limit approximation*, wherein the description transitions from a two-body system to a perturbed BH near the light ring. Based on these insights, the merger is modeled as a brief phase, matching the inspiral-plunge waveform to a damped sinusoid at the light ring location [213, 240, 421, 422]. The frequency and damping time of the QNMs are computed from the final BH's mass and spin, estimated from the EOB energy and angular momentum at the matching point. Integrating the EOB Hamiltonian equations yields the binary's evolution up to the light ring, after which each spherical harmonic waveform mode is matched to a QNM spectrum calibrated to NR simulations.

Depending on the PN order and the physical effects incorporated into the effective Hamiltonian, various models can be developed within the EOB formalism. Two prominent families have emerged: the SEOBNR models [20, 31, 171–174, 356, 397, 423], designed primarily for BBH systems, and the TEOBResumS family [21, 32, 43, 44, 178–181, 352, 406, 424–426]. For a summary on main differences we point the reader to e.g. Table II

in Ref. [427]. Within the SEOBNR family, models have been constructed to describe non-spinning, spinning, spin-precessing, and eccentric binaries. Although EOB models are computationally more efficient than full NR simulations, they still require solving the Hamiltonian equations, which can be numerically expensive. To mitigate this cost, surrogate and reduced-order models (ROMs) have been developed (see e.g. [400, 407, 428, 429]). The latest generation of SEOBNR models builds upon increasingly sophisticated descriptions of binary dynamics. For instance, SEOBNRv5HM [174] captures aligned-spin QC systems with high PN accuracy, including spin effects up to quartic order. This model serves as the foundation for further extensions: spin-precessing binaries are treated through a twisting-up procedure, yielding the SEOBNRv5PHM [31] model, while eccentricity is incorporated into the dynamics and waveform modes in the SEOBNRv5EHM [20] variant. Finally, recent work has been done to incorporate matter, leading to the construction of SEOBNRv5THM [423], an EOB model for spin-aligned BNS systems.

The TEOBResum family offers an alternative treatment of the EOB formalism by introducing the gauge-invariant concept of the *centrifugal radius* [424]. In the spinning small mass-ratio limit, expressing the radial potential in terms of this coordinate yields only minor multiplicative deviations from the Schwarzschild case, enabling a unified treatment of spin and finite-mass-ratio effects. This formalism also departs from traditional EOB approaches in its use of the radiation reaction force, resummation techniques, and NR calibration for the ringdown phase. Building on this framework, tidal effects were incorporated through an enhanced attractive tidal potential inspired by PN and GSF theories [32, 430–432]. This led to the development of the TEOBResumS models [21, 32, 43, 44, 178–181, 352, 406, 424–426], initially focused on non-precessing, quasi-circular systems. More recently, the formalism has been extended with the TEOBResumS-Dalí model [44], which describes generic CBCs with arbitrary orbital configurations, including quasi-circular, eccentric, hyperbolic, and non-planar motions. This marks the first time an IMR waveform model consistently incorporates all these effects.

4.3.2 Phenomenological family

The original motivation behind the IMRPhenom approach was to develop an approximate yet computationally efficient waveform family suitable for GW searches and parameter estimation. These models were thus initially formulated as closed-form analytical expressions in the frequency domain. The construction is organized into three distinct regimes: *inspiral*, *intermediate* (encompassing late-inspiral and merger), and *ringdown*. This segmentation ensures high accuracy across the entire frequency (and time) domain, while also making the model modular. One key advantage of this structure is its flexibility – each phase can be modified or replaced independently as more accurate or extended models become available. This modularity also facilitates the incorporation of additional physical effects into the waveform, such as spin precession, memory effects, tidal interactions, and eccentricity (see Chapter 6 for the development of the eccentric IMRPhenom model).

Indeed, this modular construction enabled the rapid development of multiple Phenom models. The earliest versions [144, 145, 433, 434] were limited in parameter space – initially non-spinning and then including aligned-spins through effective spin parameters. These models were significantly improved with the introduction of PhenomD [186, 187], which employed uncalibrated SEOBv2 waveforms in the inspiral and calibrated the merger–ringdown part to NR simulations for mass ratios up to $q = 18$ and aligned spins

up to $\chi_1 \sim 0.85$, while still including only the dominant multipole. The "twisting up" method, introduced in Section 4.1, then led to the development of QC precessing-spin models such as PhenomP [279] and PhenomPv2 [408].

The more recent aligned-spin models are IMRPhenomXAS [411] and IMRPhenomXHM [33, 308], for the dominant and HM multipoles. These models update PhenomD by incorporating double-spin effects rather than the previous single-spin approximation, and hence account for unequal-spin binaries. They form the foundation of IMRPhenomXPHM [189], a spin-precessing model for QC orbits. Though not calibrated to precessing NR simulations, IMRPhenomXPHM was selected for its accuracy and computational efficiency, becoming the primary model used in the official LVK analysis of O3 data [4].

The first non-surrogate NR-tuned spin-precessing calibrated model was developed within the IMRPhenom family: PhenomPNR [310]. This model uses PhenomDCP as the co-precessing frame model, which is based on PhenomD [186, 187] and incorporates in-plane-spin modifications. This effort was extended with IMRPhenomXO4a [292–294], which adds NR in-plane-(single)-spin tuning to IMRPhenomXHM [33, 308], improves the merger-ringdown modeling, and includes multipole asymmetries for m modes [292]. The combination of IMRPhenomXO4a and PhenomPNR has led to the development of the new IMRPhenomXPNR model [111], which improves the accuracy of waveform predictions for spin-precessing BBH systems and is one of the models proposed for the LVK analysis of O4b data. Additionally, frequency-domain models that incorporate matter effects have recently been developed within the IMRPhenomX family: IMRPhenomXP/AS_NRTidalv2[435] and IMRPhenomXP/AS_NRTidalv3[436]. Both models are currently being extended to include spin-precession effects.

The initial motivation for the IMRPhenom family was to develop efficient models for GW signals, which is why they were first designed in the frequency domain. These models reached very good accuracy due to the piecewise closed-form expressions, which allowed for several improvements and easy calibration with NR simulations. As explored in this chapter, time-domain models however provide a more direct insight into the dynamics of the system, helping to interpret certain events where the approximations used in the frequency domain fail. This idea led to the construction of the IMRPhenomT [34, 190, 191] family. The core model, IMRPhenomTP [191], models the dominant quadrupole emission in QC precessing systems and is calibrated with a large dataset of NR aligned-spin simulations. It was later extended to include higher modes in IMRPhenomTHM [34] and developed into the precessing QC model IMRPhenomTPHM [190] by applying the "twisting up" procedure. Since this model does not use the SPA to obtain closed-form expressions in the frequency domain, IMRPhenomTPHM has proven valuable in analyzing short events like GW190521 [137]. There has been recent development to extend the IMRPhenomTHM model to include the $(2, 0)$ multipole, adding memory effects [412]. Finally, the IMRPhenom family has been extended to include eccentric orbits for aligned-spin binaries, leading to the creation of the IMRPhenomTEHM model [19] – one of the core developments of this thesis – described in Chapter 6.

4.3.3 Surrogate modeling

Surrogate modeling, as described in Ref. [428], is a data-driven approach for constructing fast and accurate waveform models based exclusively on NR simulations, with minimal assumptions – such as the twisting-up for precessing models – based on waveform

morphology as done for EOB or phenomenological models. These models retain the high accuracy of NR while greatly reducing the computational cost.

The method starts with a training set of NR waveforms sampled over a carefully chosen grid in parameter space (e.g., mass ratios and spins). Instead of directly interpolating full waveforms – which are high-dimensional and computationally expensive to manipulate – the surrogate approach uses reduced bases to capture the essential waveform structure. This is done through proper orthogonal decomposition, identifying a small number of basis functions that span the waveform space efficiently. Each waveform in the training set is projected onto this reduced basis, and the time-dependent projection coefficients are then interpolated across parameter space using smooth fitting techniques (e.g., splines, Gaussian processes). This interpolation is empirical, which means that it selects a small number of specific time nodes where waveform information is most informative, dramatically reducing the cost of interpolation. This allows new waveforms to be generated for arbitrary parameter values within the training domain.

As a result, surrogate models can reproduce (sufficiently short) NR waveforms within milliseconds, which even though they are typically slower than phenomenological models, they keep the errors well below typical detector noise levels. The technique was first demonstrated for non-spinning binaries [199] but has since been extended to include aligned and precessing spins, memory effects, and eccentricity. The state-of-the-art NRSur QC BBH models include the non-precessing BBH models: NRHybSur3dq8 [183], trained on mass ratios below 8, its extension NRHybSur3dq8_CCE [414] trained on CCE (Cauchy-characteristic evolution) waveforms to include memory effects, and NRHybSur2dq15 [413], trained on a single spin dataset for $|\chi_1| \leq 0.5$ and mass ratios below 15; and the generically spin-precessing BBHs NRSur7dq4 [184], which has been trained on BBHs with mass ratios $q \leq 4$. Finally, BHPTNRSur1dq1e4 [28] is the state-of-the-art point-particle BHPT model for nonspinning BBHs, trained on BHPT data and NR simulations for $q \leq 10^4$, while NRSur2dq1Ecc [45] is the one for eccentric binaries, trained on non-spinning equal-mass waveforms with eccentricities up to $e = 0.2$.

PART II

Original scientific results

CHAPTER 5

A single spin precessing model for the final state

This chapter is based on the following article:

- Maria de Lluc Planas, Joan Llobera-Querol, and Sascha Husa. "*Building a bridge between comparable and extreme mass ratio black hole binaries: A single spin precessing model for the final state*", **Phys. Rev. D 109.12 (2024), p. 124028**. DOI: 10.1103/PhysRevD.109.124028, arXiv: 2401.13342 [gr-qc] [18].

Abstract

Modeling the gravitational wave signal from binaries beyond comparable mass is an important open issue in gravitational wave astronomy. For non-spinning binaries and when the spins are aligned with the orbital angular momentum, some first studies concerning the transition between the comparable and extreme mass ratio regime are already available, which suggest that extreme mass ratio results at times extrapolate to comparable mass ratios with surprising precision. Here we study the case of misaligned spins: We present new numerical relativity (NR) simulations performed with the Einstein Toolkit code at mass ratios up to 18 and construct a heterogeneous dataset that spans all mass ratios, including data from NR simulations, numerical approximations to extreme mass ratio binaries, and data from the geodesic approximation. As a first application we provide fits for the remnant mass and spin magnitude in single spin precessing systems, omitting consideration of the in-plane spin orientation. These fits demonstrate accuracy comparable to the state-of-the-art NRSur7dq4EmriRemnant model, all while retaining the simplicity and efficiency inherent in previous phenomenological fits.

5.1 Introduction

The LISA space mission is expected to observe gravitational waves from compact binaries with a large range of mass ratios [14, 15] up to and including extreme mass ratio inspirals (EMRI). It will be prudent to develop waveform models that accurately describe a wide range of mass ratios well before the LISA era, and to optimize LISA data analysis algorithms with such pipelines in hand. EMRI waveforms are best described via the self-force method, where one perturbs in the mass ratio of the system ([345, 437], see [438] for discussion). For comparable mass binaries, several families of waveform models have been developed [31, 32, 173, 183, 184, 189, 190, 439], which have become indispensable tools for gravitational wave data analysis, e.g. [1–4]. Such waveform models are calibrated to data from numerical relativity (NR) simulations [293, 294, 310]. However, for the foreseeable future, NR waveforms will be sparse in the parameter space of precessing (even more so for generic) black hole binaries, especially at high mass ratios (see [225, 226, 228, 440, 441] for the latest releases of NR catalogs). While simulations at, say, mass ratios of order 10^2 or 10^3 are in principle feasible in numerical relativity [442], the number, length, and accuracy of such waveforms will be severely restricted by computational cost until new computational approaches are developed (see however [215]).

It is well known that the extreme mass ratio limit and the self force expansion in mass ratio can provide useful information even for the comparable mass ratio regime [24–26], fueling hope that using such information can reduce the number of NR waveforms that are needed for calibrating waveform models. To date, work that connects the two mass ratio regimes has focused on either non-spinning binaries [28–30], the use of extreme mass ratio waveforms to calibrate quasi-circular aligned spin waveform models [31–34], or the simpler problem of models for the final mass and spin in the quasi-circular aligned spin case [27]. For misaligned spins one however faces much more complicated phenomena, and a much larger parameter space (7 instead of 3 dimensions in the absence of orbital eccentricity, as is the case here).

In this work, we make a first step to bridge the comparable mass and extreme mass ratio regimes in the misaligned spin sector, and develop precessing models for the remnant mass and spin, thus extending previous work [27] to the precessing case. An efficient and accurate remnant model for precessing systems is a key component for the advancement of precessing waveform models. Specifically, given that the ringdown frequencies are entirely characterized by the final state of the binary, remnant models play a vital role in conducting tests of general relativity through ringdown studies. Other recent remnant models in the literature include aligned spin datasets with and without information from the extreme mass ratio (EMR) limit, see for instance Refs. [27, 443], precessing datasets with information from the aligned spin EMR limit, see [444, 445], surrogate models like NRSur7dq4EmriRemnant [35], and also a machine learning approach [446].

As our input data we construct a heterogeneous dataset for quasi-circular precessing binaries. The data set combines NR waveforms from different codes, numerical solutions of the Teukolsky equation [447, 448], and information from Kerr geodesics [449]. To understand the region where no NR information is available, we rely on Kerr geodesics, which determine the final mass and spin to linear order in the mass ratio, but surprisingly provide valuable information across the parameter space, i.e. from EMRIs to comparable mass binaries.

In order to construct our model we have to compensate for the lack of a dense data set of numerical relativity simulations across a large range of mass ratios with several simplifications and approximations. As more simulations become available, along with further self-force results and possibly other analytical methods, these simplifications and approximations can be relaxed. As a first simplification, we restrict the models to the single spin case, and leave double spin effects for future work. Neglecting the spin of the smaller black hole, which is a sub-dominant effect for large mass ratios, simplifies our analysis toward focusing on the transition to large mass ratios. Furthermore we neglect the dependence of the angle of the spin in the orbital plane, which we will denote ϕ_1 below, for our models of the remnant mass and spin. While this angle is indeed an essential parameter for the recoil [291], and more accurate models of the mass and spin should take this dependence into account, we argue in Sec. 5.3 that we can neglect it for the simple models we present here. Further approximations are used to establish a common parameterization for our inhomogeneous nature of our input data set. Different numerical relativity codes use different coordinate gauges, which affects in particular spin angles or quantities such as merger times. The geodesics and numerical solutions of the Teukolsky equation again use different coordinates. In the future it will be interesting to better understand how to remove some of the ambiguities and gauge dependencies. For this work we justify not resolving these issues by the fact that the resultant remnant model proves to be accurately predictive, and can be used for the advancement of existing waveform models. Further justifications regarding the approximations we use will be given as we introduce them throughout this paper.

In Sec. 5.2 we describe the datasets we use, and the procedures chosen to blend them into a single consistent dataset. In the quasi-circular aligned spin case, generating a heterogeneous dataset is relatively straightforward, since the intrinsic parameters only consist of the masses and spins, which in turn depend only very weakly on time due to the very small amounts of infalling radiation. Hence, the time dependence of masses and spins is often neglected in aligned spin waveform models [33, 34]. For misaligned spins however, the spin angles and orientation of the orbital plane depend on time, and a coordinate frame needs to be defined judiciously to consistently parameterize the different datasets. Note that throughout this paper we refer to any black hole binary system without in-plane spin contributions as having "aligned spin" (AS), independently of whether spins are parallel or anti-parallel to the orbital angular momentum.

In Sec. 5.3 we use our heterogeneous dataset to compute the remnant mass and spin magnitude across all mass ratios for the case when only the larger black hole is spinning, as the spin on the smaller black hole becomes a subdominant effect for large mass ratios [450]. Additionally, we neglect the orientation of the in-plane component of the single spin, a decision driven by the current limitations in computational cost and tests of the impact of the in-plane angle on our results. Ultimately, a careful selection of the quantities for modeling allows us to generate simple parameterized fits for both the mass and spin magnitude of the remnant in a precessing binary. These fits can be evaluated efficiently and achieve an accuracy comparable to the NRSur7dq4EmriRemnant model [35], the current state-of-the art in remnant models.

Finally, in Sec. 5.4, we summarize and discuss the scope and limitations of the work we report here, as well as next steps.

Throughout this paper we use geometric units with $G = c = 1$. Component masses are

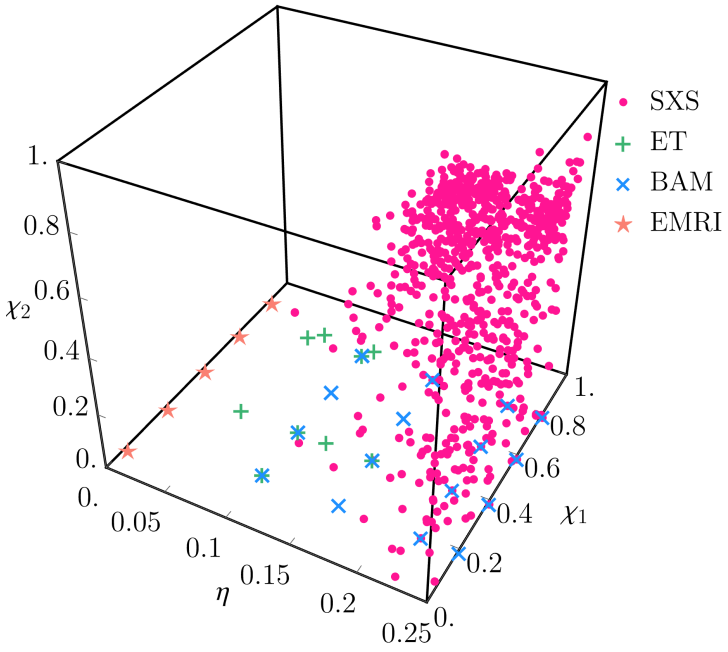

Figure 5.1: Three-dimensional representation of the precessing numerical relativity simulations used in this project described in Sec. 5.2. The visualization presents the distribution of the data in terms of their symmetric mass ratio η and the spin magnitudes of the largest and smallest black holes, denoted as χ_1 and χ_2 respectively.

denoted by m_i, we define the mass ratio $q = m_1/m_2 \geq 1$, and the symmetric mass ratio $\eta = m_1 m_2/(m_1 + m_2)^2$. The total component mass will be denoted by $M = m_1 + m_2$ and will serve as a scale parameter. The dimensionless spin magnitudes are denoted χ_i.

5.2 Precessing dataset

In Sec. 5.2.1-5.2.2 we review the ingredients for our heterogeneous dataset:

- NR waveforms from the public SXS catalogue [228], produced with the SpEC code [218], and the Cardiff group's public catalogue [226] of waveforms produced with the BAM [203, 204] code.
- NR waveforms recently produced with the public Einstein Toolkit code [451] which have not been presented previously.
- Numerical solutions of the Teukolsky equation for inspirals at mass ratio 1000 [447, 448].
- Solutions of the geodesic equation in Kerr spacetime.

In Sec. 5.2.3 we discuss how to blend all the above data into one consistent dataset for the remnant mass and spin.

Our datasets use different coordinate gauge conditions, and thus spin angles can not be expected to be exactly the same even for physically identical binaries. We expect such

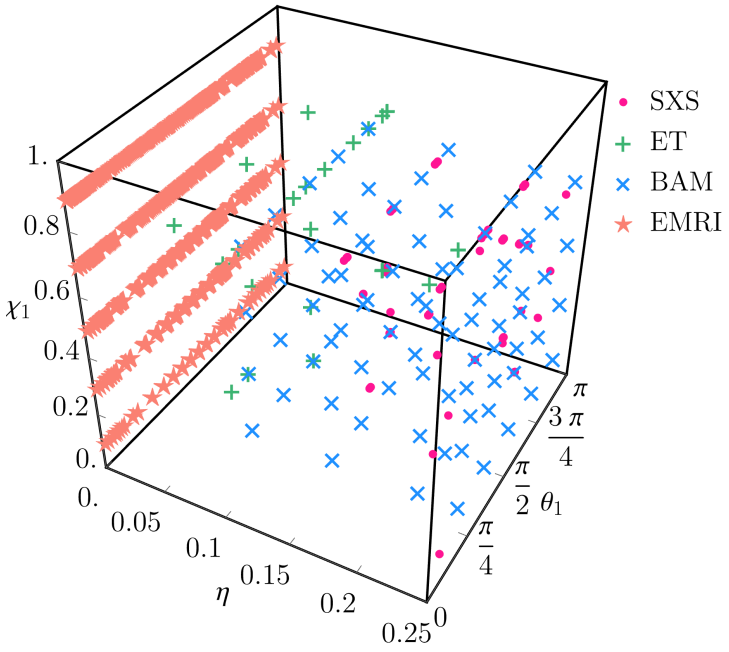

Figure 5.2: Three-dimensional representation of the single spin subset of the precessing numerical relativity simulations introduced in Sec. 5.2. It shows the distribution of the data in terms of their symmetric mass ratio η, the spin magnitude of the largest black hole χ_1, and its orientation with respect to the orbital frequency vector at the reference time θ_1.

uncertainties to only correspond to a few degrees [452], and to not play a major role at our current level of accuracy. In our work we again find approximate consistency between different datasets, this aspect will however have to be studied further in the future.

5.2.1 NR datasets

Our NR dataset spans mass ratios from $q = 1$ (equal masses) to $q = 18$. We use data from two publicly available catalogues of NR simulations, the SXS catalog [228], obtained with the SpEC code [218], and a catalog of waveforms [226] obtained with the BAM code [203, 204]. In addition we use new simulations we performed with the Einstein Toolkit (ETK) [451]. The SXS simulations are performed with the generalized harmonic formulation of the Einstein equations [212], while the BAM and ETK simulations use the moving puncture setup with the 1+log lapse and $\tilde{\Gamma}$-driver shift coordinate conditions. We have analyzed both the waveforms and apparent horizon data of all simulations to create a consistent heterogeneous dataset encompassing information from both sources. In this paper we however only discuss the remnant properties, leaving investigations into the precessing waveform dataset to future work.

All the NR points in our dataset are included in Fig. 5.1, where we show the distribution of the data in a three-dimensional subspace defined at 100 M before merger. The merger time is not defined in exactly the same way for data produced with different codes. We report details for each catalog in the subsections below, however our findings indicate that the small differences in the definition of the merger time across catalogs does not significantly impact the results at the current level of accuracy. For all datasets we shift

the time coordinate to the value of zero at the merger time. From Fig. 5.1 we can see that the majority of the points are concentrated in the comparable mass regime ($\eta \geq 0.15$), mostly from the SXS catalogue. The BAM points are located in the lower plane as they are single spin simulations, while the high mass ratio ETK simulations are dispersed in the mid-high mass ratio regime. In Fig. 5.2 we show the single spin simulations distributed in the (η, χ_1, θ_1)-parameter space, where χ_1 is the magnitude of spin of the more massive black hole, and θ_1 the angle between the spin and the axis of orbital motion $100M$ before merger. These are the simulations we are using to compute the remnant fits in Sec. 5.3.

5.2.1.1 SXS

We use 1409 quasi-circular precessing simulations from the SXS catalogue [228], which range from mass ratio 1 to 6 and $0 < \chi_1 < 0.99$, $0 < \chi_2 < 0.9$. To confine the parameter space to quasi-circular orbits, we impose a limit on the orbital eccentricity e (effectively defined as the Newtonian eccentricity, see [228]) to $e \leq 0.002$, leading to the exclusion of 13 simulations from the original catalog. The `reference_eccentricity` parameter from the metadata was utilized for this purpose. Among the 1409 simulations included in our analysis, 80 correspond to single spin configurations. The criterion for identifying single spin cases was $\chi_2(t_{\rm ref}) < 0.001$. These specific waveforms are employed for the remnant properties fits presented in this paper, with the reference time set at $t_{\rm ref} = -100\ M$ (where the merger corresponds to $t = 0$). For the SXS dataset the merger time is defined as the maximum of the L^2 norm of all the available modes, as provided by the `sxs` python package.

The simulations have been performed with the pseudo-spectral SpEC code [218], which excises spatial regions inside of pure outflow boundaries located inside but close to the apparent horizons of the black holes. Initial data are constructed to satisfy the constraints of general relativity using the Extended Conformal Thin Sandwich [453, 454] equations.

5.2.1.2 BAM dataset

We also use 80 simulations from the single spin Cardiff precessing catalog [226], which span the $1 \leq q \leq 8$, $0 < \chi_1 < 0.8$, $\chi_2 = 0$ parameter space evenly in mass ratio, spin magnitude and orientation θ_1, so $\theta_1(t_{\rm in}) \in \left\{\frac{\pi}{6}, \frac{\pi}{3}, \frac{\pi}{2}, \frac{2\pi}{3}, \frac{5\pi}{6}\right\}$. The in-plane orientation of the single spin ϕ_1 was chosen to be 0 at the relaxed time for each simulation. The eccentricity for all the simulations was reduced to 0.002 through manual iterations of the linear momenta of the punctures in the initial parameters (see Sec. II B 1 in [226] for details). For the BAM dataset the merger time is defined to be the peak of the $l = 2$ multipole modes of Ψ_4, provided in the metadata.

The simulations have been carried out in the "moving puncture" approach with the BAM code, which uses conformally flat Bowen-York puncture initial data [455]. Note that this setup for the initial data allows to analytically compute the initial orbital angular momentum analytically using the Newtonian physics formula as a cross product of position vector and linear momentum. The initial data are evolved with fixed mesh-refinement and sixth order finite differencing [203, 204].

ID	q^{ref}	χ_1	$\theta_{\mathrm{L}\chi_1}$ ($^\circ$)	χ_2	$\theta_{\mathrm{L}\chi_2}$ ($^\circ$)	$M\omega_{\mathrm{orb}}$ ($\times 10^{-2}$)	M_f/M	χ_f	$\theta_{L\chi_f}$($^\circ$)	t_{M}/M
1	4	0.4	135.0 (134.1)	0	-	1.66 (5.44)	0.981	0.368	17.27 (27.89)	2562
2	4	0.4	170.0 (170.0)	0	-	1.66 (5.29)	0.982	0.265	6.41 (9.51)	2395
3	4	0.4	170.0 (169.8)	0.4	170.0 (170.1)	1.64 (5.18)	0.982	0.257	7.20 (10.14)	2328
4	6	0.4	135.0 (134.1)	0	-	1.98 (5.35)	0.987	0.281	36.34 (46.30)	2555
5	6	0.4	135.0 (133.5)	0.4	135.0 (145.1)	1.96 (5.31)	0.987	0.283	37.67 (47.30)	2504
6	8	0.8	170.0 (169.5)	0	-	1.86 (4.83)	0.992	0.285	155.1 (156.7)	2016
7	8	0.4	90.00 (88.24)	0	-	2.06 (6.32)	0.989	0.440	36.77 (43.76)	2253
8	8	0.8	135.0 (135.1)	0	-	1.89 (5.21)	0.991	0.460	92.79 (100.7)	2433
9	8	0.8	90.00 (86.03)	0	-	2.13 (6.54)	0.986	0.700	58.90 (59.14)	2362
10	8	0.8	170.0 (169.9)	0	-	1.92 (4.80)	0.992	0.285	155.0 (157.1)	2016
11	8	0.4	15.00 (14.89)	0	-	2.49 (7.17)	0.986	0.585	6.81 (7.67)	1605
12	8	0.2	90.00 (89.98)	0	-	2.63 (6.07)	0.989	0.345	24.25 (27.09)	1047
13	8	0.4	30.00 (29.14)	0	-	2.49 (7.05)	0.986	0.573	13.45 (14.69)	1574
14	8	0.8	165.0 (164.5)	0	-	2.19 (4.70)	0.992	0.301	144.9 (146.3)	1307
15	8	0.8	15.00 (15.13)	0	-	2.61 (9.05)	0.977	0.858	9.64 (10.61)	1906
16	8	0.8	150.0 (149.2)	0	-	2.24 (4.84)	0.992	0.372	117.6 (120.5)	1274
17	8	0.8	30.00 (27.55)	0	-	2.58 (8.72)	0.978	0.847	19.33 (18.14)	1895
18	8	0.8	75.00 (74.63)	0	-	2.62 (6.87)	0.984	0.757	49.34 (52.04)	1368
19	8	0.8	105.0 (104.1)	0	-	2.47 (5.81)	0.989	0.633	68.37 (74.24)	1320
20	18	0.4	150.0 (149.9)	0	-	2.51 (5.64)	0.996	0.225	124.5 (126.8)	2234
21	18	0.4	90.00 (89.34)	0	-	2.74 (6.63)	0.996	0.395	61.30 (65.03)	2221
22	18	0.8	150.0 (149.4)	0	-	2.39 (5.00)	0.996	0.565	138.7 (139.8)	2207
23	18	0.8	30.00 (29.78)	0	-	2.93 (10.5)	0.991	0.828	24.33 (25.20)	3243
24	18	0.8	90.00 (90.35)	0	-	2.87 (6.93)	0.995	0.738	75.84 (77.67)	2243

Table 5.1: Initial and reference data (in brackets) of the numerical relativity simulations computed using the Einstein Toolkit, described in Sec. 5.2.1.3. The reference time is chosen to be 100 M before merger. From left to right, the table gives the ID of each simulation, its mass ratio, the dimensionless spin magnitude of the larger black hole, the primary spin's orientation with respect to the orbital frequency $\vec{\omega}$, the dimensionless spin of the lighter black hole, its orientation, the dimensionless orbital frequency at which the quantities are given, the dimensionless final mass of the remnant object, its spin, its orientation with respect to $\vec{\omega}$ and finally, the dimensionless merger time.

5.2.1.3 Einstein Toolkit dataset

In addition to the public data from the SXS and BAM dataset we also use higher mass ratio simulations we have recently performed with ETK [451]. We produced 24 simulations which span the region $4 \leq q \leq 18$, $0.4 \leq \chi_1 \leq 0.8$, $0 \leq \chi_2 \leq 0.4$. Due to an inappropriate configuration of the wave extraction grids, some gravitational wave signals exhibit excessive noise, making it challenging to extract the merger time directly from it. We thus rely on horizon quantities, identifying the merger time as the transition from the individual black hole spins to the remnant spin. Detailed information on these simulations can be found in Table 5.1.

The setup of our Einstein Toolkit code is very similar to that of the BAM code. Differences include the use of 8th order accurate finite difference stencils, and the eccentricity reduction algorithm described in [379]. Furthermore, fixed mesh refinement with moving cubical boxes is not used for the whole computational domain. However, for the wave extraction region and beyond the multipatch Llama code [456] is used to allow a high radial grid resolution with a reduced memory consumption. The final mass and spin are determined from the apparent horizons, which are located with the `AHFinderDirect`-code [457].

5.2.2 Extreme mass ratio limit

In the EMR case ($\eta \ll 1/4$) one can rely on black hole perturbation theory (BHPT), which assumes a perturbation of Kerr spacetime due to a small object m_2 orbiting a black hole of mass $m_1 \gg m_2$. In the test mass limit ($\eta \to 0$) the calculation of the orbital motion decouples from the calculation of the gravitational wave signal, radiation reaction vanishes and the smaller object follows a geodesic. Below we first summarize quasi-circular geodesics of Kerr spacetime and then describe our numerical dataset for mass ratio 10^3 [447], which we use for cross-checks.

5.2.2.1 Kerr geodesics

We consider the geodesic motion of a test mass m_2 in a Kerr spacetime of mass m_1 and angular momentum $|J| = am_1$. For a given black hole with parameters a and m_1 the geodesics can be parameterized by the constant orbital quantities p (semilatus rectum), e (eccentricity) and θ_- (inclination parameter), or by the energy E, angular momentum along the axis of symmetry L_z and Carter's constant Q, which are also constants of motion. The orbital quantities are defined in Boyer-Lindquist coordinates (t, r, θ, φ) [458]. In this paper we will only be interested in the circular case, where $e = 0$ and radial separation r is constant, while the angular position θ will be time dependent and oscillates between extrema determined by the inclination parameter θ_-,

$$\theta_- \leq \theta \leq (\pi - \theta_-). \tag{5.2.1}$$

The solution for the time dependent geodesic motion, and the relation between the conserved quantities (E, L_z, Q) and the orbital motion can be found, for instance, in Ref. [449], and is briefly summarized in App. 5.A. Here we follow the parameterization of [449] or [459], which is also used in the Black Hole Perturbation Toolkit software package [265]. This toolkit, among other things, provides a Mathematica implementation of Kerr geodesics, `KerrGeodesics`, which we have used in parallel to our own implementation. In order to solve for the geodesics and discuss the results it is natural to adopt a scale-invariant formulation of the problem introducing dimensionless quantities:

$$\tilde{a} = \frac{a}{m_1}\ ,\ \tilde{E} = \frac{E}{m_2}\ ,\ \tilde{L_z} = \frac{L_z}{m_1 m_2}\ ,\ \tilde{Q} = \frac{Q}{{m_1}^2 {m_2}^2}. \tag{5.2.2}$$

The conserved quantities $(\tilde{E}, \tilde{L}_z, \tilde{Q})$ can be computed algebraically from the parameters (a, p, e, θ_-), e.g.

$$\tilde{Q} = \cos^2\theta_- \left[\tilde{a}^2(1 - \tilde{E}^2) + \frac{\tilde{L}_z^2}{1 - \cos^2\theta_-}\right]. \tag{5.2.3}$$

The Carter's constant is given by $Q = L_\rho^2 = L^2 - L_z^2$ in the limit $a \to 0$. It is however useful to approximate L_ρ by the square root of the Carter's constant $\sqrt{Q}$ even for non-vanishing spin, see e.g. [459]. There, an equivalent inclination angle I (called θ_{inc} in [459]) is defined as

$$I = \frac{\pi}{2} - \text{sign}\,(L_z)\ \theta_-, \tag{5.2.4}$$

which resembles an alternative definition for an orbital inclination angle ι:

$$\cos\iota = \frac{L_z}{\sqrt{L_z^2 + Q}}, \tag{5.2.5}$$

where Q plays the role of the magnitude squared of the angular momentum orthogonal to L_z. It has been found that in general $\iota \approx I$ and that the angles I and ι automatically encode a notion of prograde and retrograde orbits ($I, \iota < 90°$ for prograde and $I, \iota > 90°$ for retrograde) [449]. In terms of the energy and angular momentum one finds that $\tilde{E}^{(p)} < \tilde{E}^{(r)}$ and $\tilde{L_z}^{(p)} < \tilde{L_z}^{(r)}$, where p stands for prograde orbits and r for retrograde, i.e. for prograde orbits the particle has higher binding energy.

Of special interest is the innermost stable spherical orbit (ISSO). Particles with small but finite mass will adiabatically inspiral to the ISSO, and then plunge into the black hole. The radiation of energy and angular momentum during the plunge is much smaller than during the inspiral, and the remnant mass and spin can therefore be approximated by the values of the energy and angular momentum at the ISSO. This aspect will be discussed further in Sec. 5.3, and concretely motivated in Fig. 5.5.

The simpler subset of aligned spin binaries is defined by setting the inclination angles I or ι to 0 or π. The L_z component of the orbital angular momentum then corresponds to the total orbital angular momentum, the final spin only has a non-vanishing z-component, and the orbital plane is preserved. In this particular case of equatorial orbits, the ISSO is referred to as innermost stable circular orbit (ISCO).

5.2.2.2 Numerical EMRI data

In this work we use the data of [447], 5925 EMRIs of mass ratio $q = 1000$, distributed in a grid of values of the spin of the largest black hole a, inclination angle I, and plunge angle θ_f (see Fig. 5.3). Reference [447] extends the work of Ori and Thorne [460] from equatorial to inclined orbits. The procedure splits the worldline into three regions: i) The adiabatic inspiral, where they use a frequency-domain BHPT code [459] to evolve the orbital quantities until they reach ii) the transition region. Closer to the ISSO, the inspiral is no longer adiabatic, requiring further considerations. iii) On reaching the plunge, E, L_z and Q are frozen to the last value of the orbit while other orbital quantities are evolved solving the geodesic equation. We thus define the merger time when the small object crosses the horizon and E, L_z and Q reach their frozen value.

In their companion paper [448], they investigate the dependence of individual-mode excitation on plunge parameters via their waveform set. The gravitational waves generated by the system are computed from the worldline by solving the Teukolsky equation in the time domain [461, 462]. Further details on the procedure can be found in Ref. [447].

For each configuration, the dataset includes all the spherical harmonic modes up to $l = 4$, plus selected higher l, m modes, and complete information on the small body's trajectory

$$\vec{x_2}(t) = -\vec{r} = r(t)(\sin\theta(t)\cos\phi(t), \sin\theta(t)\sin\theta(t), \cos\theta(t)), \tag{5.2.6}$$

by providing (r, ϕ, θ), velocity ($\mathrm{d}r/\mathrm{d}t$, $\mathrm{d}\phi/\mathrm{d}t$, $\mathrm{d}\theta/\mathrm{d}t$), and also the time evolution of the geodesic constants of motion E, L_z and Q, which are used in Sec. 5.2.3.2 to compute the remnant quantities. The natural frame for EMRIs is defined by the spin of the massive black hole, so both the waveform and trajectories are defined with respect to this frame as illustrated in Fig. 5.3. To cohesively append to our existing dataset, it is therefore necessary to transform from this frame to that used by comparable mass simulations, where the z-axis is defined not by the angular momentum of the larger black hole, but

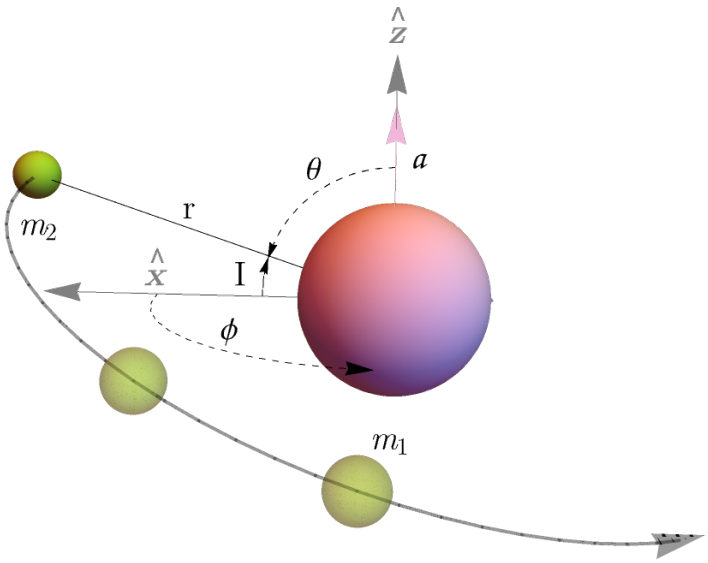

Figure 5.3: Definition of the EMRI orbital quantities provided in the dataset described in Sec. 5.2.2. The dataset spans a parameter space described by the black hole spin magnitude a, the inclination angle I and the final angle of the plunge θ_f. The spherical coordinates (r, θ, ϕ) determine the evolved position of the smaller black hole of mass m_2.

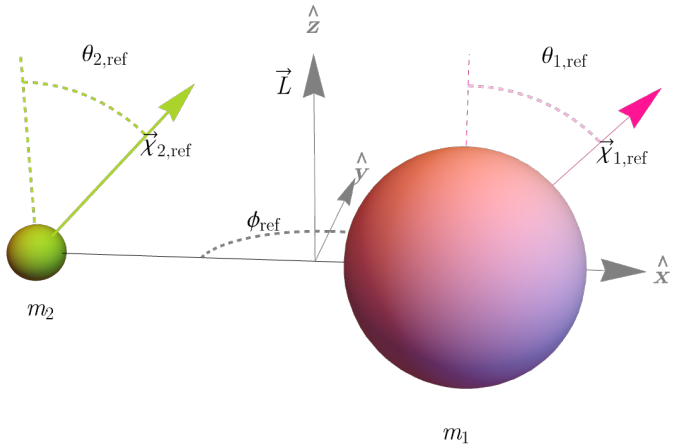

Figure 5.4: Definition of the orbital quantities employed in this project (traditional to the comparable mass simulations). All vectors are defined with respect to the orbital angular momentum $\vec{L}$, as opposed to those shown in Fig. 5.3, which are specified in terms of the larger black hole spin. Note that in this project we approximate $\vec{L}$ by $\vec{\omega}$ (5.2.9).

by the direction of the orbital angular momentum, or a similar quantity like the orbital angular velocity or Newtonian orbital angular momentum $\vec{\omega}$, as shown in Fig. 5.4.

5.2.3 Creation of a heterogeneous dataset

In this work we investigate the properties of the remnant object: the final mass and spin. The final mass of the binary is given by

$$M_f = 1 - E_{\rm rad}, \tag{5.2.7}$$

and one can then apply the conservation of angular momentum to compute the final spin $\vec{\chi_f}$:

$$M_f^2\, \vec{\chi_f} = m_1^2\, \vec{\chi_1} + m_2^2\, \vec{\chi_2} + \vec{L}. \tag{5.2.8}$$

For the numerical relativity datasets the final mass and spin were determined from the apparent horizons. In the case of the SXS and BAM dataset they were taken from the supplied metadata, and for our Einstein Toolkit dataset the numbers were averaged over appropriate portions of the late time behavior of the dataset. For the extreme mass ratio case, the determination of the final state is described below.

5.2.3.1 Choice of reference frame

In the aligned spin quasi-circular sector, creating a consistent heterogeneous dataset, which combines comparable mass and extreme mass ratio cases, is relatively straightforward. As the spins and orbital plane maintain their orientation as a consequence of equatorial symmetry, a natural class of inertial frames can be constructed, where the z-axis is the fixed axis of the orbital motion, and the angular coordinate in the orbital plane can be defined based on the separation vector. In the precessing case, this equatorial symmetry of the aligned spin vector is lost; the orbital plane and spin directions are time dependent, and there is in general no natural inertial frame. An intuitive approach to choosing a reference frame is then to work with a non-inertial frame which tracks the precession motion, which drastically simplify the dynamics and waveform [290, 297]. This can then be used to construct precessing waveform models in terms of rotating or *"twisting up"* a non-precessing waveform with an inverse rotation that maps a corresponding precessing waveform into the appropriate non-inertial frame [290, 297]. Unfortunately the natural choices in the EMR limit and comparable mass cases are not equal.

For EMRIs, as discussed above in Sec. 5.2.2, fixing an inertial frame by choosing the z-axis as the spin axis of the large BH is indeed natural, e.g. it gives rise to a conserved spin component in the z-direction of the larger BH, a conserved orbital angular momentum projection L_z, and the definition of the conserved inclination I for a fixed geodesic. In the comparable mass case, this choice has however no meaningful analog, and it has become customary to work in a co-orbital or similar frame, which is defined in the spirit of the quadrupole-aligned frame [290, 297, 298] for the gravitational wave signal. Similar behavior can be achieved by choosing the z-axis as the direction of the orbital angular momentum $\vec{L}$, or the orbital angular velocity $\vec{\omega}$. In the frame defined by the orbital angular momentum, the magnitude of the spin projections parallel and orthogonal to the orbital angular momentum are approximately preserved [146, 278] and the orbital angular momentum is approximately aligned with the direction of maximum wave emission [290].

In the EMR limit, the projection of the black hole spin onto the orbital angular momentum is preserved, in contrast to the scenario where the orbital angular momentum is replaced the orbital angular velocity $\vec{\omega}$. Some simplification of the gravitational wave signal and dynamics can also be achieved by choosing the z-axis as the direction of the total angular momentum $\vec{J}$, see e.g. [297], which only varies slowly and by a small amount, except for the case of transitional precession [297]. Furthermore, in the EMR limit, $\vec{J}$ corresponds to the spin of the largest black hole, making it a more suitable choice as the mass ratio increases.

The NRSur7dq4 model [184] uses the quadrupole aligned waveform to define the reference frame, where the z-axis is computed as the principal eigenvector of the angular momentum operator as described in [298]. In this work we have chosen to construct our co-orbital frame in terms of orbital quantities, as their formulation is more straightforward than the orbital angular momentum in a numerical relativity evolution. For some of the ETK waveforms, the gravitational wave signal is too noisy to work with the quadrupole aligned frame, due to an inappropriate configuration of the wave extraction grids. This problem and its resolution will be discussed in a separate paper. The z-axis is then chosen to point in the direction of the orbital angular velocity $\vec{\omega}$

$$\vec{\omega}(t) = \frac{\vec{r} \times \vec{v}}{r^2} = \frac{\vec{r} \times \dot{\vec{r}}}{r^2}, \tag{5.2.9}$$

where $\vec{r}$ is the vector which points from the smallest black hole to the largest ($\vec{r} = \vec{x_1} - \vec{x_2}$), and the x-axis is chosen to point in the $\vec{r}$ direction (see Fig. 5.4 for visual definition). The y-axis is defined as usual to complete an orthogonal right-handed triad.

In order to perform this alignment, one needs the time evolution of the two black hole positions, as well as the time evolution of all the quantities we include in our dataset. These are the spins and masses of both initial black holes and the remnant, the emitted waves, the radiated energy and/or orbital frequencies, although additional information on how to get these quantities are recommended to ensure consistency. Some public catalogues are hence not adequate for our purposes, e.g. the RIT catalog [225] includes precessing waveforms but it does not provide the trajectory evolution. For future work we also plan to include the most recent MAYA catalogue [440].

We adopt the same reference time for defining the spin components in a co-orbital frame as in [35, 184], which is set to $100M$ before merger. This choice facilitates direct comparisons between our remnant model and NRSur7dq4EmriRemnant [35]. The binary evolution closely approaches the merger state at this reference time, thus one can expect a simpler functional dependence for the remnant quantities. For the EMR limit, the ISSO provides an approximate plunge time. For our numerical EMRI dataset detailed in Sec. 5.2.2, we compare the numerical preserved quantities at merger with those obtained at the ISSO time. For our EMRI dataset, the ISSO time ranges from $-700M$ for the most anti-aligned cases to $-150M$ for the aligned ones. Upon comparing the values for the preserved quantities obtained by solving the geodesic equations at the ISSO with the numerical results, we observe maximum relative errors of 0.1%. Consequently, we conclude that the ISSO time can be effectively employed as the reference time for the EMR limit without impacting the transition from the comparable mass regime, where the chosen reference time is $-100M$. These observations however suggest that this choice might not be optimal. Instead, a quantity that smoothly transitions from the comparable mass reference time to the ISSO could be more suitable, such as the minimal energy circular

orbit (MECO) time [463]. We leave this as future work, to investigate further a choice of optimal reference time, which allows simple yet precise fits and an accurate match with fast post-Newtonian inspiral codes e.g., [464]. These codes serve to bridge the gap between the reference time and some earlier time where waveform models define their spin vectors.

The rotation of the vector quantities such as the black holes' spins is straightforward, consisting in a fixed rotation to the full time array. For the waveforms, it is common to decompose the waves into spherical harmonics and rotate each mode individually via Wigner matrices. Comparable mass binaries are usually described at the co-orbital frame at some reference time close to the initial time, and performing a fixed rotation to a later co-orbital frame does not suppose higher complications. More efforts need to be done however for the extreme mass ratio limit, where the natural frame is defined in terms of the largest black hole spin. From the trajectories one can obtain the vector $\vec{r} = -\vec{x_2}$, as in Eq. (5.2.6), then compute the velocity $\dot{\vec{r}}$ and finally obtain the z-axis given by $\hat{\omega}(t_{\rm ref})$. In the case of using geodesics, one just inputs the inclination angle at the reference time. Once the alignment is done for all simulations, we keep the metadata at the chosen reference time -100 M where the alignment takes place. This includes the mass ratio, the two black holes' spins and positions, the reference orbital frequency, the time of merger and finally the remnant quantities.

5.2.3.2 Extreme mass ratio limit

In the EMR limit, the final mass and spin can be computed to first order in the mass ratio from the energy and orbital angular momentum at the ISSO, since the contribution of the plunge can be neglected [465]. The quantities E and L_z are preserved for geodesics, and can thus be evaluated directly for any geodesic. This is however not true for the full angular momentum vector, which would require further knowledge about the spacetime. According to the previous discussion around Eq. (5.2.5), we approximate L_ρ by the square root of the Carter's constant $\sqrt{Q}$ and extract the direction of the final spin with respect to the z-axis. Since only the z or the in-plane components are preserved, there will be a freedom regarding the in-plane direction of the final spin that we will not be able to fix. Regardless, here we are only interested in the final spin magnitude, so the missing direction does not constrain our work.

Numerically solving the geodesic equations detailed in App. 5.A allows one to determine the constants of motion at a specific geodesic. As previously discussed, in the EMR limit, we select the ISSO time as the reference time. At this point, the conditions $R(r_{\rm ISSO}) = R'(r_{\rm ISSO}) = R''(r_{\rm ISSO}) = 0$ are satisfied (refer to Eq. (5.A.4)). Solving this set of algebraic equations provides the constants of motion (E, L_z, Q) at the ISSO, as well as the radius $r_{\rm ISSO}$. This numerical procedure is described in Ref. [466] and implemented in the `KerrGeodesics` Mathematica package, which we have utilized extensively to solve precessing geodesics throughout.

For the specific case of non-precessing orbits ($I = \{0, \pi\}$), one can derive simple analytical expressions for the energy and angular momentum at the ISCO (particular ISSO for equatorial orbits), given by:

$$\tilde{E}_{\rm ISCO}(\chi_f) = \sqrt{1 - \frac{2}{3\rho_{\rm ISCO}(\chi_f)}}, \tag{5.2.10}$$

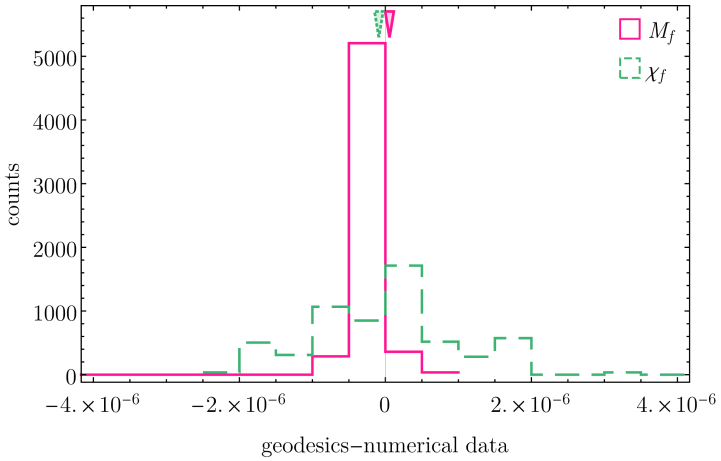

Figure 5.5: Histogram illustrating the difference between the remnant properties obtained by solving the precessing geodesic equations at the ISSO and the corresponding numerical values from the used EMRI dataset described in Sec. 5.2.2. The triangles represent the median value for each distribution.

and

$$\tilde{L}^{\rm orb}_{\rm ISCO}(\chi_f) = \frac{2\left(3\sqrt{\rho_{\rm ISCO(\chi_f)}} - 2\chi_f\right)}{\sqrt{3\rho_{\rm ISCO}(\chi_f)}}, \tag{5.2.11}$$

where $\rho_{\rm ISCO}$ is the radius at the ISCO:

$$\rho_{\rm ISCO}(\chi) = 3 + Z_2 - {\rm sign}(\chi)\sqrt{(3-Z_1)(3+Z_1+2Z_2)},$$

$$Z_1 = 1 + (1-\chi^2)^{1/3}\left[(1+\chi)^{1/3} + (1-\chi)^{1/3}\right],$$

$$Z_2 = \sqrt{3\chi^2 + Z_1^2}.$$

From these equations it is clear that the derivative of the final mass and spin with respect to the component spin is singular at $\eta = 0$ when the black hole spin is extremal and aligned with the orbital angular momentum. For other mass ratios this derivative is regular, as is the derivative with respect to η. This behavior is difficult to capture in models without further analytical insight in the region near the singular point where $\eta = 0$ and the component spins are extremal. Further work will be required to fully resolve the associated issues.

Approximating the orbital angular momentum magnitude L by $\sqrt{L_z^2 + Q}$, the remnant quantities in Eqs. (5.2.7) and (5.2.8) depend exclusively on the "preserved" quantities (E, L_z, Q). While the numerical dataset provides these values after the plunge, for the geodesic description we take these values from the ISSO and neglect the contribution from the plunge [465]. We scaled the radiated energy by η at linear order, which is consistent with our earlier discussion that the geodesic values are accurate up to order η. We compare the final mass and spin magnitude obtained from the precessing geodesic equations and the numerical EMRI data in Fig. 5.5, showing a maximum error around 10^{-6}, comparable to the numerical error expected from the simulations.

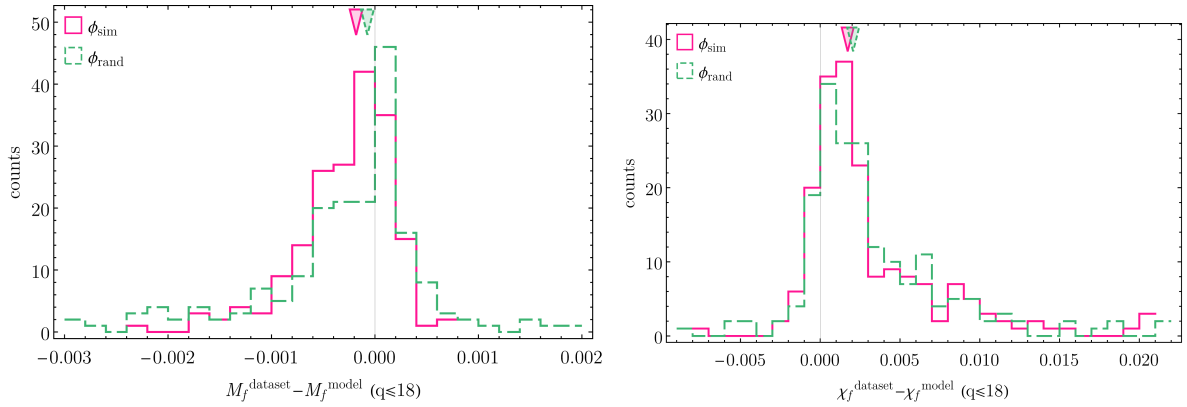

Figure 5.6: Error histograms illustrating the effect if the in-plane orientation of the single spin ϕ_1 on the NRSur7dq4EmriRemnant model for the remnant properties. We consider the corresponding ϕ_1 of each simulation ($\phi_{\rm sim}$ in the legend) and a random angle value ($\phi_{\rm rand}$) and compare the error distributions for our dataset. The top panel displays the errors associated with the final mass (with a RMSE=$5.4 \cdot 10^{-4}$ for the $\phi_{\rm sim}$ distribution and RMSE=$8.2 \cdot 10^{-4}$ for $\phi_{\rm rand}$), while the bottom panel depicts the errors related to the final spin magnitude (RMSE($\phi_{\rm sim}$)=$5.4 \cdot 10^{-3}$ and RMSE($\phi_{\rm rand}$)=$5.8 \cdot 10^{-3}$). Triangles indicate the median value for each distribution. Both plots suggest that ϕ_1 does not significantly influence the error distribution of the model, supporting our decision to exclude that dimension from our studies.

5.3 Models for the remnant mass and spin

In this section we develop fits for the remnant mass and spin for precessing binaries, extending some of the ideas which have been used in [27] to create such fits for aligned spin binaries. We use extreme mass ratio data and split the input parameter space (in a hierarchical way) by dimension to design a class of functional forms for the fits. We use information criteria to select the best fit among this class of functions preventing overfitting.

At high mass ratios, the contribution of the secondary spin becomes a subdominant effect. This makes the single spin subspace a natural arena when trying to understand the high mass ratio regime for precessing systems and gain intuition on how to bridge the gap to comparable mass binaries (through intermediate mass ratio systems). The problem thus becomes four-dimensional, with three dimensions due to the largest black hole spin, $(\chi_1, \theta_1, \phi_1)$, and one for the symmetric mass ratio η. To assess the impact of the in-plane spin orientation ϕ_1 on the remnant quantities, we utilize the NRSur7dq4EmriRemnant model, which has been calibrated to numerical relativity and includes the ϕ_1-dimension. For all configurations in our full numerical relativity single spin dataset we compute the residual error between the NR values for the remnant quantities and those obtained with NRSur7dq4EmriRemnant, first using the value of $\phi_1^{\rm ref}$ from the simulation, and then a random value. The results, depicted in Fig. 5.6, reveal that the root mean square errors are virtually unaffected by this additional dimension and that the error distribution exhibits similar behavior. This supports the decision to exclude the ϕ_1-dimension in this study, reducing our dimensionality to three free parameters and thereby lowering the computational cost of the procedure. We leave the incorporation of the ϕ_1 dependence for future work.

The twisting up procedure introduced in Sec. 5.2.3 permits to understand precession in terms of an approximate map between aligned spin binaries and precessing ones in a co-orbital frame. Our strategy will be to work in a co-orbital frame to facilitate constructing our fits as corrections to the values of the corresponding aligned spin binary configuration. The misaligned spin components induce a precessing motion of the binary, which introduces a new timescale compared to aligned spin systems. During the inspiral this precessing timescale is however much slower than the orbital one, so its effect on the energy radiated in gravitational waves is rather small. For the radiated angular momentum we will see that the situation is slightly more complicated: because the angular momentum and the component spins are time dependent vectors, the final angular momentum is affected by a non-trivial vector addition effect. For a recent discussion in the context of current waveform models see e.g. [189].

To prevent overfitting we follow Ref. [27], where aligned spin remnant fits were developed, and we use the Bayesian Information Criterion (BIC) and Akaike Information Criterion (AIC) as metrics for model selection. These criteria are designed to balance model accuracy and complexity to avoid overfitting. For further details on the definition of the information criteria see App. 5.B. We focus in particular on the BIC, which provides a more restrictive criterion for our purposes. A lower BIC value indicates a more favorable trade-off between model fit and complexity, leading to the selection of a model with improved predictive performance.

Our input dataset consists of the single spin simulations displayed in Fig. 5.2. Our calibration parameter space extends only up to $\chi_1 = 0.8$. However, we discuss extrapolation to extreme spins in App. 5.D, where we conclude that our model extrapolates well to maximally precessing spins.

We evaluate the accuracy of the remnant fits and compare with the results obtained with NRSur7dq4EmriRemnant, which is calibrated against double spin numerical relativity simulations, and with the remnant fits that are being used in existing precessing phenomenological models [189, 190], which are only calibrated to aligned spin simulations. By subtracting information from the aligned spin sector and EMR before the fits, we can construct simple parameterized fits which provide a far higher accuracy that what is currently required for gravitational wave observations, as does the NRSur7dq4EmriRemnant model, but at a much reduced complexity and computational cost.

5.3.1 Remnant mass

Since the correction of the final mass due to precession is expected to be small when parameterizing the input spins in a co-orbital frame, it is natural to directly fit the effect of precession on the aligned spin radiated energy. We then define our fitting quantity as

$$\Delta E = E_{\rm rad}^{\rm prec}\left(\eta, \chi_1, \theta_1\right) - E_{\rm rad}^{\rm AS}\left(\eta, \chi_1\cos(\theta_1), \chi_2\cos(\theta_2) = 0\right), \tag{5.3.1}$$

so the final mass of a precessing binary will be modified as

$$M_f = 1 - E_{\rm rad} = 1 - \left(E_{\rm rad}^{\rm AS}(\eta, \chi_1\cos(\theta_1)) + \Delta E(\eta, \chi_1, \theta_1)\right), \tag{5.3.2}$$

where all the input parameters are taken at the reference time. Since by design our fitted quantity ΔE has very small values, we need to ensure that poor accuracy of the aligned

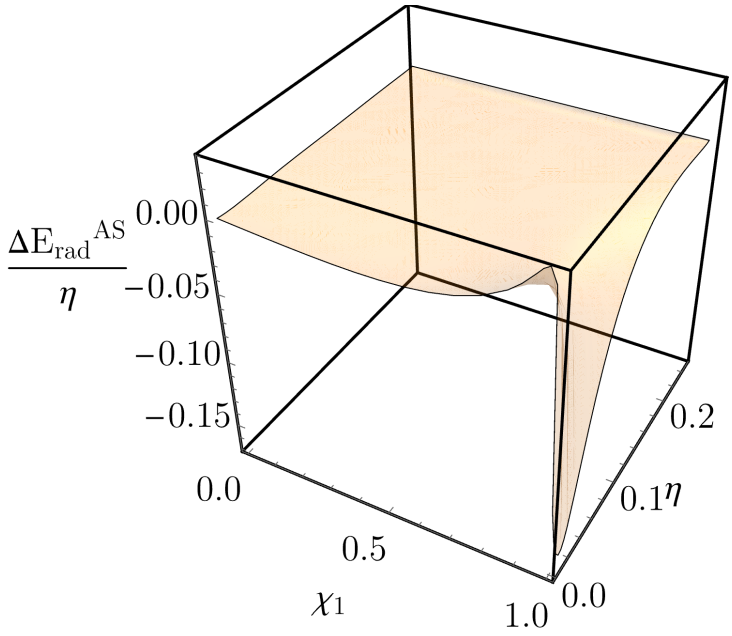

Figure 5.7: Difference between the updated aligned spin fit for the radiated energy (see Eq. (5.C.2)) and the previous one [27] used in phenomenological families IMRPhenomX [33] and IMRPhenomT [34] for single spin systems, scaled by the mass ratio. The key enhancement in the new model is a more accurate description of the singularity at $\chi_1 \to 1$ and $\eta \to 0$.

spin fit for the energy does not contaminate our error budget. What we found is that the previous fit developed in Ref. [27] did not accurately capture the radiated energy close to the joint extremal spins and extreme mass ratio limit. Hence, we first improved the aligned spin fit near this singular point as shown in Fig. 5.7, where we defined $\Delta E_{\rm rad}^{\rm AS}$ as the difference between the updated fit and the old one. The updated expression is provided in App. 5.C, Eq. (5.C.2), and will be discussed in detail elsewhere.

In order to improve the conditioning of our fitting method for the EMRI regime we use the geodesic results, which are valid at linear order in η: We subtract the resulting linear-in-η term from the numerical dataset and only include higher powers of η in our fits. Fig. 5.8 shows that the linear-in-η term is small for comparable masses, which benefits this strategy by not contributing much where the linear approximation is not valid. We therefore fit the quantity $\overline{\Delta E}$ defined as

$$\overline{\Delta E} = \Delta E - \Delta E_{\rm EMR}. \tag{5.3.3}$$

Here $\Delta E_{\rm EMR}$ is computed using the `KerrGeodesics` Mathematica package for the energy in the precessing case and Eq. (5.2.10) for the aligned spin energy case.

In order to develop a suitable ansatz for a parametric fit across the three-dimensional space (η, χ_1, θ_1) we first visualize only two dimensions and show results for fixed values of θ_1, chosen as the evenly spaced grid points of the BAM catalogue [226]: $\theta_1 \in \left\{\frac{\pi}{6}, \frac{\pi}{3}, \frac{\pi}{2}, \frac{2\pi}{3}, \frac{5\pi}{6}\right\}$. This way we ensure that each fitted surface contains numerical relativity data. By definition, $\overline{\Delta E}$ (as well as ΔE) has to vanish at the boundaries $\theta_1 \in \{0, \pi\}$, so that we recover the aligned and anti-aligned limits. The simple structure of the numerical values of ΔE (and hence $\overline{\Delta E}$) across the $\eta - \chi_1$ subspace at the fixed values of θ_1 (see e.g. Fig. 5.10) suggests that a simple polynomial ansatz can effectively capture its behavior. More specifically, our

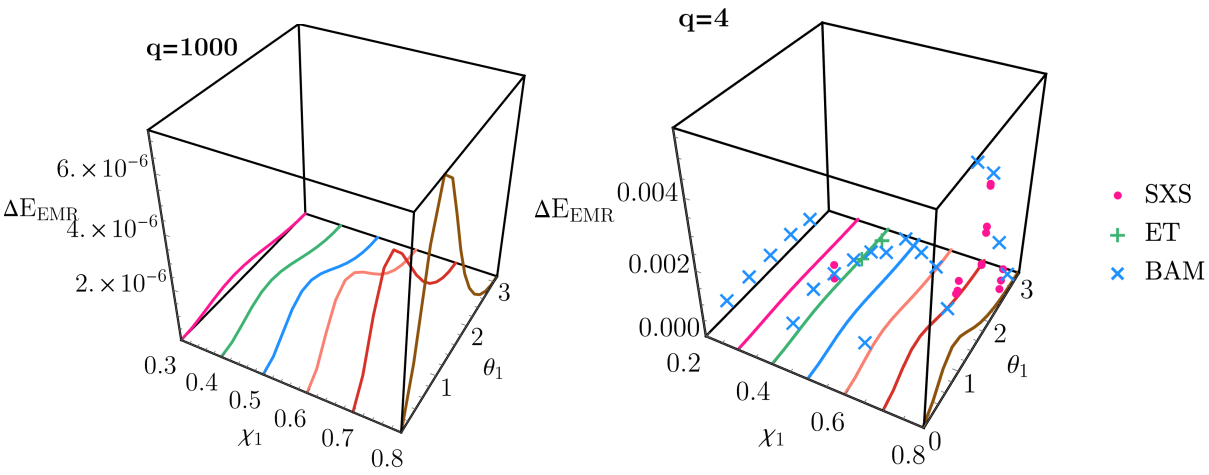

FIGURE 5.8: Numerical evaluations of ΔE as defined in Eq. (5.3.1) for the extreme mass ratio limit (denoted as $\Delta E_{\rm EMR}$) at a fixed mass ratio while varying the black hole's spin magnitude χ_1 and its orientation with respect to the orbital frequency at the reference time θ_1. The precessing and aligned spin radiated energies are obtained from the geodesic equations of motion, which provide the linear contribution in η to the energy. The precessing radiated energy at the ISSO is obtained with the `KerrGeodesics` package, whereas the aligned spin energy is computed from Eq. (5.2.10). The top panel corresponds to a mass ratio of 1000, where the geodesic equations are expected to be valid, while the lower panel corresponds to a mass ratio of 4. In the lower plot, we included the single spin simulations from Fig. 5.2 that fall into this subspace.

ansatz consists of $\eta^a\chi_1^b$-like terms using a rectangular grid in (a, b). Visually inspecting the data, the highest order fit that avoids overfitting for any fixed θ_1 is given by $a \leq 5$ and $b \leq 2$, which results in 18 terms in the polynomial ansatz. However, many of these terms can be discarded.

We set the constant term ($a = b = 0$) of the expansion to 0 because, at $\chi_1 = 0$ and $\eta \to 0$, it holds that $\overline{\Delta E} = 0$, leaving us with 17 terms. These data points with corrections set to zero are designated as AS, since one recovers the underlying aligned spin model. We utilize the `LinearModelFit` function from Mathematica [467] to fit the numerical data for each θ_1 surface and record the BIC of the resulting model across all θ_1s. Subsequently, we perform a weighted averaging of the BIC for each surface, assigning weights of 0.05 for $\theta_1 \in \{\frac{\pi}{6}, \frac{5\pi}{6}\}$, of 0.2 for $\theta_1 \in \{\frac{\pi}{3}, \frac{2\pi}{3}\}$, and finally, 0.5 for $\theta_1 = \frac{\pi}{2}$. The assignment of weights depends on the nature of the quantity being fitted: the magnitude is more significant for highly precessing systems, making the results more reliable in the region closer to in-plane spins ($\theta_1 \sim \pi/2$). Conversely, for systems close to aligned or anti-aligned configurations, the value is so small that it is overshadowed by the numerical error of the simulations. By employing weighted averaging, we ensure that the fitting procedure is not dominated by the numerical errors in our dataset, while still taking into account all cases. This process is repeated iteratively for a modified ansatz where each term is removed, saving the averaged BIC for each case. We retain the ansatz with the lowest mean BIC only if it falls below the BIC value of the initial polynomial set. This procedure is reiterated until removing more terms no longer contributes positively to the final fit. With this procedure, we obtain a final fit with only 7 terms favoured by about -44 in relative BIC. Then, for every value

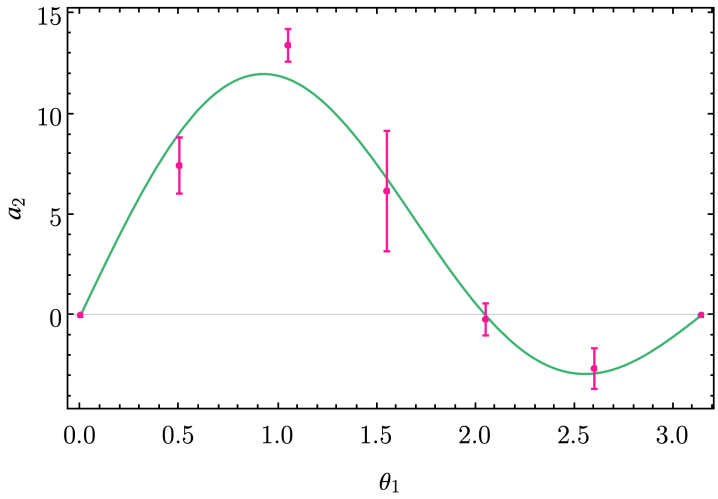

Figure 5.9: Functional dependence of the $\eta^3\chi_1$ term on the angle θ_1 (following the ansatz given by Eq. (5.3.5)), as depicted in Eq. (5.3.6). Similar results are obtained for the remaining 5 terms of the parameterized fit for $\overline{\Delta E}$. All fits were performed with the `Fit` function in Mathematica [468].

of $\theta_1 \in \left\{\frac{\pi}{6}, \frac{\pi}{3}, \frac{\pi}{2}, \frac{2\pi}{3}, \frac{5\pi}{6}\right\}$, we have

$$\{a_i\}_{i=1}^{i=7}\left(\eta^2\chi_1, \eta^3\chi_1, \eta^3\chi_1^2, \eta^4\chi_1, \eta^4\chi_1^2, \eta^5\chi_1, \eta^5\chi_1^2\right). \tag{5.3.4}$$

Upon visually inspecting each a_i, we observed that the contribution of the $\eta^2\chi_1$ term was minimal, supporting its removal from the final fit. Consequently, we are left with 6 coefficients to fit for θ_1. Thereafter, we proceed to fitting the θ_1-dependence of the coefficients a_i. As previously mentioned, at the boundaries $\theta_1 \in \{0, \pi\}$, we recover the aligned and anti-aligned limits, implying that $a_i(0) = a_i(\pi) = 0$. Given that θ_1 is an angle, it makes sense to propose a sinusoidal ansatz such as

$$a_i(\theta_1) = A_i \sin\theta_1 + B_i \sin 2\theta_1, \tag{5.3.5}$$

which will always satisfy the boundary conditions. Figure 5.9 shows the functional dependence of the $\eta^3\chi_1$ term in θ_1 and the corresponding fit from the above ansatz in Eq. (5.3.5).

The final expression for $\overline{\Delta E}(\eta, \chi_1, \theta_1)$ is given by

$$\begin{aligned}\overline{\Delta E}(\eta, \chi_1, \theta_1) = {} & \eta^3\chi_1\left[0.759123\sin(\theta_1) - 2.33392\sin(2\theta_1)\right] + \\ & \eta^3\chi_1^2\left[6.51059\sin(\theta_1) + 7.06906\sin(2\theta_1)\right] + \\ & \eta^4\chi_1\left[-11.7873\sin(\theta_1) + 22.364\sin(2\theta_1)\right] + \\ & \eta^4\chi_1^2\left[-37.0594\sin(\theta_1) - 63.3841\sin(2\theta_1)\right] + \\ & \eta^5\chi_1\left[35.0427\sin(\theta_1) - 51.36\sin(2\theta_1)\right] + \\ & \eta^4\chi_1^2\left[-37.0594\sin(\theta_1) - 63.3841\sin(2\theta_1)\right].\end{aligned} \tag{5.3.6}$$

Figure 5.10 shows ΔE computed as in Eq. (5.3.3) together with the numerical values for the entire dataset at $\theta_1 = \pi/2$. This fit can now be inserted into Eq. (5.3.2) in order to get the new model for the mass of the remnant object. To compute the final mass of the corresponding aligned system, we rely on the updated IMRPhenomX model given by Eq. (5.C.2).

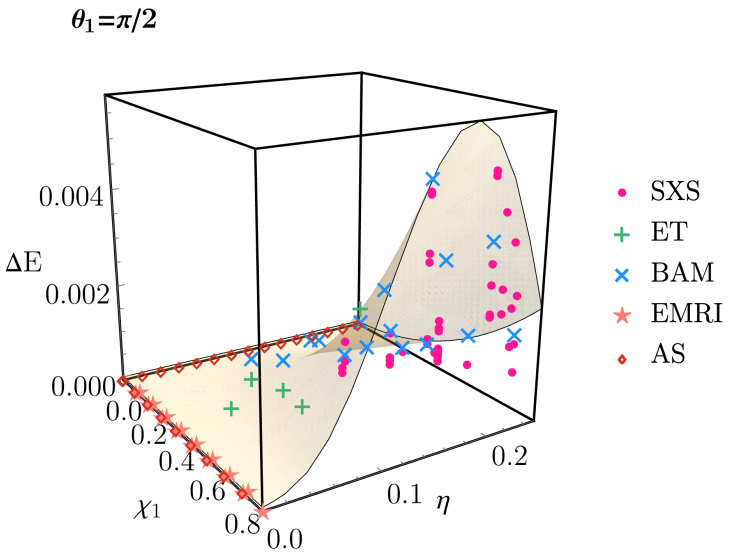

Figure 5.10: Numerical evaluation of ΔE as defined in Eq. (5.3.1), obtained from the parameterized fit $\overline{\Delta E}$ (5.3.6) and $\Delta E_{\rm EMR}$, at a fixed spin orientation $\theta_1 = \pi/2$, while varying the mass ratio η and the spin magnitude χ_1. The figure includes the single spin precessing simulations shown in Fig. 5.2 that fall into this subspace, as well as the vanishing corrections for the limits $\eta \to 0$ and $\chi_1 = 0$, denoted as AS.

We can now assess the accuracy of our new model. For the entire single spin precessing dataset, we calculate the final mass using our model (Eqs. (5.3.2), (5.3.6)), denoted as `PhenNew`. We compare this with the current IMRPhenomX model, which does not account for the ΔE correction (`PhenXP`), and with `NRSur7dq4EmriRemnant` for validation. Figure 5.11 presents the histogram of errors associated with each model. Results are based on the NR data from our dataset, comprising 184 simulations with $q \leq 18$. The EMRI dataset has been excluded from the comparison due to its large number of simulations and small errors. Table 5.2 provides the computational time required to evaluate the final masses and spins for the whole NR dataset, along with the numerical values of the median error and root mean square error (RMSE) computed as in Eq. (5.B.1). The `PhenXP` model for the final mass M_f involves evaluating the aligned spin model for the radiated energy using Eq. (5.C.2). On the other hand, `PhenNew` evaluates both Eq. (5.C.2) and the parameterized fit for $\overline{\Delta E}$ (5.3.6), as well as $\Delta E_{\rm EMR}$, using the `KerrGeodesics` package. Note that computational times refer to a straightforward implementation in Mathematica, with most of the computational time required to solve the precessing geodesic equations to obtain $\Delta E_{\rm EMR}$. An optimized implementation, and a fit to the analytically known EMR results would dramatically accelerate the evaluation. For the evaluation of the `NRSur` model, we utilized the SurfinBH python package [184] with the NRSur7dq4EmriRemnant [35] model. In this case, the evaluation time is provided as a single number for both the final mass and spin because both are returned together as an array. It takes approximately 5 milliseconds to compute the remnant properties for one binary black hole configuration, consistent with the findings in [35]. It is noteworthy that NRSur7dq4EmriRemnant incorporates the direction of the final spin, thereby introducing complexity to the model which is reflected in the computational time.

These findings demonstrate that our new model for the final mass achieves an accuracy comparable to the NRSur7dq4 model, surpassing the original `PhenXP` model, while

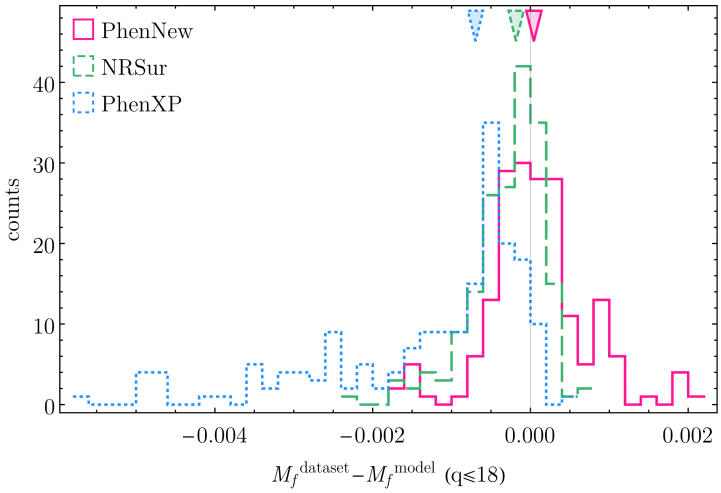

Figure 5.11: Histogram of the errors in the remnant mass computed with each of the three models for our single spin precessing dataset presented in Fig. 5.2. The model developed in this project is labeled as `PhenNew`, the underlying model as `PhenXP` and NRSur7dq4EmriRemnant as `NRSur`. The triangles above the distributions represent their median values, also included in Table 5.2. This table provides additional information on the distributions: the computational time needed to evaluate the dataset for each model, along with the root mean square errors (RMSEs). Note that the `PhenXP` model shows a sensible bias that is significantly reduced in the `PhenNew` model.

		`PhenNew`	`PhenXP`	`NRSur`
M_f	Median	$4.4 \cdot 10^{-5}$	$-7.0 \cdot 10^{-4}$	$-1.8 \cdot 10^{-4}$
	RMSE	$6.4 \cdot 10^{-4}$	$1.8 \cdot 10^{-3}$	$5.4 \cdot 10^{-4}$
χ_f	Median	$1.5 \cdot 10^{-4}$	$-8.6 \cdot 10^{-3}$	$1.7 \cdot 10^{-3}$
	RMSE	$3.4 \cdot 10^{-3}$	$1.5 \cdot 10^{-2}$	$5.4 \cdot 10^{-3}$
Av. ev. time (ms)		0.55/2.7	0.019/0.071	5.2

Table 5.2: Median value and root mean square error (RMSE) of the error distributions of the remnant mass M_f and spin magnitude χ_f for different models, with respect to the numerical relativity dataset shown in Fig. 5.2. The histograms of the distributions are shown in Figs. 5.11 and 5.15, respectively. The last row provides the averaged time (Av. ev. time) needed to evaluate the complete dataset (184 simulations) with each model for the final mass/final spin. For the NRSur7dq4EmriRemnant model (`NRSur`) only one value is provided because their python implementation jointly returns both quantities.

maintaining its computational efficiency. Additionally, PhenNew exhibits a less biased error distribution compared to the old model, which tends to overestimate the final mass.

To ensure completeness, we assessed the resulting model beyond our calibration region, specifically when $\chi_1 > 0.8$. We focused on scenarios where precession effects are maximal, corresponding to an in-plane spin configuration, i.e. $\theta_1 = \pi/2$. We include the result of the extrapolation in App. 5.D. Despite the absence of numerical data in that region, the study indicates that the extrapolation behaves well, and no dubious features emerge outside the calibration regime.

5.3.2 Remnant spin

If one assumes the twisting-up approximation and that the in-plane and aligned spin components are conserved, then one can write the final spin magnitude as

$$\chi_f^{\rm prec} = \sqrt{\chi_f^{\rm AS^2} + \frac{m_1^4}{M_f^4}\chi_\perp^2}, \tag{5.3.7}$$

where $\chi_\perp$ is the total in-plane spin. Variants of this approximation with different assumptions to compute $\chi_\perp$ have been used in the IMRPhenomX and IMRPhenomT waveform models [189, 190]. In our case, considering only the single spin sector, $\chi_\perp$ simply becomes the in-plane component of the larger black hole. However, the in-plane and orthogonal spin components are not exactly conserved, and we therefore introduce a correction term δ^2 that we fit to our numerical dataset. Note that denoting the unknown quantity as δ^2 is an abuse of notation, since it is not necessarily positive, and indeed typically is negative. Consequently, the final spin of a precessing system can be written as

$$\chi_f^{\rm prec} = \sqrt{\chi_f^{\rm AS^2} + \frac{m_1^4}{M_f^4}\chi_\perp^2 + \delta^2}, \tag{5.3.8}$$

where $\chi_1^\perp$ in the single spin case is given by $\chi_1^\perp = \chi_1 \sin(\theta_1)$, and $M_f = 1 - E_{\rm rad}$, where we use the model of the previous section to compute $E_{\rm rad}$.

One can develop the previous equation and turn it into a closed-form approximation for the extreme mass ratio limit by using Eq. (5.2.8) for both the precessing and aligned final spin, assuming that the Carter's constant is approximately the in-plane orbital angular momentum ($Q \approx L_\rho^2$). This procedure results in

$$\begin{aligned}\delta^2_{\rm EMR} = \frac{M^4}{M_f^4}\Bigg[&\frac{m_2^2}{m_1^2}\left(\tilde{L}_z^2 + \tilde{Q} - \tilde{L}_z^{\parallel^2}\right) + \\ &2\frac{m_2}{m_1}\chi_1\cos(\theta_1)\left(\sqrt{\tilde{L}_z^2 + \tilde{Q}} - \tilde{L}_z^{\parallel}\right)\Bigg].\end{aligned} \tag{5.3.9}$$

The main advantage of this expression lies in the fact that it relies exclusively on geodesic information for precessing and aligned equations. Remarkably, even for close to comparable masses, its behavior closely resembles that obtained from numerical data, up to a scaling factor, as can be seen in the lower panel of Fig. 5.12. Equation (5.3.9) consists of two contributions: the first term, quadratic in $1/q$, and the second term, linear. Both terms are shown in Fig. 5.12. The linear term dominates for extreme mass ratios (in dotted lines, covered by the continuous lines) and exhibits oscillations due to the cosine dependence

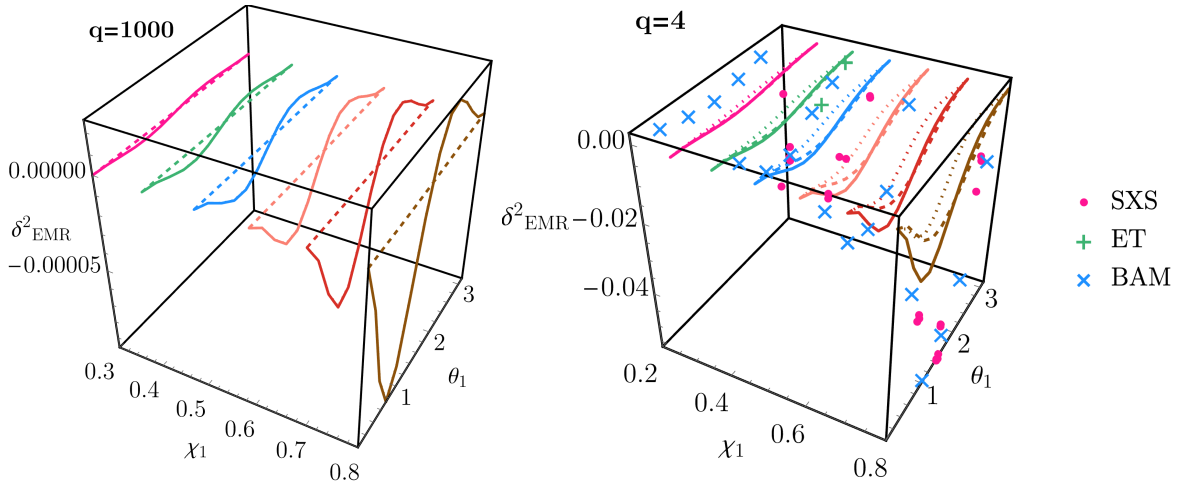

Figure 5.12: Numerical evaluation of $\delta^2_{\rm EMR}$ as defined in Eq. (5.3.9). The constants of motion L_z, Q and E are obtained from the precessing geodesic equations, while $L_z^{\parallel}$ is computed from Eq. (5.2.11). Dotted lines show the linear term in Eq. (5.3.9) and dashed lines, the quadratic term. We solve the precessing geodesic equations at the ISSO using the `KerrGeodesics` package at a fixed mass ratio, while varying the black hole's spin magnitude χ_1 and its orientation with respect to the orbital frequency at the reference time θ_1. The top panel corresponds to a mass ratio of 1000, where the geodesic equations are expected to be valid, while the lower panel corresponds to a mass ratio of 4, where they are expected to fail. In the lower plot, we included the single spin simulations from Fig. 5.2 that fall into this subspace.

of the inclination angle. However, as the mass ratio increases, these oscillations are overshadowed by the growth of the quadratic contribution (depicted by dashed lines), as shown in the lower panel of Fig. 5.12. It turns out that in order to reproduce our numerical data in the comparable mass regime it is best to keep both the linear and quadratic in η terms. Following the same motivation as for the energy, we proceed to subtract $\delta^2_{\rm EMR}$ from our fitting quantity δ^2 to capture the EMRI regime, defining

$$\overline{\delta^2} = \delta^2 - \delta^2_{\rm EMR}, \tag{5.3.10}$$

where again $\delta^2_{\rm EMR}$ is computed using the `KerrGeodesics` Mathematica package.

The fitting procedure then follows the same structure described in the previous subsection. We first compute δ^2 from Eq. (5.3.8) for all the single spin simulations in our precessing dataset. We again neglect the in-plane spin angle ϕ_1, reducing our independent variables to (q, χ_1, θ_1). We then show $\overline{\delta^2}$ for fixed values of θ_1, chosen to be the same values as for the energy: $\theta_1 \in \left\{\frac{\pi}{6}, \frac{\pi}{3}, \frac{\pi}{2}, \frac{2\pi}{3}, \frac{5\pi}{6}\right\}$. Again, at $\theta_1 \in \{0, \pi\}$, δ^2 is defined to vanish so one recovers the non-precessing limit. In order to find an appropriate ansatz in this case, we start our procedure with $a \leq 3$ and $b \leq 2$. We then followed the iterative procedure described above to reduce our grid from 11 to 7 coefficients, representing an improvement of -16.5 in BIC. Then, for every fixed value of θ_1, we have

$$\{a_i\}_{i=1}^{i=7}\left(\chi_1^2, \eta\chi_1, \eta\chi_1^2, \eta^2\chi_1, \eta^2\chi_1^2, \eta^3\chi_1, \eta^3\chi_1^2\right). \tag{5.3.11}$$

Finally, five more coefficients can be discarded when inspecting their θ_1-dependence, resulting in a very simple ansatz for $\overline{\delta^2}$:

$$\{a_i\}_{i=1}^{i=2}\left(\eta^2\chi_1^2, \eta^3\chi_1^2\right). \tag{5.3.12}$$

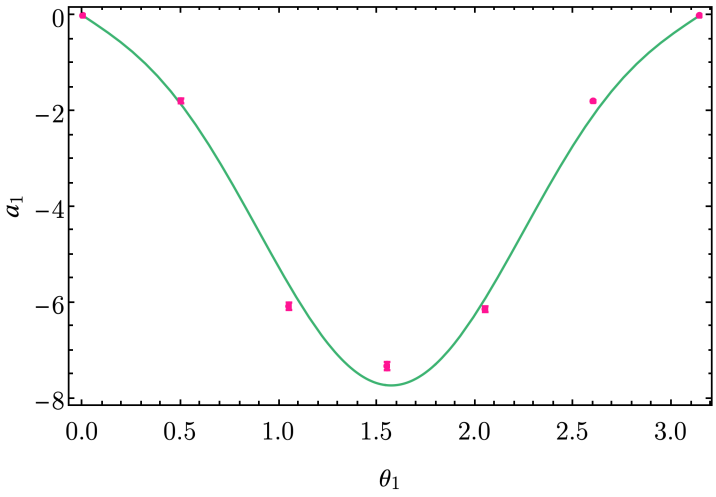

FIGURE 5.13: Functional dependence of the $\eta^2\chi_1^2$ term on θ_1 (following the ansatz given by Eq. (5.3.13)), as depicted in Eq. (5.3.14). Similar results are obtained for the remaining term of the parameterized fit for $\overline{\delta^2}$. All fits were performed with the `Fit` function in Mathematica [468].

We propose again a sinusoidal ansatz for the coefficients a_i which satisfies the boundary conditions:

$$a_i(\theta_1) = A_i \sin\theta_1 + B_i \sin 3\theta_1 . \tag{5.3.13}$$

Figure 5.13 shows an example of the functional dependence of the first fit coefficient a_1 ($\eta^3\chi_1^2$) in terms of θ_1.

The resulting fit is finally given by

$$\begin{aligned}\overline{\delta^2}(\eta,\chi_1,\theta_1) = \eta^2\chi_1^2\left[1.25552\sin(3\theta_1) - 6.47984\sin(\theta_1)\right] + \\ \eta^3\chi_1^2\left[27.0456\sin(\theta_1) - 4.71194\sin(3\theta_1)\right],\end{aligned} \tag{5.3.14}$$

and it is represented in Fig. 5.14 for $\theta_1 = \pi/2$, together with the numerical δ^2-values for the entire dataset. Note that the plot shows δ^2, which is computed from Eq. (5.3.10). This fit can now be inserted into Eq. (5.3.8) in order to get the new model for the remnant spin. In this expression, the aligned spin final spin dependence goes as $\chi_f^{\rm AS}(\eta, \chi_1\cos(\theta_1))$ and the final mass is computed using the fit for $M_f(\eta,\chi_1,\theta_1)$ shown in Eq. (5.3.2).

We can now assess the accuracy of our new model computing the final spin for our dataset using our new model, denoted as `PhenNew`. We then compare it with the current IMRPhenomX model, which ignores the δ^2 correction (`PhenXP`) and the `NRSur7dq4EmriRemnant` model. Figure 5.15 displays the error histogram for each model relative to the numerical values, equivalent to the approach in Fig. 5.11, utilizing the full dataset without the EMRI waveforms. Table 5.2 provides the median and root mean square errors, computed as in Eq. (5.B.1), of the distributions, along with the computational time required for each model evaluation. The `PhenXP` model for the final spin χ_f involves evaluating Eq. (5.3.8) assuming $\delta^2 = 0$. On the other hand, `PhenNew` evaluates Eq. (5.3.8) and the parameterized fit for $\overline{\delta^2}$ (5.3.14), as well as $\delta^2_{\rm EMR}$, using the `KerrGeodesics` package. Both models are fully assessed in Mathematica, with most of the computational time attributed to solving the precessing geodesic equations to obtain $\delta^2_{\rm EMR}$. In the case of `NRSur`, as previously mentioned, we evaluated the NRSur7dq4EmriRemnant using the `SurfinBH` package, extracting the final mass and spin from the package's output.

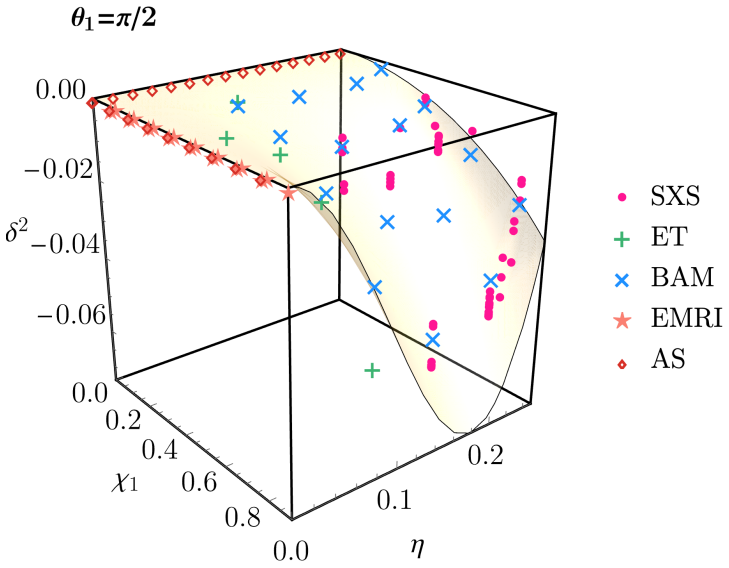

Figure 5.14: Numerical evaluation of the parameterized fit of δ^2 as defined in Eq. (5.3.8), obtained from the parameterized fit $\overline{\delta^2}$ (5.3.14) and $\delta^2_{\rm EMR}$ at a fixed spin orientation $\theta_1 = \pi/2$, while varying the mass ratio η and the spin magnitude χ_1. The figure includes the single spin precessing simulations shown in Fig. 5.2 that fall into this subspace, as well as the vanishing corrections for the limits $\eta \to 0$ and $\chi_1 = 0$, denoted as AS.

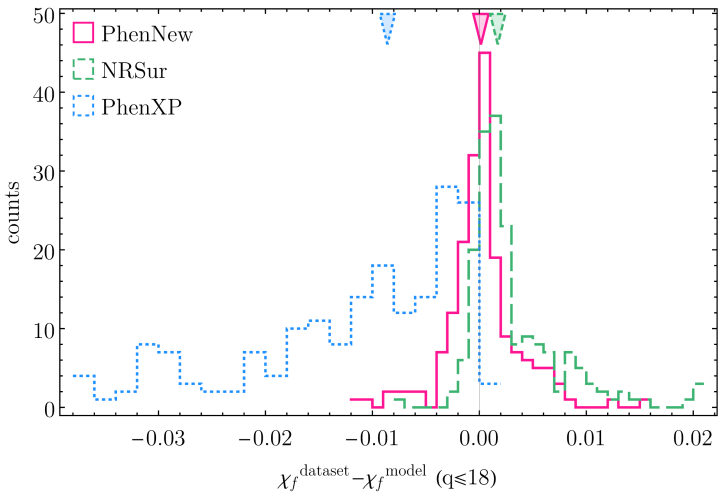

Figure 5.15: Histogram of the errors in the remnant spin computed with each of the three models for our single spin precessing dataset presented in Fig. 5.2. The model developed in this project is labeled as `PhenNew`, the underlying model as `PhenXP` and NRSur7dq4EmriRemnant as `NRSur`. The triangles represent the median of each distribution, also included in Table 5.2. This table provides additional information on the distributions: the computational time needed to evaluate the dataset for each model, along with the root mean square errors (RMSEs).

Regarding computational times, it's important to note that the provided times are for the purpose of comparison and not aimed at optimizing the code's efficiency. In the case of the model developed in this project, the majority of the evaluation time is dedicated to solving the geodesic equations. As part of future work, we anticipate parameterizing $\Delta E_{\rm EMR}$ and $\delta^2_{\rm EMR}$ to make the fits entirely parametric. The conclusions drawn from these results parallel those from the final mass: the new model offers a more accurate and less biased distribution than IMRPhenomX, achieving precision comparable to that of the NRSur7dq4EmriRemnant model while retaining the simplicity and efficiency of the model on which it is based.

To ensure completeness, we perform a final check on the extrapolation of this new remnant spin model for extreme spins (see App. 5.D). Once again, we confirm that our model is well-behaved even for extreme spins, despite not being calibrated in that regime, and it maintains the Kerr limit $|\chi_1| \leq 1$.

5.3.3 Cross-validation of the remnant model

In this last section we provide additional tests of our complete remnant model. Firstly, we compute "out-of-sample" errors to evaluate the consistency of our proposed ansätze. Finally, we test the performance of our model on the entire precessing dataset, including both double and single spin simulations.

The parameterized fits shown in Figs. 5.10 and 5.14 were obtained from our single spin precessing dataset (184 simulations), yielding the in-sample errors detailed in Table 5.2. To examine the consistency of our method, we now compute "out-of-sample" errors using a procedure that involves dividing the data into 23 sets of 8 random samples each. For each set, we construct the final mass and spin magnitude fits using the remaining 176 data points and test their performance against the 8 validation samples. The resulting root mean square error values display the following mean values over the 23 sets: $\overline{\rm RMSE}(M_f) = 6.3 \cdot 10^{-4}$ and $\overline{\rm RMSE}(\chi_f) = 3.2 \cdot 10^{-3}$. These values closely match those shown in Table 5.2, where no samples were taken to compute the fits. Therefore, we conclude that, as expected from our analysis based on information criteria, our models do not exhibit overfitting tendencies, affirming the consistency of our fitting procedure.

As a final test, we evaluate our remnant model for the complete precessing dataset outlined in Sec. 5.2.1. Although the model has been calibrated for the single spin limit, one might be interested in its performance across the full precessing quasi-circular space, as well as its comparison with the currently available remnant models. Figures 5.11 and 5.15 reveal that `PhenXP` exhibits a biased distribution for both the final mass and spin magnitude, tending to overestimate the real value. The fitting quantities ΔE and δ^2 consistently show a clear tendency in their sign, as evident in Figs. 5.10 and 5.14. These quantities appear as a small correction to the `PhenXP` model, which works for the double spin case, and hence the effect of our parameterized fits results in a slight shift towards the correct values. However, since they only account for the single spin, substantial improvements in accuracy are not expected in this scenario.

Figure 5.16 and Table 5.3 demonstrate that the error distributions obtained with `PhenNew` for the complete precessing dataset exhibit less bias compared to those obtained with `PhenXP`. However, given that `PhenNew` only considers the single spin correction, the overall performance does not exhibit a substantial improvement, as anticipated.

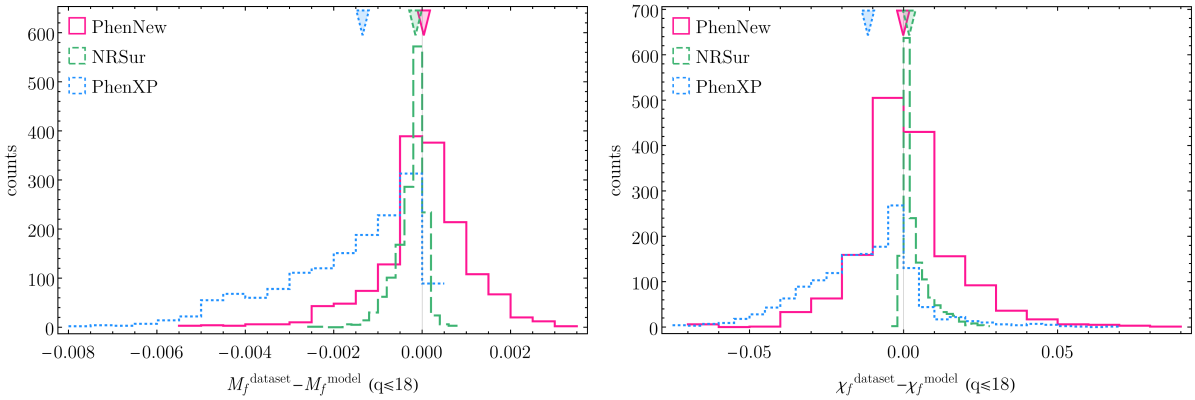

Figure 5.16: Histograms of the errors in the remnant properties with each of the three models for our full precessing dataset presented in Fig. 5.1. `PhenNew` corresponds to `PhenXP` plus the corrections derived in Secs. 5.3.1 and 5.3.2 for the final mass (top panel) and final spin (bottom), respectively, and `NRSur` corresponds to the NRSur7dq4EmriRemnant model. The triangles represent the median of each distribution. Table 5.3 provides the medians along with the root mean square errors (RMSEs) for each distribution.

		PhenNew	PhenXP	NRSur
M_f	Median	$3.7 \cdot 10^{-5}$	$-1.3 \cdot 10^{-3}$	$-1.5 \cdot 10^{-4}$
	RMSE	$1.1 \cdot 10^{-3}$	$2.3 \cdot 10^{-3}$	$4.2 \cdot 10^{-4}$
χ_f	Median	$-9.9 \cdot 10^{-5}$	$-1.2 \cdot 10^{-2}$	$1.8 \cdot 10^{-3}$
	RMSE	$1.6 \cdot 10^{-2}$	$2.2 \cdot 10^{-2}$	$6.1 \cdot 10^{-3}$

Table 5.3: Median value and root mean square error (RMSE) of the error distributions of the remnant mass M_f and spin magnitude χ_f for different models, with respect to the full numerical relativity dataset shown in Fig. 5.1. The histograms of the distributions are shown in Fig. 5.16, top and lower panel, respectively.

Incorporating the double spin correction remains a direction for future work. In Fig. 5.16, we observed a slightly biased error distribution of the remnant properties for NRSur7dq4EmriRemnant. Despite extensive tests, including waveform alignment using quadrupole alignment and different rotation methods, the small magnitude of the bias (see Table 5.3) makes it challenging to track down the source of the error. Moreover, Ref. [35] only provides absolute errors, which limits further comparisons on the relative error distributions found. While it would be interesting to further understand this issue, it is not within the scope of this project, and further exploration remains a topic for future work.

5.4 Conclusions

In this work, we presented a new parameterized remnant model for single spin precessing black hole binary systems at any mass ratio. We employed information from precessing geodesics at the ISSO to estimate the remnant properties in the extreme mass ratio regime, and numerical data at mass ratio 1000 as a cross-check. For the final mass we have fixed the term linear in symmetric mass ratio η to the values obtained from the EMR limit, and for the final spin we have fixed both the linear and quadratic terms in η terms this way. As has become customary before, we have worked in a co-orbital frame, which drastically

reduces differences between the aligned spin and precessing sectors, and in addition we have subtracted previous aligned spin fits from our data before performing the fit to the precessing dataset. These procedures have allowed us to obtain rather accurate but simple fits from a relatively small number of numerical relativity waveforms across the entire range of mass ratios. Overfitting was controlled by model selection based on the BIC information criterion, and cross-checked by performing "out-of-sample" errors tests which confirm the consistency of our remnant models, yielding RMSEs very close to those obtained for the model utilizing the full dataset.

We observe that the correction terms that map aligned spin results to the precessing case have a dominant sign. In consequence, our models remove biases that had been present in previous simple fits that only used aligned spin numerical relativity data and are being used in precessing phenomenological waveform models [189, 190]. These biases have found to be related to the typical positive sign in ΔE and negative in δ^2, leading to an overestimation trend in the underlying model.

The assessment of the resulting models is summarized in Table 5.2. Our new model `PhenNew` surpasses its underlying baseline `PhenXP` used in current phenomenological models, achieving a performance akin than NRSur7dq4EmriRemnant (`NRSur`) at much smaller computational cost. The largest contribution to the computational cost is the evaluation of the final mass and spin contributions of the geodesic approximation. While our straightforward Mathematica code could be optimized, or implemented in other languages, a further path to accelerating the evaluation would be to make a fast approximate model of the geodesic contribution. The evaluation of our fits on the complete precessing dataset reveals that the new model, `PhenNew`, exhibits a less biased distribution compared to `PhenXP`, but, not surprisingly, lacks a significant overall improvement for the double spin case. In order to develop a general model of precessing remnant mass and spin, the next steps will therefore be to extend our work to the double spin case, and also to include the dependency on the in-plane spin angles. In the double spin case one faces a significantly larger parameter space (two spin vectors instead of one) and more complex phenomenology. One complication is that since the two spins will in general rotate at different rates, whether spins add up or cancel changes over time. This will require additional numerical relativity simulations. For our modelling approach, and in general in order to better understand the phenomenology, it will be useful to have a significant number of numerical relativity simulations, where one parameter is changed at a time. One would expect that these simulations can primarily focus on the comparable mass regime, if sufficient perturbative information is available. The secondary spin is expected to function primarily as a correction to the single spin limit in scenarios involving high mass ratios, but in order to correctly model the transition from comparable to extreme mass ratios, we expect that again perturbative information will be essential.

In Sec. 5.2 we have discussed the problem of creating a consistent precessing dataset from several different numerical relativity catalogs. Here we have only used this heterogeneous dataset for models of the final state, using a reference time of $100M$ before the merger to define the input data for our fits to facilitate comparisons with NRSur7dq4EmriRemnant [35]. Future work should investigate the optimization of trade-offs related to the choice of reference time: later times minimize the spin dynamics between input parameters and results, whereas earlier times benefit the connection of the final state fits with models for the inspiral. Furthermore, ambiguities arise in the

definition of the merger time across different datasets, and in the choice of co-orbital frame. Future work will investigate these issues further. We have also created consistent datasets for the waveforms, which we have not discussed and used in this paper. This dataset is intended for the calibration of precessing waveform models to numerical relativity, where a large number of waveforms is required, and the pooling of data from different numerical relativity catalogues will be advantageous.

Acknowledgements

We would like to thank Scott A. Hughes, Anuj Apte, Gaurav Khanna and Halston Lim for providing the EMRI waveforms used in this project; Maite Mateu-Lucena for being involved in early stages of producing the dataset; Isabel Suárez-Fernández for running some of the Einstein Toolkit simulations; and Anna Heffernan, Antoni Ramos-Buades, Cecilio García-Quirós and Vijay Varma for useful comments and discussions. This work makes use of the Black Hole Perturbation Toolkit [265], in concrete the `KerrGeodesics` package. The authors thankfully acknowledge the computer resources at MareNostrum and the technical support provided by Barcelona Supercomputing Center (BSC) through funding from the Red Española de Supercomputación (RES). Maria de Lluc Planas is supported by the Spanish Ministry of Universities via an FPU doctoral grant (FPU20/05577). Joan Llobera-Querol is supported by the Comunitat Autònoma de les Illes Balears through the Direcció General de Recerca, Innovació i Transformació Digital via an FPU doctoral grant FPI/2022. This work was supported by the Universitat de les Illes Balears (UIB); the Spanish Agencia Estatal de Investigación grants PID2022-138626NB-I00, PID2019-106416GB-I00, RED2022-134204-E, RED2022-134411-T, funded by MCIN/AEI/10.13039/501100011033; the MCIN with funding from the European Union NextGenerationEU/PRTR (PRTR-C17.I1); Comunitat Autonòma de les Illes Balears through the Direcció General de Recerca, Innovació I Transformació Digital with funds from the Tourist Stay Tax Law (PDR2020/11 - ITS2017-006), the Conselleria d'Economia, Hisenda i Innovació grant numbers SINCO2022/18146 and SINCO2022/6719, co-financed by the European Union and FEDER Operational Program 2021-2027 of the Balearic Islands; the "ERDF A way of making Europe". This material is based upon work supported by NSF's LIGO Laboratory which is a major facility fully funded by the National Science Foundation.

Appendices

5.A Details on the general geodesic equations

Following Ref. [449], for geodesics in Kerr spacetime the constants of motion E, L_z and Carter's constant Q for given orbital parameters and also the parameters of the source a and $q = m_1/m_2 = M/\mu$ are given by (using Boyer-Lindquist coordinates (r, θ, ϕ, t))

$$\frac{\mathrm{d}r}{\mathrm{d}\tau} = R(r) = [(r^2 + a^2)E - aL_z]^2 - \Delta[\mu^2 r^2 + (L_z - aE)^2 + Q] = 0, \tag{5.A.1}$$

$$\frac{\mathrm{d}\theta}{\mathrm{d}\tau} = \Theta(\theta) = Q - \left[(\mu^2 - E^2)a^2 + \frac{L_z^2}{\sin^2\theta}\right]\cos^2\theta = 0, \tag{5.A.2}$$

where $\Delta = r^2 - 2Mr + a^2$. The roots of the equations correspond to the turning points of the radial and polar motion. For circular orbits ($e = 0$), we will need a third constraint $R'(r_0) = 0$, apart from $R(r_0) = 0$ and $\Theta(\theta_0) = 0$. Circular orbits are stable if $R''(r_0) < 0$. The radius which separates the stable and unstable orbits is known as the ISSO and hence satisfies $R''(r_0) = 0$. Thus, solving these four equations one can find the radius $r_0 = r_{\mathrm{ISSO}}$, the energy E, the orbital angular momentum L_z and Carter's constant Q for a given system and orbital quantities.

If we use the dimensionless quantities introduced in Eq. (5.2.2) and rearrange $\Theta(\theta_-) = 0$, we can express the Carter's constant as

$$\tilde{Q} = \cos^2\theta_- \left[\tilde{a}^2(1 - \tilde{E}^2) + \frac{\tilde{L}_z^2}{1 - \cos^2\theta_-}\right]. \tag{5.A.3}$$

Substituting this equation in $\tilde{R}(\tilde{r})$ gives

$$\tilde{R}(\tilde{r}) = f(\tilde{r})\tilde{E}^2 - 2g(\tilde{r})\tilde{E}\tilde{L}_z - h(\tilde{r})\tilde{L}_z + d(\tilde{r}), \tag{5.A.4}$$

where

$$f(\tilde{r}) = \tilde{r}^4 + \tilde{a}^2[\tilde{r}(\tilde{r} + 2) + \cos^2\theta\tilde{\Delta}], \tag{5.A.5}$$

$$g(\tilde{r}) = 2\tilde{a}\tilde{r}, \tag{5.A.6}$$

$$h(\tilde{r}) = \tilde{r}(\tilde{r} - 2) + \frac{\cos^2\theta_-}{1 - \cos^2\theta_-}\tilde{\Delta}, \tag{5.A.7}$$

$$d(\tilde{r}) = (\tilde{r}^2 + \tilde{a}^2\cos^2\theta_-)\tilde{\Delta}, \tag{5.A.8}$$

and one can then compute $\tilde{R}'(\tilde{r_0})$ and $\tilde{R}''(\tilde{r_0})$ from Eq. (5.A.4). Solving these equations yields to *four* solutions for the constants of motions, and one fixed value for the r_{ISSO} in the case of circular orbits. Considering only those solutions with positive energy, we have $(\tilde{E}^{(p)}, \tilde{L_z}^{(p)}, \tilde{Q}^{(p)})$ and $(\tilde{E}^{(r)}, \tilde{L_z}^{(r)}, \tilde{Q}^{(r)})$, where p stands for prograde orbits and r, for retrograde. It is verified that $\tilde{E}^{(p)} < \tilde{E}^{(r)}$ and $\tilde{L_z}^{(p)} < \tilde{L_z}^{(r)}$- for prograde orbits the particle has higher binding energy and co-revolves with the black hole, whereas retrograde orbits usually counter-revolves.

5.B Information criteria

We do not work with an a-priori ansatz for our parameterized fits, but rather select the best functional form from a wide class of models. We then use information criteria to perform the model selection to avoid overfitting, following [27], where aligned spin fits for the remnant quantities are constructed. In this appendix we describe the information criteria in more detail.

A basic performance metric for model adjustment is the root mean square error (RMSE). For a model of a quantity q dependent on parameters λ, and data points (λ_i, q_i) for $i = 1 \dots N$,

$$\mathrm{RMSE}\,[\mathrm{model}] = \sqrt{\frac{1}{N}\sum_{i=1}^{N}[q_i - \mathrm{model}(\lambda_i)]^2}. \tag{5.B.1}$$

Using only the RMSE to perform model selection is prone to overfitting. For this reason, when selecting the best model, one should penalize models according to its complexity, specifically the number of free coefficients. A widely-used statistical quantity is the Akaike Information Criterion (AIC) [469],

$$\mathrm{AIC} = -2\ln\mathcal{L}_{max} + 2N_{\mathrm{coeffs}}, \tag{5.B.2}$$

which compensates the accuracy of the fit with the number of coefficients. Here a lower value of the AIC indicates better suitability of the model. We have used the implementation of the AIC in the Mathematica's `LinearModelFit` function [467].

An alternative quantity that serves the same purpose, but has a different theoretical foundation, is the Bayesian Information Criterion (BIC) [470]

$$\mathrm{BIC} = -2\ln\mathcal{L}_{max} + N_{\mathrm{coeffs}}\ln N_{\mathrm{data}}. \tag{5.B.3}$$

In terms of performance, both criteria penalize the degeneracies between parameters and the BIC usually penalizes additional parameters more than AIC. To discern between models, a 1 unit difference is generally required, while 10 points would be decisive evidence. Further discussion on the criteria can be found in [471].

5.C Fit for the updated aligned radiated energy

In this appendix we provide the full parameterized expression for the aligned spin radiated energy used in this paper, which updates the one developed in Ref. [27].

Defining

$$\hat{S} := \frac{\chi_1 + q^2\chi_2}{1+q^2}, \tag{5.C.1}$$

we can write:

$$E_{\rm AS} = 0.288265\eta^5(\chi_1-\chi_2)^2 - 0.0483974\eta^2(1-1.76539\eta)\sqrt{1-4\eta}(\chi_1-\chi_2)+ \\ + \frac{1393.61\eta^7 - 1160.94\eta^6 + 372.473\eta^5 - 54.0578\eta^4 + 3.33345\eta^3 + 0.44487\eta^2 + \left(1-\frac{2\sqrt{2}}{3}\right)\eta}{\left(1.96359\eta^2 + 0.557424\eta - 0.956935\right)\hat{S}+1} \\ \Big[\left(-5.40979\eta^2 + 1.74325\eta - 0.106587\right)\hat{S}^6 + \left(0.915964\eta^2 + 0.0338535\eta - 0.0809724\right)\hat{S}^5 + \\ + \left(3.93186\eta^2 - 1.15351\eta + 0.0316422\right)\hat{S}^4 + \left(-1.16612\eta^2 + 0.379967\eta - 0.0552524\right)\hat{S}^3 + \\ + \left(-0.950876\eta^2 + 0.635553\eta - 0.173169\right)\hat{S}^2 + \left(-2.75115\eta^2 + 1.73637\eta - 0.398234\right)\hat{S} + 1\Big]. \tag{5.C.2}$$

5.D Extrapolation of the remnant model towards extreme spins

In this appendix we assess the extrapolation behavior of our parameterized remnant models focusing on the scenario where precession effects are maximized. Specifically, we explore spin magnitudes beyond the calibrated regime ($0.8 \leq \chi_1 \leq 1$), considering the case of in-plane configurations ($\theta_1 = \pi/2$).

Figure 5.17 illustrates the extrapolation results, showing a smooth continuation without exhibiting any nonphysical behavior, as well as the Kerr limit $\chi_1 \leq 1$. While these extrapolations provide valuable insights, it is important to interpret them cautiously, recognizing the need for further refinement when numerical data becomes available in the high spin magnitude regime.

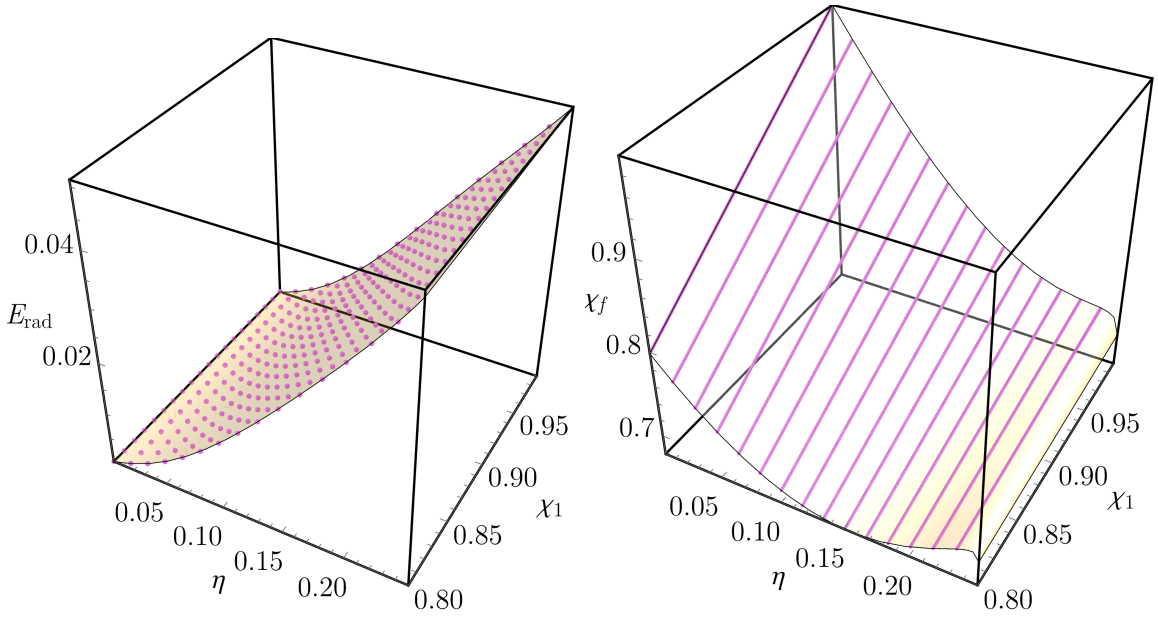

Figure 5.17: Extrapolation of the remnant fits developed in Secs. 5.3.1 (left panel) and 5.3.2 (right panel) outside of their spin calibration regime, $0.8 \leq \chi_1 \leq 1$, for a single in-plane spin configuration ($\theta_1 = \pi/2$), where precession effects are maximized.

CHAPTER 6

IMRPhenomTEHM

This chapter is based on the following article:

- Maria de Lluc Planas, Antoni Ramos-Buades, Cecilio García-Quirós, Héctor Estellés, Sascha Husa, and Maria Haney. "*Time-domain phenomenological multipolar waveforms for aligned-spin binary black holes in elliptical orbits*", arXiv: arXiv:2503.13062[gr-qc] [19].

Abstract

We introduce IMRPhenomTEHM, a new phenomenological time-domain model for eccentric aligned-spin binary black holes. Building upon the accurate quasi-circular IMRPhenomTHM model, IMRPhenomTEHM integrates the eccentric post-Newtonian (PN) dynamics, and introduces eccentric corrections into the waveform multipoles up to 3PN including spin effects. The model incorporates the dominant $(2, \pm 2)$ spherical harmonic mode, as well as the subdominant modes $(2, \pm 1), (3, \pm 3), (4, \pm 4)$ and $(5, \pm 5)$, with the assumption that the binary has circularized by the time of merger. This approach ensures a smooth transition to the non-eccentric limit, and it is shown to provide an accurate quasi-circular limit against the IMRPhenomTHM model. When comparing against 28 public eccentric numerical relativity simulations from the Simulating eXtreme Spacetimes catalog, IMRPhenomTEHM achieves lower than 2% unfaithfulness, confirming its accurate description without calibration to numerical relativity eccentric datasets. IMRPhenomTEHM provides a reliable description of the evolution of eccentric black hole binaries with aligned spins and eccentricities lower than $e = 0.4$ at a frequency of 10 Hz, making it suitable for upcoming gravitational wave observing runs. We validate the model's accuracy through parameter estimation studies, recovering injected parameters within 90% credible intervals for three NR eccentric simulations and reanalyzing GW150914 and GW190521, obtaining results consistent with the literature.

6.1 Introduction

After several observation runs, the ground-based gravitational-wave detectors LIGO, Virgo and KAGRA (LVK) [472–474] have identified numerous binary black hole (BBH), binary neutron star (BNS), and black hole-neutron star (BH-NS) events [1–4]. With increasing detector sensitivity, future observations by LVK and upcoming detectors such as the Einstein Telescope (ET) [12], Cosmic Explorer (CE) [13], and space-based detectors like LISA [15, 345] are expected to reveal more source properties of these systems. This will provide valuable insights into strong gravitational fields as well as support studies in gravitational theory, galaxy formation, cosmology, and stringent tests of general relativity [15].

Compact binary mergers are the only source of gravitational waves (GWs) observed by ground-based GW detectors. Their dynamics and associated GWs have been studied extensively, and detecting and analyzing these waves relies on constructing accurate waveform templates. Most inspiraling binaries detected by these ground-based detectors are likely formed through isolated binary evolution [475] and are expected to circularize by the time they enter the detector frequency band [36]. Indeed, most of the GW events detected by the LVK collaboration, as well as external groups [325–330], are consistent with quasi-circular binaries. However, some binaries may retain significant orbital eccentricity if they form via dynamical interactions in dense stellar environments like globular clusters or galactic nuclei [321, 322], or through the Kozai-Lidov mechanism in triple systems [323, 324]. Measuring eccentricity in GW signals can provide crucial insights into the origins and properties of binary systems. Several attempts have been made to search for signatures of eccentricity in these systems [46–55], and as the detector sensitivity increases, the detection of binaries with non-negligible orbital eccentricity is expected to increase. Thus, developing accurate waveform models is essential for understanding the astrophysical origin of the observed GW events.

State-of-the-art gravitational inspiral-merger-ringdown (IMR) waveform models accurately describe BBHs in quasi-circular (QC) orbits, including also the effects of black holes spins. These models are categorized into three main families: the Effective-One-Body (EOB) [240, 241] formalism , including the SEOBNR models [20, 31, 171–176] and TEOBResumS models [21, 32, 177–181]; the NRSurrogate models [28, 182–185], which interpolate between NR datasets; and the IMRPhenom approach [33, 34, 186–191], known for its computational efficiency due to the use of closed-form expressions. For the QC aligned-spins subspace, the previously mentioned models have been calibrated to NR simulations, showing strong agreement in the region of parameter space where NR data is available (see e.g. Ref. [476]). However, in the precessing-spin case the more complex waveform morphology and the larger parameter space pose challenges for each modeling approach. For example, the NRSur7dq4 [184] model is limited in its coverage of mass ratio, spin magnitudes and waveform length. Instead, the state-of-the-art precessing models in the SEOBNR [31] and IMRPhenom [189, 190] families rely on approximations to model precession without NR calibration, which offers broader applicability but at the cost of reduced accuracy. Nonetheless, NR calibrated precessing phenomenological models have recently been developed [294, 310].

Similar challenges exist for eccentric binaries. Publicly available NR eccentric simulations are limited, complicating both the development and validation of eccentric waveform models. However, recent progress has been made in this area. Eccentric

spinning binaries are often characterized using the post-Newtonian (PN) formalism [37–39], with the quasi-Keplerian (QK) parametrization commonly employed to describe their orbital motion [40–42]. Gravitational waveforms for inspiraling eccentric binaries have been developed both for the non-precessing case [175, 477–482] and the most general systems [306, 366, 367, 483, 484].

Assuming circularization before merger, hybrid IMR waveforms have been constructed by combining PN-inspiral waveforms with merger and ringdown signals derived from NR or the EOB formalism, which has become the common method for incorporating eccentricity into quasi-circular IMR waveform models for low eccentricity [346–348]. Within the EOB formalism, significant advancements have been made in this direction [43, 175, 176, 349–357]. Additionally, a pioneering attempt has been made to produce generic IMR waveforms within the TEOB framework [21, 358]. There has also been development within the surrogate family; however, due to the limited number of NR eccentric simulations, the only available surrogate model is restricted to comparable-mass, non-spinning binaries [45]. Outside of these primary model families, other approaches to eccentric waveform modeling have been explored [348, 485–489]. Additionally, Ref. [490] introduced a method to add eccentricity modulations to existing BBH QC models. Similarly, the `gwNRHME` framework enables the conversion of multi-modal quasi-circular waveforms into multi-modal eccentric waveforms given the quadrupolar non-spinning eccentric contribution [491–493].

In this paper, we develop the first time-domain eccentric phenomenological waveform model, IMRPhenomTEHM, which includes the $\{(l,|m|) = (2,2),(2,1),(3,3),(4,4),(5,5)\}$ spherical harmonics multipoles for aligned spins with two eccentric parameters, which is crucial for avoiding biases in parameter estimation [54, 392]. The model is based on the quasi-circular IMRPhenomTHM model [34, 191] and incorporates eccentric 3PN corrections in the non-spinning terms [37, 38], and up to 3PN spin-orbit and spin-spin interactions [39]. However, the default model limits spin contributions to 2PN for consistency with the underlying IMRPhenomTHM QC framework. We find that IMRPhenomTEHM maintains the accuracy of the underlying QC model within its expected precision, and shows good agreement with publicly available eccentric NR simulations from the Simulation eXtreme Spacetimes (SXS) collaboration [228].

This paper is structured as follows: In Sec. 6.2, we describe the building blocks of the IMRPhenomTEHM model. We first review the underlying aligned spin model IMRPhenomTHM in Sec. 6.2.2. Then we summarise the main eccentric PN expressions used in this project and outline the main modifications done to include eccentric corrections to both the frequency and the amplitude of the modes. We assess the accuracy and performance of the model in Sec. 6.3 by assessing its accuracy in the quasi-circular limit, and comparing it against 28 public eccentric NR waveforms from the SXS waveform catalogue and two other eccentric IMR models, SEOBNRv5EHM and TEOBResumS-Dalí. To assess the robustness of the model, in Sec. 6.3.4 we compute mismatches against SEOBNRv5EHM, the most accurate eccentric model currently available. In Sec. 6.3.5, we evaluate the computational efficiency of IMRPhenomTEHM by benchmarking its performance against the other eccentric waveform models used in this work. In Sec. 6.4 we demonstrate the model's applicability in parameter estimation (PE) studies by analyzing eccentric NR injections from the SXS catalog and reanalyzing two real GW events, GW150914 and GW190521. In Sec. 6.5, we summarise our main conclusions and discuss future work.

Throughout this paper, component masses are denoted by m_i. We define the mass ratio $q = m_1/m_2 \geq 1$, and the symmetric mass ratio $\eta = m_1 m_2/(m_1 + m_2)^2$. The total mass is denoted by $M = m_1 + m_2$ and serves as a scale parameter. The z-component of the dimensionless spin magnitudes are denoted $\chi_i = S_i^z/m_i^2$.

6.2 Model construction

In Sec. 6.2.1 we provide a brief outline of the new IMRPhenomTEHM model. We provide an overview of the underlying quasi-circular model in Sec. 6.2.2, while in Sec. 6.2.3 we provide a detailed description of the procedure to include eccentric PN corrections in the model.

6.2.1 Summary of the IMRPhenomTEHM model

The GW strain can be described by a complex scalar h of spin-weight -2, corresponding to two independent polarizations, (h_+) and $(h_\times)$. As is common practice, we decompose the strain using spin-weighted spherical harmonics (SWSH):

$$h(d_L, t, \iota, \varphi; \Sigma) = h_+ - i h_\times = \frac{1}{d_L} \sum_{l,m} h_{lm}(t; \Sigma)\, {}_{-2}Y_{lm}(\iota, \varphi). \tag{6.2.1}$$

Here, the modes $h_{lm}(t; \Sigma)$ reflect the time dependence and intrinsic physical properties of the source, d_L is the luminosity distance, Σ denotes the intrinsic parameters of the binary, and the SWSH basis functions ${}_{-2}Y_{lm}(\iota, \varphi)$ capture the angular dependence on the celestial sphere in the source frame.

This work focuses on eccentric spinning BBH systems, where the spins are aligned or anti-aligned with the orbital angular momentum direction, which remains preserved. The intrinsic degrees of freedom are then $\Sigma = \{m_1, m_2, \chi_1, \chi_2, e_{\rm ref}, l_{\rm ref}\}$, where m_1 and m_2 are the component masses and $\chi_{\{1,2\}} = (\mathbf{S}_{\{1,2\}}/m^2_{\{1,2\}}) \cdot \hat{\mathbf{L}}$ are the dimensionless spin components in the direction of the orbital angular momentum $\hat{\mathbf{L}}$. In our model, the elliptical orbit is defined in terms of the orbit-averaged orbital eccentricity $e_{\rm ref}$ and mean anomaly $l_{\rm ref}$ at a particular orbit-averaged frequency of the $(2, 2)$ mode $f_{\rm ref}$ (which can be related to a reference time $t_{\rm ref}$.

Each mode h_{lm} is a complex function that can be decomposed into an amplitude H_{lm} and a phase ϕ_{lm} as

$$h_{lm} = H_{lm} e^{-i\phi_{lm}} \approx H_{lm} e^{-im\phi}, \tag{6.2.2}$$

with ϕ being the orbital phase. Both the IMRPhenomTEHM and IMRPhenomTHM models construct the $m > 0$ modes phenomenologically, while the $m < 0$ modes are computed using the symmetry relation

$$h_{lm} = (-1)^l h^*_{l,-m}, \tag{6.2.3}$$

which holds due to the preservation of the orbital plane for non-precessing systems, where $*$ denotes the complex conjugate.

The IMRPhenomTEHM model is constructed by adding the eccentric post-Newtonian corrections detailed in Sec. 6.2.3 to both the amplitude and frequency (and hence phase)

of the IMRPhenomTHM modes, described in Sec. 6.2.2. The corrections, which only impact the inspiral phase of the non-eccentric model, are calculated using higher-order PN expansions of the quadrupole formula. These modes are usually provided in the literature in terms of the mean anomaly l (and hence $\phi(l)$), which leads to a dependency on the arbitrary gauge constant b, which features below in Eq. (6.2.6). A commonly used approach to eliminate this dependence is to redefine the phase following Refs. [494–498] for circular orbits and generalized for eccentric orbits in [499]. This approach can be understood as a redefinition of the mean anomaly l such that

$$\xi = l - \frac{3G\mathcal{M}}{c^3} n \log\left(\frac{x}{x'_0}\right), \tag{6.2.4}$$

where n is the radial angular frequency, and x is an orbital parameter defined as

$$x = \left(\frac{GM\omega}{c^3}\right)^{2/3}, \tag{6.2.5}$$

$\mathcal{M} = M(1 - \eta x/2) + \mathcal{O}(x^2)$ is the ADM mass corresponding to initial data with orbital parameter x, and x'_0 is given by

$$x'_0 = \left[\frac{e^{11/12-\gamma_E}}{4b}\right]^{2/3}, \tag{6.2.6}$$

where γ_E denotes Euler's constant. This results in a new orbital phase that depends on the redefined mean anomaly ξ as

$$\psi = \phi - W(l) + W(\xi) - \frac{3G\mathcal{M}}{c^3}\omega \ln\left(\frac{x}{x'_0}\right) \tag{6.2.7}$$

$$= \lambda_l - \frac{3G\mathcal{M}}{c^3}\omega \ln\left(\frac{x}{x'_0}\right) + W(\xi) \tag{6.2.8}$$

$$= \lambda_\xi + W(\xi), \tag{6.2.9}$$

where λ is the orbit averaged orbital phase and W is the oscillatory phase contribution. Note that for the non-eccentric case, W vanishes and λ is directly the orbital phase. In terms of ξ, the gauge dependency disappears, and from now one we always refer to the redefined modes h^ξ_{lm} (and amplitudes H^ξ_{lm} and phase $\psi(\xi)$), removing ξ to simplify notation:

$$h^{\rm PN}_{lm} = \frac{8GM\eta}{c^2 R} x \sqrt{\frac{\pi}{5}} H_{lm} e^{-im\psi} = \kappa\ x\ H_{lm} e^{-im\psi}, \tag{6.2.10}$$

where $\kappa = \frac{8GM\eta}{c^2R}\sqrt{\frac{\pi}{5}}$. Since we are only interested in adding the eccentric PN contribution to the IMRPhenomTHM inspiral, this leads to

$$h^{\text{insp ecc}}_{lm} = h^{\rm PN}_{lm} - h^{{\rm PN},e=0}_{lm} = \kappa \left[x H_{lm} - x^{e=0} H^{e=0}_{lm}\right] e^{-im\psi}. \tag{6.2.11}$$

The complete IMRPhenomTEHM inspiral is then obtained by substituting the phase ϕ in Eq. (6.2.11) according to Eq. (6.2.9), adding the IMRPhenomTHM inspiral as the non-eccentric contribution:

$$\begin{aligned} h^{\text{insp TEHM}}_{lm} &= h^{\text{insp THM}}_{lm} + h^{\text{insp ecc}}_{lm} = \\ &\kappa \left(x \tilde{H}^{\rm THM}_{lm} + x H_{lm} - x^{e=0} H^{e=0}_{lm}\right) e^{-im\lambda_\xi} e^{-imW}. \end{aligned} \tag{6.2.12}$$

Both W and $H_{lm}^{\rm ecc}$ vanish after the inspiral regime as they are proportional to the orbital eccentricity, and the IMRPhenomTEHM model assumes that the orbit circularizes. As a consequence, IMRPhenomTEHM falls back to IMRPhenomTHM for the merger/ringdown phase. This allows us to write the complete IMRPhenomTEHM modes as

$$h_{lm}^{\rm TEHM} = \left(\tilde{h}_{lm}^{\rm THM} + \frac{8GM\eta}{c^2 R}\sqrt{\frac{\pi}{5}}\left[xH_{lm} - x^{e=0}H_{lm}^{e=0}\right]e^{-im\lambda_\xi}\right)e^{-imW}, \tag{6.2.13}$$

where the $\{\tilde{h}/\tilde{H}\}^{\rm THM}$ denote the IMRPhenomTHM modes with an orbital frequency modified by the eccentric corrections.

6.2.2 Quasi-circular baseline: IMRPhenomTHM

The IMRPhenomTHM model [34] is the extension of the time-domain IMR phenomenological model IMRPhenomT [191] for GWs from quasi-circular BBHs which includes the subdominant multipoles $(l, m) = \{(2, \pm1), (3, \pm3), (4, \pm4), (5, \pm5)\}$. It is calibrated to NR simulations, specifically SEOB-NR hybrids, up to mass ratio 18 and to numerical solutions of the Teukolsky equation for the extreme mass ratio limit, which leads to an accurate and fast time-domain model, which has been used as a standard tool for GW astronomy [137, 476, 500].

The waveform model provides analytical expressions for amplitude and phase as a function of time, which are divided in three distinct regions:

1. *Inspiral region*: based on PN expansions augmented with higher order terms calibrated to NR information.
2. *Plunge-Merger region*: PN expansions break down and the model is directly calibrated to NR in this regime using a phenomenological ansatz.
3. *Ringdown region*: phenomenological ansatz informed by ringdown and damping frequencies from perturbation theory.

The boundary between the inspiral and merger regions is chosen depending on the mode and it varies for the amplitude and phase/frequency. The boundary between the merger and ringdown regions for both the frequency and amplitude models is set at the peak amplitude for each mode. The peak amplitude of the $(2, 2)$ mode, $H_{22}(t)$, is placed at $t = 0$ by convention. In the following, we provide an overview on its inspiral construction. We focus on this region because the eccentric model only incorporates eccentric corrections up to the merger of the QC waveform.

6.2.2.1 Inspiral construction

When the binary objects are far apart, the weak field and low velocity conditions allow the use of the PN framework to accurately describe the binary dynamics [501]. This involves numerical integration of the PN equations of motion, or alternatively using the adiabatic approximation, one arrives at the balance equations (see e.g. Ref. [232]):

$$\frac{d\phi}{dt} - \frac{v^3}{M} = 0, \tag{6.2.14}$$

$$\frac{dv}{dt} + \frac{F(v)}{ME'(v)} = 0, \tag{6.2.15}$$

where $\omega = d\phi/dt$ is the orbital frequency, $v = \omega^{1/3}$, $F(v)$ is the GW luminosity, and $E(v)$ is the system's binding energy. IMRPhenomTHM relies on TaylorT3 [232, 502], which provides an explicit expression for the orbital phase as a function of time:

$$\phi^{\rm T3}_{n/2}(t) = \phi_{\rm ref} + \phi_N(t) \sum_{k=0}^{n/2} \hat{\phi}_k \theta^k, \tag{6.2.16}$$

$$\omega^{\rm T3}_{n/2}(t) = \omega_N(t) \sum_{k=0}^{n/2} \hat{\omega}_k \theta^k, \tag{6.2.17}$$

where $\theta(t) = \left[\frac{\eta(t_0-t)}{5M}\right]^{-1/8}$, $\omega_N = \theta^3/8$, and $n/2$ corresponds to the PN order. Although TaylorT3 provides closed-form expressions, it is less accurate than other approximants at higher frequencies, see e.g. [232], and becomes singular at $t = t_0$, which depends on the intrinsic parameters of the source and the PN order employed. To improve the description of the inspiral phase, the 3.5 PN ($n = 7$ in Eq. (6.2.17)) TaylorT3 ansatz is expanded by adding 5 extra pseudo-PN terms, which are calibrated to NR simulations.Furthermore we set the merger time at $t_0 = 0$. This way one ensures an accurate description of the frequency and the phase until at least the minimum energy circular orbit time (MECO) [463]. The model then assumes

$$\omega^{\rm insp}_{22} = 2\omega = 2\left(\omega^{\rm T3}_{3.5}(t) + \omega_N(t) \sum_{k=8}^{13} \hat{c}_k \theta^k\right). \tag{6.2.18}$$

The frequency of the higher modes (HMs), $\omega_{lm} = \dot{\phi}_{lm}$, is obtained by rescaling the frequency and phase of the $(2,2)$-mode such that $\omega_{lm} = \frac{m}{2}\omega_{22}$ and $\phi_{lm} = \frac{m}{2}\phi_{22}$.

The amplitude of the emitted radiation during the inspiral phase can also be calculated using higher-order PN expansions of the quadrupole formula. For non-spinning BBHs, the model uses 3PN corrections from [503] and the 3.5PN from [504]. For aligned-spin systems, 1.5PN [505] and 2PN [506] expansions are employed. These amplitude corrections also include three unknown higher-order PN terms, which are calibrated to NR to improve accuracy up to the MECO time:

$$H^{\rm insp}_{lm}(t) = 2\eta\sqrt{\frac{16\pi}{5}}x\left(\sum_{k=0}^{7} \hat{h}^k_{lm} x^{k/2} + \sum_{k=8}^{10} \hat{d}^k_{lm} x^{k/2}\right). \tag{6.2.19}$$

Here, $\hat{d}_k$ are the unknown coefficients determined by matching the amplitude at NR-calibrated values. The modes are then given by

$$h^{\rm insp}_{lm}(t) = H^{\rm insp}_{lm}(t) \exp\left[-i\left(\frac{m}{2}\phi^{\rm insp}_{22}(t) - \Delta\phi_{lm}\right)\right], \tag{6.2.20}$$

where $\Delta\phi_{lm}$ is a fixed rotation performed such that the dominant contribution is given in the real part of each mode (see Eq. (13) in Ref. [34]).

6.2.3 Eccentric post-Newtonian corrections

We incorporate PN eccentric corrections into the IMRPhenomTHM model using the quasi-Keplerian parametrization [40–42] and the covariant spin-supplementary condition [507,

508]. The IMRPhenomTEHM model includes the full 3PN orbit-averaged dynamics, accounting for both non-spinning and spinning corrections [39], implemented in both modified harmonic (MH) PN (referred to as PN) and EOB coordinates. Additionally, we modify the waveform modes of IMRPhenomTHM by incorporating non-spinning and nonprecessing-spin eccentric corrections up to 3PN order [38, 39], formulated in MH coordinates.

We evolve the orbital elements using the secular evolution equations driven by radiation reaction derived by connecting the balance equations with the orbit-averaged energy and angular momentum fluxes [39]. Specifically, the orbital elements consist of the temporal eccentricity $e_t \equiv e$, the orbital parameter x (Eq. (6.2.5)), the mean anomaly l, and the orbit-averaged orbital phase $\lambda = \int \overline{\omega}\, \mathrm{d}t$, where the upper line indicates orbit-averaging. We incorporate the 3PN non-spinning contributions from Refs. [37, 38] in modified-harmonic coordinates, as well as the 3PN spin contributions from [39]. As detailed in Sec. 6.2.2, the IMRPhenomTHM model uses the TaylorT3 approximation to derive a closed-form expression for the orbital phase and frequency, which, by construction, corresponds to half of the $(2, 2)$-mode phase and frequency (see Eq. (6.2.18)). Ideally, we would construct the new IMRPhenomTEHM model by extending the functional form of the TaylorT3 approximant to include eccentric terms of sufficient accuracy. However, existing literature only provides a PN expansion applicable to low-eccentricity systems [482, 509], limiting the applicability of the model. Additionally, the eccentric TaylorT3 approximant has been shown to exhibit a non-monotonic frequency evolution, decreasing before the innermost stable circular orbit (ISCO), leading to a recommendation against its practical use [509].

The choice of coordinates in the secular evolution equations can substantially affect the evolution of the binary. To evaluate this impact, apart from working with PN expressions in modified-harmonic coordinates, we also incorporate the use of EOB coordinates. Comparisons between the two gauges are presented throughout the paper, with a more detailed discussion provided in the next section, where we detail how to solve the orbit-averaged secular evolution equations and obtain the modified eccentric orbital phase and frequency corrections to the IMRPhenomTHM baseline. Finally, Sec. 6.2.3.2 briefly introduces the PN expressions used for the modes' amplitudes, concluding the construction of the IMRPhenomTEHM modes.

6.2.3.1 Orbital secular evolution

To overcome the limitations of the TaylorT3 approximant discussed earlier, we proceed with a different approach to incorporate eccentric information to the IMRPhenomTEHM evolution:

1. Compute the quasi-circular $(2, 2)$ mode frequency ω_{22} from IMRPhenomTHM, and the time derivative $\dot{x}^{\mathrm{THM}} = \frac{1}{3}\left(\omega_{22}/2\right)^{-1/3} \dot{\omega}_{22}$.

2. Interpolate $\dot{x}^{\mathrm{THM}}$ as a function of the orbital frequency parameter x, $\dot{x}^{\mathrm{THM}}(x)$, so that the time dependency is removed. This is essential since the correspondence between frequency and time is different in the quasi-circular and eccentric cases.

3. Evolve the secular evolution equations $\{\dot{x}, \dot{e}, \dot{l}, \dot{\lambda}\}$ using $\dot{x}^{\mathrm{THM}}(x)$ as the quasi-circular contribution of the secular evolution equation of frequency parameter $\dot{x}$. This implies removing all the non-eccentric terms from the PN expansion for $\dot{x}$, which are

included in $\dot{x}^{\rm THM}$, and only keeping the eccentric terms of the secular equation, i.e., $\delta x_{e\neq0} = x^{\rm PN} - x^{\rm PN}_{e\neq0}$.

The system of ordinary differential equations (ODEs) can be schematically expressed in terms of the PN orders included as

$$\dot{x} = \dot{x}^{\rm THM} + \delta\dot{x}_{e\neq0}, \tag{6.2.21}$$

$$\begin{aligned}\delta\dot{x}_{e\neq0} = {}& \delta\dot{x}^{\rm Newt}_{e\neq0} + \delta\dot{x}^{\rm 1PN}_{e\neq0} + \delta\dot{x}^{\rm 1.5PN}_{e\neq0} + \delta\dot{x}^{\rm 2PN}_{e\neq0} + \delta\dot{x}^{\rm 2.5PN,tail}_{e\neq0} \\ & + \delta\dot{x}^{\rm 2.5PN,SS}_{e\neq0} + \delta\dot{x}^{\rm 3PN}_{e\neq0} + \delta\dot{x}^{\rm 3PN,SS}_{e\neq0} + \delta\dot{x}^{\rm 3PN,tail}_{e\neq0},\end{aligned} \tag{6.2.22}$$

$$\begin{aligned}\dot{e} = {}& \dot{e}^{\rm Newt} + \dot{e}^{\rm 1PN} + \dot{e}^{\rm 1.5PN} + \dot{e}^{\rm 2PN} + \dot{e}^{\rm 2.5PN}_{\rm SS} + \dot{e}^{\rm 3PN}_{\rm SS} \\ & + \dot{e}^{\rm 3PN}_{\rm inst} + \dot{e}^{\rm 3PN}_{\rm tail},\end{aligned} \tag{6.2.23}$$

$$\dot{l} = l^{\rm Newt} + l^{\rm 1PN} + l^{\rm 1.5PN} + l^{\rm 2PN}_{\rm inst} + l^{\rm 2.5PN}_{\rm tail} + l^{\rm 3PN}_{\rm SS} + l^{\rm 3PN}_{\rm inst}, \tag{6.2.24}$$

$$\dot{\lambda} = x^{3/2}. \tag{6.2.25}$$

The secular equations include 3PN non-spinning and spinning contributions, and we consider two different coordinates. Specifically, we use the expansions for $\dot{x}$, $\dot{e}$ and $\dot{l}$ in modified-harmonic (MH) PN coordinates from Refs. [37–39], as well as $\dot{e}$ and $\dot{x}$ in EOB coordinates, which were derived recently in Ref. [510] for the development of the state-of-the-art eccentric EOB model, SEOBNRv5EHM [21]. Since x is an almost gauge-independent quantity, we transform the eccentricity evolved in EOB coordinates, $e^{\rm EOB}$, into its counterpart in MH PN coordinates, $e^{\rm PN}$, using the relation provided in Ref. [510]. Once $e^{\rm PN}$ is obtained, we also recompute the mean anomaly accordingly.

One of the most interesting results of this work is the observation that different gauges can lead to significantly different system evolutions. This is because the eccentricity is a gauge-dependent quantity, meaning that certain gauges may be more suitable for aligning with NR data. While the GW signal itself is gauge-independent, differences in how eccentricity is defined and evolved (together with the coupled frequency) can affect the accuracy of the binary's trajectory and its agreement with NR waveforms. Gauge-invariant approaches to defining eccentricity have been proposed based on waveform modulations [385, 389] and catastrophe theory [511]. Throughout the paper, we use the waveform-based eccentricity definition of Ref. [385], $e^{\rm GW}$, as implemented in the `gw_eccentricity` package [386]. We also explore the two implemented eccentricity gauges and discuss their respective implications. Based on its better agreement with NR eccentric simulations and its closer correspondence to $e^{\rm GW}$, we adopt the EOB secular evolution equations as the default choice for modeling the eccentric dynamics. This is the assumption for all results unless otherwise specified.

The initial conditions for the evolution of the dynamics are the mean anomaly $l_{\rm ref}$ and the eccentricity $e_{\rm ref}$ given at a concrete reference orbit-averaged frequency of the $(2,2)$-mode, $f_{\rm ref}$, which can be translated into $x_{\rm ref}$. Following the LALSuite [111] conventions specified in Ref. [142], we set $\lambda_{\rm ref} = 0$.

Solving this set of coupled differential equations represents one of the main computational bottlenecks of the model, and the key to improving efficiency lies in the interpolation of $\dot{x}^{\rm THM}(x)$. An effective approach is to perform the interpolation on a θ-grid, as defined in Eqs (6.2.17). This parameter offers the advantage of creating a sparse grid at low frequencies, where the frequency curve evolves slowly, while providing higher

resolution at high frequencies - particularly near the merger phase. To solve the system of equations, we use the "DOP853" method, an 8th-order Runge-Kutta solver, implemented within the `solve_ivp` function in the SciPy Python package [512]. We set the absolute and relative tolerances to 10^{-12} for this work, but can be changed as suited depending on the particular application. These parameters were selected to balance computational cost with accuracy, specifically ensuring the accurate recovery of the frequency from the quasi-circular model. More details on this are given in Sec. 6.3.1.

Since the IMRPhenomTEHM model assumes circularization by the time of merger, the stopping conditions of the ODEs solver are set when the eccentricity vanishes or when the frequency reaches the IMRPhenomTHM peak frequency. We then taper the eccentricity at $t = -20M$, ensuring that all corrections reduce to zero at merger, thus recovering the IMRPhenomTHM merger/ringdown phase.

The model also supports specifying a minimum frequency $f_{\rm min}$ lower than the reference frequency $f_{\rm ref}$. In such cases, we start from the reference values and solve the system of equations backwards until $x(t)$ reaches $x_{\rm min}$. This feature provides significant flexibility, particularly for parameter estimation studies, as demonstrated in Sec. 6.4.2. A key benefit is ensuring sufficiently long waveforms, preventing failures in the integration of eccentric dynamics. Through testing, we established that the initial separation, computed at the lowest PN order (which corresponds to the QC separation at initial time, $r_{\rm min} \approx 1/x_{\rm min}$) must always be greater than $7M$. This threshold guarantees enough integration points, even for the highest eccentricities within the model's validity range, to avoid failures. Currently, the model does not support $f_{\rm ref} < f_{\rm min}$ as there is no way to ensure $r_{\rm ref} > 7M$ without internally modifying the reference frequency. Another advantage of this feature is enabling the addition of extra cycles to the time-domain waveform. This prevents tapering effects in Fourier transforms from removing relevant information within the frequency range of interest. By default, we extend the underlying QC waveform by three cycles when computing the Fourier transform.

Once the secular equations are solved, the orbit-averaged frequency and phase of the $(2,2)$ IMRPhenomTEHM mode are obtained directly as $\bar{\omega}_{22}^{\rm TEHM} = 2x^{3/2}$ and $\bar{\phi}_{22}^{\rm TEHM} = 2\lambda$ up to the peak frequency of (2,2)-mode of the IMRPhenomTHM model. It is important to remark two main features involved in the calculation of the orbit-average $(2,2)$-mode phase. First, the use of the quasi-circular IMRPhenomTHM (2,2)-mode frequency to evolve the PN/EOB secular evolution equations, which implies the use of NR-calibrated information in the $e = 0$ limit for the evolution of the x parameter. Second, a consequence of the use of the frequency of the IMRPhenomTHM model is related to the fact that the $(2,2)$-mode frequency is a wave quantity introduced in the source dynamics. This implies an inconsistency in the usual redefinition of the orbital phase to take into account tail effects and remove gauge ambiguities (see Refs. [38, 39, 499]). In order to recover the quasi-circular phase, we do not perform the phase redefinition as described in Eq. (6.2.4). Instead, we assume that, due to the inclusion of NR information, the resulting l (and hence ϕ) can be understood as ξ and ψ. We further investigate the implications of this phase redefinition in Sec. 6.3 by comparing against NR waveforms. To maintain consistency in the binary evolution when applying the phase redefinition, the input mean anomaly for the model will be set to $\xi_{\rm ref}$. Since we solve the evolution of $l(t)$ in Eqs. (6.2.21), we first obtain $l_{\rm ref}$ which is derived from $\xi_{\rm ref}$. We then obtain $\xi(l)$ and λ_ξ, as given in Eqs. (6.2.4) and (6.2.9).

The construction of the higher modes follows a process similar to that of IMRPhenomTHM: the inspiral region is constructed by assuming that $\omega_{lm} = \frac{m}{2}\omega_{22}$, and hence $\phi_{lm} = \frac{m}{2}\phi_{22}$, while the intermediate and merger/ringdown regions are built in the same manner as IMRPhenomTHM, see Sec. II.B.3 in Ref [34] for details. The orbit-averaged frequency and phase also enter in the non-eccentric contribution of the model, which is denoted as $\{\tilde{h}/\tilde{H}\}^{\rm THM}$ in Eq. (6.2.13). This approach allows us to recover the IMRPhenomTHM frequency in the limit $e \to 0$, since all the PN terms in Eq. (6.2.21) vanish and we are only left with $\dot{x}^{\rm THM}(x)$.

Finally, as shown in Eq. (6.2.13), we add the eccentric oscillatory contribution $W(\xi)$ to the modes' phases. This variable includes all 3PN order instantaneous non-spinning, spin-orbit and spin-spin contributions for eccentric binaries eccentricity expanded up to $\mathcal{O}(e^{12})$ [513].

6.2.3.2 Mode amplitudes

Once the evolution of the orbital quantities is completed, we can compute the amplitudes of the IMRPhenomTEHM modes following Eq. (6.2.13). The eccentric contributions are decoupled from the IMRPhenomTHM modes, which have been modified by introducing the new orbit-averaged eccentric orbital frequency and phase, impacting both the amplitudes and phases of all modes.

Hence, we first compute the modified IMRPhenomTHM modes, denoted as $\tilde{h}^{\rm THM}_{lm}$ in Eq. (6.2.13), which depend on $x(t)$, computed as explained in Sec. 6.2.3.1. Then, we evaluate the 3PN expressions for the modes' amplitudes $H^{\rm ecc}_{lm}(x(t), e(t), \xi(t))$ up to merger. As explained in Sec. 6.2.1 these eccentric amplitudes vanish by the time of the merger, so the peak and ringdown phases of IMRPhenomTEHM revert to IMRPhenomTHM.

We incorporate the next-to-leading order instantaneous non-spinning, spin-orbit and spin-spin contributions to the waveform modes and hereditary (tail and memory) contributions to the modes for eccentric orbits, using the 3PN non-spinning terms from Ref. [38] and the 3PN spinning contributions from Ref. [39]. As mentioned in Sec. 6.2.2, the underlying quasi-circular IMRPhenomTHM model includes only up to 2PN order for the spinning contributions. Hence, we set the same PN order for the IMRPhenomTEHM model for consistency. In Sec. 6.3.2 we investigate the effect of incorporating these terms. The IMRPhenomTEHM model uses eccentricity-expanded expressions for both instantaneous and tail contributions up to $\mathcal{O}(e^6)$ for all the available modes, $\{(2,|2|),(2,|1|),(3,|3|),(4,|4|),(5,|5|)\}$, since a non-expanded in eccentricity expression for the tail terms is not available. For the $(2,2)$ modes, we derived expansions up to $\mathcal{O}(e^{12})$ [513]. Since it does not provide a significant improvement in accuracy and only increases computational cost, this option is not set as the default in the model. We leave for future work the use of expressions not expanded in eccentricity for the waveform multipoles leveraging for instance recently developed re-summation techniques for the tail contributions [510].

6.3 Model validation

In this section, we evaluate the validity of the model across the BBH eccentric nonprecessing-spin parameter space. For these systems, the GW signal depends on six intrinsic parameters:

the mass ratio q, the total mass M, the spin components in the direction of the orbital angular momentum χ_1 and χ_2, and two parameters describing the ellipse, which we choose to be the orbital eccentricity e and the mean anomaly l at a reference time. The intrinsic parameters are denoted as Π.

To describe the source in relation to a ground-based GW detector one needs seven extrinsic parameters: the angular position of the line of sight in the source frame (ι, φ), the polarization angle Ψ, the luminosity distance of the source d_L, the sky location of the source in the detector frame (α, δ) and the coalescence time t_c. The signal can then be expressed using the antenna-pattern functions $F_{+/\times}$ [94], which account for the detector's response to the incoming waveform - described in terms of the polarizations in Eq. (6.2.1) - as

$$h(t) = F_+(\alpha, \delta, \Psi) h_+(\iota, \varphi, d_L, \Pi, t_c; t) + \tag{6.3.1}$$
$$F_\times(\alpha, \delta, \Psi) h_\times(\iota, \varphi, d_L, \Pi, t_c; t). \tag{6.3.2}$$

Given two waveforms, one can define the noise-weighted inner product or overlap as [514, 515]

$$(h_1(t)|h_2(t)) = 4\,\mathrm{Re} \int_{f_{\min}}^{f_{\max}} \mathrm{d}f \frac{\tilde{h}_1(f)\tilde{h}_2^*(f)}{S_n(f)}, \tag{6.3.3}$$

where the tilde denotes Fourier transform, the star complex conjugate, and $S_n(f)$ is the one-sided power-spectral density (PSD) of the detector's noise. We use the zero-detuned high power Advanced LIGO PSD, representing the expected sensitivity of the fifth observing run (O5) [516], with frequency limits set to $f_{\min} = 10$Hz and $f_{\max} = 2048$Hz. For NR waveforms where the orbit-averaged starting frequency of the $(2, 2)$ mode, $\bar{f}_{\rm start}$, exceeds $f_{\min}$, we set $f_{\min} = 1.35\bar{f}_{\rm start}$. This choice is consistent with Refs. [20, 356] and ensures the inclusion of as much of the inspiral phase as possible, where the effects of eccentricity are most pronounced. Given the oscillatory nature of the GW frequency in eccentric signals, we consistently refer to the orbit-averaged frequency $\bar{f}$ if not stated otherwise. To simplify notation, we omit the bar and use f throughout the text, while always referring to the orbit-averaged value.

The *faithfulness* or *match* is defined as the maximization of the normalized overlap over selected parameters. For general aligned-spin QC systems including higher modes, the standard choice of parameters to optimize the template with respect to the signal includes the coalescence time t_c, azimuthal angle φ, and an effective polarization angle κ which depends on the sky location of the source. When considering only the dominant harmonic, the angular dependence of $\mathcal{Y}^{-2}_{2,\pm 2}$ introduces a degeneracy between the inclination and polarization angle [517], and in this case the optimization is performed only over t_c and κ. Eccentric waveforms introduce additional complications due to the gauge-dependent nature of eccentricity in general relativity. In particular, we employ two different gauge choices for the eccentricity in our model, which, as we show later, lead to significantly different definitions of this parameter. Consequently, the signal and the template may be characterized by distinct eccentricity parameters, since both e and l are gauge dependent. The comparisons of eccentric waveforms with different definitions of eccentricity involve computing a mapping to connect them. For instance, Ref. [385] implements a definition of eccentricity based on the waveform which reduces to the Newtonian definition of eccentricity [386], while Ref. [388] introduces an algorithm based on the same definition of eccentricity to map different eccentric waveforms. In our comparisons against NR we adopt

an optimization method to identify the best-matching waveform for a given eccentric NR waveform. This requires optimizing over the mean anomaly and eccentricity at the initial frequency to align both waveforms at merger, following Ref. [20], to mitigate contamination from spurious frequencies. Hence, the *faithfulness* is defined as

$$\mathcal{F}_\Sigma = \max_\Sigma \frac{(h_1(t)|h_2(t))}{\sqrt{|h_1(t)||h_2(t)|}}, \tag{6.3.4}$$

where Σ stands for the set $\Sigma = \{t_c, \varphi, \kappa, e, l, f\}$ in the eccentric case and it reduces to $\Sigma_{\rm QC} = \{t_c, \varphi, \kappa\}$ for the quasi-circular case. In the case of optimizing only over the $(2,2)$ mode, $\Sigma_{22} = \Sigma - \{\kappa\}$. The optimizations are performed numerically using the `dual_annealing` function of the `scipy` [512] python package, except for the polarization κ, which is done analytically as described in [517, 518]. We finally define the mismatch as the deviation of the match from unity $\mathcal{M} = 1 - \mathcal{F}_\Sigma$.

In the following, we will use the mismatch as our metric to assess the accuracy of the IMRPhenomTEHM model across parameter space. Specifically, we first assess in Sec. 6.3.1 the recovery of the QC limit by comparing it to the underlying IMRPhenomTHM model. In Sec. 6.3.2, we compare the model against the 28 publicly available eccentric simulations from the SXS catalog, performing mismatch calculations both for the dominant harmonic and including all available modes. We also compare our results with those obtained with other state-of-the-art eccentric EOB models, SEOBNRv5EHM [20] and TEOBResumS-Dalí [21], using our same optimization procedure. In Sec. 6.3.3, we summarize the different modeling choices introduced in Sec. 6.2 and evaluate their impact on accuracy by comparing them to the same set of NR simulations. In Sec. 6.3.4 we test the model's robustness across parameter space by comparing it to the state-of-the-art SEOBNRv5EHM model. Finally, in Sec. 6.3.5 we provide benchmark comparisons across parameter space with direct comparisons with the SEOBNRv5EHM and TEOBResumS-Dalí models.

6.3.1 Quasi-circular limit

We validate the eccentric aligned-spin model IMRPhenomTEHM in the quasi-circular limit by comparing it to the underlying non-eccentric IMRPhenomTHM model. The IMRPhenomTEHM model is built upon the IMRPhenomTHM framework within the new `phenomxpy` python package [416]. Consequently, the underlying aligned-spin model differs in some aspects from the published LALSuite implementation [34], introducing minor bug fixes. One of the differences involves incorporating analytical derivatives wherever possible to mitigate instabilities associated with numerical differentiation. This enhancement improves the model's stability, particularly at positive effective spin, where minor numerical inaccuracies can lead to larger differences in the values of the NR-calibrated collocation points. However, this cannot be applied to the eccentric model due to the numerical integration of the frequency evolution. As a result, the IMRPhenomTHM and IMRPhenomTEHM models inherently exhibit slight discrepancies, constrained to numerical errors affecting the calculation of the collocation points. Furthermore, the numerical error associated with the integration of the frequency compared to the analytical expressions used in the quasi-circular IMRPhenomTHM model is more significant at lower masses, where the longer waveform duration allows for greater phase accumulation over the binary evolution. In Fig. 6.1 we present mismatch calculations for IMRPhenomTEHM

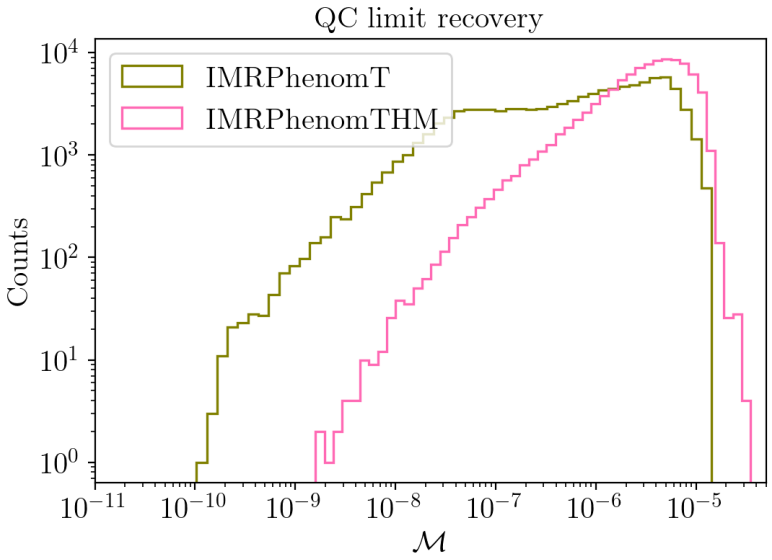

FIGURE 6.1: Mismatch distribution between the IMRPhenomTHM and IMRPhenomTEHM models computed over 10^5 non-eccentric waveforms for the dominant (2,|2|)-modes (green curve) and including higher order modes (pink curve). The configurations are randomly distributed in the IMRPhenomTHM model's validity region: mass ratio $q \in [1, 20]$, total mass $M \in [10, 300]$ $M_\odot$, z-component dimensionless spin vectors $\chi_i \in [-0.995, 0.995]$, azimuthal phase $\varphi \in [0, 2\pi]$ and inclination angle $\iota \in [0, \pi]$.

against IMRPhenomTEHM for the dominant (2,|2|)-modes and including higher order modes across 10^6 cases distributed within the IMRPhenomTHM models' validity region: mass ratio $q \in [1, 20]$, total mass $M \in [10, 300]$ $M_\odot$, z-component dimensionless spin vectors $\chi_i \in [-0.995, 0.995]$, azimuthal phase $\varphi \in [0, 2\pi]$ and inclination angle $\iota \in [0, \pi]$. Both the mismatches for the dominant harmonic and all higher modes remain below 10^{-5}, with some outliers reaching up to $3 \cdot 10^{-5}$ due to the specific construction of the models. Specifically, higher mismatches occur in the positive effective spin region due to the construction of the collocation points in the eccentric model compared to the QC baseline. This is mainly because positive aligned spins slow down the binary evolution, allowing higher frequencies near merger. This results in a steeper frequency slope, which can cause instabilities in the numerical derivatives needed for the collocation points. Additionally, as in the low-mass case, longer evolutions accumulate more numerical integration errors in the orbital frequency. Finally, these effects have a greater impact on mismatches including all modes, as expected. Since they influence the baseline construction, the accumulation of errors increases with the number of modes considered.

These results combined with the accuracy against quasi-circular NR simulations of IMRPhenomTHM (see Fig. 7 in Ref. [34]) demonstrate that the eccentric IMRPhenomTEHM model faithfully recovers the quasi-circular limit with minor discrepancies against the quasi-circular IMRPhenomTHM model due to some small differences in the construction of both models.

6.3.2 Comparison against numerical relativity waveforms

We assess the accuracy of the IMRPhenomTEHM model by computing mismatches against 28 eccentric BBH NR waveforms produced with the SpEC code [218, 228, 519] from

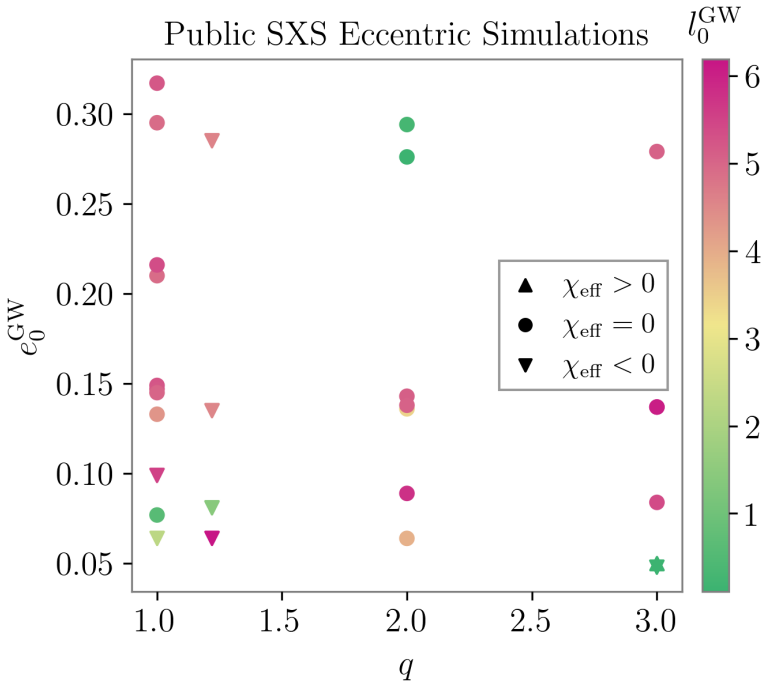

Figure 6.2: Parameter space distribution of the 28 eccentric SXS NR waveforms used in this work, shown as a scatter plot with mass ratio $q = m1/m_2$ on the x-axis, initial eccentricity measured with the `gw_eccentricity` package at the initial orbit-averaged frequency $e_0^{\rm GW}$ on the y-axis, and the dimensionless effective spin $\chi_{\rm eff} = (\chi_1 m_1 + \chi_2 m_2)/M$ indicated by the color scale.

the SXS Collaboration. In Figure 6.2, we present the distribution of these simulations across the parameter space. As shown, the NR available waveforms correspond to relatively low initial eccentricities, where the initial eccentricity is computed as the initial orbit-averaged frequency using the `gw_eccentricity` package [385], and are primarily concentrated in the non-spinning regime.

Results for the mismatches against all NR simulations are presented in Fig. 6.3. The mismatches are computed over total masses $M \in [20, 300]\ M_\odot$ using the faithfulness function defined in Eq. (6.3.4). Specifically, for the first three columns we compute the $\mathcal{M}_{22}$ mismatches by optimizing over e, l, $Mf_{\rm ref}$, φ, and t_c at the lowest mass, 20 $M_\odot$. For higher masses, we retain the optimized e, l, and $Mf_{\rm ref}$, while optimizing only over φ and t_c. For these mismatches, we only include the $(2, |2|)$ modes of the NR simulations. Each column corresponds to a different model: SEOBNRv5EHM [20], TEOBResumS-Dalí [21] and IMRPhenomTEHM, respectively. In the last column, higher order modes in NR up to $l \leq 8$ and all the available modes in the IMRPhenomTEHM model are included. We follow the same procedure as for the (2,2)-mode mismatches, but additionally optimize the polarization phase for each mass. Optimizing over higher modes for the EOB models is computationally expensive; thus, Refs. [20, 356] adopt the same parameters optimized for the $(2, 2)$-mode. To ensure a fair comparison, we limit our mismatches to the (2,2)-mode for the EOB models, as including higher modes would not be consistent across all models due to the high computational cost of optimizing them for the EOB models, which we can afford for IMRPhenomTEHM.

The results from Fig. 6.3 show that the IMRPhenomTEHM model produces

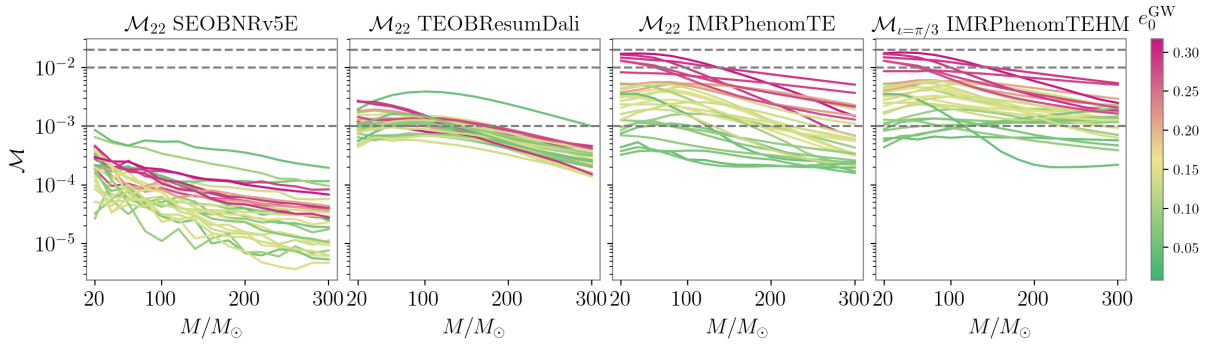

FIGURE 6.3: Mismatches for the 28 available SXS eccentric simulations shown in Fig. 6.2, comparing against different eccentric aligned-spin models. The first three columns show the $(2,2)$-mode mismatches, $\mathcal{M}_{22}$, for the SEOBNRv5EHM, TEOBResumS-Dalí and IMRPhenomTEHM models, respectively, while the fourth column presents the mismatches including all available higher modes $\mathcal{M}$ in IMRPhenomTEHM for an inclination of $\pi/3$. Line colors indicate the initial eccentricity of the NR simulations computed with the `gw_eccentricity` package, $e_{\rm GW}$, as shown in the color bar legend. All mismatches are calculated over total masses $M \in [20, 300]\ M_\odot$.

unfaithfulness below 2% when compared against eccentric NR simulations. The cases with unfaithfulness above 1% correspond to NR simulations with initial eccentricity $e_0 \sim 0.3$, where we expect that a degradation in the accuracy of the model due to the eccentricity expanded expressions used to construct the waveform, see Sec. 6.2. Additionally, when comparing the (2,|2|)-modes against NR we also compute the mismatches for the SEOBNRv5EHM and TEOBResumS-Dalí models, which show a lower unfaithfulness and the results are consistent with the ones presented in Refs. [20, 352]. Finally, IMRPhenomTEHM accurately captures the physics of higher modes, as evidenced by the fact that $\mathcal{M}_{22}$ mismatches are comparable to the full $\mathcal{M}$ mismatches at a fixed inclination of $\iota = \pi/3$. We do not include HM mismatches for the SEOBNRv5EHM and TEOBResumS-Dalí models due to their computational cost. For a reference, results for HM mismatches for these models can be found in Ref. [20], where they adopt the same parameters optimized for the $(2,2)$-mode. Unlike for those models, the degradation due to HMs is not significant for the IMRPhenomTEHM model. Due to the limited coverage of the parameter space by the available NR eccentric simulations, and to further investigate the model's performance across a broader parameter space, we extend our analysis in the next section by computing mismatches against the SEOBNRv5EHM model.

The accuracy of the higher order modes is further illustrated in Fig. 6.4, where we compare the real part of the available IMRPhenomTEHM modes for the SXS:BBH:1370 simulation against the best-fitting IMRPhenomTEHM waveform. The intrinsic parameters of this simulation correspond to $q = 2$, $\chi_{\rm eff} = 0$, $e_0^{\rm GW} = 0.294$, and $l_0^{\rm GW} = 0.28$, while the optimal values for IMRPhenomTEHM are $e_{\rm ref} = 0.251$ and $l_{\rm ref} = 3.68$ at $Mf_{\rm ref} = 0.0067$. The two waveforms show remarkable agreement, even for this case, which corresponds to one of the highest mismatches of the dataset, $\mathcal{M} = 1.43\%$.

6.3.3 Optional model parameters and choice of default settings

In the previous section, we presented the mismatches between the default model and the publicly available eccentric NR simulations across a range of masses. In this section, we

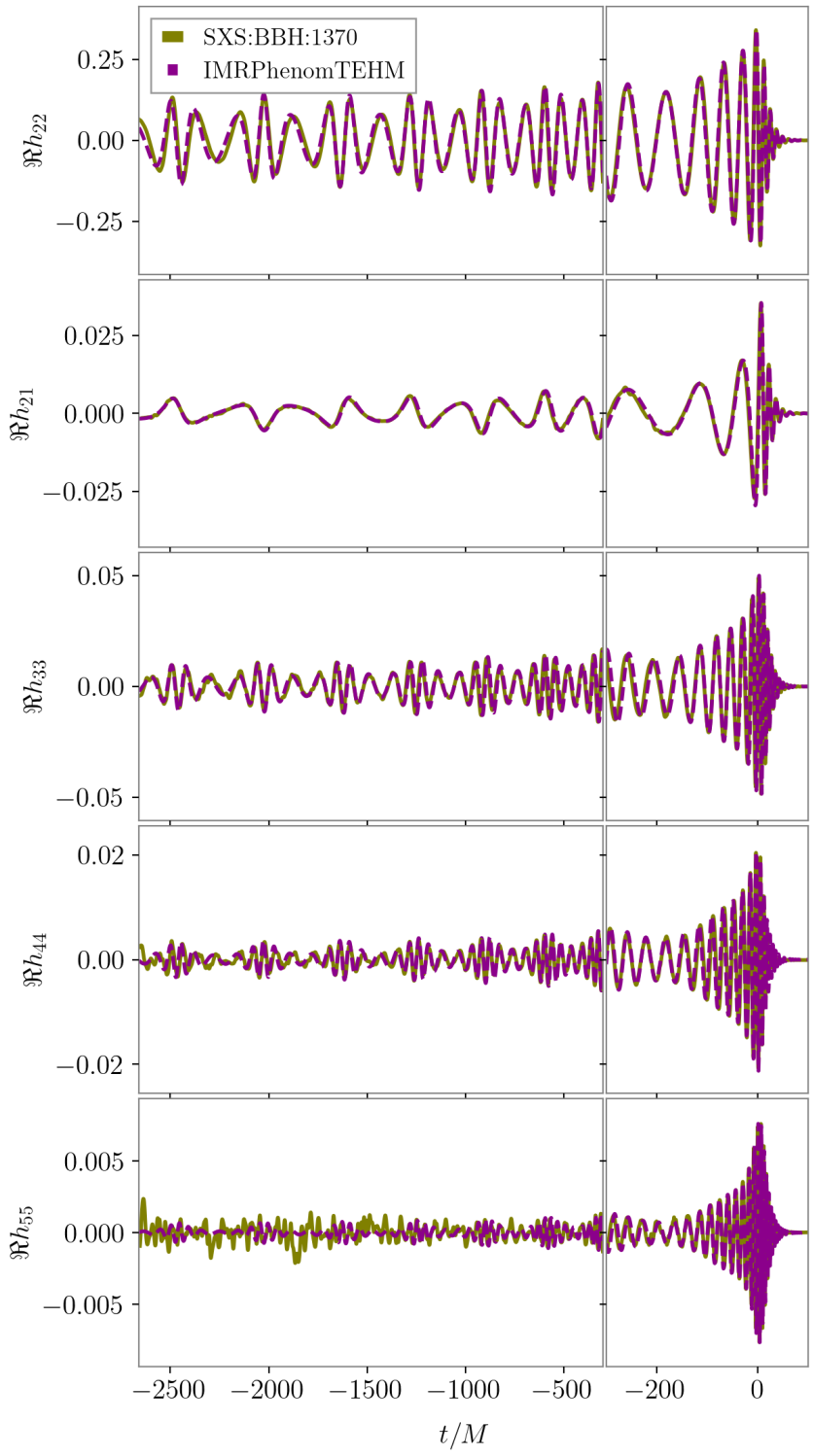

Figure 6.4: Real part of all available waveform modes in the IMRPhenomTEHM model for the nonspinning NR simulation SXS:BBH:1370 with mass ratio $q = 2$, effective spin $\chi_{\rm eff} = 0$, initial eccentricity $e_0^{\rm GW} = 0.294$, and initial mean anomaly $l_0^{\rm GW} = 0.29$ rad (green), and IMRPhenomTEHM waveform evaluated at the optimal parameters (magenta). The optimal values for IMRPhenomTEHM are $e_{\rm ref}^{\rm EOB} = 0.288$ and $l_{\rm ref} = 3.68$ rad at $Mf_{\rm ref} = Mf_{\rm min} = 0.0057$. Left panels show the inspiral region, while the right panels zooms on the merger-ringdown phase.

FIGURE 6.5: Mismatches for the $(2, |2|)$ modes $\mathcal{M}_{22}$ against the 28 eccentric NR simulations shown in Fig. 6.2, with a total mass of $M = 20M_\odot$. The x-axis corresponds to the simulation labels, arranged by increasing initial eccentricity. We compare different model configurations by varying the gauge choice (EOB vs. PN), the PN order of spinning eccentric corrections to the waveform modes' amplitudes (2PN vs. 3PN), and the application of the phase redefinition in Eqs. (6.2.4) and (6.2.9) (PR). The default options for the spinning PN order for the modes (2PN) and the phase redefinition (off) are not indicated in the legend.

focus on assessing the impact of the modeling choices introduced in Sec. 6.2 on the model's performance by recomputing the $(2, 2)$-mismatches $\mathcal{M}_{22}$. The model provides three main options.

1. *Gauge of the secular evolution equations.* We implement 3PN spinning secular evolution equations for e, l and x in the modified-harmonic gauge (denoted as PN) and in EOB coordinates. The default option in the IMRPhenomTEHM model are EOB coordinates, as it shows better agreement with NR simulations as well as a closer eccentricity definition to the one described in Ref. [386].

2. *Order of the spinning contributions to the modes.* Ref. [39] provides the full 3PN spinning contribution to the $(2, 2)$, $(2, 1)$ and $(3, 3)$ modes, which are incorporated into the model. However, the default version includes only up to the 2PN spinning contributions to be consistent with the PN information included in the quasicircular IMRPhenomTHM model, and thus have a more accurate quasicircular limit.

3. *Phase redefinition.* To remove phase gauge dependencies, it is common to apply the phase shift defined in Eq. (6.2.9). The default version does not apply this phase shift to maintain consistency with the non-eccentric IMRPhenomTHM model, assuming that this redefinition is already accounted for in the NR calibration of the model.

To assess the impact of the model's different options, we compute the $(2, 2)$ mismatch $\mathcal{M}_{22}$ for all NR simulations, and present the results at the lowest mass, $M = 20M_\odot$, in Fig. 6.5. The x-axis represents the simulation labels, ordered by increasing initial eccentricity. We evaluate all combinations of the gauge choice (EOB≡**default**, or PN) with the PN order of spin corrections in the modes (2PN≡**default**, or 3PN), and the phase redefinition (PR

off≡**default**, or PR on). First, the results show that the mismatches increase with higher eccentricities, consistent with the trend observed in Fig. 6.3. Among the different modeling options, the dominant factor affecting the mismatch is the choice of gauge, while the phase redefinition and higher-order PN spinning corrections have a negligible impact in the eccentric case. Thus, we keep the 2PN spin terms and not applying the phase redefinition as the default options of the model, so that the IMRPhenomTEHM model has a more accurate quasicircular limit. Regarding gauge choices, for low initial eccentricities, both PN and EOB gauges yield comparable accuracy, with EOB generally performing slightly better, though not significantly. However, for higher eccentricities, EOB shows a notable improvement, with mismatch reductions of up to 50%. Specifically, with the EOB gauge, mismatches remain below 2%, as also seen in Fig. 6.3, whereas they increase to 3% in certain cases when using PN. Given this improvement, along with the better alignment of $e_{\rm EOB}$ with the eccentricity definition used in the `gw_eccentricity` python package [385, 386], and in the EOB eccentric waveform models, we select EOB as the default gauge for the model.

6.3.4 Robustness across parameter space

The publicly available eccentric NR simulations provide a limited coverage of the full eccentric aligned-spin parameter space. As shown in Fig. 6.2, most simulations are non-spinning and limited to small mass ratios. In contrast, Ref. [20] presents a more comprehensive set of simulations, allowing for model validation over a broader parameter space. Additionally, various robustness tests were conducted during the LVK internal review of the SEOBNRv5EHM model. Thus, we assess the accuracy and robustness of the IMRPhenomTEHM model by comparing it to SEOBNRv5EHM across parameter space. We generate 5000 waveforms using SEOBNRv5EHM on a random uniform grid spanning in mass ratio $q \in [1, 20]$, total mass $M \in [10, 300]\ M_\odot$, reference orbital eccentricity $e \in [0, 0.4]$, reference mean anomaly $l \in [0, 2\pi]$, z-component of the dimensionless spin vectors $\chi_i \in [-1, 1]$, inclination $\iota \in [0, \pi]$, azimuthal phase $\varphi \in [0, 2\pi]$ at a dimensionless reference frequency $M\Omega_{\rm ref} = 0.03$. We first compute $(2, 2)$ mismatch $\mathcal{M}_{22}$ by optimizing over the eccentricity e and mean anomaly l at the $f_{\rm min}$ which matches the duration of the NR simulation, and then calculate the mismatch $\mathcal{M}$ including all available multipoles in both models optimizing additionally over φ.

The top row of Fig. 6.6 shows the $\mathcal{M}_{22}$ mismatches, while the bottom row presents the all-modes mismatch $\mathcal{M}$. The y-axis, shared across all plots, represent the eccentricity at the initial dimensionless orbital frequency Ω. Each column corresponds to a different parameter: mass ratio, total mass, and effective spin, respectively. As expected, we observe low mismatches (below 1%) in the regions of the parameter space where the underlying aligned-spin QC models have been tested, and where PN expansions are expected to be more reliable. In contrast, mismatches increase in unexplored regions of the parameter space where neither of the two models has been validated due to the lack of NR simulations. A visual inspection of the worst mismatch cases does not reveal any unexpected behavior in either model; rather, we find that the waveforms correspond to different binary systems, and consequently, different evolutions. Therefore, we caution against drawing conclusions on the accuracy of any model from those cases of high mismatches. The main takeaway from Fig. 6.6 is that IMRPhenomTEHM exhibits a reasonable and coherent behavior across the full parameter space, with comprehensive transitions from regions to low to higher mismatches. It demonstrates excellent agreement with SEOBNRv5EHM for small

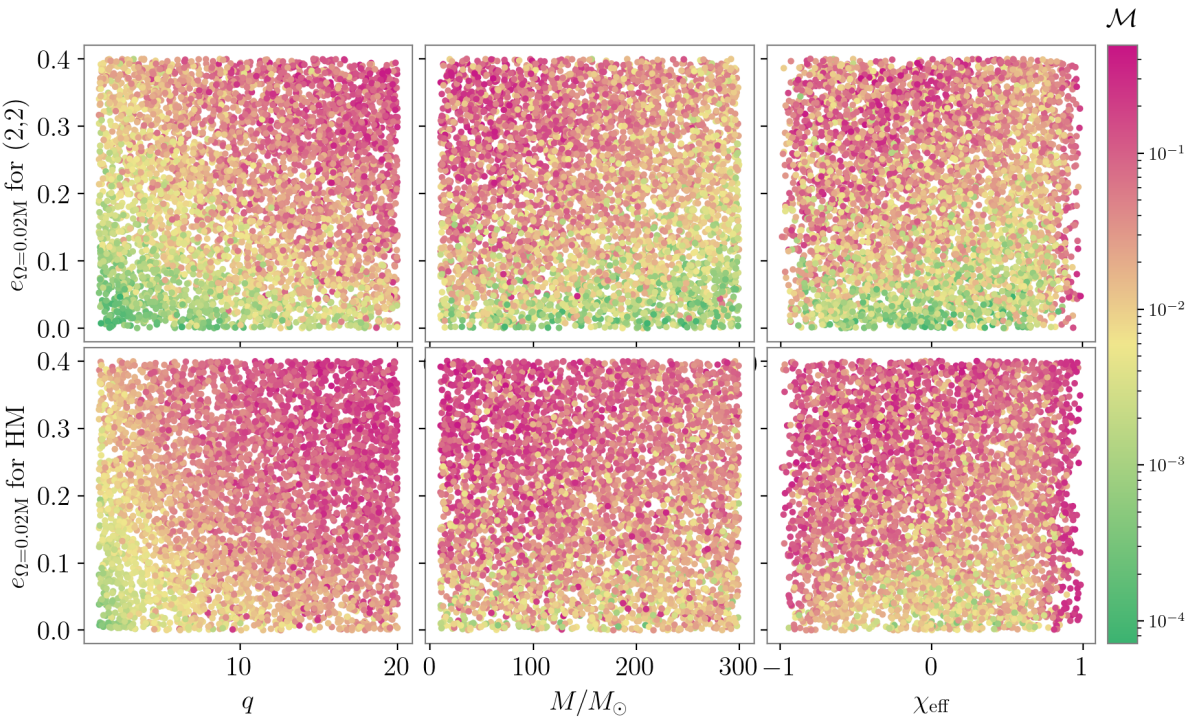

Figure 6.6: Mismatch distribution between the SEOBNRv5EHM and the IMRPhenomTEHM models computed over 5000 eccentric waveforms for the dominant $(2, |2|)$-modes (top row, $\mathcal{M}_{22}$), and including all available multipoles for each model (bottom row, $\mathcal{M}$). The configurations are uniformly distributed in mass ratio $q \in [1, 20]$, total mass $M \in [10, 300]\ M_\odot$, z-component dimensionless spin vectors $\chi_i \in [-0.995, 0.995]$, azimuthal phase $\varphi \in [0, 2\pi]$, inclination angle $\iota \in [0, \pi]$, and mean anomaly l and eccentricity e defined at $\omega = 0.02M$ $e_{\omega=0.02M}$ for the SEOBNRv5EHM model. For the IMRPhenomTEHM model, waveforms are obtained after optimizing over e, l, and $f_{\rm min}$ for $\mathcal{M}_{22}$, with φ added for $\mathcal{M}$.

mass ratios, even at relatively high initial eccentricities (close to 0.4), and progressively degrades as the mass ratio and eccentricity increase, both due to the PN expansions and the underlying QC models. For very low total mass systems, we observe higher mismatches at high eccentricities due to differences in frequency evolution, which become more pronounced in long waveforms. Conversely, for high-mass binaries, where only merger-ringdown phase is detectable, the agreement between the underlying non-eccentric models is remarkable. Finally, we note that the mismatch increases for extreme positive effective spin, as expected from the behavior of the non-eccentric baseline models [34, 174].

In conclusion we have investigated the robustness of the IMRPhenomTEHM model across parameter space by comparing with the SEOBNRv5EHM model and found agreement at comparable masses and large discrepancies in corners of parameter space. The visual inspection of the high mismatch cases reveal no unphysical behavior in the IMRPhenomTEHM multipoles, but rather waveform systematics between the models. This robustness study is complemented with all the parameter estimation runs presented in Sec. 6.4, during which the model is evaluated a larger number of times $\mathcal{O}(10^6 - 10^7)$. We leave for future work a more comprehensive study of waveform systematics in the nonprecessing-spin eccentric parameter space.

6.3.5 Timing results

One of the most outstanding features of the IMRPhenomTEHM model compared to other available IMR time-domain eccentric models [20, 21, 45, 490] is its computational efficiency. Eccentric models generally come with a higher computational cost due to the intricate time evolution of the eccentric quantities. For example, EOB eccentric models require numerical integration of the secular evolution equations, which involve evaluating lengthy PN expansions at each time step, apart from the usual integration of the Hamiltonian and equations of motion. While EOB models have proved to provide high accuracy in modeling eccentric systems, they are generally slower. In contrast, the IMRPhenomTEHM model is based on phenomenological approaches that rely on closed-form expressions, making it faster at the cost of some accuracy. While the IMRPhenomTEHM model may not capture the full range of eccentric effects with the same precision as EOB models, it offers a much more computationally efficient alternative.

The IMRPhenomTEHM model achieves a high computational efficiency by implementing a highly optimized approach to solving the orbit-averaged eccentric dynamics and evaluating the waveform modes. The method for solving the coupled differential equations from Eqs. (6.2.21) is detailed in Sec. 6.2.3.1. In summary, the key to accelerating the computation is to extract an optimal integration grid based on the QC frequency from the quasicircular IMRPhenomTHM model, which determines the rate at which the frequency evolves. This is achieved by evaluating the IMRPhenomTHM frequency on a grid constant step in the θ variable, see Eq. (6.2.17), during the inspiral region of the IMRPhenomTHM model, and then apply a constant grid of $\mathrm{d}t = 0.5M$ until the peak frequency of the IMRPhenomT model. Subsequently, this solution is interpolated and used by the solver to evaluate the right hand side of the evolution equations.

For waveform mode evaluation, we also leverage the usage of non-uniform time grids. The ODE solver extracts the minimum number of points needed to accurately describe the secularly evolving quantities. The PN expressions for the modes, as given in Refs. [38] and [39], take the form

$$H_{lm} = |H_{lm}|e^{-im\lambda} = \left(A_n(x,e)e^{-inl}\right)e^{-im\lambda}, \tag{6.3.5}$$

where the oscillatory component arises from the mean anomaly l and the orbit-average orbital phase. Henceforth, we focus on the calculation of the amplitudes, whose evaluation can be separated into two parts: (1) an "orbit-averaged" component A_n that only needs to be computed at the grid points of the secular solver, and (2) an oscillatory component from the exponentials of l, which is shared across all modes and only needs to be computed once. The former is computed on a coarser grid, interpolated and evaluated at the corresponding input constant time step needed for the Fourier transform of the signal, while the latter only needs a single computation. We leave further optimizations in other parts of the code as future work. This optimization in mode evaluation significantly reduces computational cost, particularly at low masses, where even the underlying QC model is slow due to the necessity of evaluating all quantities at each time step. Notably, no changes have been made so far to the original IMRPhenomTHM model, where similar techniques could be applied to further accelerate computations. We also leave this improvement for future work. We present benchmark results in Fig. 6.7, evaluating a waveform with $q = 3$, $\chi_1 = 0.4$, $\chi_2 = 0.3$, and $l = 1.2$ at 10Hz for different initial eccentricities, one per column ($e = 0, 0.2$). The plot shows the wall time, in

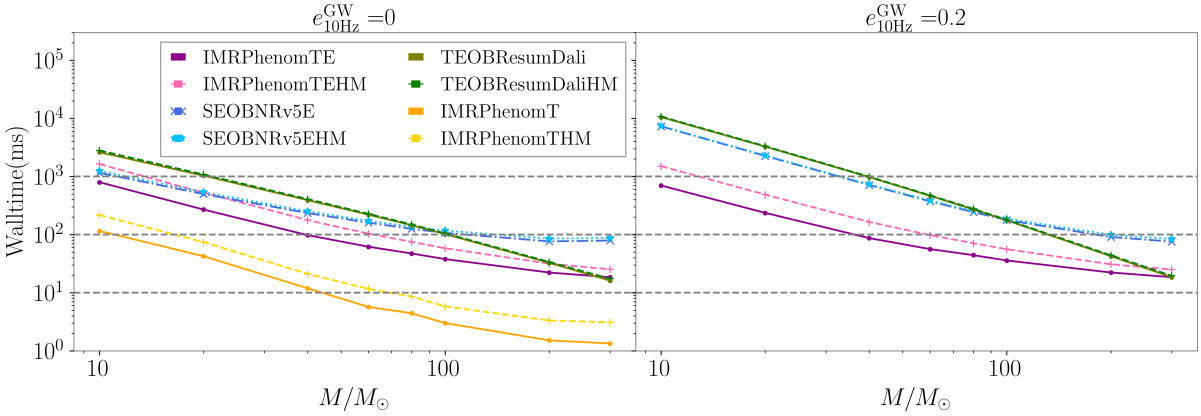

FIGURE 6.7: Benchmark results comparing the computational efficiency of different waveform models. The plot shows the wall time (in milliseconds) required to generate waveforms for a binary with mass ratio $q = 3$, spins $\chi_1 = 0.4$, $\chi_2 = 0.3$, and mean anomaly $l = 1.2$ at 10 Hz for different initial eccentricities ($e = 0, 0.2$), each represented in a separate column. Solid lines correspond to the evaluation of only the dominant harmonic, while dashed lines include all higher modes. We compare IMRPhenomTEHM, SEOBNRv5EHM, TEOBResumS-Dalí for all cases, including IMRPhenomTHM, as implemented in the `phenomxpy` package in the $e = 0$ case. The benchmark is performed over a range of total masses, $M = \{10, 20, 40, 60, 80, 100, 200, 300\}M_\odot$.

milliseconds, required to evaluate each waveform model, considering only the dominant harmonic (solid lines) and including all higher modes (dashed lines), as indicated in the legend. The benchmark is performed for different total masses using IMRPhenomTEHM, SEOBNRv5EHM, TEOBResumS-Dalí for both cases, including IMRPhenomTHM as implemented in `phenomxpy` for the non-eccentric case. For total masses below $100M_\odot$, IMRPhenomTEHM is significantly faster than the other two eccentric models. For the $e = 0.2$ case at the lowest mass $M = 10M_\odot$, we find IMRPhenomTEHM waveform generation times of around 800 ms for the dominant harmonic and 1000 ms when including all modes, compared to 8000 ms for SEOBNRv5EHM and 10^4 ms for TEOBResumS-Dalí. These results demonstrate that IMRPhenomTEHM is approximately an order of magnitude faster than the state-of-the-art EOB models, a trend that approximately holds up to total masses of $M = 100M_\odot$. At higher masses, only TEOBResumS-Dalí shows slightly faster performance evolution than the other two models, exhibiting a steeper decrease in wall time. The wall time difference between SEOBNRv5EHM and IMRPhenomTEHM remains stable, while TEOBResumS-Dalí eventually reaches the same wall time as IMRPhenomTE- approximately 11 ms at $M = 300M_\odot$- performing slightly faster than IMRPhenomTEHM. However, at this scale, these differences become negligible. We find a similar trend in the non-eccentric case, with smaller absolute differences in wall time when comparing different models. The considerable slowdown compared to QC models arises from the fact that, even though the eccentric expansions vanish, the evolution of the orbit-averaged quantities still requires numerical integration. Finally, comparing IMRPhenomTEHM with its QC counterpart, IMRPhenomTHM, we observe that the slowdown at low masses originates from IMRPhenomTHM itself. Any optimization applied to IMRPhenomTHM would thus have a substantial impact on IMRPhenomTEHM, making this a promising avenue for future improvements.

The advantage of a computationally efficient eccentric model is the ability to perform

parameter estimation studies with a wide range of configurations, as we demonstrate in Sec. 6.4.

6.4 Parameter Estimation studies

A key application of waveform models is the Bayesian inference of source parameters from GWs. In this section, we assess the performance of the eccentric, aligned-spin IMRPhenomTEHM model through PE studies. We conduct synthetic injections of three NR signals introduced in Sec. 6.3.2 into zero detector noise, and analyze two real GW events detected by the LVK Collaboration - GW150914 [61, 148] and GW190521 [89]. We compare our findings with results from the literature, specifically those obtained using the SEOBNRv5EHM model [20].

We use the Python package `bilby_pipe` [113, 117], with the nested sampler `dynesty` [115, 116]. We adopt priors on the inverse mass ratio ($1/q$) and chirp mass ($\mathcal{M}$) to ensure a uniform distribution in the component masses. The priors on the reference eccentricity $e_{\rm ref}$ and mean anomaly $l_{\rm ref}$ are uniformly distributed, with $l_{\rm ref} \in [0, 2\pi]$ and $e_{\rm ref} \in [0, e_{\rm max}]$, where $e_{\rm max}$ specified for each case. For the spin components χ_i, we use priors corresponding to the projections of a uniform and isotropic spin distribution along a direction perpendicular to the binary's orbital plane [520]. For the luminosity distance d_L, we generally use the commonly adopted prior proportional to d_L^2 [1–4], except for GW190521, where we specify a prior uniform in comoving volume as in Ref. [89]. The remaining priors, including the extrinsic parameters and the binary's orbital phase φ, are the same as in Ref. [1]. The specific prior boundaries for each parameter are detailed in the corresponding sections for each case.

Comparing eccentric parameters across different waveform models- or even within the same model but in different coordinates, as is our case- requires additional post-processing due to the gauge dependence of eccentricity in General Relativity. Thus, we present our results using a commonly established definition of eccentric parameters across models. We adopt the GW eccentricity $e^{\rm GW}$ and mean anomaly $l^{\rm GW}$ as introduced in Ref. [385, 386], which are efficiently computed using the `gw-eccentricity` Python package [385]. We thus evaluate the waveform at each sample of the posterior distribution and apply the `gw-eccentricity` package to measure $e^{\rm GW}$ and $l^{\rm GW}$ at the chosen reference time.

A summary of the PE runs performed in this study is presented in Table 6.1, with details about the waveform model used, the computational resources required, and the specific minimum and reference frequencies for each run. For all runs, we set the number of accepted steps to 60 (`naccept`=60) and the number of live points to 1000 (`nlive`=1000) for the `dynesty` sampler. Additionally, we enable distance marginalization to reduce computational cost, and we set the sampling rate to 4096 Hz. The computational efficiency of our model allows us to investigate different configurations/physical descriptions of our model and its impact on waveform systematics. In particular, we assess the effect of using the two available gauge choices for our model -EOB (default) and PN- as well as the role of higher order modes.

Incorporating higher order modes requires lowering the starting frequency to ensure all relevant modes remain within the analysis frequency band. HMs with $m > 2$ have higher frequency content for the same time interval, so one needs to adjust the starting frequency

Event (Detectors, ΔT (s)) $[f_{\rm min}, f_{\rm max}]$	Model (sampler)	Waveform settings $f_{\rm ref}(f_{\rm min})$ (Hz)	Computing resources cores × nodes	Runtime
SXS:BBH:1355 (LHV, 4) [20, 2048]	IMRPhenomTE (EOB)	20	50 × 1	14h 38min
	IMRPhenomTE (PN)	20	50 × 1	13h 57min
	IMRPhenomTEHM (EOB, $l \leq 4$)	20(10)	112 × 1	21h 49min
	IMRPhenomTEHM (PN, $l \leq 4$)	20(10)	112 × 1	21h 07min
SXS:BBH:1359 (LHV, 4) [20, 2048]	IMRPhenomTE (EOB)	20	50 × 1	15h 17min
	IMRPhenomTE (PN)	20	50 × 1	15h 10min
	IMRPhenomTEHM (EOB, $l \leq 4$)	20(10)	112 × 1	21h 57min
	IMRPhenomTEHM (PN, $l \leq 4$)	20(10)	112 × 1	21h 04min
SXS:BBH:1363 (LHV, 4) [20, 2048]	IMRPhenomTE (EOB)	20	50 × 1	15h 15min
	IMRPhenomTE (PN)	20	50 × 1	16h 47min
	IMRPhenomTEHM	20(10)	112 × 1	18h 34min
	IMRPhenomTEHM (20Hz)	20	112 × 1	8h 20
GW150914 (LH, 8) [20, 896]	IMRPhenomTHM	20(10)	112 × 1	9h 02min
	IMRPhenomTEHM (EOB, $l \leq 4$)	20(10)	112 × 1	1d 3h
	IMRPhenomTEHM (PN, $l \leq 4$)	20(10)	112 × 1	1d 2h
GW190521 (LHV, 8) [11, 521]	IMRPhenomTHM ($l \leq 4$)	5.5	112 × 1	2h 40min
	IMRPhenomTEHM ($l \leq 4$)	5.5	112 × 1	11h 06min
	IMRPhenomTEHM ($l \leq 4$, $r < 10M$)	5.5*	112 × 1	7h 32min

Table 6.1: Summary of the PE runs performed in this study. The first column lists the NR SXS simulation used for injections and the GW events, along with the detectors considered (L for Livingston, H for Hanford, and V for Virgo) and the duration of the injected signal (ΔT in seconds). The second column specifies the waveform model, including the highest l-modes and coordinates used. The **Waveform settings** column provides the reference frequency, with the minimum frequency in brackets when different. The star * next to the minimum frequency indicates that no additional waveform conditioning was applied, meaning the minimum frequency is exactly as listed. The table also includes the computing resources and runtime, enabling the total computational hours to be calculated by multiplying the resources by the runtime.

based on the highest m-mode ($m_{\rm max}$) included in the analysis,

$$f_{\rm min} = \frac{2 f_{\rm start}}{m_{\rm max}}. \tag{6.4.1}$$

As shown in Tab. 6.1, the minimum frequency is adjusted according to Eq. (6.4.1) based on the maximum number of l-modes included and the starting frequency of the analysis. As introduced in Sec. 6.2, the IMRPhenomTEHM model is capable to specify a starting frequency distinct from the reference frequency. Hence, changes in the starting frequency, due to the higher order modes or conditioning of time-domain waveforms to perform Fourier transforms, do not modify the physical configuration.

6.4.1 Numerical relativity injections

In this section, we conduct zero-noise injections for three of the publicly available eccentric NR waveforms and perform PE studies to assess the model's accuracy in recovering the injected parameters. For comparison with Refs. [20, 54], we selected the same three public SXS NR simulations: `SXS:BBH:1355`, `SXS:BBH:1359` and `SXS:BBH:1363`, corresponding to eccentricities at the initial orbit averaged frequency for each waveform of 0.077, 0.145, and 0.317 respectively. We included all NR modes up to $l = 8$, set the total mass to $M = 70 M_\odot$, fixed the inclination angle between the system's orbital angular momentum and the line of sight $\iota = 0$, and used a coalescence phase $\varphi = 0$ at a luminosity distance of $d_L = 2307$ Mpc.

This configuration yields a three-detector matched-filtered SNR, $\mathrm{SNR}^{\mathrm{N}} = 20$, when using the zero-detuned high power Advanced LIGO(for LIGO Livingston and Hanford) and Virgo PSDs at design sensitivity [472, 473, 521].

The computational efficiency of the IMRPhenomTEHM model enables us to systematically run PE studies including higher modes in in less than a day, as shown in Tab. 6.1. With these NR injections, we investigate the impact of HMs on signal recovery, and explore the influence of the coordinate choice, EOB(default) or PN. Note that the choice of simulations -all featuring equal-mass, non-spinning black holes and zero inclination- would allow us to use only the dominant $(2, |2|)$ harmonics, as only modes with $m = 2$ are visible for a face-on binary, and other analyses of these events using EOB models are typically performed with only the $(2, |2|)$ mode due to the high computational cost [20, 356]. For each simulation, we performed four different PE runs (see Tab. 6.1 for details): using either EOB or PN coordinates and including either only the dominant $(2, 2)$ harmonic or all modes up to $l = 4$. Due to the characteristics of the binaries (equal-mass and no inclination), we do not include $l = 5$ modes, as we do not expect higher modes to have a significant impact on these specific runs.

We adopt the same priors as in Refs. [20, 54]: $1/q \in [0.05, 1]$, $\mathcal{M} \in [5, 100]M_{\odot}$, $\chi_i \in [0, 0.99]$. The eccentricity prior has an upper bound of $e_{\mathrm{max}} = 0.3$ for `SXS:BBH:1355` and `SXS:BBH:1359`, whereas for `SXS:BBH:1363`, we extend the upper bound to $e_{\mathrm{max}} = 0.5$ to prevent the posterior from railing. These priors are set at a reference frequency of 20 Hz.

Fig. 6.8 displays the posterior distributions for each NR injection across the four analysis cases, showing maginalized 1D and 2D posteriors for the chirp mass $\mathcal{M}$ and the effective spin χ_{eff}, and the reference eccentricity $e_{20\mathrm{Hz}}$ and mean anomaly $l_{20\mathrm{Hz}}$. Additionally, we include the GW eccentricity and mean anomaly computed using the `gw_eccentricity` package, also evaluated at the reference frequency. Table 6.2 provides a summary of the injected intrinsic parameters alongside the recovered median values and the 90% credible intervals for each run. The results in Fig. 6.8 and Table 6.2 demonstrate the ability of the IMRPhenomTEHM model to accurately recover the binary parameters. Moreover, all posterior distributions shown in Fig. 6.8 are Gaussian and unimodal across all NR injections, even for the highest eccentricity case, `SXS:BBH:1363`. This further supports the accuracy of the model in capturing the eccentric dynamics. A key observation, consistent with the SEOBNRv5EHM injection studies in Refs. [20, 54], is that when only using the dominant harmonics, small biases appear in the recovery of the luminosity distance d_L and inclination angle ι. Similarly, we find a significantly improved recovery of d_L when HMs are included, as seen in Tab. 6.2. However, their inclusion does not lead to a comparable improvement in the recovery of the inclination angle.

A more detailed analysis is needed to understand the bias observed for `SXS:BBH:1363` when including HMs, as seen in the bottom row of Fig. 6.8. We noticed a clear shift in the QC posteriors when including HMs, as shown by the pink curve (HMs results are only shown for the default version in this case). However, this difference stems from the choice of starting frequency for the signal and the template. When including HMs, the starting frequency is lowered to 10 Hz to ensure all modes remained in band. In contrast, when keeping the same minimum frequency as in the analysis with only the $(2, 2)$ harmonic, we found equivalent posteriors, as indicated by the orange curve. This is explained because of the limited length of the NR waveform used to construct the mock

Event	Parameter	Injected value	IMRPhenomTE (EOB)	IMRPhenomTE (PN)	IMRPhenomTEHM (EOB)	IMRPhenomTEHM (PN)
SXS:BBH:1355	$M/M_\odot$	70.0	$70.70^{+3.10}_{-2.67}$	$70.71^{+3.03}_{-2.63}$	$70.56^{+2.84}_{-2.64}$	$70.64^{+2.82}_{-2.65}$
	$\mathcal{M}/M_\odot$	30.47	$30.34^{+1.19}_{-1.16}$	$30.35^{+1.17}_{-1.13}$	$30.43^{+1.17}_{-1.13}$	$30.46^{+1.15}_{-1.13}$
	$1/q$	1.0	$0.78^{+0.19}_{-0.23}$	$0.79^{+0.19}_{-0.23}$	$0.84^{+0.15}_{-0.23}$	$0.84^{+0.15}_{-0.22}$
	$\chi_{\rm eff}$	0.0	$0.00^{+0.10}_{-0.10}$	$0.00^{+0.10}_{-0.11}$	$0.00^{+0.10}_{-0.11}$	$0.00^{+0.10}_{-0.11}$
	$e_{20\rm Hz}$ $\left(e^{\rm GW}_{20\rm Hz}\right)$	- (0.07)	$0.05^{+0.05}_{-0.04}$ $\left(0.05^{+0.05}_{-0.04}\right)$	$0.04^{+0.04}_{-0.03}$ $\left(0.05^{+0.05}_{-0.04}\right)$	$0.04^{+0.05}_{-0.04}$ $\left(0.04^{+0.05}_{-0.04}\right)$	$0.03^{+0.04}_{-0.03}$ $\left(0.04^{+0.05}_{-0.04}\right)$
	$l_{20\rm Hz}$ $\left(l^{\rm GW}_{20\rm Hz}\right)$	- (1.96)	$2.04^{+2.01}_{-1.40}$ $\left(1.94^{+2.36}_{-1.37}\right)$	$2.06^{+1.98}_{-1.37}$ $\left(1.95^{+2.19}_{-1.35}\right)$	$2.04^{+2.33}_{-1.43}$ $\left(1.95^{+2.62}_{-1.42}\right)$	$2.06^{+2.49}_{-1.46}$ $\left(1.96^{+2.78}_{-1.43}\right)$
	ι[rad]	0.0	$0.61^{+0.62}_{-0.43}$	$0.61^{+0.59}_{-0.44}$	$0.47^{+0.55}_{-0.35}$	$0.48^{+0.53}_{-0.35}$
	d_L[dMpc]	2307	1827^{+442}_{-682}	1827^{+450}_{-676}	1967^{+358}_{-613}	1964^{+363}_{-592}
	φ	0.0	$3.11^{+2.87}_{-2.79}$	$3.18^{+2.79}_{-2.83}$	$3.12^{+2.83}_{-2.79}$	$3.10^{+2.84}_{-2.79}$
	$\rm SNR^N$	20.0	$19.07^{+0.10}_{-0.19}$	$19.06^{+0.10}_{-0.18}$	$19.04^{+0.11}_{-0.19}$	$19.04^{+0.11}_{-0.19}$
	$\log_{10} B_{\rm EOB/PN}$	-	$0.20^{+0.17}_{-0.17}$	-	$0.06^{+0.17}_{-0.17}$	-
SXS:BBH:1359	$M/M_\odot$	70.0	$70.26^{+2.89}_{-2.64}$	$70.31^{+2.85}_{-2.61}$	$70.43^{+2.79}_{-2.51}$	$70.48^{+2.69}_{-2.47}$
	$\mathcal{M}/M_\odot$	30.47	$30.21^{+1.12}_{-1.18}$	$30.24^{+1.15}_{-1.17}$	$30.42^{+1.14}_{-1.11}$	$30.45^{+1.12}_{-1.09}$
	$1/q$	1.0	$0.80^{+0.18}_{-0.23}$	$0.81^{+0.17}_{-0.23}$	$0.85^{+0.14}_{-0.22}$	$0.85^{+0.13}_{-0.22}$
	$\chi_{\rm eff}$	0.0	$0.00^{+0.10}_{-0.10}$	$-0.01^{+0.10}_{-0.10}$	$0.00^{+0.10}_{-0.10}$	$0.00^{+0.10}_{-0.10}$
	$e_{20\rm Hz}$ $\left(e^{\rm GW}_{20\rm Hz}\right)$	- (0.13)	$0.12^{+0.05}_{-0.05}$ $\left(0.12^{+0.05}_{-0.05}\right)$	$0.09^{+0.04}_{-0.04}$ $\left(0.12^{+0.05}_{-0.06}\right)$	$0.10^{+0.05}_{-0.05}$ $\left(0.10^{+0.05}_{-0.05}\right)$	$0.08^{+0.04}_{-0.04}$ $\left(0.10^{+0.05}_{-0.05}\right)$
	$l_{20\rm Hz}$ $\left(l^{\rm GW}_{20\rm Hz}\right)$	- (0.81)	$0.86^{+5.29}_{-0.75}$ $\left(0.89^{+5.31}_{-0.79}\right)$	$0.88^{+5.27}_{-0.77}$ $\left(0.88^{+5.30}_{-0.78}\right)$	$0.92^{+5.25}_{-0.82}$ $\left(1.00^{+5.20}_{-0.90}\right)$	$0.90^{+5.28}_{-0.81}$ $\left(0.99^{+5.20}_{-0.90}\right)$
	ι[rad]	0.0	$0.61^{+0.59}_{-0.44}$	$0.61^{+0.59}_{-0.44}$	$0.48^{+0.54}_{-0.35}$	$0.49^{+0.52}_{-0.35}$
	d_L[dMpc]	2307	1824^{+452}_{-667}	1837^{+446}_{-680}	1984^{+362}_{-616}	1981^{+370}_{-613}
	φ	0.0	$3.11^{+2.84}_{-2.80}$	$3.08^{+2.90}_{-2.79}$	$3.16^{+2.80}_{-2.84}$	$3.14^{+2.82}_{-2.84}$
	$\rm SNR^N$	20.0	$19.00^{+0.11}_{-0.20}$	$18.99^{+0.10}_{-0.20}$	$18.93^{+0.10}_{-0.20}$	$18.91^{+0.11}_{-0.20}$
	$\log_{10} B_{\rm EOB/PN}$	-	$0.17^{+0.18}_{-0.18}$	-	$0.13^{+0.17}_{-0.17}$	-
			IMRPhenomTE (EOB)	IMRPhenomTE (PN)	IMRPhenomTEHM	IMRPhenomTEHM (20 Hz)
SXS:BBH:1363	$M/M_\odot$	70.0	$71.83^{+4.75}_{-3.46}$	$71.92^{+4.00}_{-3.27}$	$75.13^{+4.04}_{-4.02}$	$72.51^{+3.07}_{-3.23}$
	$\mathcal{M}/M_\odot$	30.47	$30.68^{+1.97}_{-1.59}$	$30.86^{+1.72}_{-1.52}$	$32.39^{+1.66}_{-1.73}$	$31.00^{+1.78}_{-1.78}$
	$1/q$	1.0	$0.75^{+0.22}_{-0.24}$	$0.79^{+0.19}_{-0.24}$	$0.83^{+0.15}_{-0.23}$	$0.80^{+0.18}_{-0.26}$
	$\chi_{\rm eff}$	0.0	$0.10^{+0.12}_{-0.11}$	$0.07^{+0.12}_{-0.11}$	$0.18^{+0.11}_{-0.12}$	$0.11^{+0.12}_{-0.12}$
	$e_{20\rm Hz}$ $\left(e^{\rm GW}_{20\rm Hz}\right)$	- (0.25)	$0.26^{+0.03}_{-0.05}$ $\left(0.26^{+0.03}_{-0.05}\right)$	$0.21^{+0.02}_{-0.03}$ $\left(0.27^{+0.03}_{-0.04}\right)$	$0.22^{+0.04}_{-0.04}$ $\left(0.22^{+0.04}_{-0.04}\right)$	$0.26^{+0.04}_{-0.04}$ $\left(0.26^{+0.04}_{-0.04}\right)$
	$l_{20\rm Hz}$ $\left(l^{\rm GW}_{20\rm Hz}\right)$	- (4.27)	$4.58^{+0.67}_{-0.77}$ $\left(4.45^{+0.66}_{-0.77}\right)$	$4.63^{+0.60}_{-0.66}$ $\left(4.51^{+0.59}_{-0.66}\right)$	$4.22^{+0.77}_{-0.80}$ $\left(4.09^{+0.76}_{-0.80}\right)$	$4.68^{+0.96}_{-1.03}$ $\left(4.56^{+0.96}_{-1.01}\right)$
	ι[rad]	0.0	$0.61^{+0.59}_{-0.44}$	$0.62^{+0.61}_{-0.45}$	$0.48^{+0.53}_{-0.35}$	$0.46^{+0.52}_{-0.34}$
	d_L[dMpc]	2307	1970^{+507}_{-732}	1989^{+503}_{-736}	2317^{+433}_{-714}	2219^{+261}_{-501}
	φ	0.0	$3.15^{+2.83}_{-2.81}$	$3.15^{+2.82}_{-2.82}$	$3.19^{+2.81}_{-2.90}$	$3.03^{+2.96}_{-2.75}$
	$\rm SNR^N$	20.0	$18.84^{+0.11}_{-0.20}$	$18.83^{+0.11}_{-0.20}$	$18.51^{+0.12}_{-0.20}$	$18.84^{+0.11}_{-0.20}$
	$\log_{10} B_{\rm EOB/PN}$	-	$0.36^{+0.18}_{-0.18}$	-	-	-

Table 6.2: Injected, median values, and 90% credible intervals for the posterior distributions in Fig. 6.8 for the three NR injections (indicated at each row), recovered with IMRPhenomTEHM using different settings specified in the columns. The table reports the total mass M and chirp mass $\mathcal{M}$ (both in solar masses), the inverse mass ratio $1/q$, the effective spin parameter $\chi_{\rm eff}$, the reference eccentricity and mean anomaly ($e_{20\rm Hz}$ and $l_{20\rm Hz}$ respectively), the inclination angle ι, the luminosity distance d_L, the coalescence phase φ, and the network matched-filtered SNR, $\rm SNR^N$, for LIGO Hanford and Livingston, and Virgo detectors. In brackets, we also report the injected and recovered GW eccentricity $e_{\rm GW}$ and mean anomaly $l_{\rm GW}$. All values are given at the reference frequency of 20 Hz.

signal injection. This NR waveform is generated at a starting frequency of 20Hz, as it cannot be generated at 10Hz. Consequently, the HMs of the signal enter the frequency band during the analysis, which explains part of the biases of the IMRPhenomTEHM run starting at 10Hz. Additionally, this NR simulation starts with a considerable initial eccentricity ($e_0^{\rm GW} = 0.317$), a regime where the eccentricity expansions used in the model construction degrade its accuracy (see Fig. 6.3). Thus, we observe a small bias in the recovered effective spin parameter, although the injected value lies in the 90% credible interval, which may also be related to the length issues of the signal.

The right panels of Fig. 6.8 display the posterior distributions for the GW eccentricity $e^{\rm GW}$ and mean anomaly $l^{\rm GW}$ at a reference frequency of 20 Hz. IMRPhenomTEHM successfully recovers the injected parameters within the 90% credible intervals for both coordinates, while the reference posteriors $e_{\rm 20Hz}$ and $l_{\rm 20Hz}$ show significant differences. Notably, the EOB posteriors align more closely to the GW ones than the PN posteriors, supporting our choice of EOB as the default coordinate system. To further justify this selection, we compute the log-10 Bayes factor between the EOB (EOB) and the PN (PN) hypothesis, $\log_{10} B_{\rm EOB/PN}$, shown in Tab. 6.2. While the values are small, they consistently favor EOB coordinates.

These studies demonstrate that our model can recover the injected waveform parameters with a performance comparable to the SEOBNRv5EHM model, despite the higher mismatches. This suggests that mismatch calculations alone may not fully capture the model's ability to recover the injected waveforms. Furthermore, the significantly faster performance of IMRPhenomTEHM enabled us to explore the impact of various effects on these PE runs. We leave for future work to expand the injection study in this section to further investigate the accuracy and the role of HMs and gauge choices in the recovery of eccentric signals.

6.4.2 Analysis of real GW events

We present an analysis of the GW events GW150914 [61, 148], as the first GW signal from a BBH, and GW190521 [89], as a possible eccentric candidate, using the IMRPhenomTEHM model. The strain data for both events were obtained from the Gravitational Wave Open Source Catalog (GWOSC) [309, 522], along with the publicly available PSDs and calibration envelopes from the Gravitational Wave Transient Catalog GWTC-2.1 [3]. We conducted six different PE runs, as detailed in Tab. 6.1, using IMRPhenomTEHM but also IMRPhenomTHM [34, 191] via the `phenomxpy` [416] infrastructure for comparison. Results for both events are summarized in Tab. 6.3 and Fig. 6.9, and we now proceed to discuss each case in more detail in the following subsections. For comparison, we also include in the table the results obtained using SEOBNRv5EHM from Ref. [20].

6.4.2.1 GW150914

GW150914 is the first detected GW signal from a BBH coalescence, consistent with a QC, non-spinning, and comparable-mass binary system [61, 148]. With a SNR of approximately 23.7, it remains one of the highest-SNR events observed during the first three observing runs of the LVK Collaboration [1, 2, 4, 522]. For our analysis, we adopt the priors introduced in Sec. 6.4, with boundaries $1/q \in [0.05, 1]$, $\mathcal{M} \in [20, 50]$, and $e_{\rm 20Hz} \in [0, 0.3]$,

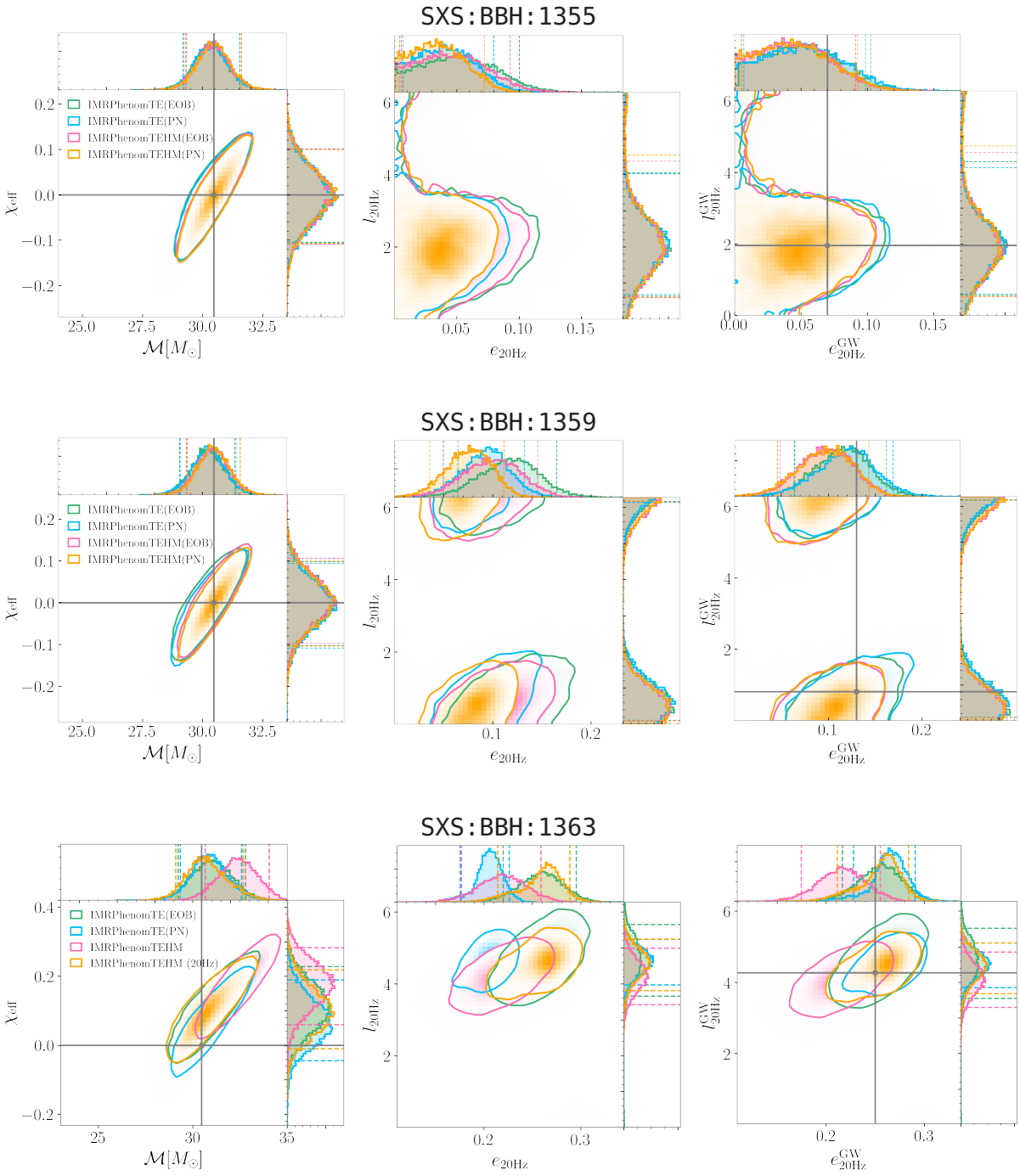

FIGURE 6.8: Posterior distributions for three NR injections, with each row corresponding to one simulation. The figure shows marginalized 2D and 1D posterior distributions for key parameters: chirp mass $\mathcal{M}$ and effective spin $\chi_{\rm eff}$ (*first column*), reference eccentricity $e_{20\rm Hz}$ and reference mean anomaly $l_{20\rm Hz}$ (*second column*), and GW eccentricity $e_{\rm GW}$ and mean anomaly $l_{\rm GW}$ (*third column*). The injected values are indicated by gray lines. Finally, we also include the log-10 Bayes factor between the EOB (EOB) and the PN (PN) hypothesis, $\log_{10} B_{\rm EOB/PN}$All parameters are measured at the reference frequency $f_{\rm ref} = 20$ Hz.

Event	Model	$M/M_\odot$	$\mathcal{M}/M_\odot$	$1/q$	$\chi_{\rm eff}$	$e^{\rm GW}$	$l^{\rm GW}$	d_L	SNR$^{\rm N}$	$\log_{10} B_{\rm E/QC}$
GW150914	IMRPhenomTHM	$71.45^{+3.00}_{-3.05}$	$30.97^{+1.31}_{-1.34}$	$0.89^{+0.10}_{-0.17}$	$-0.03^{+0.10}_{-0.11}$	-	-	453^{+145}_{-158}	$25.11^{+0.08}_{-0.13}$	-
	IMRPhenomTEHM (EOB)	$71.16^{+3.15}_{-3.01}$	$30.86^{+1.37}_{-1.33}$	$0.90^{+0.09}_{-0.16}$	$-0.03^{+0.10}_{-0.11}$	$0.03^{+0.05}_{-0.03}$	$3.92^{+2.05}_{-3.60}$	446^{+144}_{-159}	$25.13^{+0.11}_{-0.15}$	$-0.50^{+0.16}_{-0.16}$
	IMRPhenomTEHM (PN)	$71.22^{+3.20}_{-2.97}$	$30.88^{+1.38}_{-1.31}$	$0.89^{+0.10}_{-0.17}$	$-0.03^{+0.10}_{-0.11}$	$0.03^{+0.05}_{-0.03}$	$3.94^{+2.04}_{-3.59}$	452^{+143}_{-155}	$25.13^{+0.10}_{-0.14}$	$-0.68^{+0.16}_{-0.16}$
	SEOBNRv5EHM	$70.9^{+2.62}_{-2.8}$	$30.72^{+1.15}_{-1.24}$	$0.88^{+0.09}_{-0.14}$	$-0.05^{+0.09}_{-0.05}$	$0.06^{+0.07}_{-0.05}$	$3.17^{+2.49}_{-2.54}$	480^{+116}_{-125}	-	$-0.57^{+0.13}_{-0.13}$
GW190521	IMRPhenomTHM	$255.4^{+30.2}_{-33.1}$	$109.3^{+14.0}_{-18.1}$	$0.74^{+0.23}_{-0.27}$	$0.01^{+0.31}_{-0.39}$	-	-	4127^{+1662}_{-1877}	$14.37^{+0.21}_{-0.26}$	-
	IMRPhenomTEHM	$259.1^{+26.4}_{-28.3}$	$111.3^{+12.0}_{-15.5}$	$0.78^{+0.20}_{-0.27}$	$0.02^{+0.30}_{-0.34}$	$0.31^{+0.13}_{-0.28}$	$3.18^{+2.82}_{-2.88}$	4275^{+1490}_{-1732}	$14.44^{+0.21}_{-0.30}$	$0.12^{+0.13}_{-0.13}$
	IMRPhenomTEHM ($r < 10M$)	$258.5^{+26.8}_{-28.6}$	$111.1^{+12.2}_{-14.8}$	$0.78^{+0.19}_{-0.26}$	$0.01^{+0.30}_{-0.36}$	$0.29^{+0.14}_{-0.26}$	$3.02^{+2.42}_{-2.35}$	4284^{+1516}_{-1782}	$14.42^{+0.23}_{-0.28}$	$0.28^{+0.13}_{-0.13}$
	SEOBNRv5EHM	$260.7^{+20.3}_{-19.5}$	$111.4^{+9.7}_{-11.7}$	$0.73^{+0.20}_{-0.21}$	$0.05^{+0.20}_{-0.20}$	$0.29^{+0.16}_{-0.23}$	$3.14^{+2.54}_{-2.52}$	4786^{+1261}_{-1230}	-	$-0.36^{+0.11}_{-0.11}$

Table 6.3: Median values and 90% credible intervals for the posterior distributions shown in Fig. 6.9 for the two analyzed GW events (indicated in each row), recovered with IMRPhenomTEHM using different settings specified in the **Model** column and Tab. 6.1, as well as with the QC aligned-spin model IMRPhenomTHM through the `phenomxpy` infrastructure. For comparison, we also include results obtained using SEOBNRv5EHM from Tab IV, rows 2 and 7 from Ref. [20]. The table reports the same parameters as Tab. 6.2, as well as the log-10 Bayes factor between the eccentric (E) and the quasi-circular (QC) hypothesis $\log_{10} B_{\rm E/QC}$. All values are given at the reference frequency of 20 Hz for GW150914 and 5.5 Hz for GW190521.

$l_{20\rm Hz} \in [0, 2\pi]$, all defined at a reference frequency of $f_{\rm ref} = 20$ Hz. The specific run settings are detailed in Tab. 6.1.

The top rows of Fig. 6.9 and Tab. 6.3 present the results for GW150914 in the same format as those for the NR injections presented in Sec. 6.4.1. The table provides the median values along with the 90% credible intervals, while the figure display the marginalized 1D and 2D posterior distributions for the effective spin $\chi_{\rm eff}$, chirp mass $\mathcal{M}$, and GW eccentricity and mean anomaly $e^{\rm GW}$, $l^{\rm GW}$, respectively.

Our results obtained with IMRPhenomTEHM show exceptional agreement with results in the literature for this event [1, 61, 148]: the posteriors support a non-eccentric, non-spinning, comparable-mass BBH, independently of the gauge chosen for the secular evolution equations. Specifically, the recovered chirp mass $\mathcal{M}$ and effective spin $\chi_{\rm eff}$ parameters align closely with the posteriors obtained using the IMRPhenomTHM QC aligned-spin model, as seen in the upper left plot in Fig. 6.9. Regarding the eccentricity posterior, we obtain a median value of $e^{\rm GW}_{20\rm Hz} = 0.03^{+0.05}_{-0.03}$, proving support for zero eccentricity, as shown in the second and third columns of Fig. 6.9 and in Tab. 6.3. Additionally, we observe support for any mean anomaly value - although the posterior is not completely flat.

We also compute the log-10 Bayes factor between the eccentric (E) and the quasi-circular (QC) hypothesis, $\log_{10} B_{\rm E/QC}$, for each eccentric run, comparing to those obtained with IMRPhenomTHM. The values are listed in Tab. 6.3. These results indicate a slight preference for the QC hypothesis, consistent with the findings reported in Refs. [20, 54] for the SEOBNRv4EHM and SEOBNRv5EHM models. Additionally, the LVK analysis of this event [148] found no evidence of residual eccentricity.

6.4.2.2 GW190521

GW190521 is a particularly intriguing GW event that challenges our understanding of astrophysical BH formation channels, the accuracy of waveform models, and data analysis techniques. The detected signal is an exceptionally short transient, lasting approximately 0.1 seconds and spanning only about four cycles in the 30-80 Hz frequency band. The source was initially identified as a BBH merger with a total mass of approximately $150 M_\odot$

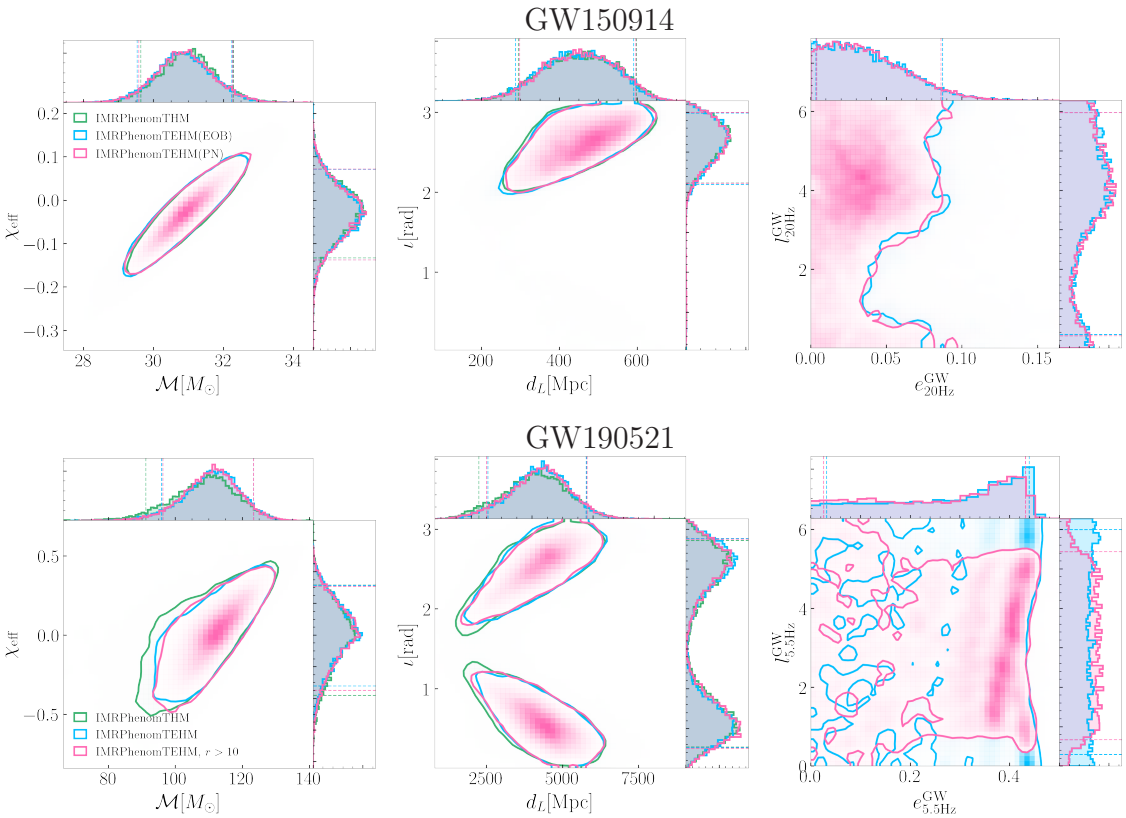

FIGURE 6.9: Posterior distributions for the parameter estimation studies of two real GW events, GW150914 (*top row*) and GW190521 (*bottom row*). The figure presents the posterior distributions of chirp mass and effective spin (*first column*), inclination angle and luminosity distance d_L (*second column*), and GW eccentricity and mean anomaly (*third column*). All parameters are measured at the reference frequency, which is $f_{\rm ref} = 20$ Hz for GW150914 and $f_{\rm ref} = 5.5$ Hz for GW190521.

in the source frame [49, 89, 137]. Due to the short signal duration, there exist strong degeneracies between source parameters, hindering a confident identification of the nature of the binary. Consequently, a wide range of alternative interpretations have been explored in the literature, including a hyperbolic collision [139], a boson star merger [138], a high-mass black hole-disk system [141], the first instance of an intermediate mass-ratio inspiral [140], and an eccentric binary merger [49], though other recent studies find no clear evidence of eccentricity [20, 54]. As in the case of GW150914, we adopt the priors introduced in Sec. 6.4, with boundaries $1/q \in [0.17, 1]$, $\mathcal{M} \in [60, 200]$, and $e_{5.5\rm Hz} \in [0, 0.5]$, $l_{5.5\rm Hz} \in [0, 2\pi]$, all defined at the reference frequency $f_{\rm ref} = 5.5$ Hz. The specific settings for all the runs performed are detailed in Tab. 6.1.

The bottom rows of Fig. 6.9 and Tab. 6.3 show the results for GW190521. The recovered chirp mass $\mathcal{M}$ and effective spin $\chi_{\rm eff}$ parameters lie within the posteriors obtained using the IMRPhenomTHM model, as shown in the bottom left plot in Fig. 6.9. These results are anticipated, since the main difference in the QC parameters arises when including precessing spin effects, as seen for instance in Refs. [20, 89, 137]. Regarding the eccentricity posterior, we find mostly uninformative posteriors. While the median values in Tab. 6.3 suggest high eccentricities, this simply reflects the properties of the given prior. Similarly, the mean anomaly posteriors are uninformative and consistent with a uniform prior. It is worth noting that the in the bottom right panel in Fig. 6.9, $e^{\rm GW}$ posteriors

do not reach the prior boundary, which arises because $e^{\rm GW}$ is generally slightly lower than $e^{\rm EOB}$. We leave for future work to explore the impact of directly using prior on $e^{\rm GW}$ to ensure consistency. These results are expected due to the quasi-circularity condition imposed in the merger-ringdown of IMRPhenomTEHM. This implies that any waveform with any eccentricity will exhibit a QC merger-ringdown phase, thus implying support for any case. Therefore, accurately measuring eccentricity in high-mass systems, where only the late part of the evolution falls within the frequency band of current detectors, requires incorporating eccentricity effects in that part of the waveform, which would likely involve calibration to NR. We plan to address these improvements in future work. We also compute the log-10 Bayes factor between the eccentric (E) and the quasi-circular (QC) hypothesis, $\log_{10} B_{\rm E/QC}$, for each eccentric run, comparing to those obtained with IMRPhenomTHM. The values are listed in Tab. 6.3. Even though these results indicate a slight preference for the eccentric hypothesis, the uncertainties in the default option allow support for the QC hypothesis as well. This aligns with previous findings using eccentric EOB models [20, 54, 55], where no evidence for eccentricity can be claimed for this event.

Finally, our posteriors on eccentricity differ from those obtained with the SEOBNRv4EHM and SEOBNRv5EHM models, as shown in Refs. [20, 54]. This discrepancy arises because IMRPhenomTEHM allows the starting frequency to be different than the reference frequency. In contrast, the SEOBNRv4EHM and SEOBNRv5EHM models are constrained to the have the same starting frequency and reference frequency ($f_{\rm ref} = f_{\rm min}$), and for sufficiently high starting frequency they do not generate waveforms, see Refs. [20, 356] for details. This artificial cut-off in waveform generation affects the priors, preventing uniform support across the full eccentricity range—especially restricting high eccentricities at high masses. To illustrate this, we impose a similar condition as in the SEOBNRv5EHM model by requiring an initial separation $r > 10M$, using the 3PN expansion from Ref. [39]. The resulting posteriors, shown in pink in the bottom row of Fig. 6.9, display almost no support for eccentricities $\gtrsim 0.3$ with mean anomaly near 0, i.e., periastron passage. This is expected, as highly eccentric systems starting near periastron have shorter waveforms than those starting near apastron. While our model does not exhibit the same posterior cuts as SEOBNRv5EHM due to differences in dynamics, this test confirms that truncating waveform generation can artificially restrict priors, a limitation we avoid by extending the waveform duration. We consider generating waveforms across the full parameter space a more realistic approach. However, extra caution needs to be taken into account when generating waveforms with initial eccentricities >0.5 at high frequencies due to the underlying PN prescription of eccentric effects and the tapering applied at merger to enforce a quasicircular merger ringdown.

A key aspect of the new IMRPhenomTEHM model is computational efficiency. The model is only 3 to 5 times slower than IMRPhenomTHM while offering a significant speedup compared to other eccentric models (see e.g. [20, 180, 356]). The significant reduction in wall time makes IMRPhenomTEHM a highly competitive model for parameter estimation studies. This efficiency sets IMRPhenomTEHM as a strong candidate to become a standard tool for parameter estimation in current and future GW detectors.

6.5 Conclusions

In this work, we presented IMRPhenomTEHM, a time-domain, multipolar waveform model designed for aligned-spin BBHs in elliptical orbits. IMRPhenomTEHM extends the time-domain phenomenological PhenomT waveform family [34, 190, 191] by incorporating 3PN eccentric corrections for the eccentric dynamics into the state-of-the-art quasicircular aligned-spin model IMRPhenomTHM. The model includes the waveform modes $(l, |m|) = \{(2,2), (2,1), (3,3), (4,4), (5,5)\}$, with PN corrections expanded in eccentricity up to $\mathcal{O}(e^6)$. IMRPhenomTEHM thus provides a reliable description of eccentric binaries with mass ratios $q \in [1, 20]$, aligned spins $\chi_i \in [-0.995, 0.995]$, and eccentricities up to $e = 0.4$ at 10 Hz. By default, we solve the secular evolution equations in EOB coordinates, but the model also supports modified-harmonic coordinates. Additionally, it allows for the inclusion of up to 3PN spinning eccentric effects in the GW modes [39, 513].

The construction of the IMRPhenomTEHM model is outlined in Sec. 6.2, with a summary provided in Sec. 6.2.1. The underlying QC model, IMRPhenomTHM, which serves as the foundation for the eccentric extension, is summarized in Sec. 6.2.2, while Sec. 6.2.3 describes the incorporation of the eccentric corrections in both the QC dynamics and waveform modes. We assess IMRPhenomTEHM's accuracy in the QC limit by computing mismatches against IMRPhenomTHM in Sec. 6.3.1, achieving values below 10^{-5} across the entire QC parameter space - a crucial characteristic to avoid biases in parameter estimation studies due to an inaccurate implementation of the quasicircular limit [54, 387]. In Sec. 6.3.2 we compute mismatches against 28 publicly available SXS eccentric simulations, and compare to other state-of-the-art eccentric models, TEOBResumS-Dalí and SEOBNRv5EHM. We find mismatches below 2% for most cases, with higher values than those for the SEOBNRv5EHM and TEOBResumS-Dalí models, yet sufficiently low to accurately recover posterior distributions in Bayesian inference studies, as confirmed in Sec. 6.4. To further investigate the robustness and accuracy of the IMRPhenomTEHM model, we computed mismatches against SEOBNRv5EHM in Sec. 6.3.4. Our results indicate that higher mismatches occur in regions of parameter space with limited coverage by NR waveforms, thus dominated by waveform systematic errors, whereas for mass ratios below 10 and eccentricities up to 0.4 at 10 Hz, mismatches remain below 5%. Furthermore, in Sec. 6.3.5, we estimate the model's computational efficiency, finding that IMRPhenomTEHM is the fastest time-domain eccentric IMR waveform model to date compared to SEOBNRv5EHM and TEOBResumS-Dalí. Section 6.4 demonstrates the model's applicability in PE studies. In Sec. 6.4.1, we injected three NR eccentric simulations, successfully recovering both the quasicircular and eccentric injected parameters within their 90% credible intervals. Finally, in Sec. 6.4.2, we reanalyzed the GW events GW150914 and GW190521, obtaining results consistent with the literature, particularly those from SEOBNRv5EHM [20].

An important feature of IMRPhenomTEHM is the ability to set a reference frequency different from the minimum frequency, significantly enhancing its practical applications. This ensures that one can freely choose the starting frequency for each physical configuration, preventing waveform generation errors that arise when initializing the PN/EOB evolution at small separations. Additionally, extending the waveform duration can also improve the conditioning routines on time-domain signals for Fourier transforming the waveforms. Consequently, this prevents the need for artificial cuts in priors for PE studies, as demonstrated for the high-mass short-duration event, GW190521, and providing

consistent results with Refs. [20, 54].

A key advantage of IMRPhenomTEHM is its computational efficiency, making it highly competitive for parameter estimation studies. We find that the model is only a few times slower than IMRPhenomTHM, while showing a significant improvement in speed compared to the eccentric SEOBNRv5EHM or TEOBResumS-Dalí models. The reduction in wall time (see e.g. Fig. 6.7) makes IMRPhenomTEHM a practical choice for large-scale Bayesian inference studies, positioning it as a strong candidate for standard parameter estimation pipelines in both current and future GW detector networks. Given these benchmarks and the proven accuracy of the model, we are currently undertaking a systematic re-analysis of GW events of interest reported by the LVK, which we plan to present in a follow-up paper.

Looking ahead, further improvements to IMRPhenomTEHM are planned to enhance its accuracy and applicability. While the current accuracy is sufficient for existing detectors, refinements are necessary for next-generation observatories. One key limitation of IMRPhenomTEHM is the treatment of eccentric corrections in the mode amplitudes. Currently, we rely on PN expansions up to $\mathcal{O}(e^6)$, which break down at high eccentricities due to the lack of closed-form tail terms. Future work will explore non-expanded expressions, leveraging recent re-summation techniques for tail contributions [510]. Additionally, highly eccentric waveforms at high frequencies may introduce nonphysical effects due to enforcing a quasi-circular merger-ringdown transition. Calibration to eccentric NR waveforms in this phase is necessary, particularly for high-mass and highly eccentric systems, when they have not circularized before merger. Although IMRPhenomTEHM can generate waveforms beyond its formal validity range without failing, careful interpretation is required in the cases described above. A detailed study of these regimes is left for future work. Expanding the model's applicability to include spin precession alongside eccentricity is another promising direction. A "twisting-up" approach [146, 290, 297, 298, 523], guided by PN evolution accounting for both eccentricity and spin-precession effects, could incorporate both effects. The modular structure of phenomenological models makes this a feasible short-term goal. These developments are crucial for next-generation GW detectors, where detection and accurate characterization of generic binaries, including spin precession and eccentricity, will provide valuable insights into the formation channels of these sources.

Acknowledgements

The authors thank Quentin Henry for valuable discussions and for providing additional material that contributed to this work. We also sincerely thank Gonzalo Morras for his helpful comments on the manuscript.

We thankfully acknowledge the computer resources at MareNostrum and the technical support provided by Barcelona Supercomputing Center (BSC) through funding from the Red Española de Supercomputación (RES). The authors are also grateful for computational resources provided by the cluster HAWK provided by Cardiff University and supported by STFC grants ST/I006285/1 and ST/V005618/1. This research has made use of data or software obtained from the Gravitational Wave Open Science Center (gwosc.org), a service of the LIGO Scientific Collaboration, the Virgo Collaboration, and KAGRA. This material is based upon work supported by NSF's LIGO Laboratory which is a major facility fully funded by the National Science Foundation. LIGO is funded by the U.S. National Science

Foundation. Virgo is funded by the French Centre National de Recherche Scientifique (CNRS), the Italian Istituto Nazionale della Fisica Nucleare (INFN) and the Dutch Nikhef, with contributions by Polish and Hungarian institutes.

Maria de Lluc Planas is supported by the Spanish Ministry of Universities via an FPU doctoral grant (FPU20/05577, EST24/00621). A. Ramos-Buades is supported by the Veni research programme which is (partly) financed by the Dutch Research Council (NWO) under the grant VI.Veni.222.396; acknowledges support from the Spanish Agencia Estatal de Investigación grant PID2022-138626NB-I00 funded by MICIU/AEI/10.13039/501100011033 and the ERDF/EU; is supported by the Spanish Ministerio de Ciencia, Innovación y Universidades (Beatriz Galindo, BG23/00056) and co-financed by UIB. CG is supported by the Swiss National Science Foundation (SNSF) Ambizione grant PZ00P2_223711. This work was supported by the Universitat de les Illes Balears (UIB); the Spanish Agencia Estatal de Investigación grants PID2022-138626NB-I00, PID2019-106416GB-I00, RED2022-134204-E, RED2022-134411-T, funded by MCIN/AEI/10.13039/501100011033; the MCIN with funding from the European Union NextGenerationEU/PRTR (PRTR-C17.I1); Comunitat Autonòma de les Illes Balears through the Direcció General de Recerca, Innovació I Transformació Digital with funds from the Tourist Stay Tax Law (PDR2020/11 - ITS2017-006), the Conselleria d'Economia, Hisenda i Innovació grant numbers SINCO2022/18146 and SINCO2022/6719, co-financed by the European Union and FEDER Operational Program 2021-2027 of the Balearic Islands; the "ERDF A way of making Europe".

CHAPTER 7

Eccentric or circular? A reanalysis of gravitational wave events

This chapter is based on the following article:

- Maria de Lluc Planas, Antoni Ramos-Buades, Cecilio García-Quirós, Héctor Estellés, Sascha Husa, and Maria Haney. "*Eccentric or circular? A reanalysis of gravitational wave events for orbital eccentricity signatures*", arXiV: arXiv:2504.15833[gr-qc] [22].

Abstract

We present a reanalysis of 17 gravitational-wave events detected with Advanced LIGO and Advanced Virgo in their first three observing runs, using the new IMRPhenomTEHM model – a phenomenological time-domain multipolar waveform model for aligned-spin black-hole binaries in elliptical orbits with two eccentric parameters: eccentricity and mean anomaly. We also analyze all events with the underlying quasi-circular model IMRPhenomTHM to study the impact of including eccentricity and compare the eccentric and quasi-circular binary hypotheses. The high computational efficiency of IMRPhenomTEHM enables us to explore the impact of two different eccentricity priors –uniform and log-uniform– as well as different sampler and data settings. We find evidence for eccentricity in two publicly available LVK events, GW200129 and GW200208_22, with Bayes factors favoring the eccentric hypothesis over the quasi-circular aligned-spin scenario: $\log_{10}\mathcal{B}_{\mathrm{E/QC}} \in \left[1.30^{+0.15}_{-0.15}, 5.14^{+0.15}_{-0.15}\right]$ and $\log_{10}\mathcal{B}_{\mathrm{E/QC}} \in \left[0.49^{+0.08}_{-0.08}, 1.14^{+0.08}_{-0.08}\right]$, respectively. Additionally, the two high-mass events GW190701 and GW190929 exhibit potential eccentric features. For all four events, we conduct further analyses to study the impact of different sampler settings. We also investigate waveform systematics by exploring the support for spin precession using IMRPhenomTPHM and NRSur7dq4, offering new insights into the formation channels of detected binaries. Our results highlight the importance of considering eccentric waveform models in future observing runs, alongside precessing models, as they can help mitigate potential biases in parameter estimation studies. This will be particularly relevant with the expected increase in the diversity of the binary black hole population with new detectors.

7.1 Introduction

The first three observing runs of the Advanced Ligo and Advanced Virgo detectors [472, 473] have led to the detection of more than 90 gravitational wave (GW) events [1–4, 325–330], all originating from compact object binaries. The majority of these events have been identified as binary black-hole (BBH) mergers, although several binary neutron star (BNS) and neutron star-black hole (NSBH) mergers have also been observed [5, 6, 8]. One of the key open questions in GW astrophysics is understanding the formation channels of these binaries.

The main uncertainty in the formation process stems from the fact that solely GW emission cannot drive widely separated binary stars into merging black holes (BHs) [319]. Therefore, to explain the formation of the observed population of BBHs two main formation scenarios have been proposed in the literature, *isolated evolution* and *dynamical formation*. Within these two scenarios many formation sub-channels exists, for instance, common-envelope evolution [524], Population III stars [525], or Zeipel-Kozai-Lidov oscillations [526–528], see Ref. [320] for a detailed review.

BBHs formed from isolated binary evolutions are expected to circularize due to efficient angular momentum loss via gravitational radiation long before they enter the sensitive frequency band of ground-based detectors [36]. Consequently, many existing GW waveform models for BBH mergers are constructed under the assumption of quasi-circular (QC) orbits [20, 21, 31–34, 171–184, 186–191]. Moreover, the LIGO-Virgo-KAGRA Collaboration (LVK) [1–4], as well as independent studies [325–330], have found that the observed GW signals are largely consistent with QC binaries, and a variety of mechanisms have been proposed for this case, such as common envelope evolution [331–335], chemically homogeneous evolution [336–338], stable mass accretion onto a black hole from its stellar companion [339, 340] or ambient gas-driven fallback [341].

The alternative formation channel, *dynamical formation*, can also lead to compact binary mergers within a Hubble time. In this scenario, the merger progenitors do not evolve together but instead form binaries dynamically through encounters in dense environments such as young star clusters, globular clusters, and galactic nuclei [342–344]. Frequent interactions in these regions can lead to compact objects swapping in and out of multiple binaries before ultimately merging. During a three-body interaction, gravitational binding energy from the initial binary is transferred to the ejected object, reducing the separation of the remaining binary and increasing the likelihood of a merger. Future observations by the LVK and next-generation detectors, such as the Einstein Telescope (ET) [11, 12], Cosmic Explorer (CE) [13], and space-based observatories like LISA [15, 345], will provide access to a broader frequency range and significantly increase the number of detected events. This will enhance our ability to probe the properties of compact binaries, making it critical to develop robust methods for characterizing their evolutionary histories.

The formation history of a binary is imprinted on its component masses, spins, and orbital eccentricity. Identifying these signatures in GW observations is crucial for distinguishing between formation channels, yet it remains challenging due to the high-dimensional parameter space of compact binaries and the sensitivity limits of current detectors. Orbital eccentricity in BBH mergers is a smoking gun of dynamical formation. Eccentricity can also help identify dark matter particles in ultralight boson clouds around BHs [529]. Since isolated binaries are expected to circularize before entering the LVK band,

the detection of eccentricity in a BBH merger would strongly suggest a dynamical origin such as globular clusters or galactic nuclei [321, 322], or through the Kozai-Lidov mechanism in triple systems [323, 324]. By studying the effects of eccentricity on GW signals, we can help quantify the fraction of BBH mergers arising from dynamical interactions. Several studies have attempted to identify signatures of eccentricity in compact binary mergers. Early analyses primarily incorporated a single eccentricity parameter using the likelihood reweighting (importance sampling) method [47, 530], used in works such as [46–53]. More recently, efforts have expanded to include two eccentricity parameters [19, 20, 54, 55], as neglecting one of these parameters has been shown to introduce biases in parameter estimation (PE) studies [54, 392].

Most of the aforementioned studies were constrained by various limitations, such as sampling only on non-eccentric parameters and reweighting with eccentric models, restricting the analysis to a limited number of events, or relying on machine learning techniques to mitigate the high computational cost of eccentric waveform models with two eccentric parameters. In Ref. [19], we recently introduced IMRPhenomTEHM, a time-domain phenomenological multipolar eccentric waveform model, which is built upon the aligned-spin QC model IMRPhenomTHM and represents the most computationally efficient eccentric inspiral-merger-ringdown (IMR) model to date. There, we already presented PE studies of two real events: GW150914 [61, 148], the first detected GW signal from a BBH, and GW190521 [89], a high total mass signal with potential signatures of eccentricity identified in the literature [49, 139]. These preliminary studies demonstrated the efficiency and accuracy of the model, recovering posteriors consistent with the literature. Neither of the events showed significant evidence for eccentricity. Specifically, the posteriors for GW190521 were uninformative, which aligns with the short duration of the signal and the fact that IMRPhenomTEHM, like other state-of-the-art eccentric models, assumes circularization at merger. As a result, we would not expect to observe imprints of eccentricity in the merger-ringdown part of the signal, which was observed by the detectors. These findings are also reflected in recent studies on this event [54, 55, 510].

In this work, we further analyze 17 BBH merger GW events identified in the literature as showing interesting features, such as precession, unequal masses, or potential eccentricity. We present results obtained using a uniform prior for eccentricity versus a logarithmic prior, and compare Bayes factors between the eccentric and QC hypotheses. We identify four events, GW190701, GW190929, GW200129, and GW200208_22, with a preference for the eccentric hypothesis, consistent with the findings in the literature [47, 55]. Among these, GW200129 and GW200208_22 show more support for eccentricity, while the evidence for eccentricity in GW190701 and GW190929 remains inconclusive. For these specific events, we conduct additional studies to examine the impact of various effects such as data treatment and sampler settings on the recovery of eccentricity. Moreover, we perform additional runs for these events using IMRPhenomTPHM, the precessing time-domain phenomenological waveform model from the same IMRPhenomT family, to study the preference for eccentricity over precession. Motivated by claims of precession for GW200129 [313], which were found only in precessing models that include mode asymmetries, we also conduct NRSur7dq4 [184] runs for this event.

This paper is structured as follows: In Sec.7.2, we describe the methodology employed in this work. In Sec. 7.3, we present our results starting with an overview of all analyzed events, followed by a discussion of those that exhibit evidence of eccentricity. Finally, in

Sec. 7.4, we summarize our main findings and discuss potential avenues for future research.

7.2 Methodology

In this section, we outline the methodology employed throughout this work. First, in Sec. 7.2.1, we revisit the notation and conventions used for parameterization. In Sec. 7.2.2, we describe the waveform models used for the analysis: the eccentric IMRPhenomTEHM model and its QC counterpart, IMRPhenomTHM, as well as a brief introduction to the precessing models IMRPhenomTPHM and NRSur7dq4. Next, in Sec. 7.2.3, we present the public data used for the analysis of the GW events. Finally, in Sec. 7.2.4, we introduce our methods for performing Bayesian inference and its application to determining whether a detected GW event is more likely to be described by a BBH moving on an eccentric or QC orbit.

7.2.1 Notation and conventions

Throughout this paper, component masses are denoted by m_i with $i = 1, 2$. We define the mass ratio $q = m_1/m_2 \geq 1$, the total mass $M = m_1 + m_2$, and the symmetric mass ratio $\eta = m_1 m_2/M^2$. The chirp mass is given by $\mathcal{M} = \frac{(m_1 m_2)^{3/5}}{M^{1/5}}$. Note that masses refer in general to the detector's frame. The z-component of the dimensionless spin magnitudes are denoted $\chi_i = S_i^z/m_i^2$, which correspond to the projections of the dimensionless component spin vectors onto the orbital angular momentum. We also report the effective-spin parameter $\chi_{\rm eff}$ [143–145], which captures the dominant nonprecessing-spin effects defined as

$$\chi_{\rm eff} = \frac{m_1\chi_1 + m_2\chi_2}{M}. \tag{7.2.1}$$

For the precessing runs performed with IMRPhenomTPHM and NRSur7dq4, we also provide the effective spin precession parameter $\chi_{\rm p}$ [146]. This parameter quantifies the in-plane spin effects, and corresponds to an approximate average over many precession cycles of the spins in the precessing orbital plane, given by

$$\chi_{\rm p} = \frac{S_{\rm p}}{A_1 m_1^2}. \tag{7.2.2}$$

Here, $S_{\rm p}$ is the average spin magnitude, given by

$$S_{\rm p} = \max(A_1 S_{1\perp}, A_2 S_{2\perp}), \tag{7.2.3}$$

where $A_1 = 2 + 3/2q$, and $A_2 = 2 + 3q/2$.

Comparing eccentric parameters across different waveform models requires additional post-processing due to the gauge dependence of eccentricity in General Relativity. The IMRPhenomTEHM model, for instance, allows for two different gauges for the eccentric parameters, denoted as $e^{\rm PN}$ and $e^{\rm EOB}$ corresponding to modified-harmonic PN (MH) and alternatively Effective-One-Body (EOB, *default*) coordinates (see Sec. III C in Ref. [19] for more details). However, gauge-invariant approaches to define eccentricity have been proposed, based on waveform modulations [385, 389] and catastrophe theory [511]. In this work, we adopt the waveform-based eccentricity definition from Ref. [386], denoted as $e^{\rm GW}$, and implemented in the `gw_eccentricity` python package [385]. This definition is

computed by measuring the instantaneous angular GW frequency of the $(2,2)$ spherical harmonic mode, ω_{22}, at the pericenters and apocenters of the orbits,

$$e^{\rm GW} = \cos(\psi/3) - \sqrt{3}\sin(\psi/3), \tag{7.2.4}$$

$$\psi = \arctan\left(\frac{1-e^2_{\omega_{22}}}{2e_{\omega_{22}}}\right), \tag{7.2.5}$$

$$e_{\omega_{22}} = \frac{\omega^{1/2}_{22,p} - \omega^{1/2}_{22,a}}{\omega^{1/2}_{22,p} + \omega^{1/2}_{22,a}}, \tag{7.2.6}$$

where $\omega^{1/2}_{22,p}$ and $\omega^{1/2}_{22,a}$ are the GW frequency of the $(2,2)$-mode at the periastra and apastra, respectively. Similarly, the GW mean anomaly is given by [142, 385]

$$l^{\rm GW}(t) = 2\pi\frac{t - t^p_i}{t^p_{i+1} + t^p_i}, \tag{7.2.7}$$

where t^p_i is the time of the $i-$th periastron passage measured from ω_{22}.

7.2.2 Waveform models

State-of-the-art gravitational IMR waveform models accurately describe BBHs in QC orbits, including also the effects of black holes spins. These models fall into three main families: the EOB formalism [240, 241], including SEOBNR [20, 31, 171–176] and TEOBResumS models [21, 32, 177–181]; NRSurrogate models [28, 182–185], which interpolate between NR datasets; and the IMRPhenom approach [33, 34, 186–191], known for its computational efficiency.

For the QC aligned-spin subspace, the models are calibrated to NR simulations and demonstrate strong agreement in the region where NR data is available [33, 34, 172, 183, 188]. Here, we employ the QC IMRPhenomTHM model [34], an extension of the time-domain IMR phenomenological model IMRPhenomT [191] to also include the subdominant spherical harmonics $(l,m) = \{(2,\pm1),(3,\pm3),(4,\pm4),(5,\pm5)\}$ in addition to the $(2,\pm2)$-modes. The model is calibrated to SEOB-NR hybrids, up to mass ratio 18, and to Teukolsky-based solutions in the extreme mass ratio limit. This results in an accurate and efficient model, widely used in GW astronomy [137, 476, 500].

Modeling precessing-spin binaries presents challenges due to the more complex waveform morphology and the larger parameter space involved, affecting all different modeling approaches [31, 184, 190, 294, 310]. In this work, we rely on both the IMRPhenomTPHM and NRSur7dq4 models. The state-of-the-art precessing time-domain model, IMRPhenomTPHM [190], uses approximations to model precession without NR calibration. While this increases its applicability across the parameter space, it comes at the cost of reduced accuracy. It includes the same multipoles as the underlying aligned-spin model IMRPhenomTHM, and the default implementation used in this work uses a numerical integration of the Euler angles to parameterize the binary evolution. One limitation of non-calibrated precessing models is the neglect of m-mode asymmetries, which can lead to biases in PE studies, as demonstrated in Ref. [313, 531]. To account for the limitations of this model, we also use the NRSur7dq4 [184] model, a more accurate precessing QC model, to study the precessing hypothesis for GW200129 claimed in other studies [313]. A key advantage of NRSur7dq4 is that it includes mode-m asymmetries,

which arise naturally from the numerical relativity simulations used in its calibration. NRSur7dq4 is however limited in its mass ratio, spin magnitudes, and waveform length coverage.

Similar challenges arise in modeling eccentric binaries. The increased parameter space and the limited availability of NR eccentric simulations complicate both the development and validation of accurate waveform models. A common approach in the literature is the assumption of circularization before merger, which has been used to construct hybrid IMR waveforms by combining EOB/PN-inspiral waveforms with merger and ringdown signals from NR or the EOB formalism [346–348]. Significant progress has been made within the EOB framework [43, 175, 176, 349–357], including recent efforts to develop generic IMR waveforms [21, 358]. Surrogate modeling has also been explored, but due to the scarcity of NR eccentric simulations, current models are reduced to comparable-mass and non-spinning binaries [45, 493]. The recently developed gwNRHME framework can convert multi-modal QC waveforms into multi-modal eccentric waveforms, for a given quadrupolar eccentric waveform from a non-spinning system [389, 491–493].

In this work, we use IMRPhenomTEHM, the first eccentric model of the IMRPhenomT family, which extends the QC IMRPhenomTHM [34, 191] model to eccentric binaries. It includes the full 3PN orbit-averaged dynamics, accounting for both non-spinning and spinning corrections [39], implemented in both modified harmonic PN (referred to as PN) and EOB coordinates (default option). Additionally, the waveform modes of IMRPhenomTHM are modified by incorporating non-spinning eccentric corrections up to 3PN for the non-spinning contributions [38], and up to 2PN nonprecessing-spin eccentric corrections [39], formulated in MH coordinates and expanded in eccentricity up to $\mathcal{O}(e^6)$. This limits the applicability of the model to BBHs with aligned spins and eccentricities below $e = 0.4$ at an orbit-averaged $(2, 2)$-mode frequency of 10 Hz.

7.2.3 GW real events data

We analyze 17 GW events from the public strain data available at the Gravitational Wave Open Science Center (GWOSC) [309, 522], using power spectral densities (PSDs) and calibration uncertainties provided by the LVK Collaboration. These events span the three observing runs (O1-O3) from mid-2015 to March 2020. During O1, the LIGO detectors were the only ones operational [532], and Virgo joined at the end of O2 in 2017 [1].

The selection of events in this work is based on particular and interesting features identified in previous studies. From GWTC1 [1], we analyze most of the detecting events, excluding those with very low total mass, such as GW170817 [5] (a binary neutron star merger) and GW170608. From GWTC2 [2, 3], we include GW190412 [268] due to its asymmetric masses and the impact of higher-order multipoles (HMs); GW190620, which has been argued to support a non-eccentricity explanation [53]; GW190701 and GW190706, both of which showed potential signs of eccentricity [55]; GW190814 [7], the most asymmetric system yet measured with GWs, with a secondary component being either the lightest BH or the heaviest NS ever discovered in a double compact-object system; and GW190828 and GW190929. Finally, from GWTC3 [4], we revisit GW200208_22, which showed potential eccentricity signatures [55, 315], and GW200129, initially reported as the first precessing binary detection [313] but later found to be affected by glitches [317, 533].

Several studies have been conducted to mitigate the known glitches in the event

GW200129, including the use of machine learning techniques [318, 534]. In this work, we use the frame files provided in the public release of Ref. [317] to assess the impact of glitch subtraction on the eccentricity posteriors. Specifically, Ref [317] employs the `gw_subtract` [533, 535] and `BayesWave` [536] glitch mitigation techniques. The `gw_subtract` method estimates and removes instrumental noise by using an auxiliary sensor at LIGO Livingston that monitors the noise source. The transfer function between this sensor and the main strain data channel is computed over a long period, allowing for an estimate of the noise contribution, which is then subtracted from the strain data. The effectiveness of this method depends on the accuracy of both the sensor and the transfer function estimate. This is the preferred technique employed in most analyses of this event [55, 313, 316] and is also used in the GWTC-3 LVK analysis [4]. On the other hand, `BayesWave` is a data analysis algorithm that models astrophysical signals, instrumental glitches, and Gaussian noise using a trans-dimensional Reversible-Jump Markov Chain Monte Carlo method [537]. It represents the signal with a waveform model and incoherent non-Gaussian noise with sine-Gaussian wavelets, while simultaneously modeling the PSD with a combination of cubic splines and Lorentzians. The algorithm infers posterior distributions for the signal, glitch, and PSD, from which one can draw realizations of the glitch and subtract them from the detector strain.

7.2.4 Parameter estimation: Bayesian inference

Bayesian inference is the standard statistical framework in GW astronomy to measure the source properties of the detected GW events. The Bayes' theorem allows to obtain a distribution of the set of parameters λ which characterize the GW source, provided that the observed GW signal in the detector data d can be described by a theoretical signal model $h_M(t;\lambda)$. The posterior probability distribution on λ given the signal model h_M, $P(\lambda|d,h_M)$, is given by

$$P(\lambda|d,h_M) = \frac{P(d|\lambda,h_M)P(\lambda|h_M)}{P(d|h_M)}. \tag{7.2.8}$$

Here, $P(d|\lambda,h_M)$ is the likelihood function, $P(\lambda|h_M)$ is the prior probability distribution, and $P(d|h_M)$ is the so called evidence of the model hypothesis h_M, normally represented by $\mathcal{Z}$, and defined as

$$\mathcal{Z} = P(d|h_M) = \int \mathrm{d}\lambda P(d|\lambda,h_M)P(\lambda|h_M). \tag{7.2.9}$$

In this work, we use `bilby` [113, 117] to compute the posterior distributions. By default, we use the nested sampler `dynesty` [115, 116], fixing the number of autocorrelation times to use before a point to `naccept=60` and the number of live points to `nlive=1000`.

For a detector with stationary, Gaussian noise, the likelihood function is

$$P(d|\lambda,h_M) \propto \exp\left[-\frac{1}{2}\langle d-h_M(\lambda)|d-h_M(\lambda)\rangle\right], \tag{7.2.10}$$

where the noise-weighted inner product is defined as

$$\langle A|B\rangle = 2\,\mathrm{Re}\int_{f_{\rm low}}^{f_{\rm high}} \mathrm{d}f \frac{\tilde{A}^*(f)\tilde{B}(f)+\tilde{A}(f)\tilde{B}^*(f)}{S_n(f)}. \tag{7.2.11}$$

Here, tildes denote Fourier transforms, asterisks denote complex conjugates, and $S_n(f)$ is the one-sided PSD of the detector. The integration limits $[f_{\rm low}, f_{\rm high}]$ define the detector's bandwidth, with $f_{\rm low} = 20$ Hz in all cases, while $f_{\rm high}$ varies per run according to the official LVK reanalysis [1–4]. For multiple detectors, we assume uncorrelated noise, so the network likelihood is the product of individual likelihoods.

Bayesian-inferred posteriors provide a useful tool for comparing different models. Specifically, they allow us to estimate the preference for an eccentric model, E, over a QC model, by comparing their probabilities given the detector data:

$$\mathcal{O}_{\rm E/QC} = \frac{P(h_{\rm E}|d)}{P(h_{\rm QC}|d)} = \frac{p(h_{\rm E})p(d|h_{\rm E})}{p(h_{\rm QC})p(d|h_{\rm QC})} = \tag{7.2.12}$$

$$= \frac{p(h_{\rm E})}{p(h_{\rm QC})}\frac{\mathcal{Z}_{\rm E}}{\mathcal{Z}_{\rm QC}} = \frac{p(h_{\rm E})}{p(h_{\rm QC})}\mathcal{B}_{\rm E/QC}. \tag{7.2.13}$$

The first ratio represents our *prior belief* about the occurrence of eccentric versus QC events in the universe. This prior knowledge can be inferred from previous GW observing runs, which provide event rate estimates for different populations. The second ratio, $\mathcal{B}_{\rm E/QC}$, is the Bayes factor, which quantifies the relative evidence for eccentricity compared to the QC assumption based on the observed data. In this work, we compute the log-10 Bayes factor, $\log_{10}\mathcal{B}_{\rm E/QC}$, which is positive when the eccentric model is preferred. Following Jeffreys' scale of evidence [103], we consider $\log_{10}\mathcal{B}_{\rm E/QC} > 1$ as a threshold for strong support in favor of eccentricity.

We adopt priors on the inverse mass ratio $(1/q)$ and chirp mass $(\mathcal{M})$ to ensure a uniform distribution in the component masses. For the spin components χ_i, we use priors corresponding to the projections of a uniform and isotropic spin distribution along a direction perpendicular to the binary's orbital plane [520]. For the luminosity distance d_L, we follow the simple prior proportional to d_L^2 [1–4], which distributes mergers uniformly through a stationary Euclidean universe. We set the starting frequency for the waveform generation at 10 Hz to ensure that the $l \leq 4$ modes remain within the analysis frequency band. Higher modes with $m > 2$ have higher frequency content over the same time interval, so the starting frequency must be adjusted based on the highest m-mode included in the analysis. While we include all available modes of the IMRPhenomTEHM model, we limit the starting frequency to the $l = 4$ mode. This is because the additional time required for conditioning, along with the small effect of the $(5, 5)$ mode at lower frequencies, make further reduction unnecessary for the waveform. Regarding the two extra priors for eccentric models, we set a uniform distribution for the mean anomaly at the reference frequency of 10 Hz, $l_{10\ \rm Hz} \in [0, 2\pi]$. For the eccentricity at the reference time, we consider two choices: *a)* a uniform prior, $e_{10\ \rm Hz} \in [0, 0.5]$, and *b)* a log-uniform prior with bounds $e_{10\ \rm Hz} \in [10^{-4}, 0.5]$. We analyze both priors to compare the resulting posterior distributions. The log-uniform prior is often used to express ignorance of the order of magnitude of the eccentricity, and is consistent with the astrophysical expectations that typical eccentricities will be very small. However, using a uniform prior avoids imposing a lower bound on the log-uniform prior, which could significantly affect Bayes factors by assigning excessive weight to low eccentricities in the evidence integral (Eq. (7.2.9)). The remaining priors, including the extrinsic parameters and the binary's orbital phase φ, are the same as in Ref. [1].

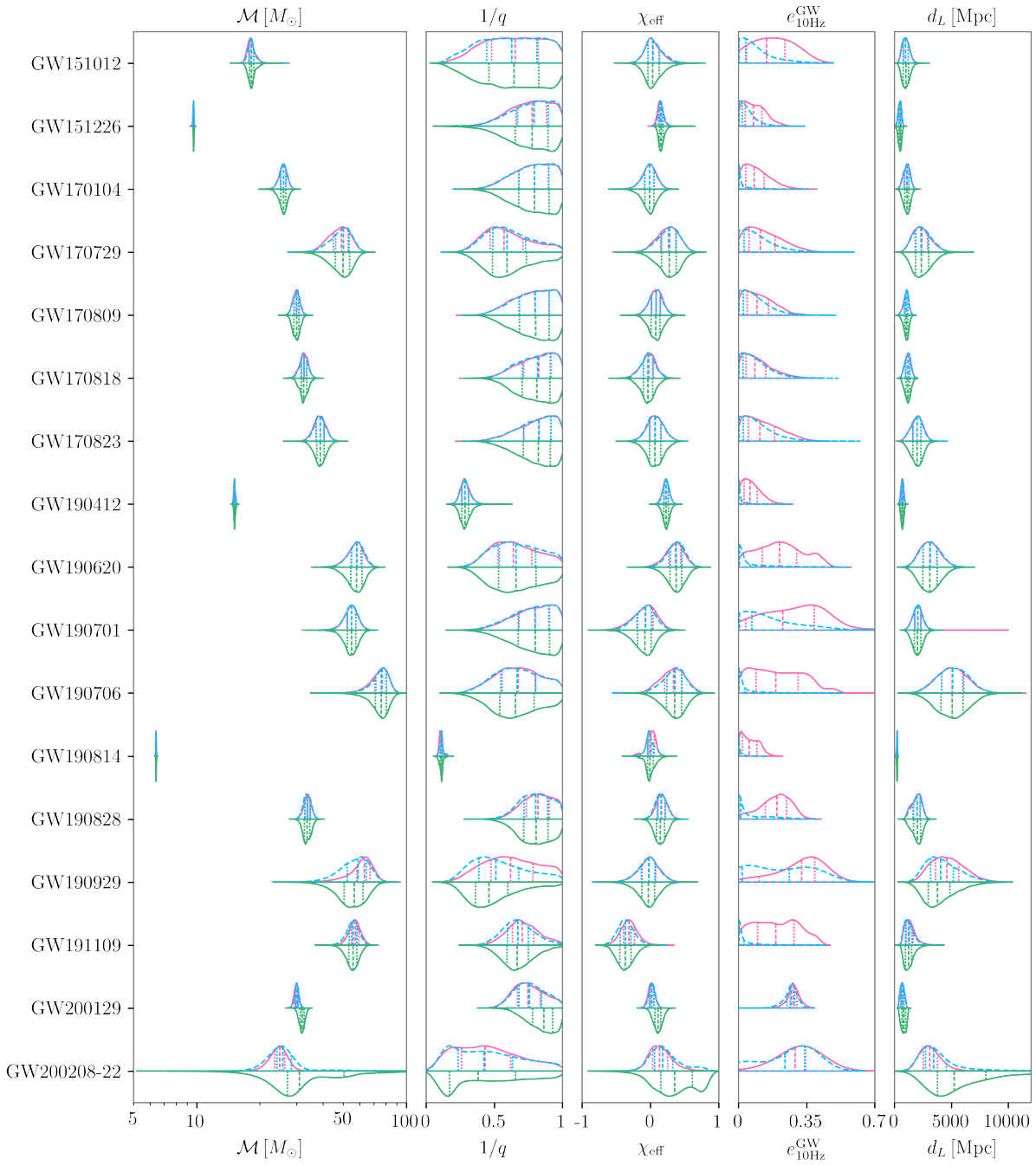

Figure 7.1: Marginal probability distributions for the chirp mass $\mathcal{M}$ in solar masses, inverse mass ratio $1/q$, effective spin $\chi_{\rm eff}$, reference GW eccentricity $e^{\rm GW}$, and luminosity distance d_L in Mpc for all analyzed events in this work, at a reference frequency of 10 Hz. The upper half of each violin plot represents the marginal posterior distributions for IMRPhenomTEHM using a uniform eccentricity prior (pink) and a logarithmic eccentricity prior (dashed blue), while the lower half shows those of the QC IMRPhenomTHM model (green). Vertical lines indicate the 90% credible intervals of each distribution.

7.3 Results

Figure 7.1 shows the marginal posterior probability distributions for the 17 BBH GW events analyzed in this study. The upper half of each violin plot presents the results obtained with the eccentric IMRPhenomTEHM model, while the lower half shows the results for the QC IMRPhenomTHM model. For the eccentric model, we include the distributions obtained with both the uniform and log-uniform eccentricity priors. In cases where no eccentricity signatures are found, the QC parameters exhibit qualitatively consistent distributions for both the IMRPhenomTHM and IMRPhenomTEHM models, regardless of the prior used.

A key outcome of this study is to demonstrate the ability of the IMRPhenomTEHM model to perform PE on large sets of events, including events with low total mass such as GW190814 [7]. This event, as found by the LVK Collaboration, corresponds to a compact binary system consisting of a $23.2^{+1.1}_{-1.0} M_\odot$ black hole and a $2.59^{+0.08}_{-0.09} M_\odot$ compact object, whose nature remains uncertain [7]. We do not find evidence of eccentricity in GW190814. Our analysis yields a GW eccentricity of $e^{\rm GW}_{\rm 10Hz} = 0.06^{+0.08}_{-0.05}$ with a negative significance of $\log_{10} \mathcal{B}_{\rm E/QC} = -0.24^{+0.18}_{-0.18}$ for the uniform prior, and $e^{\rm GW}_{\rm 10Hz} = 0.00^{+0.04}_{-0.00}$ with $\log_{10} \mathcal{B}_{\rm E/QC} = 0.04^{+0.18}_{-0.18}$ for the log-uniform prior, with negative values within errors. Notably, the model proves efficient in performing PE for this low-mass event, motivating a dedicated reanalysis of low-mass events in a companion paper [538], where we conduct the first full IMR study to search for eccentric features in these events.

Regarding the eccentricity posteriors, we find clear support for eccentricity in two events, GW200129, and GW200208_22, regardless of the prior choice. Both events have shown to exhibit signatures of eccentricity in previous studies [55, 315], and our analysis reveals distributions that agree across the different priors. These two events, however, warrant further investigation, and we present summarized results for both in Secs. 7.3.1 and 7.3.2.

We compute the log-10 Bayes factors between the eccentric and the QC hypotheses (both aligned and precessing spins), as defined in Eq. (7.2.8), and display them as a function of the measured eccentricity in Fig. 7.2. For GW200129, we observe a high value of the Bayes factor in favour of the eccentric hypothesis, which is also supported when using a log-uniform prior. In contrast, for GW200208_22, we find a $\log_{10} \mathcal{B}_{\rm E/QC}$ greater than 1 only when using the uniform prior. Detailed studies on both events are provided in Secs. 7.3.1 and 7.3.2, respectively. There are two additional events of particular interest. The first is GW190701, for which Ref. [55] finds support for eccentricity, while our analysis notably reduces this support when using a log-uniform prior. The second event is GW190929, where we observe some support for non-zero eccentricity. Nevertheless, for both cases the log-uniform prior shifts the eccentricity values lower. Still, the eccentric hypothesis cannot be completely ruled out, as residual support for eccentricity persists even when using finer sampler settings. These two events are studied in more detail in Sec. 7.3.3.

Furthermore, the posteriors for these four events differ significantly between the eccentric and QC waveform model. In particular, the last two rows of Fig. 7.1 show notable discrepancies in the chirp mass and the effective spin parameters between the QC and eccentric model results. A more detailed discussion of these discrepancies is provided in the following sections.

Event	Model	$M/M_\odot$	$\mathcal{M}/M_\odot$	$1/q$	$\chi_{\rm eff}$	$\chi_{\rm p}$	$e^{\rm GW}_{10\rm Hz}$	$l^{\rm GW}_{10\rm Hz}$	d_L	$\rm SNR^N$	$\log_{10}\mathcal{B}_{\rm E(P)/QC}$
GW190701	IMRPhenomTHM	$127.74^{+14.41}_{-13.52}$	$54.77^{+6.56}_{-6.90}$	$0.80^{+0.18}_{-0.30}$	$-0.08^{+0.22}_{-0.28}$	–	–	–	2034^{+733}_{-676}	$11.38^{+0.13}_{-0.25}$	–
	IMRPhenomTEHM Uni	$127.75^{+14.33}_{-13.93}$	$54.89^{+6.35}_{-7.02}$	$0.80^{+0.18}_{-0.29}$	$-0.07^{+0.24}_{-0.33}$	–	$0.29^{+0.17}_{-0.28}$	$3.41^{+2.54}_{-3.07}$	2054^{+700}_{-691}	$11.60^{+0.42}_{-0.39}$	$0.23^{+0.13}_{-0.13}$
	IMRPhenomTEHM Uni nlive=2000	$126.97^{+15.26}_{-14.17}$	$54.47^{+6.88}_{-7.41}$	$0.80^{+0.18}_{-0.31}$	$-0.09^{+0.26}_{-0.32}$	–	$0.29^{+0.17}_{-0.28}$	$3.35^{+2.61}_{-3.06}$	2024^{+715}_{-693}	$11.56^{+0.39}_{-0.36}$	$0.24^{+0.11}_{-0.11}$
	IMRPhenomTEHM LogUni	$127.83^{+14.80}_{-13.83}$	$54.85^{+6.67}_{-7.06}$	$0.80^{+0.18}_{-0.29}$	$-0.08^{+0.23}_{-0.29}$	–	$0.06^{+0.34}_{-0.06}$	$3.21^{+2.77}_{-2.89}$	2055^{+731}_{-683}	$11.41^{+0.22}_{-0.28}$	$0.08^{+0.12}_{-0.12}$
	IMRPhenomTEHM LogUni nlive=2000	$127.71^{+14.90}_{-14.14}$	$54.81^{+6.73}_{-7.35}$	$0.80^{+0.18}_{-0.30}$	$-0.08^{+0.23}_{-0.29}$	–	$0.06^{+0.35}_{-0.06}$	$3.22^{+2.76}_{-2.87}$	2040^{+724}_{-676}	$11.40^{+0.29}_{-0.27}$	$0.09^{+0.10}_{-0.10}$
	IMRPhenomTPHM	$130.58^{+17.82}_{-14.80}$	$55.98^{+7.91}_{-7.68}$	$0.80^{+0.18}_{-0.31}$	$-0.06^{+0.24}_{-0.29}$	$0.46^{+0.40}_{-0.35}$	–	–	2126^{+753}_{-711}	$11.37^{+0.15}_{-0.28}$	$0.05^{+0.12}_{-0.12}$
GW190929	IMRPhenomTHM	$141.64^{+23.26}_{-20.72}$	$56.32^{+13.07}_{-13.67}$	$0.46^{+0.41}_{-0.20}$	$-0.03^{+0.23}_{-0.27}$	–	–	–	3795^{+2916}_{-1675}	$9.96^{+0.40}_{-0.52}$	–
	IMRPhenomTEHM Uni	$150.66^{+22.43}_{-21.91}$	$62.99^{+10.09}_{-14.75}$	$0.61^{+0.34}_{-0.30}$	$-0.02^{+0.24}_{-0.27}$	–	$0.35^{+0.08}_{-0.32}$	$3.64^{+2.24}_{-3.19}$	4566^{+2692}_{-2042}	$10.24^{+0.39}_{-0.53}$	$0.56^{+0.11}_{-0.11}$
	IMRPhenomTEHM Uni nlive=2000	$150.33^{+22.74}_{-21.26}$	$63.00^{+10.16}_{-15.03}$	$0.62^{+0.33}_{-0.31}$	$-0.02^{+0.24}_{-0.28}$	–	$0.35^{+0.08}_{-0.32}$	$3.57^{+2.35}_{-3.13}$	4602^{+2618}_{-2042}	$10.23^{+0.40}_{-0.52}$	$0.56^{+0.09}_{-0.09}$
	IMRPhenomTEHM LogUni	$144.78^{+23.75}_{-21.91}$	$59.03^{+12.31}_{-15.37}$	$0.51^{+0.40}_{-0.24}$	$-0.02^{+0.23}_{-0.27}$	–	$0.18^{+0.25}_{-0.17}$	$3.43^{+2.54}_{-3.08}$	4048^{+2878}_{-1821}	$10.07^{+0.46}_{-0.57}$	$0.19^{+0.10}_{-0.10}$
	IMRPhenomTEHM LogUni nlive=2000	$144.59^{+23.86}_{-21.98}$	$58.81^{+12.54}_{-15.33}$	$0.51^{+0.41}_{-0.25}$	$-0.02^{+0.24}_{-0.28}$	–	$0.19^{+0.24}_{-0.18}$	$3.32^{+2.64}_{-2.97}$	4060^{+2915}_{-1822}	$10.07^{+0.46}_{-0.57}$	$0.19^{+0.09}_{-0.09}$
	IMRPhenomTPHM	$146.93^{+41.35}_{-21.57}$	$57.46^{+18.60}_{-14.45}$	$0.44^{+0.42}_{-0.22}$	$0.03^{+0.28}_{-0.26}$	$0.39^{+0.43}_{-0.30}$	–	–	3716^{+3077}_{-1626}	$10.03^{+0.59}_{-0.58}$	$0.09^{+0.11}_{-0.11}$
GW200129 GWOSC	IMRPhenomTHM	$73.54^{+3.52}_{-3.28}$	$31.83^{+1.56}_{-1.56}$	$0.86^{+0.12}_{-0.19}$	$0.11^{+0.10}_{-0.11}$	–	–	–	818^{+317}_{-347}	$26.27^{+0.13}_{-0.17}$	–
	IMRPhenomTEHM Uni	$69.81^{+2.51}_{-2.34}$	$29.93^{+1.17}_{-1.23}$	$0.75^{+0.21}_{-0.16}$	$0.02^{+0.08}_{-0.08}$	–	$0.28^{+0.05}_{-0.06}$	$2.77^{+3.10}_{-2.40}$	686^{+288}_{-272}	$26.94^{+0.13}_{-0.20}$	$5.14^{+0.15}_{-0.15}$
	IMRPhenomTEHM LogUni	$70.18^{+2.33}_{-2.24}$	$30.09^{+1.17}_{-1.10}$	$0.76^{+0.19}_{-0.17}$	$0.02^{+0.08}_{-0.08}$	–	$0.27^{+0.05}_{-0.07}$	$2.60^{+3.35}_{-2.29}$	689^{+297}_{-257}	$26.92^{+0.15}_{-0.20}$	$4.19^{+0.15}_{-0.15}$
	IMRPhenomTHM nlive=2000(H1)	$74.59^{+5.79}_{-5.48}$	$32.17^{+2.52}_{-2.61}$	$0.83^{+0.15}_{-0.23}$	$0.12^{+0.16}_{-0.17}$	–	–	–	1168^{+586}_{-585}	$14.73^{+0.11}_{-0.20}$	–
	IMRPhenomTEHM Uni nlive=2000(H1)	$72.90^{+5.76}_{-4.54}$	$31.41^{+2.57}_{-2.20}$	$0.82^{+0.16}_{-0.23}$	$0.09^{+0.16}_{-0.15}$	–	$0.18^{+0.14}_{-0.16}$	$3.08^{+2.88}_{-2.76}$	1166^{+535}_{-578}	$14.83^{+0.19}_{-0.26}$	$-0.06^{+0.08}_{-0.08}$
	IMRPhenomTEHM LogUni nlive=2000(H1)	$74.37^{+5.72}_{-5.14}$	$32.07^{+2.51}_{-2.42}$	$0.83^{+0.15}_{-0.22}$	$0.12^{+0.16}_{-0.16}$	–	$0.01^{+0.21}_{-0.01}$	$3.15^{+2.82}_{-2.81}$	1181^{+563}_{-596}	$14.75^{+0.15}_{-0.21}$	$0.02^{+0.08}_{-0.08}$
GW200129 gw_subtract	IMRPhenomTHM	$73.05^{+3.53}_{-3.18}$	$31.49^{+1.60}_{-1.53}$	$0.81^{+0.17}_{-0.18}$	$0.09^{+0.10}_{-0.11}$	–	–	–	894^{+328}_{-367}	$25.93^{+0.12}_{-0.17}$	–
	IMRPhenomTEHM Uni	$70.42^{+2.36}_{-1.94}$	$30.08^{+1.12}_{-0.96}$	$0.71^{+0.18}_{-0.13}$	$0.02^{+0.08}_{-0.07}$	–	$0.26^{+0.04}_{-0.07}$	$2.72^{+3.29}_{-2.42}$	775^{+290}_{-310}	$26.49^{+0.14}_{-0.20}$	$4.00^{+0.15}_{-0.15}$
	IMRPhenomTEHM LogUni	$70.64^{+2.30}_{-2.02}$	$30.20^{+1.11}_{-0.98}$	$0.72^{+0.18}_{-0.14}$	$0.03^{+0.08}_{-0.07}$	–	$0.26^{+0.04}_{-0.07}$	$2.79^{+3.20}_{-2.53}$	773^{+290}_{-311}	$26.49^{+0.15}_{-0.20}$	$3.35^{+0.15}_{-0.15}$
	IMRPhenomTPHM	$73.28^{+4.04}_{-3.36}$	$31.56^{+1.71}_{-1.61}$	$0.79^{+0.18}_{-0.18}$	$0.08^{+0.11}_{-0.11}$	$0.42^{+0.39}_{-0.30}$	–	–	896^{+323}_{-333}	$25.99^{+0.17}_{-0.19}$	$0.11^{+0.14}_{-0.14}$
	NRSur7dq4	$73.31^{+3.38}_{-2.79}$	$30.18^{+2.01}_{-1.71}$	$0.54^{+0.38}_{-0.13}$	$0.00^{+0.12}_{-0.12}$	$0.81^{+0.15}_{-0.54}$	–	–	1121^{+193}_{-287}	$26.20^{+0.16}_{-0.23}$	$2.12^{+0.14}_{-0.14}$
GW200129 BayesA	IMRPhenomTHM	$76.65^{+3.50}_{-3.26}$	$33.19^{+1.55}_{-1.55}$	$0.86^{+0.13}_{-0.17}$	$0.22^{+0.09}_{-0.10}$	–	–	–	967^{+329}_{-405}	$26.71^{+0.11}_{-0.15}$	–
	IMRPhenomTEHM Uni	$74.32^{+2.66}_{-2.22}$	$32.05^{+1.24}_{-1.03}$	$0.81^{+0.16}_{-0.15}$	$0.17^{+0.08}_{-0.07}$	–	$0.21^{+0.05}_{-0.08}$	$2.93^{+3.13}_{-2.70}$	854^{+332}_{-349}	$27.04^{+0.14}_{-0.19}$	$1.86^{+0.15}_{-0.15}$
	IMRPhenomTEHM LogUni	$74.64^{+2.92}_{-2.27}$	$32.22^{+1.35}_{-0.98}$	$0.82^{+0.15}_{-0.14}$	$0.18^{+0.08}_{-0.07}$	–	$0.19^{+0.06}_{-0.14}$	$3.28^{+2.69}_{-2.97}$	858^{+336}_{-337}	$27.03^{+0.16}_{-0.26}$	$1.30^{+0.15}_{-0.15}$
	IMRPhenomTPHM	$77.54^{+3.66}_{-3.75}$	$33.52^{+1.48}_{-1.66}$	$0.84^{+0.14}_{-0.16}$	$0.23^{+0.09}_{-0.11}$	$0.48^{+0.34}_{-0.29}$	–	–	1061^{+268}_{-398}	$26.76^{+0.12}_{-0.16}$	$0.11^{+0.15}_{-0.15}$
	NRSur7dq4	$77.26^{+4.70}_{-4.32}$	$33.13^{+1.74}_{-1.99}$	$0.77^{+0.20}_{-0.21}$	$0.19^{+0.10}_{-0.12}$	$0.58^{+0.33}_{-0.36}$	–	–	1170^{+259}_{-440}	$26.84^{+0.12}_{-0.17}$	$1.17^{+0.15}_{-0.15}$
GW200129 BayesB	IMRPhenomTHM	$75.48^{+3.56}_{-3.40}$	$32.63^{+1.59}_{-1.54}$	$0.85^{+0.13}_{-0.18}$	$0.18^{+0.10}_{-0.10}$	–	–	–	968^{+325}_{-400}	$26.30^{+0.12}_{-0.15}$	–
	IMRPhenomTEHM Uni	$72.69^{+2.52}_{-2.29}$	$31.26^{+1.15}_{-1.09}$	$0.77^{+0.18}_{-0.15}$	$0.11^{+0.08}_{-0.08}$	–	$0.24^{+0.04}_{-0.07}$	$2.95^{+3.10}_{-2.72}$	806^{+324}_{-325}	$26.75^{+0.15}_{-0.19}$	$2.90^{+0.15}_{-0.15}$
	IMRPhenomTEHM LogUni	$73.11^{+2.70}_{-2.30}$	$31.46^{+1.26}_{-1.09}$	$0.78^{+0.17}_{-0.14}$	$0.12^{+0.08}_{-0.08}$	–	$0.22^{+0.05}_{-0.08}$	$3.00^{+3.05}_{-2.79}$	820^{+341}_{-351}	$26.73^{+0.15}_{-0.21}$	$2.13^{+0.15}_{-0.15}$
	IMRPhenomTPHM	$75.95^{+3.63}_{-3.56}$	$32.80^{+1.55}_{-1.67}$	$0.82^{+0.16}_{-0.16}$	$0.17^{+0.10}_{-0.11}$	$0.46^{+0.36}_{-0.30}$	-	-	1028^{+286}_{-378}	$26.35^{+0.13}_{-0.16}$	$0.04^{+0.14}_{-0.14}$
	NRSur7dq4	$75.15^{+4.62}_{-3.27}$	$31.69^{+2.47}_{-2.05}$	$0.67^{+0.29}_{-0.20}$	$0.11^{+0.13}_{-0.13}$	$0.75^{+0.21}_{-0.47}$	–	–	1182^{+220}_{-431}	$26.51^{+0.15}_{-0.18}$	$1.70^{+0.14}_{-0.14}$
GW200129 BayesC	IMRPhenomTHM	$75.00^{+3.62}_{-3.24}$	$32.47^{+1.55}_{-1.52}$	$0.86^{+0.13}_{-0.18}$	$0.16^{+0.10}_{-0.10}$	–	–	–	987^{+324}_{-415}	$25.59^{+0.12}_{-0.16}$	–
	IMRPhenomTEHM Uni	$72.55^{+2.61}_{-2.44}$	$31.23^{+1.22}_{-1.18}$	$0.79^{+0.17}_{-0.16}$	$0.10^{+0.08}_{-0.08}$	–	$0.24^{+0.04}_{-0.08}$	$2.78^{+3.27}_{-2.56}$	831^{+347}_{-348}	$26.05^{+0.15}_{-0.20}$	$2.82^{+0.15}_{-0.15}$
GW200208_22	IMRPhenomTHM	$90.39^{+108.92}_{-29.85}$	$30.32^{+48.65}_{-8.45}$	$0.39^{+0.53}_{-0.30}$	$0.37^{+0.45}_{-0.45}$	–	–	–	5066^{+9043}_{-2711}	$7.22^{+0.56}_{-1.89}$	–
	IMRPhenomTHM nlive=2000	$95.10^{+153.18}_{-34.29}$	$30.91^{+62.42}_{-8.73}$	$0.38^{+0.54}_{-0.29}$	$0.36^{+0.46}_{-0.46}$	–	–	–	5247^{+10830}_{-2852}	$7.19^{+0.58}_{-3.49}$	
	IMRPhenomTEHM Uni	$65.35^{+45.54}_{-7.84}$	$24.95^{+4.62}_{-3.57}$	$0.43^{+0.46}_{-0.31}$	$0.13^{+0.33}_{-0.23}$	–	$0.33^{+0.05}_{-0.16}$	$2.99^{+2.94}_{-2.69}$	3101^{+2176}_{-1264}	$8.37^{+0.53}_{-0.98}$	$0.96^{+0.12}_{-0.12}$
	IMRPhenomTEHM Uni nlive=2000	$65.75^{+52.42}_{-8.39}$	$24.73^{+6.41}_{-4.05}$	$0.39^{+0.48}_{-0.27}$	$0.15^{+0.31}_{-0.24}$	–	$0.34^{+0.08}_{-0.18}$	$3.07^{+2.87}_{-2.74}$	3021^{+2662}_{-1260}	$8.44^{+0.64}_{-1.15}$	$1.14^{+0.08}_{-0.08}$
	IMRPhenomTEHM LogUni	$68.43^{+112.66}_{-10.34}$	$25.82^{+39.26}_{-4.19}$	$0.42^{+0.48}_{-0.31}$	$0.18^{+0.51}_{-0.28}$	–	$0.31^{+0.09}_{-0.30}$	$3.02^{+2.95}_{-2.72}$	3466^{+7332}_{-1504}	$8.09^{+0.76}_{-2.17}$	$0.09^{+0.11}_{-0.11}$
	IMRPhenomTEHM LogUni nlive=2000	$68.54^{+114.84}_{-10.36}$	$25.95^{+40.04}_{-4.35}$	$0.43^{+0.48}_{-0.32}$	$0.19^{+0.52}_{-0.29}$	$0.00^{+0.00}_{-0.00}$	$0.29^{+0.09}_{-0.28}$	$3.07^{+2.90}_{-2.78}$	3482^{+7371}_{-1539}	$8.06^{+0.77}_{-2.17}$	$0.49^{+0.08}_{-0.08}$
	IMRPhenomTPHM	$99.61^{+136.58}_{-38.39}$	$33.15^{+57.49}_{-9.57}$	$0.42^{+0.50}_{-0.32}$	$0.36^{+0.47}_{-0.48}$	$0.41^{+0.42}_{-0.31}$	-	-	5308^{+10430}_{-2855}	$7.22^{+0.68}_{-2.38}$	$-0.26^{+0.10}_{-0.10}$
	IMRPhenomXPHM	$173.89^{+100.26}_{-106.75}$	$45.51^{+31.26}_{-19.64}$	$0.16^{+0.63}_{-0.10}$	$0.67^{+0.21}_{-0.62}$	$0.43^{+0.37}_{-0.29}$	-	-	5816^{+7900}_{-2947}	$7.33^{+1.15}_{-2.04}$	–

Table 7.1: Median values and 90% credible intervals of the posterior distributions for the analyzed GW events (indicated in each row). The parameters displayed are the total mass M and chirp mass $\mathcal{M}$ in solar masses (both in the detector's frame), the inverse mass ratio $1/q$, the effective spin parameter $\chi_{\rm eff}$, the reference GW eccentricity, $e^{\rm GW}_{10\rm Hz}$, and GW mean anomaly $l^{\rm GW}_{10\rm Hz}$, the luminosity distance d_L, and the network matched-filtered SNR, $\rm SNR^N$. The last column shows the log-10 Bayes factor between the eccentric (E) and the QC aligned-spin (QC) hypothesis $\log_{10}\mathcal{B}_{\rm E/QC}$, or between the the QC precessing-spin (P) and QC hypothesis $\log_{10}\mathcal{B}_{\rm P/QC}$. The spins and eccentric parameters are given at the reference frequency of 10 Hz. For GW200129, we present results obtained using different datasets: first, the non-deglitched publicly released `GWOSC` data [309], followed by the `gw_subtract` data, and finally, the `BayesWave` technique, which provides three distinct draws: `BayesA`, `BayesB`, and `BayesC`. For GW200208_22, we include the official LVK samples using the IMRPhenomXPHM model from GWTC-3 [4].

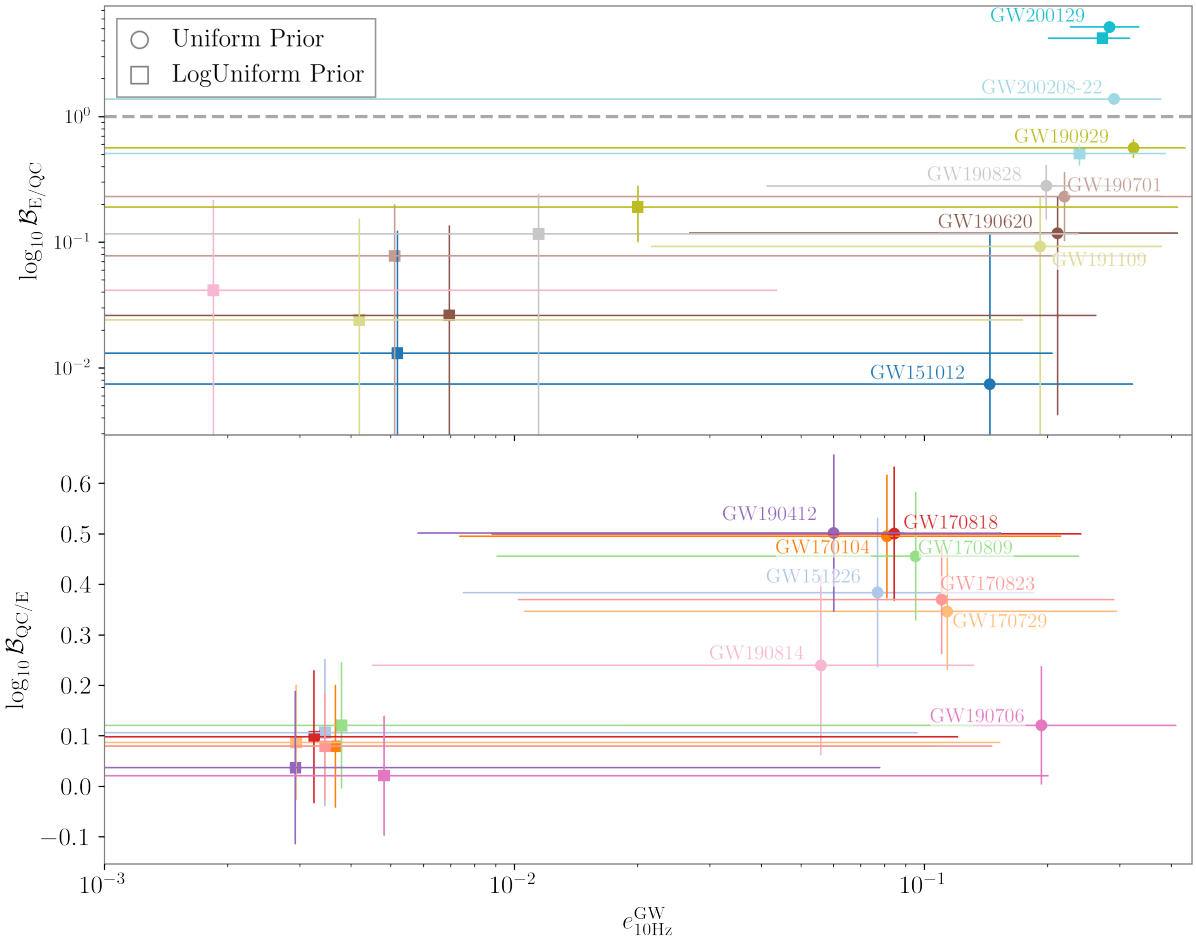

Figure 7.2: Log-10 Bayes factors comparing the eccentric (E) and aligned quasi-circular (QC) hypotheses for each analyzed GW event, plotted against the mean inferred GW eccentricity at the reference frequency, $e^{\mathrm{GW}}_{10\mathrm{Hz}}$. The top panel displays the factor for cases that favor the eccentric hypothesis ($\log_{10} \mathcal{B}_{\mathrm{E/QC}} \geq 0$), while the bottom panel shows the events that favor the QC hypothesis ($\log_{10} \mathcal{B}_{\mathrm{QC/E}} \geq 0$). In the top panel, we include a dashed gray line at $\log_{10} \mathcal{B}_{\mathrm{E/QC}} = 0$ to indicate the threshold for support in favor of the eccentric hypothesis. Circles denote results obtained using a uniform eccentricity prior, whereas squares represent those using a logarithmic prior. Horizontal lines indicate the 90% credible intervals for the GW eccentricity posteriors. Different colors distinguish the GW events, with labels placed next to their corresponding uniform prior points.

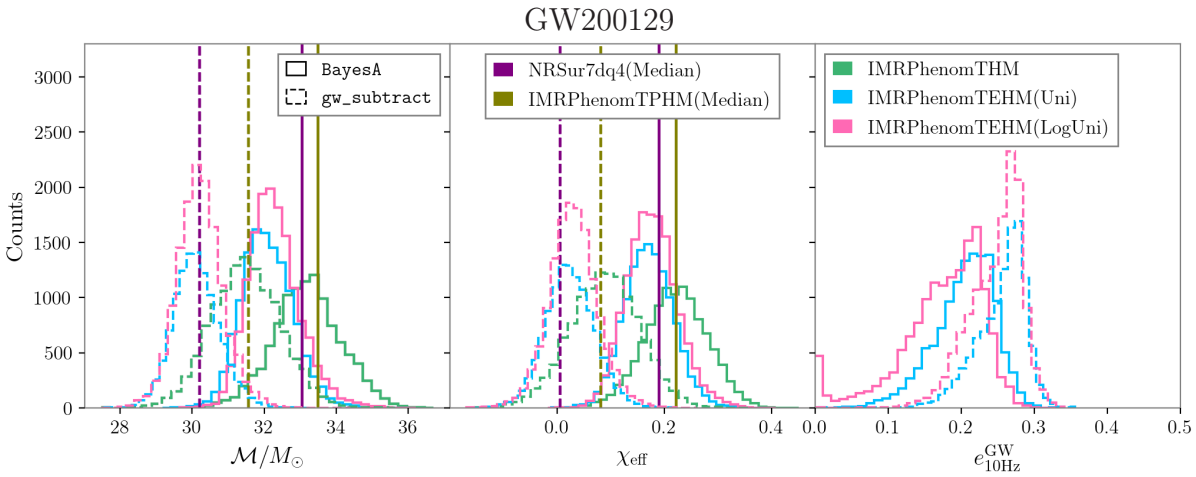

Figure 7.3: Posterior distributions for the chirp mass, effective spin, and GW eccentricity at a reference frequency of 10 Hz for GW200129. Results are shown for the `gw_subtract` (*dashed-lines*) and `BayesA` (*continuous-lines*) glitch mitigation techniques. The distributions are provided for both the QC IMRPhenomTHM (*green*) and eccentric IMRPhenomTEHM models, using uniform (Uni, *blue*) and log-uniform (LogUni, *pink*) priors. The median values for the IMRPhenomTPHM (*dark green*) and NRSur7dq4 (*purple*) runs are included for comparison to highlight the impact of precessing features on the posterior distributions for both datasets.

7.3.1 GW200129

GW200129 is an event of particular interest due to various imprints suggesting a possible dynamical formation channel. Additionally, the binary's low mass –allowing for several inspiral cycles within the detector's frequency band– and its relatively high SNR (~ 26, see Tab. 7.1 for details) make it well-suited for characterizing these effects. Previous studies have identified signatures of spin precession [313], evidence of a significant kick velocity [314], and indications of orbital eccentricity [55, 315], as well as false violations of general relativity due to waveform systematics [316]. The GWTC-3 catalog [4] reports an effective-spin parameter of $\chi_{\rm eff} = 0.11^{+0.11}_{-0.16}$, a total mass of $M = 63.3^{+4.5}_{-3.4} M_\odot$, a luminosity distance of $d_L = 890^{+260}_{-370}$ Mpc, and a network matched-filter signal-to-noise ratio of SNR $= 26.8^{+0.2}_{-0.2}$. However, this event also presents a glitch in LIGO Livingston data within the 20–50 Hz frequency range, and different glitch mitigation techniques have been shown to significantly affect the support for spin precession [317, 318].

To further investigate the nature of GW200129, we present the first eccentric analysis using standard PE techniques typically applied to QC binaries [4]. Additionally, we extensively investigate various glitch mitigation techniques and their impact on eccentricity recovery, employing both a uniform eccentricity prior and a log-uniform prior. Specifically, we consider data obtained directly from GWOSC for all three detectors, as well as the glitch-mitigated data from Ref. [317], where the `gw_subtract` mitigation technique and `BayesWave` were applied. For the latter, we use three different glitch draws, denoted as `BayesA`, `BayesB`, and `BayesC`. Due to inconsistencies identified in the Virgo detector, as detailed in Ref. [317], we restrict our deglitched analyses to the LIGO detectors. Additionally, we analyze this event using the QC precessing-spin model of the IMRPhenomT family, IMRPhenomTPHM [190], as well as the NRSur7dq4 model [184].

Our findings are summarized in Tab. 7.1 and are largely consistent with those reported in Ref. [55]. We observe large variations in the measurement of parameters depending on the data used for the analysis. Specifically, the original data containing the glitch (labeled as `GWOSC`) favors the presence of orbital eccentricity over the QC hypothesis. The Bayes factors shown in Tab. 7.1 strongly support, when using non-precessing models, the eccentric hypotheses over the QC scenario, with $\log_{10}\mathcal{B}_{\rm E/QC}$=$5.14^{+0.15}_{-0.15}$ and $\log_{10}\mathcal{B}_{\rm E/QC}$=$4.19^{+0.15}_{-0.15}$ when using a uniform and log-uniform prior in eccentricity, respectively. However, different glitch mitigation techniques introduce significant variations in these factors, as previously observed with precessing QC models. For this reason, we do not perform precessing QC runs on these non-deglitched data, as the noise artifact has been shown to limit the conclusions of the analysis [313, 317].

The results obtained using `gw_subtract` are shown in Tab. 7.1. For these data, we perform PE runs using all models, IMRPhenomTHM, IMRPhenomTPHM, NRSur7dq4, and IMRPhenomTEHM, both using a uniform and log-uniform prior in eccentricity. Figure 7.3 shows the posterior distributions for the chirp mass, effective spin, and eccentricity evaluated at a reference frequency of 10 Hz. Results for IMRPhenomTEHM include both uniform (denoted as Uni) and log-uniform (LogUni) eccentricity priors. Furthermore, the median values obtained from the QC precessing-spin IMRPhenomTPHM and NRSur7dq4 runs are indicated in Fig. 7.3. These results closely align with the results obtained with the `GWOSC` dataset, exhibiting strong support for a GW eccentricity of $e^{\rm GW}_{\rm 10Hz} = 0.26^{+0.04}_{-0.07}$ consistent between the uniform and log-uniform prior, with Bayes factors of $4.00^{+0.15}_{-0.15}$ and $3.35^{+0.15}_{-0.15}$, respectively. These values strongly suggest a preference for the eccentric hypothesis, though slightly lower than that obtained with the non-deglitched data. Notably, the QC precessing-spin hypothesis also remains favored over the aligned-spin QC scenario. As already reported in Ref. [313], the IMRPhenomTPHM model shows minor support for spin precession, and we find a Bayes factor of $\log_{10}\mathcal{B}_{\rm P/QC}$=$0.11^{+0.14}_{-0.14}$, while NRSur7dq4 is notably preferred over the QC aligned-spin hypothesis, with a Bayes factor of $\log_{10}\mathcal{B}_{\rm P/QC}$=$2.12^{+0.14}_{-0.14}$. However, these values remain significantly smaller than those obtained with the eccentric IMRPhenomTEHM model, regardless of the prior choice. An interesting feature observable in Fig. 7.3 is that the median values of the recovered chirp mass and effective spin using NRSur7dq4 for `gw_subtract` data (dashed lines in the plot) agree much better with the distributions obtained using IMRPhenomTEHM rather than IMRPhenomTHM. However, this is not the case for IMRPhenomTPHM, which recovers values more consistent with those of the aligned-spin run (shown in light green in the plots). We thus find that the eccentric model posteriors agree better with the precessing surrogate, indicating a preference for dynamical effects in this event over the aligned-spin QC hypothesis, and highlighting the degeneracy between eccentricity and precession. For studies of similar degeneracies in the context of other events, see e.g. Refs. [539, 540]. A more detailed study would require the inclusion of spin-precessing effects in IMRPhenomTEHM, which we leave for future work.

To visually assess the impact of incorporating eccentricity and to compare it with the precessing scenario, we show in the top panel of Fig. 7.5 the whitened data using the `gw_subtract` data, overlaid with the reconstructed maximum likelihood waveforms from the two eccentric runs with IMRPhenomTEHM using uniform and log-uniform eccentricity priors, the aligned-spin QC run with IMRPhenomTHM, and the NRSur7dq4 waveform. Notably, the two eccentric reconstructions show excellent

agreement with each other, while both differ from the QC models.

Recent studies on GW200129 have investigated the use of the `BayesWave` mitigation technique [317, 318]. The analyses in GWTC-3 [4] use a single draw of the glitch mitigation model, while a more detailed study on GW200129 [317] marginalizes over multiple draws. In this study, we employ the three glitch realizations provided in their public release [309], labeled `BayesA`, `BayesB`, and `BayesC`. We perform parameter estimation with the three draws using the IMRPhenomTHM and IMRPhenomTEHM models with a uniform prior on eccentricity. Due to the high similarity between `BayesB` and `BayesC` (see Tab. 7.1), we exclude `BayesC` from further runs with the precessing-spin models and log-uniform prior. A summary of all performed runs is given in Tab. 7.1, and the results for `BayesA` –the run which exhibits the least support for dynamical features (both precession and eccentricity)– are shown in Fig. 7.3, along with those for `gw_subtract` introduced above. We find that the eccentric hypothesis is preferred over the precessing one for all the `BayesWave` draws, although this preference is not as strong as for the `gw_subtract` data. While different mitigation techniques significantly impact the support for eccentricity, both in terms of recovered values and Bayes factors (see Tab. 7.1), the preference for the eccentric hypothesis over the precessing QC scenario persists overall. The weakest support for eccentricity comes from the `BayesA` draw with a log-uniform prior, where the inferred eccentricity is $e_{10\mathrm{Hz}}^{\mathrm{GW}} = 0.19^{+0.06}_{-0.14}$, and the log-10 Bayes factor is $\log_{10}\mathcal{B}_{\mathrm{E/QC}} = 1.30^{+0.15}_{-0.15}$. This data also shows the lowest preference for the precessing hypothesis in the NRSur7dq4 model, with a Bayes factor of $\log_{10}\mathcal{B}_{\mathrm{P/QC}} = 1.17^{+0.15}_{-0.15}$, which, as noted before, remains lower than the support for eccentricity.

We also revisit the possibility of this event being QC spin-precessing, and we find consistently lower support for this hypothesis compared to the eccentric scenario, regardless of the model, prior, or data used, as shown in Tab. 7.1. Specifically, the preference for the eccentric hypothesis over the precessing one ranges from $\log_{10}\mathcal{B}_{\mathrm{E/P}} \in [0.13, 1.88]$, as can be directly inferred from the table.

The variability in the evidence for eccentricity across different datasets suggests residual systematics in the glitch subtraction may still be influencing the analysis. Studies performing independent analyses on the LIGO detectors show that the support for eccentricity is much reduced when using only the LIGO Hanford detector, which is free from glitches. This is consistent with the lack of SNR in LIGO Hanford, due to the particular antenna patterns of this event [55]. To further investigate this, we performed three additional runs using only the Hanford data –listed in Tab. 7.1 under "H1"– and found results consistent with those obtained using `BayesA` data, although with broader and less informative posteriors. Notably, the recovered Bayes factors are inconclusive, with values consistent with zero, in line with the substantially lower SNR ($\sim$15) compared to that obtained when including Livingston data ($\sim$27). Nonetheless, our study consistently favors the eccentric hypothesis over the QC scenario, both for aligned and precessing spins. Our results, together with previous studies [55, 313], indicate a preference for dynamical formation channels, supported by spin precession or orbital eccentricity. However, distinguishing between eccentricity and precession or the combination of them requires generic spin eccentric waveform models. We plan to extend the IMRPhenomTEHM waveform model to precessing-spin binaries in future work.

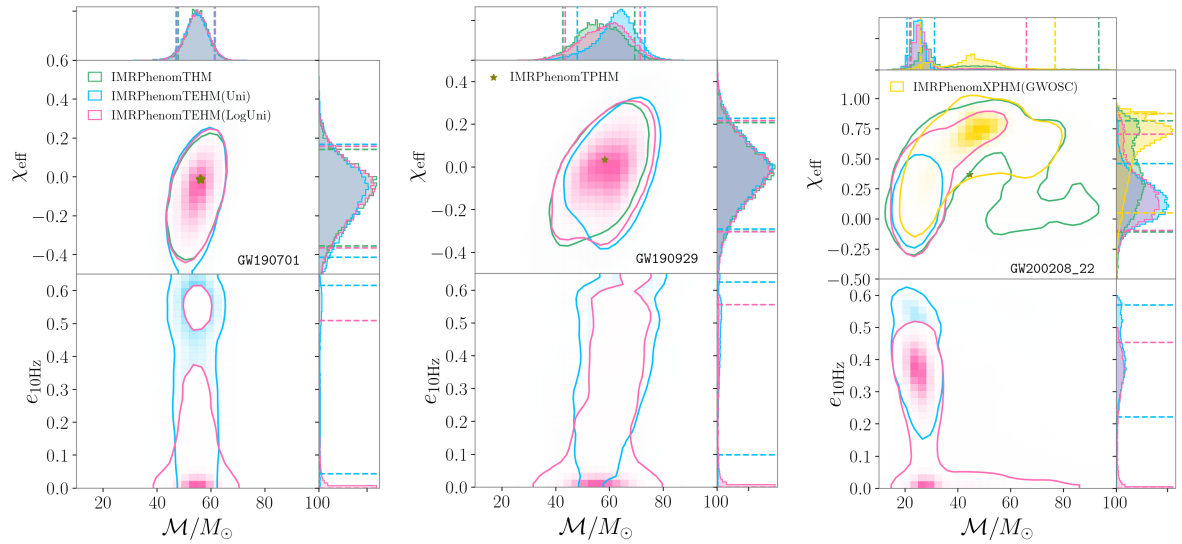

Figure 7.4: Marginalized 2D and 1D posterior distributions of GW190701 (*left*), GW190929 (*middle*), and GW200208_22 (*right*) for the highest number of live points runs described in Tab. 7.1. For each GW event we show the chirp mass and effective spin (*top row*), and chirp mass and eccentricity(*bottom row*) parameters; for the QC model IMRPhenomTHM (*green*), and the eccentric IMRPhenomTEHM model using both a uniform (Uni, *blue*) and a log-uniform (LogUni, *magenta*) priors in eccentricity. We include as a dark green star the median value of the posterior distribution obtained by IMRPhenomTPHM. All parameters are measured at a reference frequency of $f_{\rm ref} = 10$ Hz.

7.3.2 GW200208_22

GW200208_22 is another event with evidence for the eccentric hypothesis [55, 315]. For this analysis, we increase the upper bound of the eccentricity prior to $e_{\rm max} = 0.65$ to prevent the posteriors from railing. For this high value of eccentricity, the underlying eccentricity expansions in the model degrade its accuracy [19]. However, since the waveform starts at an orbit averaged $(2, 2)$-frequency of 10Hz to ensure accurate higher-mode content, and the likelihood integration begins at 20Hz, the eccentricity is expected to have substantially decayed by 20Hz. As a result, any inaccuracies due to the eccentricity expansions are negligible at this frequency. The runs for this event are summarized in Tab. 7.1. We perform PE runs with IMRPhenomTHM, IMRPhenomTPHM, and IMRPhenomTEHM with both uniform and log-uniform priors, employing the default `bilby` settings specified in Sec. 7.2.4. Furthermore, we repeat the IMRPhenomTHM and IMRPhenomTEHM runs with an increased number of live points (`nlive=2000`) to assess stochastic sampler systematics in the multi-modalities observed in the QC parameters.

The high-resolution runs are shown in the third column of Fig.7.4, together with those of IMRPhenomXPHM from the GWTC-3 release [4, 309]. This figure presents the 2D and 1D posterior distributions for the chirp mass, effective spin, and eccentricity –each evaluated at the reference frequency of 10 Hz– for the three remaining special events, with one event per column. Notably, in these plots, we display the eccentricity as defined within the model rather than the GW eccentricity, which is listed in Tab. 7.1. This choice is motivated by the degradation of the waveform at higher eccentricities at 10 Hz, which prevents `gw_eccentricity` from functioning correctly. Since some cycles before the reference frequency are required to obtain the GW eccentricity values, we are evaluating

the PN expansions at $e \sim 0.65 - 0.7$, which leads to non-physical behavior in the waveform. However, since these values do not directly enter the waveform, we consider it more informative to show the full posterior, providing a clearer understanding of the range of eccentricities relevant at 20 Hz.

According to the values from the public samples in the GWTC-2.1 catalog [3], using the IMRPhenomXPHM model (included in Tab. 7.1), GW200208_22 is identified as a BBH with total mass $M = 174^{+100}_{-106}$, effective spin $\chi_{\rm eff} = 0.67^{+0.21}_{-0.62}$, and a relatively low SNR of $7.3^{+1.1}_{-2.0}$. As can be seen in Fig. 7.4, the IMRPhenomXPHM posteriors are not well constrained due to the low SNR. Thus, we study the use of more demanding sampler settings in `bilby`, both for the IMRPhenomTHM and IMRPhenomTEHM runs. We perform extra runs by increasing the number of live points to `nlive=2000` to reduce the multimodalities in the chirp mass and the eccentricity posteriors observed in the `nlive=1000` IMRPhenomTEHM and IMRPhenomTHM runs.

The uniform IMRPhenomTEHM runs indicate a strong preference for the eccentric hypothesis over the QC one, with Bayes factors of $\log_{10} \mathcal{B}_{\rm E/QC} = 0.96^{+0.12}_{-0.12}$ and $\log_{10} \mathcal{B}_{\rm E/QC} = 1.14^{+0.08}_{-0.08}$ for the low- and high- resolution runs, respectively. These factors suggest support for elliptical orbits, with inferred GW eccentricities of $e^{\rm GW}_{\rm 10Hz} = 0.33^{+0.05}_{-0.16}$ and $e^{\rm GW}_{\rm 10Hz} = 0.34^{+0.08}_{-0.18}$. However, this preference is reduced when using a log-uniform prior, yielding Bayes factors of $\log_{10} \mathcal{B}_{\rm E/QC} = 0.09^{+0.11}_{-0.11}$ and $\log_{10} \mathcal{B}_{\rm E/QC} = 0.49^{+0.08}_{-0.08}$, with corresponding GW eccentricities of $e^{\rm GW}_{\rm 10Hz} = 0.31^{+0.09}_{-0.30}$ and $e^{\rm GW}_{\rm 10Hz} = 0.29^{+0.09}_{-0.28}$, which diminish the evidence of orbital eccentricity in this event. Nonetheless, as shown in Figs. 7.1 and 7.4, the log-uniform run recovers some support at the peak of the uniform-run distribution. Combined with the increase in the Bayes factor at higher resolution, this suggests that the lower preference observed in this case may be influenced by the event's low SNR. In particular, the imposition of a prior that strongly favors non-eccentricity may lead to a preference for the QC hypothesis without necessarily providing strong evidence against the eccentric scenario.

We highlight that the inclusion of eccentricity can improve the measurement of binary parameters. As shown in the right column of Fig.7.4, masses, spins, and extrinsic parameters like the luminosity distance (see Tab.7.1 for details), are more tightly constrained when using the eccentric model compared to the QC model. Additionally, the masses inferred with the eccentric model are significantly lower than those obtained with the QC models, while the spins tend to concentrate closer to 0 –consistent with ensuring the same waveform duration. While IMRPhenomXPHM estimates a total mass of $\sim 174 M_\odot$, IMRPhenomTEHM infers $\sim 65 M_\odot$, substantially reducing the total mass and allowing more waveform cycles to fall within the detector's frequency band, making it a more favorable system for eccentricity detection. These differences in binary parameter recovery underscore the importance of incorporating eccentric models in routine PE studies.

The evidence for eccentricity in this event is less significant due to its low SNR, which makes it more challenging to identify eccentric signatures, particularly when using a log-uniform prior in eccentricity. However, given the obtained Bayes factors, we cannot rule out the presence of eccentric features. In contrast, precession signatures appear disfavored, as indicated by the Bayes factor comparing the eccentric nonprecessing-spin hypothesis to the QC precessing-spin one: $\log_{10} \mathcal{B}_{\rm P/QC} = -0.26^{+0.10}_{-0.10}$.

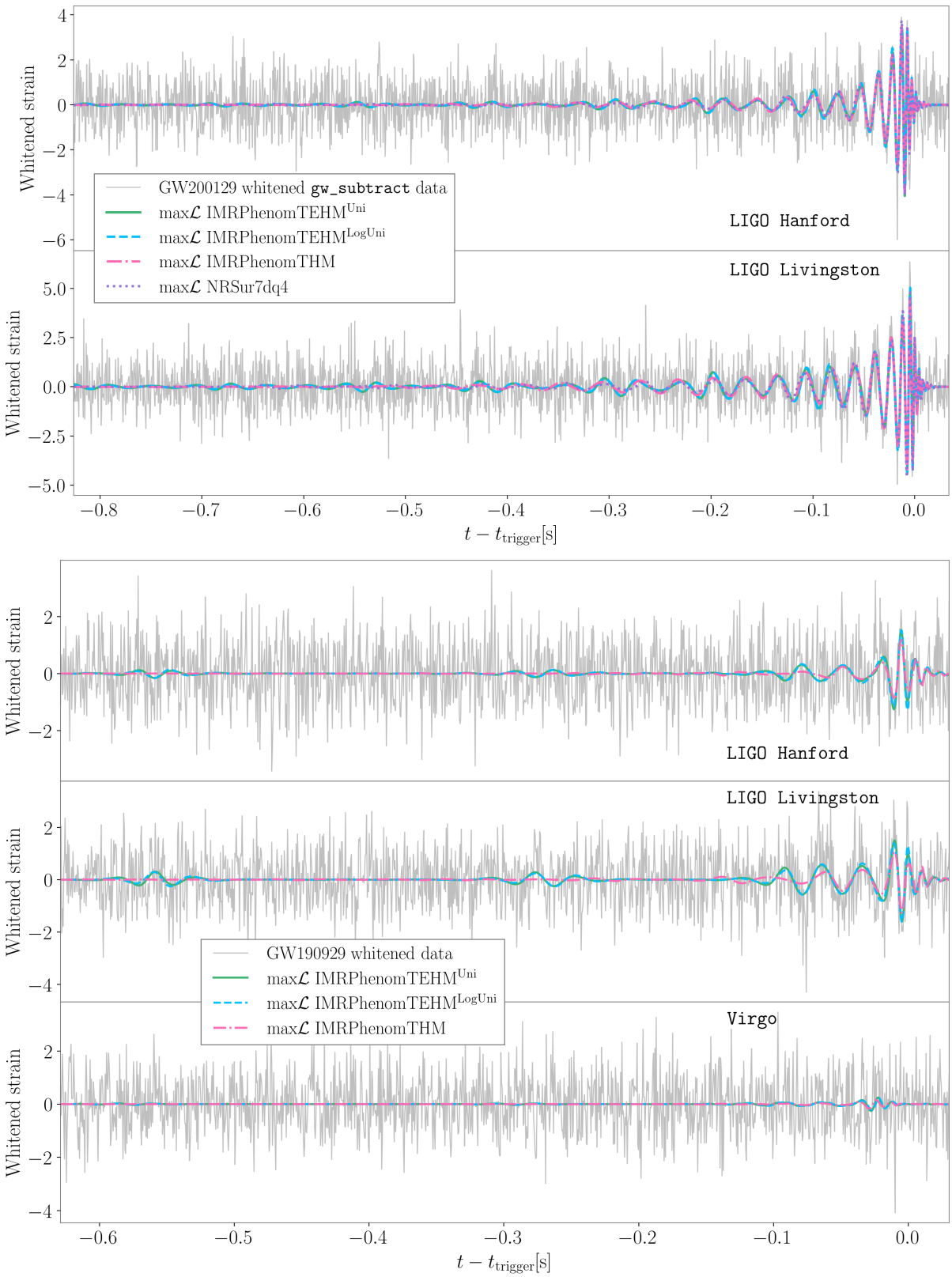

Figure 7.5: Whitened strain data (gray) and maximum likelihood waveform reconstructions for two events. *Top*: GW200129 using whitened data from the `gw_subtract` glitch mitigation technique. *Bottom*: GW190929. Waveforms correspond to maximum likelihood configurations from different models: eccentric model IMRPhenomTEHM with uniform (solid green) and log-uniform (dashed cyan) priors, the QC aligned-spin model IMRPhenomTHM (dash-dotted magenta), and for GW200129, the NRSur7dq4 model (dotted purple).

7.3.3 High mass events: GW190701 & GW190929

The two additional events that require further investigation are GW190701 and GW190929. These events have both been identified as non-spinning BBHs, with relatively high total masses: specifically, we find with IMRPhenomTHM $M = 127.74^{+14.41}_{-13.52} M_\odot$ for GW190701 and $M = 141.64^{+23.26}_{-20.72} M_\odot$ for GW190929. Additionally, both events show a relatively low SNR of $11.38^{+0.13}_{-0.25}$ for GW190701 and $9.96^{+0.40}_{-0.52}$ for GW190929, when using the IMRPhenomTHM model. Both events show slight preference for the eccentric hypothesis with log-10 Bayes factors ranging from $0.09^{+0.10}_{-0.10}$ to $0.23^{+0.13}_{-0.13}$ for GW190701, and from $0.19^{+0.09}_{-0.09}$ to $0.56^{+0.11}_{-0.11}$ for GW190929, depending on the eccentricity prior considered. The runs for these events are summarized in Tab. 7.1, and the higher resolution runs for IMRPhenomTHM and IMRPhenomTEHM with both eccentric priors are presented in the first and second columns of Fig. 7.4.

GW190701 was first identified as a candidate for eccentricity in Ref. [55] using SEOBNRv4EHM [356], reporting a GW eccentricity of $e^{\rm GW}_{10Hz} = 0.35^{+0.32}_{-0.11}$ and log-10 Bayes factors of 3.0 and 2.61 for uniform and log-uniform eccentricity priors, respectively. The main difficulty in assessing evidence of eccentricity for this event is the very high total mass inferred from eccentric models (see Tab. 7.1 for details), which implies that only a few cycles of the signal enter the detector's sensitive band, primarily capturing the merger-ringdown phase. As highlighted in our reanalysis of GW190521 [19], making strong eccentricity claims in such cases is problematic, given the underlying assumption of circularization at merger in current eccentric models. Furthermore, GW190701 contains a known glitch, which we do not remove to be consistent with the data used in the GWTC-2.1 catalog [3, 522].

To our knowledge, no other references have reported signs of eccentricity in GW190929. However, in our study, this event exhibits the strongest support for eccentricity among the high-mass events, even when using a log-uniform prior. Despite this, the usual caveats associated with high total mass and low SNR must be carefully considered when interpreting these results.

As for GW200208_22, we increase the upper bound of the eccentricity prior to $e_{\rm max} = 0.65$ to prevent posterior railing. Our results using a uniform prior in eccentricity for both events suggest support across a wide range of eccentricities, with a preference for higher values. However, this support is largely suppressed when using a log-uniform prior (see Fig. 7.1 and Tab. 7.1). Nevertheless, the eccentricity posteriors from the log-uniform prior runs still show some support in the most probable region of the uniform prior eccentricity posteriors. To assess the impact of sampler systematics in the observed multimodalities we perform higher-resolution runs with an increased number of live points (`nlive=2000`). The results of these high-resolution runs are shown in the first two panels of Fig. 7.4. As seen in Tab. 7.1 and the violin plots in Fig. 7.1, the choice of sampler settings does not introduce significant differences in this case. For both events, we find a similar pattern: while the uniform prior produces a broad posterior distribution in eccentricity, spanning from 0 to the upper bound of 0.65 with a peak around 0.5, the log-uniform prior significantly increases support for the QC hypothesis. However, it still retains some support for the mode around $e_{\rm 10Hz} \sim 0.5$.

An important consideration, already discussed in our reanalysis of GW190521 [19], is that IMRPhenomTEHM allows waveform generation for any reference frequency

contained in the underlying eccentric dynamics. This is not the case for other eccentric models, such as SEOBNRv4EHM and SEOBNRv5EHM, which we do not have the ability to specify a reference frequency distinct from the starting frequency and impose constraints on waveform generation at small binary separations.

The observed multimodalities and the high total mass of these events complicates obtaining clear evidence of eccentricity, even if the Bayes factors slightly favor the eccentric hypothesis. Overall, high-mass events pose a challenge as only a few cycles before merger remain in the detector's sensitive band while our model –as well as all state-of-the-art eccentric models [20, 21, 180, 181, 352, 356, 488]– assumes circularity at merger. In the bottom panel of Fig. 7.5, we show the whitened data for GW190929, overlaid with the maximum likelihood waveforms from the two eccentric IMRPhenomTEHM runs (with uniform and log-uniform eccentricity priors), along with the aligned-spin quasi-circular run using IMRPhenomTHM. As for GW200129, the eccentric reconstructions show remarkable agreement with each other. In this case, they differ from the QC waveform even at merger, although all reconstructions yield a similar ringdown. As seen from the comparison, it is difficult to definitively favor one waveform over another, particularly given the impact of tapering and model-specific transition treatments near merger for such short signals. Therefore, in high-mass events, extra caution is needed to ensure that the evidence of eccentricity is not caused by spurious effects in the waveform due to the specifics on which different models transition from inspiral to merger. We leave for future work the incorporation of eccentric effects in the merger and ringdown of IMRPhenomTEHM.

7.4 Conclusions

In this work, we analyze 17 GW events from BBHs that have been identified in the literature as particularly interesting due to their support for dynamical formation channels. For this analysis, we use the new phenomenological time-domain multipolar waveform model IMRPhenomTEHM [19], which incorporates two eccentric parameters: eccentricity and mean anomaly. This model builds upon the QC aligned-spin IMRPhenomTHM model and includes up to 3PN eccentric corrections to both the dynamics and waveform multipoles.

Previous eccentric studies have relied on resampling techniques, iterative fitting, or machine learning algorithms [47, 55, 541][1]. In contrast, this work allows, for the first time, the routine use of an eccentric waveform model with the standard analysis tools of the LVK Collaboration due to its high computational efficiency. We conduct analysis with the aligned-spin QC model IMRPhenomTHM and the eccentric IMRPhenomTEHM, employing both uniform and log-uniform priors in eccentricity for all events. For the four events requiring further investigations, we perform additional runs, varying data and sampler settings, as well as runs with the precessing models IMRPhenomTPHM and NRSur7dq4. To complement our results, we provide a data release [542] containing all the posterior samples generated in this work.

Our results provide valuable insights into the measurement of eccentricity in PE studies and their interpretation, highlighting the need to include eccentricity in PE studies to prevent biased in inferred parameters. In particular, we find support for eccentricity in four

[1]Note that Ref. [55] employs machine learning algorithms to analyze the bulk of GW events, as well as the `parallel Bilby` [118] code for a subset of events.

events: GW190701, GW190929, GW200129, and GW200208_22. Given these indications and thanks to the computational efficiency of the model, we performed additional studies to assess the robustness of our findings and to explore the impact of glitch subtraction and waveform systematics.

Our analysis of GW200129 provides evidence for orbital eccentricity, as this feature is consistently supported across all eccentricity priors and glitch mitigation techniques. This reinforces the interpretation of a dynamical formation channel, as suggested by previous studies [55, 313]. The non-deglitched `GWOSC` data yield the highest Bayes factors for eccentricity. Using the `gw_subtract` mitigation method, widely adopted in LVK analyses, we continue to find robust support for eccentricity, albeit slightly lower than in the uncorrected data. The `BayesWave` mitigation, particularly the `BayesA` draw, exhibits the least support for dynamical features (both precession and eccentricity), highlighting the impact of the glitch treatment on parameter estimation. However, even with this mitigation, the eccentric hypothesis remains favored over both the aligned-spin and precessing QC hypotheses. Given the high SNR and total mass of GW200129, which make it a good candidate for detecting eccentricity in ground-based detectors, our findings support the presence of orbital eccentricity. While we cannot entirely rule out precession, our results suggest that eccentricity is the dominant feature. One of the main limitations in our analysis stems from the lack of precessing-spin effects in the IMRPhenomTEHM model, which is crucial to distinguish features from spin precession and eccentricity. Some first IMR eccentric precessing-spin models have recently emerged, see e.g. Refs. [21, 44, 358], and we plan to extend IMRPhenomTEHM to the fully generic parameter space including both eccentricity and spin precession in future work.

Our analysis of GW200208_22 also provides some support for the eccentric hypothesis, although the conclusions are not as definitive as those for GW200129. The evidence for eccentricity is strengthened by using a uniform prior, yielding a log Bayes factor of $1.14^{+0.08}_{-0.08}$. However, the log-uniform prior provides minor support in favor of eccentricity with a log-10 Bayes factors of $0.49^{+0.08}_{-0.08}$. In both cases the results show that the eccentric hypothesis remains favored over QC precessing-spin and QC aligned-spin models, particularly in the higher-resolution PE runs. However, the relatively low SNR of the event complicate the analysis, and make robust conclusions more challenging.

Finally, GW190701 and GW190929 are two high-mass BBH events that show minor preference for the eccentricity hypothesis, though their characterization remains challenging due to their large total masses and low signal-to-noise ratios. The high inferred total masses imply that only the final cycles before merger are observed, where eccentric waveform models, including IMRPhenomTEHM, typically assume circularization. For GW190929, we find stronger support for eccentricity among the high-mass events, although systematic uncertainties remain. We find that the uniform prior favors the eccentricity scenario (log-10 Bayes factors of $0.56^{+0.09}_{-0.09}$), while the log-uniform prior suppresses this support (log-10 Bayes factors of $0.19^{+0.09}_{-0.09}$). GW190701 was previously identified as an eccentric candidate in Ref. [55], with $\log_{10}\mathcal{B}_{\rm E/QC}$ values of 3.0 and 2.11 for uniform and log-uniform priors, respectively. While our log-10 Bayes factors also show a slight preference for the eccentric hypothesis over the aligned-spin QC scenario, they oscillate depending on the sampler settings and choice or eccentricity priors, ranging between $\sim 0.05 - 0.24$. These low values, combined with the presence of a known glitch, prevent strong conclusions and do not support the claim obtained with SEOBNRv4EHM. Even though our results suggest

possible eccentricity signatures in these events, the short duration of the signals and the limitations of the eccentric modeling near merger prevent strong claims, highlighting the need for improved waveform models that include eccentric corrections up to merger.

Our findings emphasize the crucial need for eccentric waveform models in GW PE analyses. This study identifies significant signs of eccentricity in 2 out of approximately 90 events detected by the LVK Collaboration, suggesting that future observing runs may reveal a comparable or even higher occurrence rate. Omitting eccentricity leads to systematic biases in key parameters such as chirp mass and effective spin, which arise from the waveform systematics introduced when eccentricity is ignored. Since eccentric waveforms are typically shorter than their QC counterparts, the total mass is underestimated to match the observed signal duration. Similarly, we observe a strong interplay between eccentricity and the effective spin parameter, as previously noted in Fig. 8 of Ref. [19]. This interplay underscores the necessity of developing a fully generic, spin-precessing eccentric model suitable for comprehensive GW analyses. Moreover, eccentricity provides valuable insights into the dynamical formation channels of binary systems, and as such, improving waveform models for generic orbits is essential. These models must not only be accurate, but also computationally efficient to enable their systematic application across large datasets.

Finally, the high computational efficiency introduced by IMRPhenomTEHM enables us to perform PE for low total-mass events with very long duration signals. This opens the door to a more detailed investigation of recent claims of eccentricity in GW200105 [56], one of the NSBH events reported in Ref. [8]. In an upcoming paper, we analyze this event using, for the first time, a fully eccentric IMR waveform model with standard stochastic sampling techniques [538].

Acknowledgements

The authors would like to thank Nihar Gupte for the LSC Publication & Presentation Committee review of this manuscript. We thankfully acknowledge the computer resources (MN5 Supercomputer), technical expertise and assistance provided by Barcelona Supercomputing Center (BSC) through funding from the Red Española de Supercomputación (RES) (AECT-2024-3-0027); and the computer resources (Picasso Supercomputer), technical expertise and assistance provided by the SCBI (Supercomputing and Bioinformatics) center of the University of Málaga (AECT-2025-1-0035). This research has made use of data or software obtained from the Gravitational Wave Open Science Center (gwosc.org), a service of the LIGO Scientific Collaboration, the Virgo Collaboration, and KAGRA. This material is based upon work supported by NSF's LIGO Laboratory which is a major facility fully funded by the National Science Foundation. LIGO is funded by the U.S. National Science Foundation. Virgo is funded by the French Centre National de Recherche Scientifique (CNRS), the Italian Istituto Nazionale della Fisica Nucleare (INFN) and the Dutch Nikhef, with contributions by Polish and Hungarian institutes.

Maria de Lluc Planas is supported by the Spanish Ministry of Universities via an FPU doctoral grant (FPU20/05577, EST24/00621). A. Ramos-Buades is supported by the Veni research programme which is (partly) financed by the Dutch Research Council (NWO) under the grant VI.Veni.222.396; acknowledges support from the Spanish Agencia Estatal de Investigación grant PID2022-138626NB-I00 funded by

MICIU/AEI/10.13039/501100011033 and the ERDF/EU; is supported by the Spanish Ministerio de Ciencia, Innovación y Universidades (Beatriz Galindo, BG23/00056) and co-financed by UIB. CG is supported by the Swiss National Science Foundation (SNSF) Ambizione grant PZ00P2_223711. This work was supported by the Universitat de les Illes Balears (UIB); the Spanish Agencia Estatal de Investigación grants PID2022-138626NB-I00, PID2019-106416GB-I00, RED2022-134204-E, RED2022-134411-T, funded by MCIN/AEI/10.13039/501100011033; the MCIN with funding from the European Union NextGenerationEU/PRTR (PRTR-C17.I1); Comunitat Autonòma de les Illes Balears through the Direcció General de Recerca, Innovació I Transformació Digital with funds from the Tourist Stay Tax Law (PDR2020/11 - ITS2017-006), the Conselleria d'Economia, Hisenda i Innovació grant numbers SINCO2022/18146 and SINCO2022/6719, co-financed by the European Union and FEDER Operational Program 2021-2027 of the Balearic Islands; the "ERDF A way of making Europe".

CHAPTER 8

First eccentric IMR analysis of neutron star-black hole mergers

This chapter is based on the following article:

- Maria de Lluc Planas, Sascha Husa, Antoni Ramos-Buades, Jorge Valencia. "*First eccentric inspiral-merger-ringdown analysis of neutron star-black hole mergers*", arXiv: arXiv:2506.01760[astro-ph] [23].

Abstract

The gravitational wave event GW200105 was the first confident neutron star-black hole (NSBH) merger identified by the LIGO-Virgo-KAGRA collaboration. A recent analysis [56] with an eccentric precessing waveform model that describes the inspiral phase of the $l = 2$ and $m = \{0, \pm 2\}$ modes has identified this event as the first NSBH merger with strong evidence of orbital eccentricity. In this paper we perform the first analysis of this event with an aligned-spin eccentric waveform model that describes the full inspiral, merger, and ringdown, includes subdominant harmonics, and is partially calibrated to numerical relativity simulations. This analysis confirms the results and finds evidence in favor of eccentricity even with a log-uniform prior in eccentricity. We also analyze the NSBH events GW200115 and GW230529, completing the analysis of all NSBHs with IMRPhenomTEHM, and find that these signal are consistent with vanishing eccentricity. Finally, we briefly discuss computational challenges when performing the analysis with time-domain eccentric waveform models.

8.1 Introduction

The LIGO-Virgo-KAGRA collaboration (LVK) has reported the detection of 77 GW events, found consistent with compact object mergers with a false alarm rate of less than one per year – see the latest catalog [4] from the first three observing runs of the current ground based gravitational-wave (GW) detector network [472–474], and [9] for an event from the fourth run. Of these, sixty-nine events have been identified as binary black holes (BBHs), four as NSBH signals – the three analyzed here, plus GW191219, limited by the accuracy of current models for such high mass ratios, two as binary neutron stars (BNSs), and two as either a NSBH or BBH [7, 9]. GW190814, previously analyzed with IMRPhenomTEHM in [22], falls within this last category. Further events have been detected in public data by other authors, see e.g. [327, 543–546]. Understanding the populations of such objects and their formation channels is one of the main goals of GW astronomy, see paper for recent LVK results [136].

In order to compare models of binary formation and stellar evolution with observational GW data, it is necessary to accurately determine the parameters of the sources, in particular the component masses, spin vectors and the orbital eccentricity, which are commonly referred to as intrinsic parameters, and extrinsic parameters such as the luminosity distance. These parameters are measured by comparing the data recorded by the GW detectors with accurate theoretical models of the waveform using the methods of Bayesian inference [113, 520].

Stellar mass compact binaries formed through isolated binary evolution are expected to circularize [475], i.e. shed orbital eccentricity before entering the detector band: At early times, processes like mass transfer and common-envelope evolution [524, 547, 548] tend to circularize the orbit before the black holes form. Any residual eccentricity is efficiently radiated away through GW emission [36, 549], so field-formed compact binaries are expected to enter the LVK band with negligible eccentricity. This has motivated an initial focus of the field of waveform modeling on the quasi-circular (QC) sector, i.e. the case when orbital eccentricity can be neglected. Interactions with other objects at sufficiently late times before the coalescence can however result in retaining orbital eccentricity in the sensitive frequency band of the detectors [550–552]. Prominent examples of such channels are capture or multi-body interactions in dense star clusters [321, 322, 553–555] or Zeipel-Kozai-Lidov oscillations in triple systems [323, 324, 556–558]. Detecting eccentricity in GW signals is therefore a crucial step toward identifying coalescing binaries that likely did not form through isolated binary evolution, see e.g. [47, 53, 315, 559, 560].

Waveform models that are routinely used for data analysis by the LVK Collaboration [1, 3, 4], and which describe the entire waveform from the inspiral to the merger and ringdown (IMR), have recently been extended to include orbital eccentricity [19–21, 45, 358], and have been applied to measure orbital eccentricity in events identified as BBH signals [22, 47, 54, 55, 387, 541]. The results are not entirely conclusive, as many of the signals are short, and in some cases contaminated by noise glitches (deviations from Gaussianity in the noise), although significant evidence points to orbital eccentricity in the case of the event GW200129 [22, 55]. For the two events identified as BNS mergers [5, 6], analysis with IMR models is computationally expensive, and analyses with perturbative post-Newtonian (PN) waveforms or reweighting techniques have not found evidence for eccentricity but provided upper limits [561, 562]. For the NSBH event GW200105 [8], recent analysis [56] based on a PN eccentric precessing inspiral model which includes the $l = 2$ and $m = \{0, \pm 2\}$

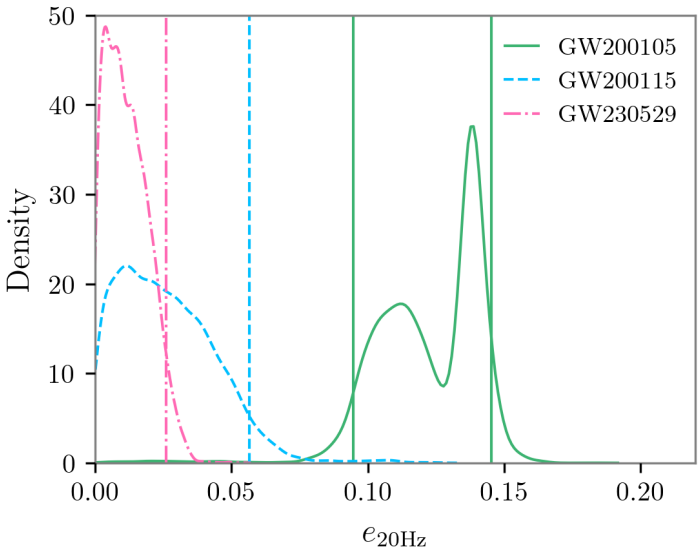

Figure 8.1: One-dimensional posterior distributions for the orbital eccentricity measured at a reference frequency of 20 Hz for the NSBH events GW200105 (solid green), GW200115 (dashed blue), and GW230529 (dot-dashed pink) obtained using the IMRPhenomTEHM model with a uniform eccentricity prior. Vertical lines indicate the 90% credible intervals.

modes [367] found a value of $e_{20} = 0.145^{+0.007}_{-0.097}$ at a reference frequency of 20 Hz. This result is a milestone in understanding the population of compact binaries, and likely will be studied in great detail by the community, e.g. to further sharpen the result, to deepen the astrophysical interpretation, to understand waveform systematics, and as a benchmark for data analysis algorithms.

Here we present the first full IMR aligned-spin eccentric parameter estimation (PE) analysis of three NSBHs, GW200105, GW200115 [8], and GW230529 [9], using the waveform model IMRPhenomTEHM [19]. It includes subdominant harmonics, and is calibrated to numerical relativity (NR) simulations in the QC sector. Crucially, it remains computationally efficient, enabling PE for low-mass systems using classical sampling techniques at a moderate computational cost. Our main findings are summarized in Fig. 8.1: Our analysis provides strong evidence for orbital eccentricity in GW200105, while no such support is found for GW200115 or GW230529. These results reinforce the finding of eccentricity in [56], now with a fully IMR waveform model with higher multipoles. Despite the presence of unexplained features in the eccentricity posteriors for GW200105, we report our results given the novelty and relevance of this analysis. Potential origins of these structures are discussed in the main text and Appendix 8.A discusses eccentric waveform systematics for PE, with a full investigation left for future work.

In Sec. 8.2, we outline our methods, in Sec. 8.3 we describe our results, and we finally address the implications of this work and next steps in Sec. 8.4.

8.2 Methodology

In GW astronomy, the source parameters are determined by Bayesian inference comparing waveform models with the observed data. The gold standard for waveform accuracy for comparable mass binaries are numerical solutions to the Einstein equations with error

estimates. Due to their high computational cost, only $\sim 10^4$ waveforms exist for the nine-dimensional BBH parameter space [226, 228, 519], with even fewer available for binaries involving neutron stars [563–565]. Waveform models used for PE often incorporate additional theoretical input to improve accuracy, such as PN descriptions of the inspiral [82], the Effective-One-Body (EOB) formalism [240, 241], or insights from small mass-ratio perturbation theory [566].

The waveform model we use here to measure eccentricity is IMRPhenomTEHM [19], which extends the QC IMR model IMRPhenomTHM [34, 191] to describe GWs from eccentric BBHs. Besides the dominant $(2, \pm 2)$ spherical harmonic mode, the model also includes $(l, m) = \{(2, \pm 1), (3, \pm 3), (4, \pm 4), (5, \pm 5)\}$. IMRPhenomTEHM is not calibrated to eccentric NR waveforms, but through extending IMRPhenomTHM, it is calibrated to QC NR waveforms up to mass ratio 1/18. The model has several limitations: First, as in other current state-of-the-art IMR eccentric models [20, 21, 352, 353], it is assumed that the binary circularizes at the time of merger. Additionally, the use of eccentricity-expanded PN approximations for the description of the inspiral limits the applicability of the model to binaries with eccentricities up $e \sim 0.4$ at an orbit-average GW frequency of 10 Hz, which is safely outside the posterior support for the three events discussed here. Second, the model does not include matter effects due to the neutron star, in particular tidal effects during the inspiral or disruption effects. For the mass ratios of the events we study here and the values of the primary spin component (see Tab. 8.1 for details), tidal disruption is not expected [567–574]. Moreover, at the moderate signal-to-noise ratios (SNR) of these events, tidal effects during the inspiral are not expected to be observable [8, 575, 576]. Finally, IMRPhenomTEHM assumes spins aligned or anti-aligned with the orbital angular momentum (non-precessing spins). For GW200105 and GW200115, neither the original discovery paper [8] nor the recent inspiral-only analysis including both eccentricity and spin precession [56] provides evidence for spin precession. Similarly, no indications of spin precession were reported for GW230529 [9]. Consequently, spin precession is not expected to have a significant impact on our results.

The construction and validation of the model are presented in [19]. In particular, it was benchmarked against 28 publicly available eccentric NR simulations produced by the Simulating eXtreme Spacetimes (SXS) Collaboration [228, 347], as well as against the spinning eccentric waveform model SEOBNRv5EHM [20], which, although more accurate, is computationally restrictive for the analysis considered here. In [22], we reanalyze 17 BBH GW events using IMRPhenomTEHM, finding results consistent with those obtained using SEOBNRv4EHM in combination with the machine learning algorithm `DINGO` [577] for PE [55]. These results indicate that, at current SNRs and for moderate eccentricities, IMRPhenomTEHM can be used to reliably measure eccentricity.

We perform Bayesian inference with the `bilby` framework [113] and the nested sampling algorithm `dynesty` [106, 115, 116, 578] to compute posterior distributions for the signal parameters. More specifically, we use `parallel_bilby` [118], which uses the MPI library [579] to parallelize across computing nodes to accelerate the runs. We employ the default nested sampling method, i.e. using the `acceptance-walk` method for the Markov Chain Monte Carlo (MCMC) evolution with an average number of accepted steps per MCMC chain of `naccept=60` and number of live points `nlive=1000`.

The GW strain data, noise power spectral densities (PSDs) and calibration envelope data are obtained from the public release by the LVK Collaboration [580, 581], and

correspond to those used in the published LVK analyses [8, 9]. For our analysis, we set the starting frequency for likelihood integration to 20 Hz, consistent with the original studies. For GW200105, the frequency range 46−51 Hz is excluded from the Virgo PSD due to additional calibration systematics, following the original LVK studies. LIGO Hanford was not observing at the time of the event and Livingston data underwent a data cleaning procedure to mitigate noise artifacts from scattered light below 25 Hz.

We sample on a 13-dimensional parameter space representing non-precessing spin BBHs in eccentric orbits. The parameters describing the source properties are the components masses m_i, with $i = 1, 2$, the dimensionless spins $\chi_i = S_i/m_i^2$, where S_i are the projections of the component angular momentum vectors along the orbital angular momentum, and finally the reference orbital eccentricity $e_{20\mathrm{Hz}}$ and mean anomaly $l_{20\mathrm{Hz}}$ at a reference frequency of 20 Hz. Additionally, we sample on the extrinsic parameters relating the source and detector frames: the coalescence time, coalescence phase, luminosity distance, inclination, polarization angle, right ascension and declination.

The priors on the mass ratio $q = m_1/m_2$ with $m_1 > m_2$ and chirp mass $\mathcal{M} = (m_1 m_2)^{3/5}/(m_1 + m_2)^{1/5}$ are chosen to correspond to a uniform distribution in the component masses. For the spin components χ_i, we use priors corresponding to the projections of a uniform and isotropic spin distribution along a direction perpendicular to the binary's orbital plane [520], with bounds $\chi_i \in [-0.99, 0.99]$. For the luminosity distance d_L, we follow the simple prior proportional to d_L^2 [1–4], which is justified by the relatively close distance of both events. We set a uniform distribution for the mean anomaly, $l_{20\mathrm{Hz}} \in [0, 2\pi]$, while for eccentricity we consider two choices: *a)* a uniform prior, $e_{20\mathrm{Hz}} \in [0, 0.5]$, and *b)* a log-uniform prior with bounds $e_{20\mathrm{Hz}} \in [10^{-4}, 0.5]$, where the specific lower cutoff of the latter is chosen for consistency with a common choice in the literature. The log-uniform prior expresses ignorance of the order of magnitude of the eccentricity. However, at the present SNR, it would not be possible to measure very small eccentricities, and we consider our uniform prior results as more relevant.

As is standard in GW PE, we perform likelihood integration in the frequency domain starting at 20 Hz. For time-domain waveforms, this requires starting early enough to ensure all relevant harmonics enter the band by that frequency – especially important for eccentric signals, which contain multiple mean anomaly harmonics. Appendix 8.A details these considerations and related waveform systematics. By default, we condition the waveform starting three QC cycles before 17 Hz, and set the reference frequency to 20 Hz, consistent with [56]. To assess low-frequency effects, we also ran tests for GW200105 with varied starting frequencies and durations.

8.3 Results

Our key result is shown in Fig. 8.1: our analysis for GW200105 finds support of eccentricity $e_{20\mathrm{Hz}} = 0.12^{+0.02}_{-0.03}$, similarly as in [56], with a Bayes factor of $\log_{10} \mathcal{B}_{\mathrm{E/QC}} = 1.22^{+0.12}_{-0.12}$, while GW200115 and GW230529 are consistent with QC binaries with eccentricities $e_{20\mathrm{Hz}} = 0.02^{+0.03}_{-0.02}$ and $e_{20\mathrm{Hz}} = 0.01^{+0.02}_{-0.01}$, respectively, supported by Bayes factors ($\log_{10} \mathcal{B}_{\mathrm{E/QC}} = -0.91^{+0.13}_{-0.13}$), and ($\log_{10} \mathcal{B}_{\mathrm{E/QC}} = -1.36^{+0.12}_{-0.12}$). We verified the robustness of the results for GW200105 presented in Fig. 8.1 by performing PE runs with varying priors and sampler configurations. A selection of these results for each GW event is summarized in Tab. 8.1, which reports the median values and corresponding 90% credible

Event	Model	$M/M_\odot$	$\mathcal{M}/M_\odot$	$1/q$	$\chi_{\rm eff}$	$e_{\rm 20Hz}$	$l_{\rm 20Hz}$	d_L [Mpc]	$\rm SNR^N$	$\log_{10}\mathcal{B}_{\rm E/QC}$
GW200105	THM	$11.49^{+1.96}_{-2.04}$	$3.62^{+0.01}_{-0.01}$	$0.22^{+0.17}_{-0.07}$	$-0.01^{+0.17}_{-0.27}$	–	–	275^{+108}_{-112}	$13.81^{+0.18}_{-0.31}$	–
	TEHM (Uni)	$10.83^{+1.06}_{-0.60}$	$3.58^{+0.03}_{-0.02}$	$0.24^{+0.04}_{-0.05}$	$-0.12^{+0.15}_{-0.11}$	$0.12^{+0.02}_{-0.03}$	$3.25^{+2.73}_{-2.94}$	255^{+104}_{-102}	$14.39^{+0.32}_{-0.42}$	$1.22^{+0.12}_{-0.12}$
	TEHM (LogUni)	$11.38^{+1.87}_{-1.82}$	$3.62^{+0.01}_{-0.02}$	$0.22^{+0.15}_{-0.07}$	$-0.03^{+0.17}_{-0.24}$	$0.00^{+0.11}_{-0.00}$	$3.16^{+2.82}_{-2.86}$	276^{+106}_{-112}	$13.84^{+0.47}_{-0.31}$	$0.11^{+0.11}_{-0.11}$
	THM (Uni, 64 s)	$11.55^{+2.04}_{-1.92}$	$3.62^{+0.01}_{-0.01}$	$0.21^{+0.15}_{-0.07}$	$-0.00^{+0.17}_{-0.24}$	–	–	272^{+107}_{-112}	$13.78^{+0.19}_{-0.32}$	–
	TEHM (Uni, 64 s)	$10.73^{+1.40}_{-0.57}$	$3.58^{+0.03}_{-0.02}$	$0.25^{+0.04}_{-0.06}$	$-0.14^{+0.18}_{-0.11}$	$0.13^{+0.02}_{-0.04}$	$3.99^{+2.00}_{-3.66}$	251^{+107}_{-104}	$14.31^{+0.30}_{-0.43}$	$1.00^{+0.12}_{-0.12}$
	TEHM (Uni, 13.3 Hz)	$10.76^{+1.55}_{-0.58}$	$3.58^{+0.03}_{-0.02}$	$0.25^{+0.04}_{-0.07}$	$-0.13^{+0.19}_{-0.10}$	$0.13^{+0.02}_{-0.03}$	$3.16^{+2.83}_{-2.87}$	254^{+107}_{-105}	$14.36^{+0.31}_{-0.43}$	–
	TEHM (Uni, L(L1)=25 Hz)	$10.89^{+0.83}_{-0.52}$	$3.58^{+0.02}_{-0.02}$	$0.24^{+0.03}_{-0.04}$	$-0.11^{+0.12}_{-0.10}$	$0.12^{+0.02}_{-0.03}$	$3.17^{+2.78}_{-2.86}$	258^{+104}_{-105}	$14.41^{+0.27}_{-0.39}$	–
	IMRPhenomNSBH	$11.34^{+2.28}_{-1.81}$	$3.62^{+0.01}_{-0.01}$	$0.22^{+0.15}_{-0.08}$	$-0.02^{+0.19}_{-0.21}$	–	–	285^{+116}_{-124}	$13.46^{+0.17}_{-0.28}$	–
GW200115	THM	$8.06^{+1.61}_{-1.45}$	$2.58^{+0.01}_{-0.01}$	$0.22^{+0.19}_{-0.08}$	$-0.10^{+0.20}_{-0.27}$	–	–	288^{+139}_{-109}	$11.40^{+0.22}_{-0.46}$	–
	TEHM (Uni)	$7.72^{+1.79}_{-1.36}$	$2.58^{+0.01}_{-0.01}$	$0.25^{+0.24}_{-0.10}$	$-0.17^{+0.25}_{-0.29}$	$0.02^{+0.03}_{-0.02}$	$3.17^{+2.79}_{-2.84}$	285^{+142}_{-110}	$11.40^{+0.24}_{-0.48}$	$-0.91^{+0.13}_{-0.13}$
GW230529	THM	$5.22^{+0.93}_{-0.50}$	$2.03^{+0.00}_{-0.00}$	$0.41^{+0.33}_{-0.17}$	$-0.10^{+0.19}_{-0.14}$	–	–	212^{+109}_{-104}	$11.43^{+0.19}_{-0.29}$	–
	TEHM (Uni)	$5.14^{+0.96}_{-0.45}$	$2.03^{+0.00}_{-0.00}$	$0.44^{+0.34}_{-0.19}$	$-0.13^{+0.20}_{-0.14}$	$0.01^{+0.02}_{-0.01}$	$3.05^{+2.90}_{-2.75}$	210^{+116}_{-105}	$11.42^{+0.19}_{-0.32}$	$-1.36^{+0.12}_{-0.12}$

Table 8.1: Median values and 90% credible intervals of the posterior distributions for GW200105, GW200115, and GW230529, indicated in each row. The IMRPhenomNSBH [582] posteriors for GW200105 are taken from the official LVK public release [8]. The parameters displayed are the total mass M and chirp mass $\mathcal{M}$ (both in solar masses), the inverse mass ratio $1/q$, the effective-spin parameter $\chi_{\rm eff}$, the reference eccentricity $e_{\rm 20Hz}$ and mean anomaly $l_{\rm 20Hz}$, the luminosity distance d_L, and the network matched-filtered SNR $\rm SNR^N$. The last column shows the log-10 Bayes factor between the eccentric (E) and the QC aligned-spin (QC) hypothesis $\log_{10}\mathcal{B}_{\rm E/QC}$. The spins and eccentric parameters are given at the reference frequency of 20 Hz.

intervals for key source properties. For GW200105, the table also includes the official LVK posteriors [8] obtained using the IMRPhenomNSBH model [582] for comparison.

In Fig. 8.2 we present the GW200105 posterior distributions for some key source properties obtained with two QC models, IMRPhenomTHM, implemented via the `phenomxpy` infrastructure [416], and IMRPhenomNSBH, alongside the eccentric IMRPhenomTEHM model using both uniform and log-uniform priors in eccentricity. We begin by considering the QC waveform models: we find excellent agreement between IMRPhenomTHM and IMRPhenomNSBH (see also Tab. 8.1 for quantitative results), indicating that the tidal effects do not significantly influence the recovered parameters. While this does not entirely rule out the possibility of degeneracy between tidal and eccentric effects – both influencing the frequency evolution – it does suggest that tidal contributions are subdominant and unlikely to induce significant biases in this case.

The incorporation of eccentric effects produces notable shifts in some QC parameters, such as effective spin and component masses, due to their strong correlation with the length of the signal. As a consequence, the IMRPhenomTEHM results with a uniform eccentricity prior (pink) favor lower mass values compared to the QC runs. This shift compensates for the shortening of the waveform induced by eccentricity, and consequently also impacts the inferred spin. The use of a log-uniform prior suppresses the measured value of eccentricity due to its strong weight at low eccentricities. However, we observe that even a log-uniform prior in eccentricity yields a subdominant posterior mode at $e_{\rm 20Hz} \sim 0.11$. Although this support remains subdominant, it induces clear deviations from the QC results in the mass and spin distributions. This observation is further supported by a nominally positive log-10 Bayes factor between the eccentric and QC hypotheses, $\log_{10}\mathcal{B}_{\rm E/QC} = 0.11^{+0.11}_{-0.11}$. While this value alone is not enough to claim strong evidence for eccentricity, it is still notable given the relatively low SNR of the event and the strong preference for low eccentricities imposed by the log-uniform prior.

Biases in the recovered QC parameters due to unmodeled eccentricity were already evident in earlier studies [19, 22, 55, 56]. For GW200105, our eccentricity measurement

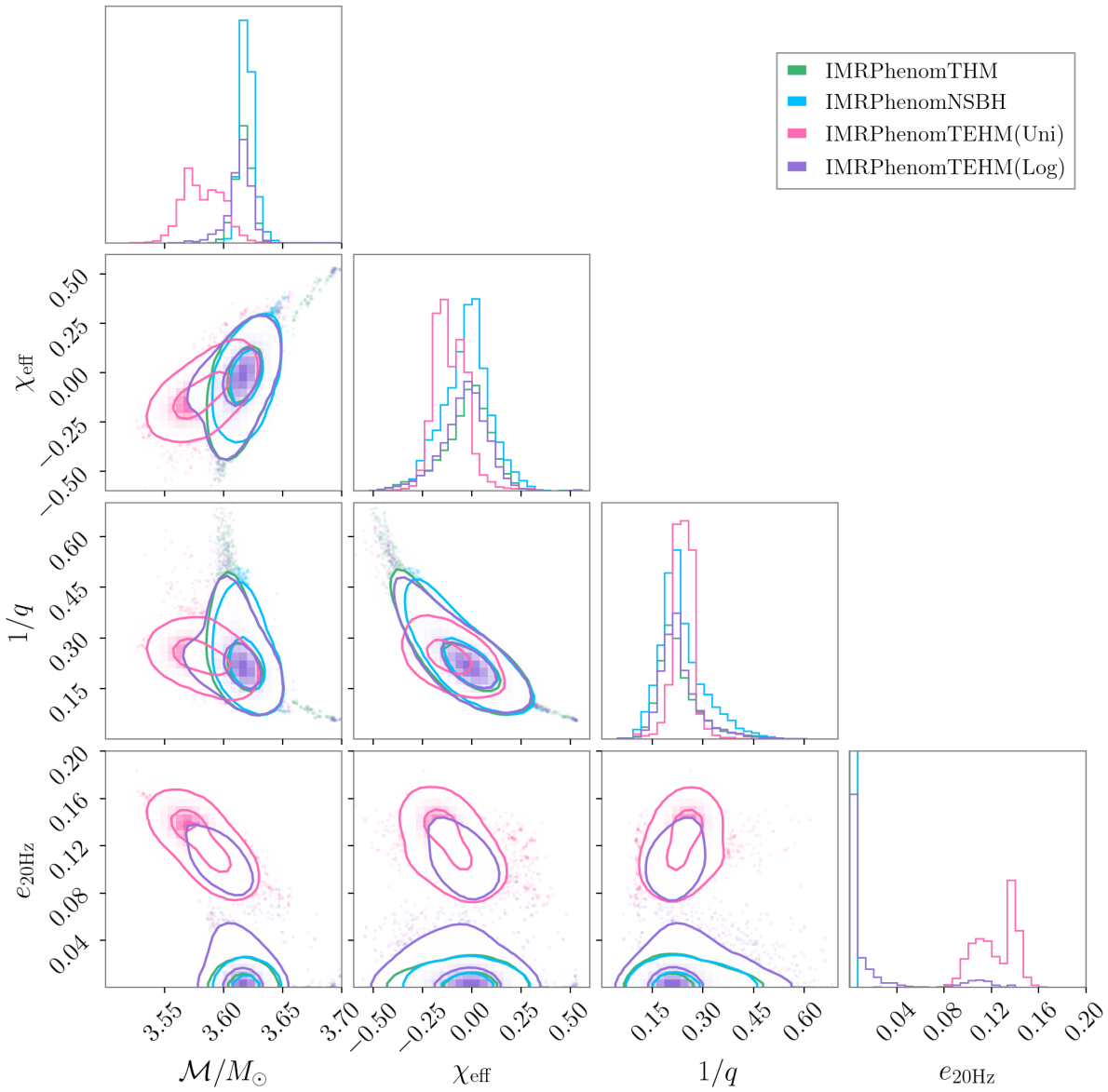

Figure 8.2: Marginalized one- and two-dimensional posterior distributions for GW200105. We show results from the QC models IMRPhenomTHM (green) and IMRPhenomNSBH (cyan, taken from the official LVK public release [8]), as well as the eccentric model IMRPhenomTEHM using a uniform prior in eccentricity (pink) and a log-uniform prior (purple). Parameters shown include the chirp mass $\mathcal{M}$, effective spin $\chi_{\rm eff}$, mass ratio q, and eccentricity at 20 Hz ($e_{\rm 20Hz}$).

using a uniform prior reveals a bimodal posterior with peaks at $e \sim 0.11$ and $e \sim 0.14$, corresponding to log-likelihood values of $\log \mathcal{L} \sim 95$ and $\log \mathcal{L} \sim 100$, respectively. These modes are highlighted in Fig. 8.3 by a star and a square. This bimodality likely arises from correlations between eccentricity and QC parameters, such as the component masses and aligned spin, which influence the duration of the signal. Notably, the distinct peaks in the eccentricity posterior coincide with secondary peaks in the posteriors of the primary mass and the aligned spin component.

We find that the higher peak in eccentricity at $e \sim 0.14$ corresponds to a lower primary component mass ($m_1 \sim 8M_\odot$), which in turn implies a lower mass ratio of $1/q \sim 0.25$ (see Fig. 8.2). The reduced primary mass leads to a longer waveform, partially compensating for the signal shortening caused by eccentricity. Notably, this eccentric solution is also associated with a more strongly anti-aligned primary spin component ($\chi_1 \sim -0.2$), in contrast to the near-zero aligned spin obtained in the quasi-circular case. Since an anti-aligned spin tends to shorten the inspiral, this highlights a nontrivial interplay between eccentricity, mass, and spin in shaping the waveform duration and its frequency evolution.

Besides correlations and degeneracies between eccentricity, masses and spins, there are several explanations that can account for the observed bimodality in the eccentricity posterior. Firstly, the relatively low network matched-filtered SNR of GW200105 (∼14) inherently complicates the interpretation of this event and the determination of the dominant source of variation in the waveform frequency and duration. However, we note that the same data was analyzed in [56] without observing such a bimodality and in the following, we report several tests performed to systematically assess the differences found. Across all variations we observe that the bimodality in the eccentricity posterior persists.

Investigating whether spin-precession could be responsible for this behavior is challenging. The posterior reported in [56] for the effective precession parameter, $\chi_{\rm p} = 0.06^{+0.13}_{-0.05}$, indicates only weak support for precession, making it unlikely to significantly alter the results. Notably, the inferred eccentricity remains very similar across both precessing and non-precessing analyses. To better understand the nature of the two peaks observed in our eccentricity posterior, we computed mismatches between the corresponding waveforms shown in Fig. 8.3, using the PSDs from the detection. While the mismatch between the unprojected waveforms is relatively large ($\mathcal{M} \sim 0.4$), it reduces significantly when the waveforms are projected onto the detector response, yielding $\mathcal{M} \sim 0.06$. Since this low mismatch is model-dependent, it is plausible that introducing an additional degree of freedom, such as spin precession, could help break the degeneracy, as seen in [56]. We further analyzed the accumulation of SNR and log-likelihood as a function of frequency for both peaks to assess whether the inspiral-only setup in [56] could break the degeneracy. However, we found that most of the contribution comes from the 30–400 Hz range – indicating that the merger-ringdown region does not significantly influence the results, and that the early inspiral, where the two waveforms are more different, is not the primary driver of signal recovery. To assess the impact of known low-frequency noise contamination in LIGO Livingston, we performed an additional run in which the likelihood integration for LIGO Livingston started at 25 Hz. This run still yielded a bimodal posterior with uncertainties consistent with the original analysis as seen in Fig. 8.4, reinforcing the robustness of the previous observations. As an additional test, we performed a zero-noise injection using the maximum likelihood parameters from the default IMRPhenomTEHM run with a uniform prior in eccentricity, employing the Advanced LIGO and Virgo PSD

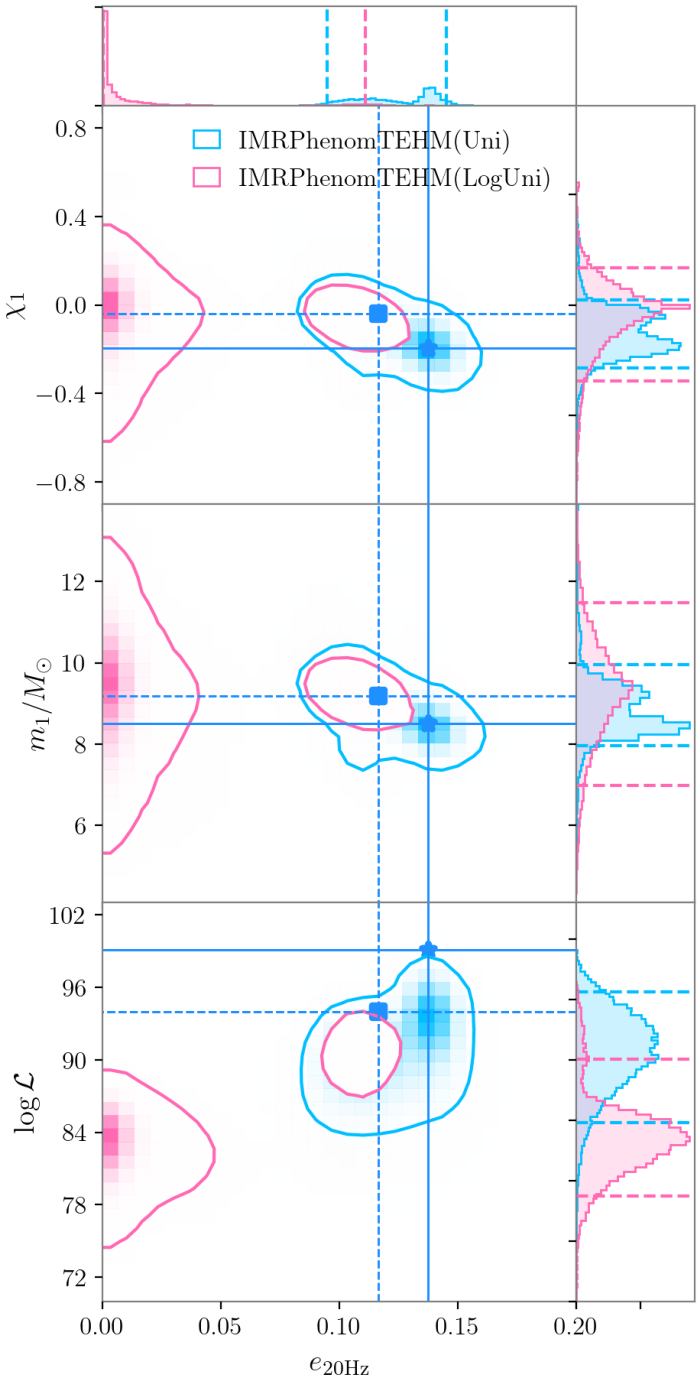

Figure 8.3: Marginalized one- and two-dimensional posterior distributions for GW200105, recovered using the IMRPhenomTEHM model with two different eccentricity priors: uniform (Uni, green) and log-uniform (LogUni, blue). The figure shows the joint distribution of the primary aligned spin component χ_1 (*top panel*), the primary mass $m_1/M_\odot$ (*middle panel*), and the log-likelihood $\log \mathcal{L}$ (*bottom panel*), as a function of the eccentricity measured at 20 Hz ($e_{20,\mathrm{Hz}}$). The blue star marks the maximum-likelihood sample from the uniform prior run, while the blue square indicates the second peak in the posterior distribution also present in the uniform prior run.

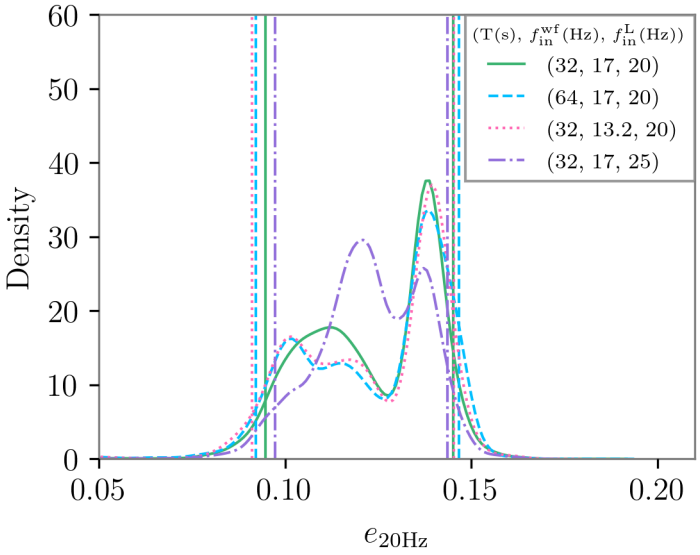

Figure 8.4: Posterior density distributions for the eccentricity at 20 Hz, $e_{\rm 20Hz}$, using the IMRPhenomTEHM (TEHM, or TE when restricting to the $(2,2)$-mode) model under different prior choices and starting frequencies. Solid lines correspond to a starting frequency of 17 Hz (default runs, see Tab. 8.1), dashed lines to 20 Hz, dotted to 13.3 Hz, and dot-dashed lines.

curves. The recovered eccentricity posterior does not exhibit any bimodality, suggesting that the observation in the real data may be driven by noise or model degeneracies, consistent again with the findings above.

Finally, we also investigate possible systematics due to the signal duration and low frequency resolution, further developed in Appendix 8.A. To test the potential impact of harmonic content at 20 Hz, we compare the difference between starting the waveform generation at 17 Hz, and 13.3 Hz to ensure that all $l \leq 3$ modes are in band by 20 Hz. As shown in Fig. 8.4, the bimodality in the eccentricity posterior persisted in both cases.

Finally, we find no significant improvement in convergence when lowering the starting frequency, suggesting that the limited duration constrains sensitivity to low-frequency content. The LVK assigns a 32-second duration to GW200105, which limits frequency resolution below 30 Hz. An extended 64-second run failed to resolve frequencies below 25 Hz and yielded a posterior consistent with the previously observed bimodality. Further extending the duration is not feasible, as the cleaned Virgo data used in our analysis is limited to 64 seconds. Given that prior tests also suggest low-frequency content has minimal impact on the observed features, we do not expect this limitation to significantly affect our results. Nonetheless, it highlights an important consideration for future observing runs using eccentric models.

8.4 Conclusions

This work presents the first PE analysis of NSBH events using a full IMR eccentric waveform model, marking a significant step forward in the complete interpretation of GW events. Our analysis with IMRPhenomTEHM finds that GW200115 and GW230529 are consistent with QC NSBH inspirals, while GW200105 shows compelling evidence for

non-zero eccentricity. This supports recent claims made in [56] using an inspiral-only, eccentric, spin-precessing waveform model. While some systematic uncertainties remain, our results provide evidence in favor of eccentricity and signal the beginning of a new era in which robust eccentricity measurements are becoming feasible. To complement our results, we provide a data release [583] containing all the posterior samples generated in this work.

The outcome of all our investigations of GW200105 indicates that the IMRPhenomTEHM model supports a non-zero eccentricity, with an estimated value of $e_{20\mathrm{Hz}} = 0.12^{+0.02}_{-0.03}$ and a Bayes factor of $\log_{10}\mathcal{B}_{\mathrm{E/QC}} = 1.22^{+0.12}_{-0.12}$ under a uniform prior. When using a more restrictive log-uniform prior, we still find a subdominant mode at non-zero eccentricity, also modestly supported with $\log_{10}\mathcal{B}_{\mathrm{E/QC}} = 0.11^{+0.11}_{-0.11}$. Although the log-uniform prior may not be well suited for low-SNR events such as this, the presence of a subdominant mode consistent with eccentricity is expected and notably was only observed in [56] when using a higher lower bound for the eccentricity prior.

Runs with a uniform eccentricity prior show a bimodal posterior. Nonetheless, all tested configurations consistently support non-zero eccentricity with similar confidence intervals. Our tests indicate that the bimodality arises from a degeneracy between waveform projections onto the detectors, which could be broken by introducing additional parameters – likely explaining why it vanishes when using the precessing eccentric model `pyEFPE`. Our investigations also highlight the importance of longer waveform durations to resolve low-frequency content for eccentric analysis, reinforcing the need for extended-duration analyses in future studies. A detailed summary of relevant systematics is provided in Appendix 8.A.

Finally, it is worth highlighting that data quality may also influence the analysis of GW200105, as the event was affected in both detectors. This noise was subtracted from the publicly available strain data using the BayesWave algorithm [584], and we have confirmed that it does not affect the eccentricity findings. Notably, the only other event in GWTC-3 reanalyzed with IMR eccentric models that shows strong evidence for eccentricity – GW200129 [4, 22, 55] – is also known to have data quality concerns [317]. While both events retain support for eccentricity even after applying various glitch mitigation strategies or excluding the affected data segments, these issues underscore the importance of carefully assessing data quality in future analyses. Nonetheless, the results presented here provide valuable insights into the population properties and formation channels of compact binary mergers, marking an important step forward in GW astrophysics.

Acknowledgements

The authors sincerely thank Cecilio García-Quirós, Héctor Estellés, and Maria Haney for valuable discussions; and Alicia M. Sintes for her insights on frequency-domain resolution for long signals. We also thank Geraint Pratten for his very helpful review of the manuscript as part of the LSC Publication & Presentation Committee. We thankfully acknowledge the computer resources (MN5 Supercomputer), technical expertise and assistance provided by Barcelona Supercomputing Center (BSC) through funding from the Red Española de Supercomputación (RES) (AECT-2024-3-0027); and the computer resources (Picasso Supercomputer), technical expertise and assistance provided by the SCBI (Supercomputing and Bioinformatics) center of the University of Málaga (AECT-2025-1-0035, AECT-2025-1-0034). This research has made use of data or software obtained from the Gravitational

Wave Open Science Center (gwosc.org), a service of the LIGO Scientific Collaboration, the Virgo Collaboration, and KAGRA. This material is based upon work supported by NSF's LIGO Laboratory which is a major facility fully funded by the National Science Foundation. LIGO is funded by the U.S. National Science Foundation. Virgo is funded by the French Centre National de Recherche Scientifique (CNRS), the Italian Istituto Nazionale della Fisica Nucleare (INFN) and the Dutch Nikhef, with contributions by Polish and Hungarian institutes.

Maria de Lluc Planas is supported by the Spanish Ministry of Universities via an FPU doctoral grant (FPU20/05577, EST24/00621). A. Ramos-Buades is supported by the Veni research programme which is (partly) financed by the Dutch Research Council (NWO) under the grant VI.Veni.222.396; acknowledges support from the Spanish Agencia Estatal de Investigación grant PID2022-138626NB-I00 funded by MICIU/AEI/10.13039/501100011033 and the ERDF/EU; is supported by the Spanish Ministerio de Ciencia, Innovación y Universidades (Beatriz Galindo, BG23/00056) and co-financed by UIB. Jorge Valencia is supported by the Spanish Ministry of Universities via an FPU doctoral grant (FPU22/02211). This work was supported by the Universitat de les Illes Balears (UIB); the Spanish Agencia Estatal de Investigación grants PID2022-138626NB-I00, PID2019-106416GB-I00, RED2022-134204-E, RED2022-134411-T, funded by MCIN/AEI/10.13039/501100011033; the MCIN with funding from the European Union NextGenerationEU/PRTR (PRTR-C17.I1); Comunitat Autonòma de les Illes Balears through the Direcció General de Recerca, Innovació I Transformació Digital with funds from the Tourist Stay Tax Law (PDR2020/11 - ITS2017-006), the Conselleria d'Economia, Hisenda i Innovació grant numbers SINCO2022/18146 and SINCO2022/6719, co-financed by the European Union and FEDER Operational Program 2021-2027 of the Balearic Islands; the "ERDF A way of making Europe".

Appendices

8.A Systematics in eccentric GW parameter estimation

Likelihood-based PE analyses in GW astronomy are typically performed in the frequency domain for ground based detectors, where events are sufficiently short that the response and noise power spectral density can be approximated as constant during an event, and the likelihood integral is then performed in the frequency domain. For time-domain waveform models, this requires special considerations, as a fixed starting time translates to different starting frequencies for different harmonics. Ensuring that all relevant harmonics are within the detector band at the beginning of the likelihood integration demands that the waveform starts sufficiently early in time. While this requirement applies to any multipolar time-domain model, it is especially important for eccentric systems, where each multipole contains a superposition of harmonics of the mean anomaly. Accurately capturing these components can significantly increase computational cost, particularly for low-mass binaries. In contrast, purely frequency-domain models do not share these constraints, making them computationally cheaper to ensure that the information content of all multipoles is used consistently.

For generic time-domain multipolar models, incorporating higher-order modes requires lowering the starting frequency to ensure that all relevant modes are excited at the beginning of the analysis band, typically set to 20 Hz for current ground-based detectors. Since modes with $m > 2$ contain higher-frequency content over the same time interval, the waveform must start earlier to capture them. The appropriate starting frequency can be adjusted based on the highest m-mode ($m_{\rm max}$) included in the analysis, following

$$f^{\rm wf}_{\rm min} = \frac{2 f^{\rm L}_{\rm start}}{m_{\rm max}}. \tag{8.A.1}$$

Hence, to ensure that multipoles with $l \leq 3$ (as considered in this study) are within band at the likelihood starting frequency of 20 Hz, waveform generation would ideally begin at 13.3 Hz. However, after performing several tests and evaluating the impact on GW200105 (see Tab. 8.1 and Fig. 8.4), we found that including such low frequencies had a negligible effect compared to the increased computational cost. Therefore, we set the default starting frequency for waveform generation to 17 Hz in all runs.

Eccentric waveforms can be decomposed in harmonics of the mean anomaly, which describe the morphology of the signal [36]. Using the Stationary Phase Approximation (SPA) [305] one can estimate the starting frequency where the j-th mean anomaly harmonic, $j \in (-N, +N)$ with $N \in \mathbb{N}$, enters in band,

$$f_j \approx \left(1 + \frac{j}{2}\right) f^{\rm wf}_{\rm start}. \tag{8.A.2}$$

The approximation in Eq. (8.A.2) becomes more inaccurate for $j < -2$ where the $f_j = 0$ (numerical evolutions show that $f_j < 1$). The conclusion of Eq. (8.A.2) is that including the full content of the positive harmonics at 20 Hz would require lower frequencies. However,

for the parameter space considered and some waveform inspections, the harmonics with $j > 2$ show a negligible contribution.

A key difference between `pyEFPE` and IMRPhenomTEHM is that the former uses the SPA to derive closed-form expressions for the waveform modes, directly evaluated in the frequency domain. In contrast, time-domain models such as IMRPhenomTEHM require a numerical transformation to the frequency domain. This demands additional care to ensure that all relevant modes are excited within the analysis band, as discussed above. However, our tests confirm that setting a sufficiently low starting frequency for waveform generation in IMRPhenomTEHM yields a clean Fourier transform and results in frequency-domain waveforms consistent with those from `pyEFPE`. Thus, differences in our PE results cannot be attributed to this modeling choice. Instead, these investigations revealed a more critical issue for eccentric PE: the limited signal duration assigned to GW200105 (32 seconds) restricts the frequency resolution in `bilby`, where $\mathrm{d}f = 1/D$, making it challenging to capture low-frequency content below approximately 30 Hz. We found that only a significantly longer duration – around $D \sim 128$ seconds – produced a clean and well-resolved frequency-domain waveform. While this low-frequency range has limited impact on the overall SNR or likelihood accumulation for this event, we still observe variations in posterior structure when modifying the waveform content between $20-30\,\mathrm{Hz}$, as shown in Fig. 8.4. This suggests that even when low-frequency contributions do not dominate signal reconstruction, they can still impact parameter inference. This is particularly relevant for eccentric binaries, which contain more low-frequency structure than QC systems, since eccentricity is higher at low frequencies. While current detectors and low-SNR events like GW200105 may not benefit substantially from these low frequencies, future high-SNR detections and more sensitive detectors may require longer waveform durations to fully capture low-frequency content. This emphasized the need for extended-duration analyses in future studies where eccentric waveform models might be routinely used, and more towards next observatories more sensitive in the low frequencies.

CHAPTER 9

Conclusions

Accurate and efficient waveform models are essential to detect and interpret signals from CBCs and to extract physical properties of the sources. Waveform modeling and Bayesian PE form the backbone of GW data analysis, and their refinement directly impacts our ability to test GR, uncover the astrophysical formation channels of compact binaries, and probe extreme gravitational dynamics. This thesis contributes to this field by developing novel tools for waveform modeling across three particularly challenging regimes: the transition from comparable mass to extreme mass ratios, spin-precession, and orbital eccentricity. These effects encode rich dynamical information and are crucial for fully generic models that aim to describe the diverse BBH population expected from future observing runs with increased sensitivity.

The first part of the original results of the thesis focuses on spin-precession and its impact across the entire mass ratio dimension. In Chapter 5, we introduce a new parameterized remnant model for single-spin precessing QC BBHs at arbitrary mass ratios, aiming to improve the modeling of the ringdown stage in precessing systems. By leveraging precessing geodesic dynamics at the ISSO and validating the results with NR data up to mass ratio 1000, we construct fits for the final mass and spin that incorporate consistent corrections from the EMR limit. Working in a co-orbital frame and subtracting aligned-spin fits before training on precessing datasets allowed us to isolate precession-induced corrections with high accuracy while keeping the model simple and generalizable. Overfitting was controlled using the BIC, and validation through out-of-sample error estimates showed performance competitive with NRSur7dq4EmriRemnant at significantly lower computational cost. Notably, we identified consistent trends in the mapping between aligned-spin and precessing results, enabling the removal of systematic biases in previous models such as those underlying IMRPhenomXPHM and IMRPhenomTPHM. The resulting model surpasses the baseline in accuracy and provides an improved ringdown description for future precessing waveform models.

The second part of the thesis focuses on orbital eccentricity in BBHs. We present the first time-domain eccentric model for aligned-spin BBHs within the IMRPhenomT family [34, 190, 191], and apply it to the reanalysis of BBH and NSBH events detected by the LVK Collaboration. In Chapter 6, we present IMRPhenomTEHM, a time-domain, multipolar waveform model for aligned-spin BBHs in elliptical orbits. It incorporates 3PN-order eccentric corrections into the state-of-the-art QC model IMRPhenomTHM and includes modes $(l, |m|) = (2,2), (2,1), (3,3), (4,4), (5,5)$ with eccentric corrections

up to $\mathcal{O}(e^6)$. A key feature of IMRPhenomTEHM is the ability to set a reference frequency independently from the minimum frequency, enhancing its flexibility and enabling better conditioning for Fourier transforms – an advantage particularly useful for time-dependent quantities such as the eccentricity. In the circular limit, IMRPhenomTEHM recovers IMRPhenomTHM with mismatches below 10^{-5}. Across a broad parameter range ($q \in [1, 20]$, $\chi_i \in [-0.995, 0.995]$, $e \lesssim 0.4$ at 10 Hz), it performs competitively with TEOBResumS-Dalí and SEOBNRv5EHM, achieving mismatches against NR below 2%. While slightly less accurate than these models, IMRPhenomTEHM remains robust for PE studies – validated both on NR injections and real events (GW150914 and GW190521) – and is currently the most computationally efficient eccentric IMR model available. This enables large-scale Bayesian inference studies, demonstrated through a reanalysis of 17 BBH events in Chapter 7 and three NSBH events in Chapter 8. These analysis represent the first routine use of an eccentric waveform model with standard LVK analysis tools, while previous eccentric PE studies often relied on resampling techniques, iterative fitting, or machine learning approaches [47, 55, 541][1]. In Chapter 7, we analyze all selected BBH events using both the QC aligned-spin IMRPhenomTHM and eccentric IMRPhenomTEHM models, adopting uniform and log-uniform priors in eccentricity. We identify support for eccentricity in four events: GW190701, GW190929, GW200129, and GW200208_22. For these, we perform extended analyses with different datasets, samplers, and precessing models (IMRPhenomTPHM and NRSur7dq4). GW200129 is particularly compelling due to indications of dynamical formation – evidenced by both precession and eccentricity. However, its analysis is complicated by a known glitch in the data. Our results show that the eccentric hypothesis remains robust across various priors and glitch mitigation strategies – more so than the precessing hypothesis, which is generally suppressed under the `BayesWave` mitigation (particularly the `BayesA` draw). Given its high SNR and total mass, GW200129 is a strong candidate for showing eccentric features in ground-based detectors. While precession cannot be entirely ruled out, our findings suggest eccentricity is the dominant feature. For the other three events, we conduct additional PE runs to assess waveform systematics. These highlight current limitations in eccentric models near merger, particularly for high-mass systems where short signals hinder robust conclusions – especially in the cases of GW190701 and GW190929. GW200208_22 presents a somewhat different challenge: despite favoring the eccentric hypothesis over both aligned and precessing QC models, the relatively low SNR complicates the analysis and the strength of the conclusion. Finally, the recent evidence for eccentricity in GW200105 using a PN precessing-spin model [56, 367], and the ability of IMRPhenomTEHM to run `bilby`, even for low-mass events like GW190814, motivated a reanalysis of all confirmed NSBH mergers, GW200105, GW200115 [8], and GW230529 [9], presented in Chapter 8. This study represents the first parameter estimation analysis of NSBH events using a full IMR eccentric model, finding support for eccentricity in GW200105 and consistency with a QC inspiral for GW200115 and GW230529, thus opening new avenues for understanding the dynamical formation of compact binaries. While several systematic uncertainties – such as signal duration, waveform degeneracies, and data quality – still limit the interpretation, the results demonstrate the importance and feasibility of eccentric IMR analyses in the future. A key result of this entire reanalysis is the demonstration that neglecting eccentricity can bias key parameters such as the chirp mass and effective spin. This underscores the importance of including eccentricity in waveform models for PE, especially in light of the growing evidence for an eccentric subpopulation among CBCs

[1] Ref. [55] uses machine learning to analyze most events, and `parallel Bilby`[118] for a subset.

in future observing runs.

Together, these projects contribute to advancing waveform modeling for precessing and eccentric binaries – two essential components for building a fully generic BBH model. This thesis demonstrates how theoretical insights, high-efficiency waveform implementations, and comprehensive PE studies can converge to enable the routine use of such models within standard GW data analysis pipelines. The evidence we find for eccentricity in some events suggests that dynamical formation channels may play a more significant role in the observed BBH population than previously thought. Moreover, the systematic biases introduced by waveform limitations emphasize the need for continued efforts toward more general, accurate, and efficient models. The methods, models, and datasets developed here will support future analyses with more sensitive detectors, including 3G ground-based observatories and space missions like LISA, where eccentricity and precession are expected to be more prevalent. Neglecting these features in upcoming observing runs will not only limit our understanding of the BBH population in the Universe, but may also become problematic given the upgraded sensitivities – making accurate and complete models essential to avoid biases in the recovery of source parameters. This thesis thus paves the way for these developments and lays the foundation for future modeling efforts aimed at characterizing the full diversity of GW signals. At the same time, it provides clear pathways for incorporating all relevant physical features to achieve a generic BBH model across the complete nine-dimensional parameter space.

Looking ahead, the two main branches of this thesis can now be merged toward the overarching goal of constructing a fully generic BBH model across the full nine-dimensional parameter space. First, although the final spin model developed in Chapter 5 was limited to the single-spin case, it lays the groundwork for future extensions to double-spin systems and in-plane spin effects. This model can be incorporated into current IMRPhenom models, which have shown biases in predicting the final state, as seen in Figure 5.11 and Figure 5.15. While such refinements may not yet be necessary for the sensitivity of current detectors, we expect next-generation observatories to better resolve the ringdown phase, requiring more accurate modeling of the remnant properties. In parallel, the precessing dataset constructed in this work – comprising consistently preprocessed waveforms from multiple NR catalogs and Teukolsky waveforms – marks a significant step toward the development of a fully NR-calibrated precessing model. Recent efforts have been made to calibrate precessing models within the phenomenological family in the Fourier domain [292–294, 310], mainly in the comparable-mass regime. The dataset compiled here, combined with newly available simulations, enables these calibration efforts to be extended across the full mass-ratio range. In particular, the dataset includes the evolution of Euler angles, which can be used to calibrate the rotations required to map the waveform from the co-precessing frame (now updated with the new final state model) to the inertial frame. Further improvements to IMRPhenomTEHM are also planned to enhance its accuracy and suitability for routine use in next-generation observatories. One current limitation lies in the modeling of eccentric corrections to the mode amplitudes, which rely on PN expansions up to $\mathcal{O}(e^6)$ due to the absence of closed-form tail terms. These expansions break down at high eccentricities, and we aim to explore non-expanded expressions using recent resummation techniques for these tail contributions [510]. Additionally, highly eccentric waveforms at high frequencies may introduce nonphysical features due to the QC merger-ringdown transition currently imposed in the model. Addressing this would

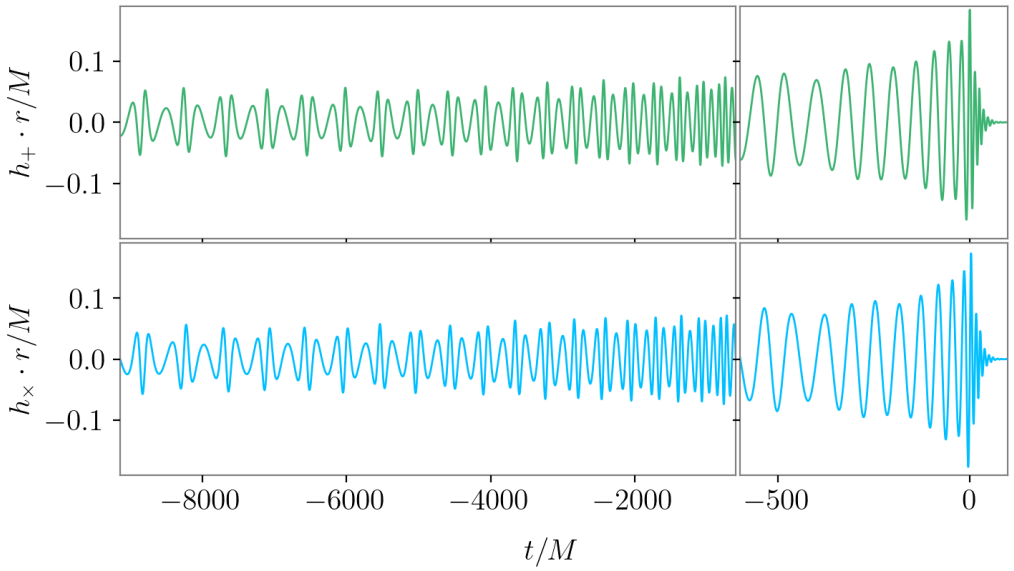

Figure 9.1: First demonstration of a IMRPhenomTPEHM waveform, constructed by twisting up the IMRPhenomTEHM co-precessing waveform using PN-informed Euler angles computed via the `phenomxpy` infrastructure. The plot shows the GW polarizations (*top*: plus, *bottom*: cross) for a BBH with $q = 3$, $\vec{\chi_1} = \vec{\chi_2} = (0.4, 0.4, 0.4)$, $e_{10\mathrm{Hz}} = 0.3$, $l_{10\mathrm{Hz}} = \pi$ rad, and $\iota = \varphi = 0$ in the L_0-inertial frame. This prototype model incorporates only spin-precession effects in the twisting-up angles.

require calibration against eccentric NR waveforms in the merger-ringdown regime – a challenge given the current scarcity of such simulations, which also limits the parameter space covered by existing surrogate models. While our model has proven more efficient than other IMR eccentric models, it remains too computationally expensive for very low-mass events such as BNS mergers. Further development of acceleration techniques will therefore be essential to extend its use to low-mass events and next-generation detectors. That said, current eccentric models appear sufficiently accurate to identify eccentricity in existing GW detections and show good agreement with NR simulations, suggesting they are adequate for present analyses. Given that eccentricity modeling is still in its early stages – lagging behind precession, which itself has only recently begun to be calibrated – we expect progress in this area to follow a similar pace.

The most promising future direction is to combine spin precession and eccentricity into a single waveform model. By applying the twisting-up approach [146, 297] to a co-precessing IMRPhenomTEHM waveform – accounting with the final state modification – and using PN-informed evolution that accounts for both eccentricity and spin precession, both effects can be incorporated in a unified framework. The modular structure of phenomenological models makes this integration a realistic short-term goal, and initial steps in this direction have already been taken. The new `phenomxpy` Python package [416] provides a consistent and flexible modular framework, which has enabled testing the twisting-up procedure on a IMRPhenomTEHM waveform as the co-precessing base, leading to the first prototype of the IMRPhenomTPEHM model, as illustrated in Figure 9.1. Although this preliminary version uses QC PN-informed spin-precession only (evolving spin and orbital angular momenta to obtain Euler angles or quaternions), it can be easily upgraded to include expressions that simultaneously account for eccentricity and precession, e.g. [367], allowing for full generic rotation to the inertial frame. While a few initial IMR waveform models

incorporating both eccentricity and spin precession have recently emerged – see e.g. [21, 44, 358] – the new IMRPhenomTPEHM model represents a natural candidate for routine analysis within the LVK. Its demonstrated efficiency, along with its expected accuracy in the generic regime after the proposed improvements, positions it as a promising tool for achieving full coverage of the BBH merger parameter space. This development is crucial for next-generation GW detectors, where both the detection and accurate characterization of generic binaries will offer unprecedented insights into their formation channels. Moreover, failing to account for these effects could introduce significant biases in the recovered source parameters. Exciting science lies ahead, and developing accurate, efficient, and generic BBH models is a central part of this journey. This thesis lays a solid foundation for such efforts, setting the cornerstone for the first generic phenomenological BBH waveform model.

Appendices

APPENDIX A

Fourier domain representation

The Fourier transform $\tilde{x}(t)$ of a time series $x(t)$ consists of decomposing it into its sine and cosine representation, according to

$$\tilde{x}(f) = \frac{1}{\sqrt{2\pi}} \int_{-\infty}^{\infty} \mathrm{d}t x(t) e^{-i2\pi ft}. \tag{A..1}$$

The inverse Fourier transform is then given by

$$x(t) = \frac{1}{\sqrt{2\pi}} \int_{-\infty}^{\infty} df \tilde{x}(f) e^{i2\pi ft}. \tag{A..2}$$

The parameter f has dimensions of $1/t$, and it is interpreted as a frequency. In general, the inverse Fourier transform $\tilde{x}(f)$ is a complex function of the frequency, which has the property

$$\tilde{x}(-f) = \tilde{x}^*(f) \text{ if } x(t) \in \mathbb{R}. \tag{A..3}$$

In gravitational wave data analysis it is typical to work with data sets that correspond to a constant sampling frequency, so that the observed data is an equally spaced time series as in Equation (2.3.1). Hence, we need to define the *discrete Fourier transform* (DFT), the operation in Equation (A..1) but appropriate for a finite set of discretely-sampled points. The DFT of the discrete samples $x_j = x(t_0 + \Delta j), j = 0, ..., N-1$ is defined, in our conventions, as

$$\tilde{x}(f_k) = \tilde{x}_k = \Delta t \sum_{j=0}^{N-1} x_j e^{-i2\pi jk/N}, \tag{A..4}$$

where $f_k = k\Delta f = \frac{k}{N\Delta t}$, with $k = -n/2, -N/2+1, ..., N/2-1$. The inverse discrete Fourier transform (IDFT) is then defined as

$$x(t_j) = x_j = \frac{1}{\Delta t N} \sum_{k=-N/2}^{N/2-1} \tilde{x}_k e^{-i2\pi jk/N}. \tag{A..5}$$

The DFT and IDFT assume that the signal is periodic with period $N\Delta t$. However, the rate at which we sample the signal determines if the finite set of samples can reconstruct the complete signal, and it is given by the Sampling Theorem [585]:

Theorem A..1 (**Sampling Theorem**). *If a continuous time signal contains no frequency components higher than the so called Nyquist frequency f_{Ny}, then it can be completely determined by uniform samples taken at a rate f_s twice the Nyquist frequency or higher:*

$$\text{If } \tilde{x}(f) = 0 \text{ for } |f| \geq f_{Ny} \Rightarrow \; f_s \geq 2f_{Ny} \text{ or } \Delta t \leq \frac{1}{2f_{Ny}}. \tag{A..6}$$

A.A Parseval's theorem and the power spectral density

Parseval's theorem establishes the relation between the integrals of the absolute squares of $x(t)$ and its Fourier transform $\tilde{x}(f)$, which is usually called the energy present in the signal

$$E = \int_{-\infty}^{\infty} \mathrm{d}t|x(t)|^2 = \int_{-\infty}^{\infty} \mathrm{d}t|\tilde{x}(f)|^2. \tag{A.A.1}$$

We define $E_x(f) = |\tilde{x}(f)|^2$ as the *Energy Spectral Density* of the signal. In general, the total energy E is infinite if the signal has support for all t, so it is useful to define a well-defined quantity, the total power P, as

$$P = \lim_{T\to\infty} \frac{1}{T} \int_{-T/2}^{T/2} \mathrm{d}t|x(t)|^2 = \int_{-\infty}^{\infty} df P_x(f) = \int_0^{\infty} S_x(f), \tag{A.A.2}$$

where the *Power Spectral Density* (PSD) $P_x(f)$ is defined as

$$P_x(f) = \lim_{T\to\infty} \frac{1}{T} \int_{-\infty}^{\infty} \left| \int_{-T/2}^{T/2} \mathrm{d}t x(t) e^{-i2\pi ft} \right|^2 = \lim_{T\to\infty} \frac{1}{T} \left|\tilde{x}_T(f)\right|^2, \tag{A.A.3}$$

where $\tilde{x}_T(f)$ denotes the Fourier transform of $x(t)$ between $-T/2$ and $T/2$.

The second equality in Equation (A.A.2) holds by applying Parseval's Theorem (A.A.1) and the definition of the Fourier transform (A..1). If the integral is over the positive frequencies, then the *One-Sided Power Spectral Density* $S_x(f) = 2P_x(f)$, and the definition requires a factor 2 in Equation (A.A.3).

A.B Convolution theorem

The convolution of an input signal $x(t)$ and the system impulse response $K(t)$ in a *linear system* is defined in the time domain as

$$(x * K)(t) = \int_{-\infty}^{\infty} \mathrm{d}t' x(t') K(t - t'). \tag{A.B.1}$$

The convolution theorem establishes that the convolution in the time domain is the multiplication of the Fourier transforms in the frequency domain

$$(x * K)(t) \Longleftrightarrow \tilde{x}(f)\tilde{K}(f), \tag{A.B.2}$$

where $\tilde{K}(f)$ is usually called the transfer function or kernel.

A.C Correlation theorem

The correlation of two functions $x(t)$ and $y(t)$ is a measure of the match in shape between the two signals when they are shifted relative to one another by an amount t

$$(x \otimes y)(t) = \int_{-\infty}^{\infty} \mathrm{d}t' x(t') y(t + t'). \tag{A.C.1}$$

The correlation theorem establishes that

$$(x \otimes y)(t) \Longleftrightarrow \tilde{x}^*(f)\tilde{y}(f). \tag{A.C.2}$$

Parseval's Theorem (A.A.1) is the special case where $y = x$ at $t = 0$.

Finally, one can define the *auto-correlation function* of a time series $x(t)$, $C_x(t)$, setting $x = y$ and an appropriate normalization so that the integral does not diverge:

$$C_x(t) = \lim_{T\to\infty} \int_{-T/2}^{T/2} \mathrm{d}t' x(t')x(t+t'). \tag{A.C.3}$$

Using this last definition for the auto-correlation function, one can rewrite the Power Spectral Density (A.A.3) as

$$P_x(f) = \int_{-\infty}^{\infty} \mathrm{d}t C_x(t) e^{-i2\pi ft}. \tag{A.C.4}$$

This last expression implies that the Fourier transform of the auto-correlation function $C_x(t)$ is the power spectral density $P_x(t)$.

APPENDIX B

Permission letters

This appendix compiles the permissions granted by the co-authors of the publications presented in this thesis, authorizing Maria de Lluc Planas Llompart to include them in Chapter 5, Chapter 6, Chapter 7, and Chapter 8.

Universitat de les Illes Balears

Dr. Sascha Husa, as co-author of the following articles:

- Maria de Lluc Planas, Joan Llobera-Querol, and Sascha Husa. "*Building a bridge between comparable and extreme mass ratio black hole binaries: A single spin precessing model for the final state*", **Phys. Rev. D 109.12 (2024), p. 124028**. DOI: 10.1103/PhysRevD.109.124028, arXiv: 2401.13342 [gr-qc].
- Maria de Lluc Planas, Antoni Ramos-Buades, Cecilio García-Quirós, Héctor Estellés, Sascha Husa, and Maria Haney. "*Time-domain phenomenological multipolar waveforms for aligned-spin binary black holes in elliptical orbits*", arXiv: arXiv:2503.13062[gr-qc]
- Maria de Lluc Planas, Antoni Ramos-Buades, Cecilio García-Quirós, Héctor Estellés, Sascha Husa, and Maria Haney. "*Eccentric or circular? A re-analysis of gravitational wave events for orbital eccentricity signatures*", arXiV: arXiv:2504.15833[gr-qc]
- Maria de Lluc Planas, Sascha Husa, Antoni Ramos-Buades, and Jorge Valencia. "*First eccentric inspiral-merger-ringdown analysis of neutron star-black hole mergers*"

I DECLARE:

Accept that Ms Maria de Lluc Planas Llompart presents the cited articles as the principal author and as a part of her doctoral thesis and that said articles cannot, therefore, form part of any doctoral thesis.

And for all intents and purposes, hereby sign this document.

Signature,

April 30, 2025.

Universitat de les Illes Balears

Mr. Joan Llobera Querol, as co-author of the following articles:

- Maria de Lluc Planas, Joan Llobera-Querol, and Sascha Husa. "*Building a bridge between comparable and extreme mass ratio black hole binaries: A single spin precessing model for the final state*", **Phys. Rev. D 109.12 (2024), p. 124028**. DOI: 10.1103/PhysRevD.109.124028, arXiv: 2401.13342 [gr-qc].

I DECLARE:

Accept that Ms Maria de Lluc Planas Llompart presents the cited articles as the principal author and as a part of her doctoral thesis and that said articles cannot, therefore, form part of any doctoral thesis.

And for all intents and purposes, hereby sign this document.

Signature,

Joan Llobera Querol

April 28, 2025.

Universitat de les Illes Balears

Dr. Antoni Ramos Buades, as co-author of the following articles:

- Maria de Lluc Planas, Antoni Ramos-Buades, Cecilio García-Quirós, Héctor Estellés, Sascha Husa, and Maria Haney. "*Time-domain phenomenological multipolar waveforms for aligned-spin binary black holes in elliptical orbits*", arXiv: arXiv:2503.13062[gr-qc]
- Maria de Lluc Planas, Antoni Ramos-Buades, Cecilio García-Quirós, Héctor Estellés, Sascha Husa, and Maria Haney. "*Eccentric or circular? A re-analysis of gravitational wave events for orbital eccentricity signatures*", arXiV: arXiv:2504.15833[gr-qc]
- Maria de Lluc Planas, Sascha Husa, Antoni Ramos-Buades, and Jorge Valencia. "*First eccentric inspiral-merger-ringdown analysis of neutron star-black hole mergers*"

I DECLARE:

Accept that Ms Maria de Lluc Planas Llompart presents the cited articles as the principal author and as a part of her doctoral thesis and that said articles cannot, therefore, form part of any doctoral thesis.

And for all intents and purposes, hereby sign this document.

Signature,

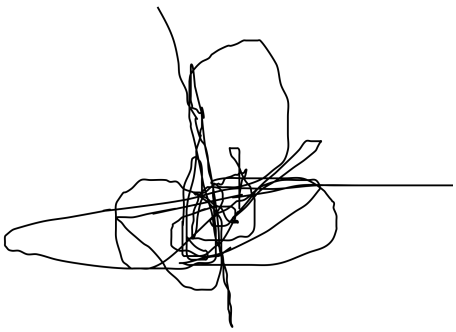

April 30, 2025.

Universitat de les Illes Balears

Dr. Maria Haney, as co-author of the following articles:

- Maria de Lluc Planas, Antoni Ramos-Buades, Cecilio García-Quirós, Héctor Estellés, Sascha Husa, and Maria Haney. "*Time-domain phenomenological multipolar waveforms for aligned-spin binary black holes in elliptical orbits*", arXiv: arXiv:2503.13062[gr-qc]
- Maria de Lluc Planas, Antoni Ramos-Buades, Cecilio García-Quirós, Héctor Estellés, Sascha Husa, and Maria Haney. "*Eccentric or circular? A re-analysis of gravitational wave events for orbital eccentricity signatures*", arXiV: arXiv:2504.15833[gr-qc]

I DECLARE:

Accept that Ms Maria de Lluc Planas Llompart presents the cited articles as the principal author and as a part of her doctoral thesis and that said articles cannot, therefore, form part of any doctoral thesis.

And for all intents and purposes, hereby sign this document.

Signature,

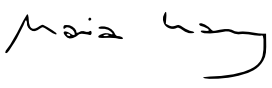

April 28, 2025.

Universitat de les Illes Balears

Dr. Héctor Estellés Estrella, as co-author of the following articles:

- Maria de Lluc Planas, Antoni Ramos-Buades, Cecilio García-Quirós, Héctor Estellés, Sascha Husa, and Maria Haney. "*Time-domain phenomenological multipolar waveforms for aligned-spin binary black holes in elliptical orbits*", arXiv: arXiv:2503.13062[gr-qc]
- Maria de Lluc Planas, Antoni Ramos-Buades, Cecilio García-Quirós, Héctor Estellés, Sascha Husa, and Maria Haney. "*Eccentric or circular? A re-analysis of gravitational wave events for orbital eccentricity signatures*", arXiV: arXiv:2504.15833[gr-qc]

I DECLARE:

Accept that Ms Maria de Lluc Planas Llompart presents the cited articles as the principal author and as a part of her doctoral thesis and that said articles cannot, therefore, form part of any doctoral thesis.

And for all intents and purposes, hereby sign this document.

Signature,

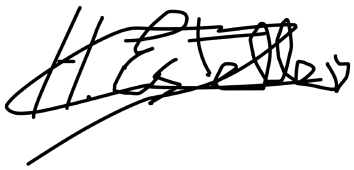

April 28, 2025.

Universitat de les Illes Balears

Dr. Cecilio García Quirós, as co-author of the following articles:

- Maria de Lluc Planas, Antoni Ramos-Buades, Cecilio García-Quirós, Héctor Estellés, Sascha Husa, and Maria Haney. "*Time-domain phenomenological multipolar waveforms for aligned-spin binary black holes in elliptical orbits*", arXiv: arXiv:2503.13062[gr-qc]
- Maria de Lluc Planas, Antoni Ramos-Buades, Cecilio García-Quirós, Héctor Estellés, Sascha Husa, and Maria Haney. "*Eccentric or circular? A re-analysis of gravitational wave events for orbital eccentricity signatures*", arXiV: arXiv:2504.15833[gr-qc]

I DECLARE:

Accept that Ms Maria de Lluc Planas Llompart presents the cited articles as the principal author and as a part of her doctoral thesis and that said articles cannot, therefore, form part of any doctoral thesis.

And for all intents and purposes, hereby sign this document.

Signature.

April 28, 2025.

Universitat de les Illes Balears

Mr. Jorge Valencia, as co-author of the following articles:

- Maria de Lluc Planas, Sascha Husa, Antoni Ramos-Buades, and Jorge Valencia. "*First eccentric inspiral-merger-ringdown analysis of neutron star-black hole mergers*"

I DECLARE:

Accept that Ms Maria de Lluc Planas Llompart presents the cited articles as the principal author and as a part of her doctoral thesis and that said articles cannot, therefore, form part of any doctoral thesis.

And for all intents and purposes, hereby sign this document.

Signature,

April 30, 2025.

Bibliography

[1] B. P. Abbott et al. (LIGO Scientific Collaboration and Virgo Collaboration), "Gwtc-1: a gravitational-wave transient catalog of compact binary mergers observed by ligo and virgo during the first and second observing runs", Phys. Rev. X **9**, 031040 (2019).

[2] R. Abbott et al. (LIGO Scientific Collaboration and Virgo Collaboration), "Gwtc-2: compact binary coalescences observed by ligo and virgo during the first half of the third observing run", Phys. Rev. X **11**, 021053 (2021).

[3] The LIGO Scientific Collaboration and the Virgo Collaboration, "Gwtc-2.1: deep extended catalog of compact binary coalescences observed by ligo and virgo during the first half of the third observing run", Phys. Rev. D **109**, 022001 (2024).

[4] R. Abbott et al. (LIGO Scientific Collaboration, Virgo Collaboration, and KAGRA Collaboration), "Gwtc-3: compact binary coalescences observed by ligo and virgo during the second part of the third observing run", Phys. Rev. X **13**, 041039 (2023).

[5] LIGO Scientific Collaboration and Virgo Collaboration (LIGO Scientific Collaboration and Virgo Collaboration), "Gw170817: observation of gravitational waves from a binary neutron star inspiral", Phys. Rev. Lett. **119**, 161101 (2017).

[6] B. P. Abbott et al. (LIGO Scientific, Virgo), "GW190425: Observation of a Compact Binary Coalescence with Total Mass $\sim 3.4 M_{\odot}$", Astrophys. J. Lett. **892**, L3 (2020).

[7] L. S. Collaboration and V. Collaboration, "Gw190814: gravitational waves from the coalescence of a 23 solar mass black hole with a 2.6 solar mass compact object", The Astrophysical Journal Letters **896**, L44 (2020).

[8] The LIGO Scientific Collaboration, the Virgo Collaboration, and the KAGRA Collaboration, "Observation of gravitational waves from two neutron star–black hole coalescences", The Astrophysical Journal Letters **915**, L5 (2021).

[9] A. G. Abac et al. (LIGO Scientific, Virgo„ KAGRA, VIRGO), "Observation of Gravitational Waves from the Coalescence of a 2.5-4.5 $M_{\odot}$ Compact Object and a Neutron Star", Astrophys. J. Lett. **970**, L34 (2024).

[10] *LIGO Laboratory Caltech*, https://www.ligo.caltech.edu/news/ligo20250320.

[11] A. Abac et al., "The Science of the Einstein Telescope", arXiv (2025).

[12] M. Maggiore et al., "Science Case for the Einstein Telescope", JCAP **03**, 050 (2020).

[13] D. Reitze et al., "Cosmic Explorer: The U.S. Contribution to Gravitational-Wave Astronomy beyond LIGO", Bull. Am. Astron. Soc. **51**, 035 (2019).

[14] The eLISA Consortium, "The gravitational universe", (2013).

[15] P. A. Seoane et al. (LISA), "Astrophysics with the Laser Interferometer Space Antenna", Living Rev. Rel. **26**, 2 (2023).

[16] "New horizons for fundamental physics with LISA", Living Reviews in Relativity **25**, 4, 4 (2022).

[17] N. Afshordi et al. (LISA Consortium Waveform Working Group), "Waveform Modelling for the Laser Interferometer Space Antenna", (2023).

[18] M. d. L. Planas, J. Llobera-Querol, and S. Husa, "Building a bridge between comparable and extreme mass ratio black hole binaries: A single spin precessing model for the final state", Phys. Rev. D **109**, 124028 (2024).

[19] M. d. L. Planas, A. Ramos-Buades, C. Garcia-Quiros, H. Estelles, S. Husa, and M. Haney, "Time-domain phenomenological multipolar waveforms for aligned-spin binary black holes in elliptical orbits", (2025).

[20] A. Gamboa et al., "Accurate waveforms for eccentric, aligned-spin binary black holes: The multipolar effective-one-body model SEOBNRv5EHM", (2024).

[21] R. Gamba, D. Chiaramello, and S. Neogi, "Toward efficient effective-one-body models for generic, nonplanar orbits", Phys. Rev. D **110**, 024031 (2024).

[22] M. d. L. Planas, A. Ramos-Buades, C. García-Quirós, H. Estellés, S. Husa, and M. Haney, "Eccentric or circular? A reanalysis of binary black hole gravitational wave events for orbital eccentricity signatures", (2025).

[23] M. d. L. Planas, S. Husa, A. Ramos-Buades, and J. Valencia, "First eccentric inspiral-merger-ringdown analysis of neutron star-black hole mergers", (2025).

[24] A. Le Tiec et al., "Periastron Advance in Spinning Black Hole Binaries: Gravitational Self-Force from Numerical Relativity", Phys. Rev. D **88**, 124027 (2013).

[25] A. Albertini, A. Nagar, A. Pound, N. Warburton, B. Wardell, L. Durkan, and J. Miller, "Comparing second-order gravitational self-force, numerical relativity, and effective one body waveforms from inspiralling, quasicircular, and nonspinning black hole binaries", Phys. Rev. D **106**, 084061 (2022).

[26] B. Wardell, A. Pound, N. Warburton, J. Miller, L. Durkan, and A. Le Tiec, "Gravitational Waveforms for Compact Binaries from Second-Order Self-Force Theory", Phys. Rev. Lett. **130**, 241402 (2023).

[27] X. Jiménez-Forteza, D. Keitel, S. Husa, M. Hannam, S. Khan, and M. Pürrer, "Hierarchical data-driven approach to fitting numerical relativity data for nonprecessing binary black holes with an application to final spin and radiated energy", Phys. Rev. **D95**, 064024 (2017).

[28] T. Islam, S. E. Field, S. A. Hughes, G. Khanna, V. Varma, M. Giesler, M. A. Scheel, L. E. Kidder, and H. P. Pfeiffer, "Surrogate model for gravitational wave signals from nonspinning, comparable-to large-mass-ratio black hole binaries built on black hole perturbation theory waveforms calibrated to numerical relativity", Phys. Rev. D **106**, 104025 (2022).

[29] T. Islam, S. E. Field, and G. Khanna, "Remnant black hole properties from numerical-relativity-informed perturbation theory and implications for waveform modeling", Phys. Rev. D **108**, 064048 (2023).

[30] T. Islam, "Interplay between numerical relativity and black hole perturbation theory in the intermediate-mass-ratio regime", Phys. Rev. D **108**, 044013 (2023).

[31] A. Ramos-Buades, A. Buonanno, H. Estellés, M. Khalil, D. P. Mihaylov, S. Ossokine, L. Pompili, and M. Shiferaw, "Next generation of accurate and efficient multipolar precessing-spin effective-one-body waveforms for binary black holes", Phys. Rev. D **108**, 124037 (2023).

[32] A. Nagar, S. Bernuzzi, W. Del Pozzo, G. Riemenschneider, S. Akcay, G. Carullo, P. Fleig, S. Babak, K. W. Tsang, M. Colleoni, F. Messina, G. Pratten, D. Radice, P. Rettegno, M. Agathos, E. Fauchon-Jones, M. Hannam, S. Husa, T. Dietrich, P. Cerdá-Duran, J. A. Font, F. Pannarale, P. Schmidt, and T. Damour, "Time-domain effective-one-body gravitational waveforms for coalescing compact binaries with nonprecessing spins, tides, and self-spin effects", Phys. Rev. D **98**, 104052 (2018).

[33] C. García-Quirós, M. Colleoni, S. Husa, H. Estellés, G. Pratten, A. Ramos-Buades, M. Mateu-Lucena, and R. Jaume, "Multimode frequency-domain model for the gravitational wave signal from nonprecessing black-hole binaries", Phys. Rev. D **102**, 064002 (2020).

[34] H. Estelles, S. Husa, M. Colleoni, D. Keitel, M. Mateu-Lucena, C. Garcia-Quiros, A. Ramos-Buades, and A. Borchers, "Time-domain phenomenological model of gravitational-wave subdominant harmonics for quasicircular nonprecessing binary black hole coalescences", Phys. Rev. D **105**, 084039 (2022).

[35] M. Boschini et al., "Extending black-hole remnant surrogate models to extreme mass ratios", Phys. Rev. D **108**, 084015 (2023).

[36] P. C. Peters, "Gravitational radiation and the motion of two point masses", Phys. Rev. **136**, B1224–B1232 (1964).

[37] K. G. Arun, L. Blanchet, B. R. Iyer, and S. Sinha, "Third post-Newtonian angular momentum flux and the secular evolution of orbital elements for inspiralling compact binaries in quasi-elliptical orbits", Phys. Rev. D **80**, 124018 (2009).

[38] M. Ebersold, Y. Boetzel, G. Faye, C. K. Mishra, B. R. Iyer, and P. Jetzer, "Gravitational-wave amplitudes for compact binaries in eccentric orbits at the third post-Newtonian order: Memory contributions", Phys. Rev. D **100**, 084043 (2019).

[39] Q. Henry and M. Khalil, "Spin effects in gravitational waveforms and fluxes for binaries on eccentric orbits to the third post-Newtonian order", Phys. Rev. D **108**, 104016 (2023).

[40] T. Damour and N. Deruelle, "General relativistic celestial mechanics of binary systems. I. The post-Newtonian motion.", Annales de L'Institut Henri Poincare Section (A) Physique Theorique **43**, 107–132 (1985).

[41] T. Damour and G. Schaefer, "Higher Order Relativistic Periastron Advances and Binary Pulsars", Nuovo Cim. B **101**, 127 (1988).

[42] G. Schäfer and N. Wex, "Second post-newtonian motion of compact binaries", Physics Letters A **174**, 196–205 (1993).

[43] A. Nagar, A. Bonino, and P. Rettegno, "Effective one-body multipolar waveform model for spin-aligned, quasicircular, eccentric, hyperbolic black hole binaries", Phys. Rev. D **103**, 104021 (2021).

[44] S. Albanesi, R. Gamba, S. Bernuzzi, J. Fontbuté, A. Gonzalez, and A. Nagar, *Effective-one-body modeling for generic compact binaries with arbitrary orbits*, 2025.

[45] T. Islam, V. Varma, J. Lodman, S. E. Field, G. Khanna, M. A. Scheel, H. P. Pfeiffer, D. Gerosa, and L. E. Kidder, "Eccentric binary black hole surrogate models for the gravitational waveform and remnant properties: comparable mass, nonspinning case", Phys. Rev. D **103**, 064022 (2021).

[46] B. Abbott et al. (LIGO Scientific, Virgo), "Search for eccentric binary black hole mergers with Advanced LIGO and Advanced Virgo during their first and second observing runs", Astrophys. J. **883**, 149 (2019).

[47] I. Romero-Shaw, P. Lasky, and E. Thrane, "Searching for eccentricity: Signatures of dynamical formation in the first gravitational-wave transient catalogue of LIGO and Virgo", Mon. Not. Roy. Astron. Soc. **490**, 5210–5218 (2019).

[48] A. Nitz, A. Lenon, and D. Brown, "Search for eccentric binary neutron star mergers in the first and second observing runs of Advanced LIGO", Astrophys. J. **890**, 1 (2020).

[49] I. M. Romero-Shaw, P. D. Lasky, E. Thrane, and J. C. Bustillo, "GW190521: orbital eccentricity and signatures of dynamical formation in a binary black hole merger signal", Astrophys. J. Lett. **903**, L5 (2020).

[50] V. Gayathri, J. Healy, J. Lange, B. O'Brien, M. Szczepanczyk, I. Bartos, M. Campanelli, S. Klimenko, C. O. Lousto, and R. O'Shaughnessy, "Eccentricity estimate for black hole mergers with numerical relativity simulations", Nature Astron. **6**, 344–349 (2022).

[51] M. Favata, C. Kim, K. G. Arun, J. Kim, and H. W. Lee, "Constraining the orbital eccentricity of inspiralling compact binary systems with Advanced LIGO", Phys. Rev. D **105**, 023003 (2022).

[52] E. O'Shea and P. Kumar, "Correlations in gravitational-wave reconstructions from eccentric binaries: A case study with GW151226 and GW170608", Phys. Rev. D **108**, 104018 (2023).

[53] I. M. Romero-Shaw, P. D. Lasky, and E. Thrane, "Signs of Eccentricity in Two Gravitational-wave Signals May Indicate a Subpopulation of Dynamically Assembled Binary Black Holes", Astrophys. J. Lett. **921**, L31 (2021).

[54] A. Ramos-Buades, A. Buonanno, and J. Gair, "Bayesian inference of binary black holes with inspiral-merger-ringdown waveforms using two eccentric parameters", Phys. Rev. D **108**, 124063 (2023).

[55] N. Gupte et al., *Evidence for eccentricity in the population of binary black holes observed by LIGO-Virgo-KAGRA*, Apr. 2024.

[56] G. Morras, G. Pratten, and P. Schmidt, "Orbital eccentricity in a neutron star - black hole binary", (2025).

[57] M. P. Haugan and C. Lämmerzahl, "Principles of Equivalence: Their Role in Gravitation Physics and Experiments That Test Them", Lecture Notes in Physics, 195–212.

[58] A. Einstein, "Die Feldgleichungen der Gravitation", Sitzungsber. Preuss. Akad. Wiss. Berlin, 844–847 (1915).

[59] Y. Choquet-Bruhat and R. P. Geroch, "Global aspects of the Cauchy problem in general relativity", Commun. Math. Phys. **14**, 329–335 (1969).

[60] A. Einstein, "Näherungsweise Integration der Feldgleichungen der Gravitation. (German) [Approximate integration of the field equations of gravitation]", German, Sitzungsber. Preuss. Akad. Wiss. Berlin, 688–696 (1916).

[61] LIGO Scientific Collaboration and Virgo Collaboration, "Observation of gravitational waves from a binary black hole merger", Phys. Rev. Lett. **116**, 061102 (2016).

[62] F. A. E. Pirani, "On the Physical significance of the Riemann tensor", Acta Phys. Polon. **15**, 389–405 (1956).

[63] F. A. E. Pirani, "Invariant formulation of gravitational radiation theory", Phys. Rev. **105**, 1089–1099 (1957).

[64] A. Trautman, "Radiation and Boundary Conditions in the Theory of Gravitation", Bull. Acad. Pol. Sci. Ser. Sci. Math. Astron. Phys. **6**, 407–412 (1958).

[65] H. Bondi, F. A. E. Pirani, and I. Robinson, "Gravitational waves in general relativity. 3. Exact plane waves", Proc. Roy. Soc. Lond. A **251**, 519–533 (1959).

[66] I. Robinson and A. Trautman, "Some spherical gravitational waves in general relativity", Proc. Roy. Soc. Lond. A **265**, 463–473 (1962).

[67] R. K. Sachs, "Gravitational waves in general relativity. 8. Waves in asymptotically flat space-times", Proc. Roy. Soc. Lond. A **270**, 103–126 (1962).

[68] M. G. J. Van der Burg and H. Bondi, "Gravitational waves in general relativity ix. conserved quantities", Proceedings of the Royal Society of London. Series A. Mathematical and Physical Sciences **294**, 112–122 (1966).

[69] S. M. Carroll, *Spacetime and Geometry* (Cambridge University Press, July 2019).

[70] M. Sieniawska and M. Bejger, "Continuous Gravitational Waves from Neutron Stars: Current Status and Prospects", Universe **5**, 217 (2019).

[71] *LISA Consortium*, https://www.lisamission.org/.

[72] S. Kalita and B. Mukhopadhyay, "Continuous gravitational wave from magnetized white dwarfs and neutron stars: possible missions for LISA, DECIGO, BBO, ET detectors", Mon. Not. Roy. Astron. Soc. **490**, [Erratum: Mon.Not.Roy.Astron.Soc. 491, 4396–4397 (2020)], 2692–2705 (2019).

[73] N. Christensen, "Stochastic gravitational wave backgrounds", Reports on Progress in Physics **82**, 016903 (2018).

[74] B. P. Abbott et al. (LIGO Scientific, Virgo), "Upper Limits on the Stochastic Gravitational-Wave Background from Advanced LIGO's First Observing Run", Phys. Rev. Lett. **118**, [Erratum: Phys.Rev.Lett. 119, 029901 (2017)], 121101 (2017).

[75] H. Xu et al., "Searching for the Nano-Hertz Stochastic Gravitational Wave Background with the Chinese Pulsar Timing Array Data Release I", Res. Astron. Astrophys. **23**, 075024 (2023).

[76] J. Antoniadis et al. (EPTA, InPTA:), "The second data release from the European Pulsar Timing Array - III. Search for gravitational wave signals", Astron. Astrophys. **678**, A50 (2023).

[77] G. Agazie et al. (NANOGrav), "The NANOGrav 15 yr Data Set: Evidence for a Gravitational-wave Background", Astrophys. J. Lett. **951**, L8 (2023).

[78] D. J. Reardon et al., "Search for an Isotropic Gravitational-wave Background with the Parkes Pulsar Timing Array", Astrophys. J. Lett. **951**, L6 (2023).

[79] A. W. G., P. R. Brady, J. D. E. Creighton, and É. É. Flanagan, "A power filter for the detection of burst sources of gravitational radiation in interferometric detectors", International Journal of Modern Physics D **09**, 303–307 (2000).

[80] B. P. Abbott et al. (LIGO Scientific, Virgo), "The basic physics of the binary black hole merger GW150914", Annalen Phys. **529**, 1600209 (2017).

[81] M. Maggiore, "Gravitational Waves (Volume I)", in *Oxford univ. press* (Oxford University Press, 2007) Chap. 4.1, pp. 167–176.

[82] L. Blanchet, "Post-newtonian theory for gravitational waves", Living Reviews in Relativity **27**, 4 (2024).

[83] J. M. Weisberg, J. H. Taylor, and L. A. Fowler, "Gravitational waves from an orbiting pulsar", Scientific American **245**, 74–82 (1981).

[84] *LIGO - A Gravitational-Wave Interferometer*, https://www.ligo.caltech.edu/page/ligo-gw-interferometer.

[85] *Virgo*, https://www.virgo-gw.eu/.

[86] *GEO*, https://www.geo600.org/.

[87] *KAGRA Large-scale Cryogenic Graviational wave Telescope Project*, https://gwcenter.icrr.u-tokyo.ac.jp/en/.

[88] *LIGO Laboratory Caltech*, http://www.ligo.caltech.edu/news/ligo20200326.

[89] LIGO Scientific Collaboration and Virgo Collaboration, "Gw190521: a binary black hole merger with a total mass of 150 $M_{\odot}$", Phys. Rev. Lett. **125**, 101102 (2020).

[90] R. Abbott et al. (LIGO Scientific, Virgo), "Properties and Astrophysical Implications of the 150 $M_{\odot}$ Binary Black Hole Merger GW190521", Astrophys. J. Lett. **900**, L13 (2020).

[91] *LIGO India*, https://www.ligo-india.in/.

[92] C. J. Moore, R. H. Cole, and C. P. L. Berry, "Gravitational-wave sensitivity curves", Class. Quant. Grav. **32**, 015014 (2015).

[93] S. W. Hawking and W. Israel, *Three Hundred Years of Gravitation* (1989).

[94] B. F. Schutz, "Networks of gravitational wave detectors and three figures of merit", Class. Quant. Grav. **28**, 125023 (2011).

[95] N. Andersson et al., "The Transient Gravitational-Wave Sky", Class. Quant. Grav. **30**, 193002 (2013).

[96] H. Fischer, *A history of the central limit theorem: from classical to modern probability theory* (Jan. 2011).

[97] G. D. Birkhoff, "Proof of the ergodic theorem", Proceedings of the National Academy of Sciences **17**, 656–660 (1931).

[98] L. Wainstein and V. Zubakov, *Extraction of Signals from Noise* (Prentice-Hall, Englewood Cliffs, NJ, 1962).

[99] B. Allen, "χ^2 time-frequency discriminator for gravitational wave detection", Phys. Rev. D **71**, 062001, 062001 (2005).

[100] S. A. Usman et al., "The PyCBC search for gravitational waves from compact binary coalescence", Class. Quant. Grav. **33**, 215004 (2016).

[101] P. Joshi et al., "How Many Times Should We Matched Filter Gravitational Wave Data? A Comparison of GstLAL's Online and Offline Performance", (2025).

[102] J. Roulet, L. Dai, T. Venumadhav, B. Zackay, and M. Zaldarriaga, "Template Bank for Compact Binary Coalescence Searches in Gravitational Wave Data: A General Geometric Placement Algorithm", Phys. Rev. D **99**, 123022 (2019).

[103] H. Jeffreys, *The theory of probability*, Third (Oxford University Press, 1961).

[104] N. Metropolis, A. W. Rosenbluth, M. N. Rosenbluth, A. H. Teller, and E. Teller, "Equation of State Calculations by Fast Computing Machines", The Journal of Chemical Physics **21**, 1087–1092 (1953).

[105] W. K. Hastings, "Monte carlo sampling methods using markov chains and their applications", Biometrika **57**, 97–109 (1970).

[106] J. Skilling, "Nested Sampling", in Bayesian inference and maximum entropy methods in science and engineering: 24th international workshop on bayesian inference and maximum entropy methods in science and engineering, Vol. 735, edited by R. Fischer, R. Preuss, and U. V. Toussaint, American Institute of Physics Conference Series (Nov. 2004), pp. 395–405.

[107] E. Thrane and C. Talbot, "An introduction to Bayesian inference in gravitational-wave astronomy: Parameter estimation, model selection, and hierarchical models", **36**, e010 (2019).

[108] S. Sharma, "Markov Chain Monte Carlo Methods for Bayesian Data Analysis in Astronomy", Annual Review of Astronomy and Astrophysics **55**, 213–259 (2017).

[109] A. Gelman and D. B. Rubin, "Inference from Iterative Simulation Using Multiple Sequences", Statistical Science **7**, 457–472 (1992).

[110] A. Sokal, "Monte carlo methods in statistical mechanics: foundations and new algorithms", in *Functional integration: basics and applications*, edited by C. DeWitt-Morette, P. Cartier, and A. Folacci (Springer US, Boston, MA, 1997), pp. 131–192.

[111] LIGO Scientific Collaboration, Virgo Collaboration, and KAGRA Collaboration, *LVK Algorithm Library - LALSuite*, Free software (GPL), 2018.

[112] K. Wette, "SWIGLAL: Python and Octave interfaces to the LALSuite gravitational-wave data analysis libraries", SoftwareX **12**, 100634 (2020).

[113] G. Ashton et al., "BILBY: A user-friendly Bayesian inference library for gravitational-wave astronomy", Astrophys. J. Suppl. **241**, 27 (2019).

[114] G. Ashton and C. Talbot, "Bilby-MCMC: an MCMC sampler for gravitational-wave inference", Mon. Not. Roy. Astron. Soc. **507**, 2037–2051 (2021).

[115] J. S. Speagle, "dynesty: a dynamic nested sampling package for estimating Bayesian posteriors and evidences", Monthly Notices of the Royal Astronomical Society **493**, 3132–3158 (2020).

[116] S. Koposov, J. Speagle, K. Barbary, G. Ashton, E. Bennett, J. Buchner, C. Scheffler, B. Cook, C. Talbot, J. Guillochon, P. Cubillos, A. A. Ramos, M. Dartiailh, Ilya, E. Tollerud, D. Lang, B. Johnson, jtmendel, E. Higson, T. Vandal, T. Daylan, R. Angus, patelR, P. Cargile, P. Sheehan, M. Pitkin, M. Kirk, J. Leja, joezuntz, and D. Goldstein, *Joshspeagle/dynesty: v2.1.4*, version v2.1.4, June 2024.

[117] I. M. Romero-Shaw et al., "Bayesian inference for compact binary coalescences with bilby: validation and application to the first LIGO–Virgo gravitational-wave transient catalogue", Mon. Not. Roy. Astron. Soc. **499**, 3295–3319 (2020).

[118] R. J. E. Smith, G. Ashton, A. Vajpeyi, and C. Talbot, "Massively parallel bayesian inference for transient gravitational-wave astronomy", Monthly Notices of the Royal Astronomical Society **498**, 4492–4502 (2020).

[119] C. M. Biwer, C. D. Capano, S. De, M. Cabero, D. A. Brown, A. H. Nitz, and V. Raymond, "PyCBC Inference: A Python-based parameter estimation toolkit for compact binary coalescence signals", Publ. Astron. Soc. Pac. **131**, 024503 (2019).

[120] N. Karnesis, M. L. Katz, N. Korsakova, J. R. Gair, and N. Stergioulas, "Eryn: a multipurpose sampler for Bayesian inference", Mon. Not. Roy. Astron. Soc. **526**, 4814–4830 (2023).

[121] M. Breschi, R. Gamba, and S. Bernuzzi, "Bayesian inference of multimessenger astrophysical data: Methods and applications to gravitational waves", Phys. Rev. D **104**, 042001 (2021).

[122] R. M. Wald, *General Relativity* (Chicago Univ. Pr., Chicago, USA, 1984).

[123] R. Penrose, "Gravitational collapse and space-time singularities", Phys. Rev. Lett. **14**, 57–59 (1965).

[124] K. Schwarzschild, "On the gravitational field of a mass point according to Einstein's theory", Sitzungsber. Preuss. Akad. Wiss. Berlin, 189–196 (1916).

[125] M. D. Kruskal, "Maximal extension of schwarzschild metric", Phys. Rev. **119**, 1743–1745 (1960).

[126] R. P. Kerr, "Gravitational Field of a Spinning Mass as an Example of Algebraically Special Metrics", Phys. Rev. Lett. **11**, 237–238 (1963).

[127] E. T. Newman, E. Couch, K. Chinnapared, A. Exton, A. Prakash, and R. Torrence, "Metric of a rotating, charged mass", Journal of Mathematical Physics **6**, 918–919 (1965).

[128] W. Israel, "Event horizons in static vacuum space-times", Phys. Rev. **164**, 1776–1779 (1967).

[129] B. Carter, "Axisymmetric Black Hole Has Only Two Degrees of Freedom", Phys. Rev. Lett. **26**, 331–333 (1971).

[130] V. P. Frolov and I. D. Novikov, eds., *Black hole physics: Basic concepts and new developments* (1998).

[131] J. R. Oppenheimer and G. M. Volkoff, "On Massive Neutron Cores", Physical Review **55**, 374–381 (1939).

[132] C. E. Rhoades and R. Ruffini, "Maximum mass of a neutron star", Phys. Rev. Lett. **32**, 324–327 (1974).

[133] V. Kalogera and G. Baym, "The Maximum Mass of a Neutron Star", The Astrophysical Journal **470**, L61 (1996).

[134] M. Sasaki, T. Suyama, T. Tanaka, and S. Yokoyama, "Primordial black holes—perspectives in gravitational wave astronomy", Classical and Quantum Gravity **35**, 063001, 063001 (2018).

[135] G. Rakavy and G. Shaviv, "Instabilities in Highly Evolved Stellar Models", Astrophysical Journal **148**, 803 (1967).

[136] R. Abbott et al. (KAGRA, VIRGO, LIGO Scientific), "Population of Merging Compact Binaries Inferred Using Gravitational Waves through GWTC-3", Phys. Rev. X **13**, 011048 (2023).

[137] H. Estellés et al., "A Detailed Analysis of GW190521 with Phenomenological Waveform Models", Astrophys. J. **924**, 79 (2022).

[138] J. C. Bustillo, N. Sanchis-Gual, A. Torres-Forné, J. A. Font, A. Vajpeyi, R. Smith, C. Herdeiro, E. Radu, and S. H. W. Leong, "Gw190521 as a merger of proca stars: a potential new vector boson of 8.7×10^{-13} eV", Phys. Rev. Lett. **126**, 081101 (2021).

[139] R. Gamba, M. Breschi, G. Carullo, S. Albanesi, P. Rettegno, S. Bernuzzi, and A. Nagar, "Gw190521 as a dynamical capture of two nonspinning black holes", Nature Astronomy **7**, 11–17 (2023).

[140] A. H. Nitz and C. D. Capano, "Gw190521 may be an intermediate-mass ratio inspiral", The Astrophysical Journal Letters **907**, L9 (2021).

[141] M. Shibata, K. Kiuchi, S. Fujibayashi, and Y. Sekiguchi, "Alternative possibility of gw190521: gravitational waves from high-mass black hole-disk systems", Phys. Rev. D **103**, 063037 (2021).

[142] P. Schmidt, I. W. Harry, and H. P. Pfeiffer, "Numerical Relativity Injection Infrastructure", (2017).

[143] É. Racine, "Analysis of spin precession in binary black hole systems including quadrupole-monopole interaction", Phys. Rev. D **78**, 044021 (2008).

[144] P. Ajith, M. Hannam, S. Husa, Y. Chen, B. Brügmann, N. Dorband, D. Müller, F. Ohme, D. Pollney, C. Reisswig, L. Santamaria, and J. Seiler, "Inspiral-merger-ringdown waveforms for black-hole binaries with nonprecessing spins", Phys. Rev. Lett. **106**, 241101 (2011).

[145] L. Santamaria, F. Ohme, P. Ajith, B. Brügmann, N. Dorband, M. Hannam, S. Husa, P. Mösta, D. Pollney, C. Reisswig, E. L. Robinson, J. Seiler, and B. Krishnan, "Matching post-newtonian and numerical relativity waveforms: systematic errors and a new phenomenological model for nonprecessing black hole binaries", Phys. Rev. D **82**, 064016 (2010).

[146] P. Schmidt, F. Ohme, and M. Hannam, "Towards models of gravitational waveforms from generic binaries II: Modelling precession effects with a single effective precession parameter", Phys. Rev. D **91**, 024043 (2015).

[147] A. H. Mroue and H. P. Pfeiffer, "Precessing Binary Black Holes Simulations: Quasicircular Initial Data", (2012).

[148] B. P. Abbott et al. (LIGO Scientific, Virgo), "Properties of the Binary Black Hole Merger GW150914", Phys. Rev. Lett. **116**, 241102 (2016).

[149] B. P. Abbott et al. (LIGO Scientific, Virgo), "Binary Black Hole Mergers in the first Advanced LIGO Observing Run", Phys. Rev. X **6**, [Erratum: Phys.Rev.X 8, 039903 (2018)], 041015 (2016).

[150] F. Pretorius, "Evolution of Binary Black-Hole Spacetimes", Phys. Rev. L **95**, 121101 (2005).

[151] M. Campanelli et al., "Accurate Evolutions of Orbiting Black-Hole Binaries without Excision", Phys. Rev. L **96**, 111101 (2006).

[152] J. G. Baker et al., "Gravitational-Wave Extraction from an Inspiraling Configuration of Merging Black Holes", Phys. Rev. L **96**, 111102 (2006).

[153] A. Ashtekar, M. Campiglia, and S. Shah, "Dynamical Black Holes: Approach to the Final State", Phys. Rev. D **88**, 064045 (2013).

[154] H. Yang, K. Yagi, J. Blackman, L. Lehner, V. Paschalidis, F. Pretorius, and N. Yunes, "Black hole spectroscopy with coherent mode stacking", Phys. Rev. Lett. **118**, 161101 (2017).

[155] E. Berti et al., "Testing General Relativity with Present and Future Astrophysical Observations", Class. Quant. Grav. **32**, 243001 (2015).

[156] B. P. Abbott et al. (LIGO Scientific, Virgo), "Tests of general relativity with GW150914", Phys. Rev. Lett. **116**, [Erratum: Phys.Rev.Lett. 121, 129902 (2018)], 221101 (2016).

[157] E. Berti, K. Yagi, H. Yang, and N. Yunes, "Extreme Gravity Tests with Gravitational Waves from Compact Binary Coalescences: (II) Ringdown", Gen. Rel. Grav. **50**, 49 (2018).

[158] E. Berti, K. Yagi, and N. Yunes, "Extreme Gravity Tests with Gravitational Waves from Compact Binary Coalescences: (I) Inspiral-Merger", Gen. Rel. Grav. **50**, 46 (2018).

[159] e. Witten Louis, *Gravitation: an introduction to current research.* (Wiley, New York, 1962).

[160] J. W. York Jr., "Kinematics and Dynamics of General Relativity", in Workshop on Sources of Gravitational Radiation (1978), pp. 83–126.

[161] M. Shibata and T. Nakamura, "Evolution of three-dimensional gravitational waves: harmonic slicing case", Phys. Rev. D **52**, 5428–5444 (1995).

[162] T. W. Baumgarte and S. L. Shapiro, "On the numerical integration of Einstein's field equations", Phys. Rev. D **59**, 024007 (1998).

[163] H. Friedrich and A. D. Rendall, "The Cauchy problem for the Einstein equations", Lect. Notes Phys. **540**, edited by B. G. Schmidt, 127–224 (2000).

[164] P. Grandclement and J. Novak, "Spectral methods for numerical relativity", Living Rev. Rel. **12**, 1 (2009).

[165] T. W. Baumgarte and S. L. Shapiro, *Numerical Relativity: Solving Einstein's Equations on the Computer* (Cambridge University Press, 2010).

[166] L. Lehner and F. Pretorius, "Numerical Relativity and Astrophysics", Ann. Rev. Astron. Astrophys. **52**, 661–694 (2014).

[167] V. Cardoso, L. Gualtieri, C. Herdeiro, and U. Sperhake, "Exploring New Physics Frontiers Through Numerical Relativity", Living Rev. Relativity **18**, 1 (2015).

[168] M. D. Duez and Y. Zlochower, "Numerical Relativity of Compact Binaries in the 21st Century", Rept. Prog. Phys. **82**, 016902 (2019).

[169] A. Le Tiec, A. H. Mroue, L. Barack, A. Buonanno, H. P. Pfeiffer, N. Sago, and A. Taracchini, "Periastron Advance in Black Hole Binaries", Phys. Rev. Lett. **107**, 141101 (2011).

[170] M. van de Meent, "Self-force corrections to the periapsis advance around a spinning black hole", Phys. Rev. Lett. **118**, 011101 (2017).

[171] A. Bohé et al., "Improved effective-one-body model of spinning, nonprecessing binary black holes for the era of gravitational-wave astrophysics with advanced detectors", Phys. Rev. D **95**, 044028 (2017).

[172] R. Cotesta, A. Buonanno, A. Bohé, A. Taracchini, I. Hinder, and S. Ossokine, "Enriching the Symphony of Gravitational Waves from Binary Black Holes by Tuning Higher Harmonics", Phys. Rev. D **98**, 084028 (2018).

[173] S. Ossokine et al., "Multipolar effective-one-body waveforms for precessing binary black holes: Construction and validation", Phys. Rev. D **102**, 044055 (2020).

[174] L. Pompili, A. Buonanno, H. Estellés, M. Khalil, M. van de Meent, D. P. Mihaylov, S. Ossokine, M. Pürrer, A. Ramos-Buades, A. K. Mehta, R. Cotesta, S. Marsat, M. Boyle, L. E. Kidder, H. P. Pfeiffer, M. A. Scheel, H. R. Rüter, N. Vu, R. Dudi, S. Ma, K. Mitman, D. Melchor, S. Thomas, and J. Sanchez, "Laying the foundation of the effective-one-body waveform models seobnrv5: improved accuracy and efficiency for spinning nonprecessing binary black holes", Phys. Rev. D **108**, 124035 (2023).

[175] X. Liu, Z. Cao, and L. Shao, "Validating the Effective-One-Body Numerical-Relativity Waveform Models for Spin-aligned Binary Black Holes along Eccentric Orbits", Phys. Rev. D **101**, 044049 (2020).

[176] Z. Cao and W.-B. Han, "Waveform model for an eccentric binary black hole based on the effective-one-body-numerical-relativity formalism", Phys. Rev. D **96**, 044028 (2017).

[177] S. Akcay, R. Gamba, and S. Bernuzzi, "Effective one body gravitational waveforms for dynamical captures in non-spinning black hole binaries", Phys. Rev. D **103**, 024014 (2021).

[178] A. Nagar, F. Messina, P. Rettegno, D. Bini, T. Damour, A. Geralico, S. Akcay, and S. Bernuzzi, "Nonlinear-in-spin effects in effective-one-body waveform models of spin-aligned, inspiralling, neutron star binaries", Phys. Rev. D **99**, 044007 (2019).

[179] A. Nagar et al., "Noncircularized, spinning binary black hole merger waveforms with next-to-next-to-next-to-leading order spin-orbit terms from the effective one body formalism", Phys. Rev. D **102**, 024077 (2020).

[180] A. Nagar, R. Gamba, P. Rettegno, V. Fantini, and S. Bernuzzi, "Effective-one-body waveform model for noncircularized, planar, coalescing black hole binaries: the importance of radiation reaction", Phys. Rev. D **110**, 084001 (2024).

[181] A. Nagar, D. Chiaramello, R. Gamba, S. Albanesi, S. Bernuzzi, V. Fantini, M. Panzeri, and P. Rettegno, "Effective-one-body waveform model for noncircularized, planar, coalescing black hole binaries. II. High accuracy by improving logarithmic terms in resummations", Phys. Rev. D **111**, 064050 (2025).

[182] J. Blackman, S. E. Field, M. A. Scheel, C. R. Galley, D. A. Hemberger, P. Schmidt, and R. Smith, "A surrogate model of gravitational waveforms from numerical relativity simulations of precessing binary black hole mergers", Phys. Rev. D **95**, 104023 (2017).

[183] V. Varma, S. E. Field, M. A. Scheel, J. Blackman, L. E. Kidder, and H. P. Pfeiffer, "Surrogate model of hybridized numerical relativity binary black hole waveforms", Phys. Rev. D **99**, 064045 (2019).

[184] V. Varma, S. E. Field, M. A. Scheel, J. Blackman, D. Gerosa, L. C. Stein, L. E. Kidder, and H. P. Pfeiffer, "Surrogate models for precessing binary black hole simulations with unequal masses", Phys. Rev. Res. **1**, 033015 (2019).

[185] K. Rink, R. Bachhar, T. Islam, N. E. M. Rifat, K. Gonzalez-Quesada, S. E. Field, G. Khanna, S. A. Hughes, and V. Varma, "Gravitational wave surrogate model for spinning, intermediate mass ratio binaries based on perturbation theory and numerical relativity", Phys. Rev. D **110**, 124069 (2024).

[186] S. Husa, S. Khan, M. Hannam, M. Pürrer, F. Ohme, X. Jiménez-Forteza, and A. Bohé, "Frequency-domain gravitational waves from non-precessing black-hole binaries. I. New numerical waveforms and anatomy of the signal", Phys. Rev. D **93**, 044006 (2016).

[187] S. Khan, S. Husa, M. Hannam, F. Ohme, M. Pürrer, X. Jiménez-Forteza, and A. Bohé, "Frequency-domain gravitational waves from non-precessing black-hole binaries. II. A phenomenological model for the advanced detector era", Phys. Rev. D **93**, 044007 (2016).

[188] L. London, S. Khan, E. Fauchon-Jones, C. García, M. Hannam, S. Husa, X. Jiménez-Forteza, C. Kalaghatgi, F. Ohme, and F. Pannarale, "First higher-multipole model of gravitational waves from spinning and coalescing black-hole binaries", Phys. Rev. Lett. **120**, 161102 (2018).

[189] G. Pratten et al., "Computationally efficient models for the dominant and subdominant harmonic modes of precessing binary black holes", Phys. Rev. D **103**, 104056 (2021).

[190] H. Estellés, M. Colleoni, C. García-Quirós, S. Husa, D. Keitel, M. Mateu-Lucena, M. d. L. Planas, and A. Ramos-Buades, "New twists in compact binary waveform modeling: A fast time-domain model for precession", Phys. Rev. D **105**, 084040 (2022).

[191] H. Estelles, A. Ramos-Buades, S. Husa, C. Garcia-Quiros, M. Colleoni, L. Haegel, and R. Jaume, "Phenomenological time domain model for dominant quadrupole gravitational wave signal of coalescing binary black holes", Phys. Rev. D **103**, 124060 (2021).

[192] B. Aylott, J. G. Baker, W. D. Boggs, M. Boyle, P. R. Brady, D. A. Brown, B. Brügmann, L. T. Buchman, A. Buonanno, L. Cadonati, J. Camp, M. Campanelli, J. Centrella, S. Chatterji, N. Christensen, T. Chu, P. Diener, N. Dorband, Z. B. Etienne, J. Faber, S. Fairhurst, B. Farr, S. Fischetti, G. Guidi, L. M. Goggin, M. Hannam, F. Herrmann, I. Hinder, S. Husa, V. Kalogera, D. Keppel, L. E. Kidder, B. J. Kelly, B. Krishnan, P. Laguna, C. O. Lousto, I. Mandel, P. Marronetti, R. Matzner, S. T. McWilliams, K. D. Matthews, R. A. Mercer, S. R. P. Mohapatra, A. H. Mroué, H. Nakano, E. Ochsner, Y. Pan, L. Pekowsky, H. arald P Pfeiffer,

D. Pollney, F. Pretorius, V. Raymond, C. Reisswig, L. Rezzolla, O. Rinne, C. Robinson, C. Röver, L. Santamaría, B. Sathyaprakash, M. A. Scheel, E. Schnetter, J. Seiler, S. L. Shapiro, D. Shoemaker, U. Sperhake, A. Stroeer, R. Sturani, W. Tichy, Y. T. Liu, M. van der Sluys, J. R. van Meter, R. Vaulin, A. Vecchio, J. Veitch, A. Viceré, J. T. Whelan, and Y. Zlochower, "Testing gravitational-wave searches with numerical relativity waveforms: results from the first numerical injection analysis (ninja) project", Classical and Quantum Gravity **26**, 165008 (2009).

[193] P. Ajith, M. Boyle, D. A. Brown, B. Brügmann, L. T. Buchman, L. Cadonati, M. Campanelli, T. Chu, Z. B. Etienne, S. Fairhurst, M. Hannam, J. Healy, I. Hinder, S. Husa, L. E. Kidder, B. Krishnan, P. Laguna, Y. T. Liu, L. London, C. O. Lousto, G. Lovelace, I. MacDonald, P. Marronetti, S. Mohapatra, P. Mösta, D. Müller, B. C. Mundim, H. Nakano, F. Ohme, V. Paschalidis, L. Pekowsky, D. Pollney, H. P. Pfeiffer, M. Ponce, M. Pürrer, G. Reifenberger, C. Reisswig, L. Santamaría, M. A. Scheel, S. L. Shapiro, D. Shoemaker, C. F. Sopuerta, U. Sperhake, B. Szilágyi, N. W. Taylor, W. Tichy, P. Tsatsin, and Y. Zlochower, "The ninja-2 catalog of hybrid post-newtonian/numerical-relativity waveforms for non-precessing black-hole binaries", Classical and Quantum Gravity **29**, 124001 (2012).

[194] B. P. Abbott et al. (LIGO Scientific, Virgo), "Directly comparing GW150914 with numerical solutions of Einstein's equations for binary black hole coalescence", Phys. Rev. D **94**, 064035 (2016).

[195] J. Healy et al., "Targeted numerical simulations of binary black holes for GW170104", Phys. Rev. D **97**, 064027 (2018).

[196] J. Lange et al., "Parameter estimation method that directly compares gravitational wave observations to numerical relativity", Phys. Rev. D **96**, 104041 (2017).

[197] P. Kumar et al., "Template Banks for Binary black hole searches with Numerical Relativity waveforms", Phys. Rev. D **89**, 042002 (2014).

[198] J. Blackman, S. E. Field, M. A. Scheel, C. R. Galley, C. D. Ott, M. Boyle, L. E. Kidder, H. P. Pfeiffer, and B. Szilágyi, "Numerical relativity waveform surrogate model for generically precessing binary black hole mergers", Phys. Rev. D **96**, 024058 (2017).

[199] J. Blackman, S. E. Field, C. R. Galley, B. Szilágyi, M. A. Scheel, M. Tiglio, and D. A. Hemberger, "Fast and Accurate Prediction of Numerical Relativity Waveforms from Binary Black Hole Coalescences Using Surrogate Models", Phys. Rev. Lett. **115**, 121102 (2015).

[200] F. Ohme, M. Hannam, and S. Husa, "Reliability of complete gravitational waveform models for compact binary coalescences", Phys. Rev. D **84**, 064029 (2011).

[201] I. MacDonald, S. Nissanke, H. P. Pfeiffer, and H. P. Pfeiffer, "Suitability of post-Newtonian/numerical-relativity hybrid waveforms for gravitational wave detectors", Class. Quant. Grav. **28**, edited by L. Lehner, H. P. Pfeiffer, and E. Poisson, 134002 (2011).

[202] M. Boyle, "Uncertainty in hybrid gravitational waveforms: Optimizing initial orbital frequencies for binary black-hole simulations", Phys. Rev. D **84**, 064013 (2011).

[203] B. Bruegmann, J. A. Gonzalez, M. Hannam, S. Husa, U. Sperhake, and W. Tichy, "Calibration of Moving Puncture Simulations", Phys. Rev. D **77**, 024027 (2008).

[204] S. Husa, J. A. Gonzalez, M. Hannam, B. Bruegmann, and U. Sperhake, "Reducing phase error in long numerical binary black hole evolutions with sixth order finite differencing", Class. Quant. Grav. **25**, 105006 (2008).

[205] Y. Zlochower, J. G. Baker, M. Campanelli, and C. O. Lousto, "Accurate black hole evolutions by fourth-order numerical relativity", Phys. Rev. D **72**, 024021 (2005).

[206] C. O. Lousto and Y. Zlochower, "Foundations of multiple-black-hole evolutions", Phys. Rev. D **77**, 024034 (2008).

[207] I. Ruchlin, J. Healy, C. O. Lousto, and Y. Zlochower, "Puncture initial data for black-hole binaries with high spins and high boosts", Phys. Rev. D **95**, 024033 (2017).

[208] U. Sperhake, "Binary black-hole evolutions of excision and puncture data", Phys. Rev. D **76**, 104015 (2007).

[209] H. Witek, M. Zilhao, G. Ficarra, and M. Elley, *Canuda: a public numerical relativity library to probe fundamental physics*, May 2020.

[210] F. Herrmann, I. Hinder, D. Shoemaker, and P. Laguna, "Unequal Mass Binary Black Hole Plunges and Gravitational Recoil", in New Frontiers in Numerical Relativity (NFNR 2006) (Jan. 2006).

[211] L. Pekowsky, R. O'Shaughnessy, J. Healy, and D. Shoemaker, "Comparing gravitational waves from nonprecessing and precessing black hole binaries in the corotating frame", Phys. Rev. D **88**, 024040 (2013).

[212] F. Pretorius, "Numerical relativity using a generalized harmonic decomposition", Classical and Quantum Gravity **22**, 425–451 (2005).

[213] A. Buonanno, G. B. Cook, and F. Pretorius, "Inspiral, merger and ring-down of equal-mass black-hole binaries", Phys. Rev. D **75**, 124018 (2007).

[214] F. Pretorius and D. Khurana, "Black hole mergers and unstable circular orbits", Class. Quant. Grav. **24**, edited by M. Campanelli and L. Rezzolla, S83–S108 (2007).

[215] M. Fernando, D. Neilsen, Y. Zlochower, E. W. Hirschmann, and H. Sundar, "Massively parallel simulations of binary black holes with adaptive wavelet multiresolution", Phys. Rev. D **107**, 064035 (2023).

[216] T. Andrade et al., "GRChombo: An adaptable numerical relativity code for fundamental physics", J. Open Source Softw. **6**, 3703 (2021).

[217] Z. B. Etienne, J. A. Faber, Y. T. Liu, S. L. Shapiro, and T. W. Baumgarte, "Filling the holes: Evolving excised binary black hole initial data with puncture techniques", Phys. Rev. D **76**, 101503 (2007).

[218] SXS Collaboration, *The Spectral Einstein Code (SpEC)*, https://www.black-holes.org/code/SpEC.html, 2019.

[219] N. Deppe, W. Throwe, L. E. Kidder, N. L. Vu, K. C. Nelli, C. Armaza, M. S. Bonilla, F. Hébert, Y. Kim, P. Kumar, G. Lovelace, A. Macedo, J. Moxon, E. O'Shea, H. P. Pfeiffer, M. A. Scheel, S. A. Teukolsky, N. A. Wittek, et al., *SpECTRE v2025.04.21*, 10.5281/zenodo.15259042, version 2025.04.21, Apr. 2025.

[220] Georgia Tech, *Einstein at Georgia Tech*, https://einstein.gatech.edu/catalog/, 2016.

[221] K. Jani, J. Healy, J. A. Clark, L. London, P. Laguna, and D. Shoemaker, "Georgia Tech Catalog of Gravitational Waveforms", Class. Quant. Grav. **33**, 204001 (2016).

[222] J. Healy, C. O. Lousto, Y. Zlochower, and M. Campanelli, "The rit binary black hole simulations catalog", Classical and Quantum Gravity **34**, 224001 (2017).

[223] J. Healy, C. O. Lousto, J. Lange, R. O'Shaughnessy, Y. Zlochower, and M. Campanelli, "Second rit binary black hole simulations catalog and its application to gravitational waves parameter estimation", Phys. Rev. D **100**, 024021 (2019).

[224] J. Healy and C. O. Lousto, "Third rit binary black hole simulations catalog", Phys. Rev. D **102**, 104018 (2020).

[225] J. Healy and C. O. Lousto, "Fourth rit binary black hole simulations catalog: extension to eccentric orbits", Phys. Rev. D **105**, 124010 (2022).

[226] E. Hamilton et al., "Catalog of precessing black-hole-binary numerical-relativity simulations", Phys. Rev. D **109**, 044032 (2024).

[227] A. H. Mroué, M. A. Scheel, B. Szilágyi, H. P. Pfeiffer, M. Boyle, D. A. Hemberger, L. E. Kidder, G. Lovelace, S. Ossokine, N. W. Taylor, A. ı. Zengino ğlu, L. T. Buchman, T. Chu, E. Foley, M. Giesler, R. Owen, and S. A. Teukolsky, "Catalog of 174 binary black hole simulations for gravitational wave astronomy", Phys. Rev. Lett. **111**, 241104 (2013).

[228] M. Boyle et al., "The SXS Collaboration catalog of binary black hole simulations", Class. Quant. Grav. **36**, 195006 (2019).

[229] SXS Collaboration, *SXS Gravitational Waveform Database*, https://www.black-holes.org/waveforms, 2019.

[230] J. Droste, "The field of a single centre in Einstein's theory of gravitation, and the motion of a particle in that field", Koninklijke Nederlandse Akademie van Wetenschappen Proceedings Series B Physical Sciences **19**, 197–215 (1917).

[231] H. A. Lorentz and J. Droste, "The motion of a system of bodies under the influence of their mutual attraction, according to einstein's theory", in *Collected papers: volume v* (Springer Netherlands, Dordrecht, 1937), pp. 330–355.

[232] A. Buonanno, B. Iyer, E. Ochsner, Y. Pan, and B. S. Sathyaprakash, "Comparison of post-Newtonian templates for compact binary inspiral signals in gravitational-wave detectors", Phys. Rev. D **80**, 084043 (2009).

[233] T. Damour and N. Deruelle, "Generalized lagrangian of two point masses in the post-post newtonian approximation of general relativity", Comptes Rendus des Seances de l'Academie des Sciences. Serie 2 **293**, 537–540 (1981).

[234] T. Damour and N. Deruelle, "Radiation reaction and angular momentum loss in small angle gravitational scattering", Physics Letters A **87**, 81–84 (1981).

[235] T. Damour, "The Motion of Compact Bodies and Gravitational Radiation", Fundam. Theor. Phys. **9**, edited by B. Bertotti, F. de Felice, and A. Pascolini, 89–106 (1984).

[236] T. Damour, "Gravitational radiation reaction in the binary pulsar and the quadrupole-formula controversy", Phys. Rev. Lett. **51**, 1019–1021 (1983).

[237] A. K. Leibovich, B. A. Pardo, and Z. Yang, "Radiation reaction for nonspinning bodies at 4.5PN in the effective field theory approach", Phys. Rev. D **108**, 024017 (2023).

[238] T. Damour, B. R. Iyer, and B. S. Sathyaprakash, "A Comparison of search templates for gravitational waves from binary inspiral", Phys. Rev. D **63**, [Erratum: Phys.Rev.D 72, 029902 (2005)], 044023 (2001).

[239] T. Damour, B. R. Iyer, and B. S. Sathyaprakash, "Improved filters for gravitational waves from inspiralling compact binaries", Phys. Rev. D **57**, 885–907 (1998).

[240] A. Buonanno and T. Damour, "Effective one-body approach to general relativistic two-body dynamics", Phys. Rev. D **59**, 084006 (1999).

[241] A. Buonanno and T. Damour, "Transition from inspiral to plunge in binary black hole coalescences", Phys. Rev. D **62**, 064015 (2000).

[242] A. Pound and B. Wardell, "Black hole perturbation theory and gravitational self-force", 10.1007/978-981-15-4702-7_38-1 (2021).

[243] T. Regge and J. A. Wheeler, "Stability of a Schwarzschild singularity", Phys. Rev. **108**, 1063–1069 (1957).

[244] F. J. Zerilli, "Gravitational field of a particle falling in a schwarzschild geometry analyzed in tensor harmonics", Phys. Rev. D **2**, 2141–2160 (1970).

[245] F. J. Zerilli, "Effective potential for even-parity regge-wheeler gravitational perturbation equations", Phys. Rev. Lett. **24**, 737–738 (1970).

[246] C. V. Vishveshwara, "Scattering of Gravitational Radiation by a Schwarzschild Black-hole", Nature **227**, 936–938 (1970).

[247] W. H. Press, "Long Wave Trains of Gravitational Waves from a Vibrating Black Hole", Astrophys. J. Lett. **170**, L105–L108 (1971).

[248] S. Chandrasekhar and S. L. Detweiler, "The quasi-normal modes of the Schwarzschild black hole", Proc. Roy. Soc. Lond. A **344**, 441–452 (1975).

[249] S. A. Teukolsky, "Rotating black holes - separable wave equations for gravitational and electromagnetic perturbations", Phys. Rev. Lett. **29**, 1114–1118 (1972).

[250] S. A. Teukolsky and W. H. Press, "Perturbations of a rotating black hole. III - Interaction of the hole with gravitational and electromagnet ic radiation", Astrophys. J. **193**, 443–461 (1974).

[251] B. S. DeWitt and R. W. Brehme, "Radiation damping in a gravitational field", Annals Phys. **9**, 220–259 (1960).

[252] Y. Mino, M. Sasaki, and T. Tanaka, "Gravitational radiation reaction to a particle motion. 2: Spinning particle", (1997).

[253] T. C. Quinn and R. M. Wald, "Axiomatic approach to electromagnetic and gravitational radiation reaction of particles in curved spacetime", Phys. Rev. D **56**, 3381–3394 (1997).

[254] S. Detweiler and B. F. Whiting, "Self-force via a green's function decomposition", Phys. Rev. D **67**, 024025 (2003).

[255] S. E. Gralla and R. M. Wald, "A Rigorous Derivation of Gravitational Self-force", Class. Quant. Grav. **25**, [Erratum: Class.Quant.Grav. 28, 159501 (2011)], 205009 (2008).

[256] A. Pound, B. Wardell, N. Warburton, and J. Miller, "Second-Order Self-Force Calculation of Gravitational Binding Energy in Compact Binaries", Phys. Rev. Lett. **124**, 021101 (2020).

[257] N. Warburton, A. Pound, B. Wardell, J. Miller, and L. Durkan, "Gravitational-Wave Energy Flux for Compact Binaries through Second Order in the Mass Ratio", Phys. Rev. Lett. **127**, 151102 (2021).

[258] R. Fujita, "Gravitational radiation for extreme mass ratio inspirals to the 14th post-Newtonian order", Prog. Theor. Phys. **127**, 583–590 (2012).

[259] R. Fujita, "Gravitational Waves from a Particle in Circular Orbits around a Schwarzschild Black Hole to the 22nd Post-Newtonian Order", Prog. Theor. Phys. **128**, 971–992 (2012).

[260] C. Kavanagh, A. C. Ottewill, and B. Wardell, "Analytical high-order post-Newtonian expansions for spinning extreme mass ratio binaries", Phys. Rev. D **93**, 124038 (2016).

[261] T. Hinderer and E. E. Flanagan, "Two timescale analysis of extreme mass ratio inspirals in Kerr. I. Orbital Motion", Phys. Rev. D **78**, 064028 (2008).

[262] S. Isoyama, R. Fujita, N. Sago, H. Tagoshi, and T. Tanaka, "Impact of the second-order self-forces on the dephasing of the gravitational waves from quasicircular extreme mass-ratio inspirals", Phys. Rev. D **87**, 024010 (2013).

[263] L. M. Burko and G. Khanna, "Self-force gravitational waveforms for extreme and intermediate mass ratio inspirals. III: Spin-orbit coupling revisited", Phys. Rev. D **91**, 104017 (2015).

[264] M. van de Meent and H. P. Pfeiffer, "Intermediate mass-ratio black hole binaries: Applicability of small mass-ratio perturbation theory", Phys. Rev. Lett. **125**, 181101 (2020).

[265] *Black Hole Perturbation Toolkit*, (bhptoolkit.org).

[266] J. N. Goldberg, A. J. Macfarlane, E. T. Newman, F. Rohrlich, and E. C. G. Sudarshan, "Spin-s Spherical Harmonics and ð", J. Math. Phys. **8**, 2155–2161 (1967).

[267] Y. Wiaux, L. Jacques, and P. Vandergheynst, "Fast spin +-2 spherical harmonics transforms", J. Comput. Phys. **226**, 2359–2371 (2007).

[268] L. S. Collaboration and V. Collaboration, "Gw190412: observation of a binary-black-hole coalescence with asymmetric masses", Phys. Rev. D **102**, 043015 (2020).

[269] C. Hoy, C. Mills, and S. Fairhurst, "Evidence for subdominant multipole moments and precession in merging black-hole-binaries from GWTC-2.1", Phys. Rev. D **106**, 023019 (2022).

[270] N. Andersson, "Evolving test fields in a black hole geometry", Phys. Rev. D **55**, 468–479 (1997).

[271] S. A. Teukolsky, "Perturbations of a rotating black hole. 1. Fundamental equations for gravitational electromagnetic and neutrino field perturbations", Astrophys. J. **185**, 635–647 (1973).

[272] E. W. Leaver, "An Analytic representation for the quasi normal modes of Kerr black holes", Proc. Roy. Soc. Lond. A **402**, 285–298 (1985).

[273] Maria de Lluc Planas, *Beyond the Stationary Phase Approximation: an alternative approach to model gravitational waves from precessing compact binaries in the Fourier Domain*, Master's thesis:UIB Repository, 2021.

[274] E. Hamilton, L. London, and M. Hannam, "Ringdown frequencies in black holes formed from precessing black-hole binaries", Phys. Rev. D **107**, 104035 (2023).

[275] E. Berti and A. Klein, "Mixing of spherical and spheroidal modes in perturbed Kerr black holes", Phys. Rev. D **90**, 064012 (2014).

[276] L. T. London, J. Healy, and D. Shoemaker, "Erratum: modeling ringdown: beyond the fundamental quasinormal modes [phys. rev. d 90, 124032 (2014)]", Phys. Rev. D **94**, 069902 (2016).

[277] T. A. Apostolatos, C. Cutler, G. J. Sussman, and K. S. Thorne, "Spin induced orbital precession and its modulation of the gravitational wave forms from merging binaries", Phys. Rev. D **49**, 6274–6297 (1994).

[278] L. E. Kidder, "Coalescing binary systems of compact objects to postNewtonian 5/2 order. 5. Spin effects", Phys. Rev. D **52**, 821–847 (1995).

[279] M. Hannam, P. Schmidt, A. Bohé, L. Haegel, S. Husa, et al., "Simple Model of Complete Precessing Black-Hole-Binary Gravitational Waveforms", Phys.Rev.Lett. **113**, 151101 (2014).

[280] B. J. Kelly and J. G. Baker, "Decoding mode mixing in black-hole merger ringdown", Phys. Rev. D **87**, 084004 (2013).

[281] L. London, "Notes on the spheroidal harmonic multipole moments of gravitational radiation", arXiv:2006.11449 (2020).

[282] S. Bernuzzi and A. Nagar, "Binary black hole merger in the extreme-mass-ratio limit: a multipolar analysis", Phys. Rev. D **81**, 084056 (2010).

[283] E. Barausse, A. Buonanno, S. A. Hughes, G. Khanna, S. O'Sullivan, and Y. Pan, "Modeling multipolar gravitational-wave emission from small mass-ratio mergers", Phys. Rev. D **85**, 024046 (2012).

[284] A. Dhani, "Importance of mirror modes in binary black hole ringdown waveform", Phys. Rev. D **103**, 104048 (2021).

[285] S. Ma, K. Mitman, L. Sun, N. Deppe, F. Hébert, L. E. Kidder, J. Moxon, W. Throwe, N. L. Vu, and Y. Chen, "Quasinormal-mode filters: A new approach to analyze the gravitational-wave ringdown of binary black-hole mergers", Phys. Rev. D **106**, 084036 (2022).

[286] V. Varma, D. Gerosa, L. C. Stein, F. Hébert, and H. Zhang, "High-accuracy mass, spin, and recoil predictions of generic black-hole merger remnants", Phys. Rev. Lett. **122**, 011101 (2019).

[287] M. Boyle, L. E. Kidder, S. Ossokine, and H. P. Pfeiffer, "Gravitational-wave modes from precessing black-hole binaries", (2014).

[288] M. Favata, "The gravitational-wave memory effect", Class. Quantum Gravity **27**, 84036 (2010).

[289] A. Buonanno, Y. Chen, and T. Damour, "Transition from inspiral to plunge in precessing binaries of spinning black holes", Phys. Rev. D **74**, 104005 (2006).

[290] P. Schmidt, M. Hannam, S. Husa, and P. Ajith, "Tracking the precession of compact binaries from their gravitational-wave signal", Phys. Rev. D **84**, 024046 (2011).

[291] B. Bruegmann, J. A. Gonzalez, M. Hannam, S. Husa, and U. Sperhake, "Exploring black hole superkicks", Phys. Rev. D **77**, 124047 (2008).

[292] P. Kolitsidou, J. E. Thompson, and M. Hannam, "Impact of antisymmetric contributions to signal multipoles in the measurement of black-hole spins", Phys. Rev. D **111**, 024050 (2025).

[293] S. Ghosh, P. Kolitsidou, and M. Hannam, "First frequency-domain phenomenological model of the multipole asymmetry in gravitational-wave signals from binary-black-hole coalescence", Phys. Rev. D **109**, 024061 (2024).

[294] J. E. Thompson, E. Hamilton, L. London, S. Ghosh, P. Kolitsidou, C. Hoy, and M. Hannam, "PhenomXO4a: a phenomenological gravitational-wave model for precessing black-hole binaries with higher multipoles and asymmetries", Phys. Rev. D **109**, 063012 (2024).

[295] A. Ramos-Buades, P. Schmidt, G. Pratten, and S. Husa, "Validity of common modeling approximations for precessing binary black holes with higher-order modes", Phys. Rev. D **101**, 103014 (2020).

[296] S. A. Hughes and R. D. Blandford, "Black hole mass and spin coevolution by mergers", Astrophys. J. Lett. **585**, L101–L104 (2003).

[297] P. Schmidt, M. Hannam, and S. Husa, "Towards models of gravitational waveforms from generic binaries: A simple approximate mapping between precessing and non-precessing inspiral signals", Phys. Rev. D **86**, 104063 (2012).

[298] M. Boyle, R. Owen, and H. P. Pfeiffer, "Geometric approach to the precession of compact binaries", Phys. Rev. D **84**, 124011 (2011).

[299] E. P. Wigner, *Group theory and its application to the quantum mechanics of atomic spectra* (Academic Press, New York, 1959), p. 372.

[300] A. Bohe, S. Marsat, G. Faye, and L. Blanchet, "Next-to-next-to-leading order spin-orbit effects in the near-zone metric and precession equations of compact binaries", Class. Quant. Grav. **30**, 075017 (2013).

[301] S. Marsat, A. Bohé, L. Blanchet, and A. Buonanno, "Next-to-leading tail-induced spin–orbit effects in the gravitational radiation flux of compact binaries", Class. Quant. Grav. **31**, 025023 (2014).

[302] K. Chatziioannou, A. Klein, N. Yunes, and N. Cornish, "Constructing Gravitational Waves from Generic Spin-Precessing Compact Binary Inspirals", Phys. Rev. D **95**, 104004 (2017).

[303] S. Ossokine, L. E. Kidder, and H. P. Pfeiffer, "Precession-tracking coordinates for simulations of compact-object-binaries", Phys. Rev. D **88**, 084031 (2013).

[304] Maria de Lluc Planas, *Testing the use of quaternions in the description of the gravitational wave signal of precessing binary systems*, Undergraduate's thesis:UIB Repository, 2021.

[305] C. Cutler and É. E. Flanagan, "Gravitational waves from merging compact binaries: How accurately can one extract the binary's parameters from the inspiral waveform?", Phys. Rev. D **49**, 2658–2697 (1994).

[306] A. Klein, N. Cornish, and N. Yunes, "Gravitational waveforms for precessing, quasicircular binaries via multiple scale analysis and uniform asymptotics: The near spin alignment case", Phys. Rev. D **88**, 124015 (2013).

[307] A. Klein, N. Cornish, and N. Yunes, "Fast Frequency-domain Waveforms for Spin-Precessing Binary Inspirals", Phys. Rev. D **90**, 124029 (2014).

[308] C. García-Quirós, S. Husa, M. Mateu-Lucena, and A. Borchers, "Accelerating the evaluation of inspiral–merger–ringdown waveforms with adapted grids", Class. Quant. Grav. **38**, 015006 (2021).

[309] The LIGO Scientific Collaboration, the Virgo Collaboration, and the KAGRA Collaboration, "Open data from the third observing run of ligo, virgo, kagra, and geo", The Astrophysical Journal Supplement Series **267**, 29 (2023).

[310] E. Hamilton, L. London, J. E. Thompson, E. Fauchon-Jones, M. Hannam, C. Kalaghatgi, S. Khan, F. Pannarale, and A. Vano-Vinuales, "Model of gravitational waves from precessing black-hole binaries through merger and ringdown", Phys. Rev. D **104**, 124027 (2021).

[311] N. J. Cornish, "Time-Frequency Analysis of Gravitational Wave Data", 10.1103/PhysRevD.102.124038 (2020).

[312] M. C. Digman and N. J. Cornish, "LISA Gravitational Wave Sources in a Time-varying Galactic Stochastic Background", Astrophys. J. **940**, 10 (2022).

[313] M. Hannam, C. Hoy, J. E. Thompson, S. Fairhurst, V. Raymond, M. Colleoni, D. Davis, H. Estellés, C.-J. Haster, A. Helmling-Cornell, S. Husa, D. Keitel, T. J. Massinger, A. Menéndez-Vázquez, K. Mogushi, S. Ossokine, E. Payne, G. Pratten, I. Romero-Shaw, J. Sadiq, P. Schmidt, R. Tenorio, R. Udall, J. Veitch, D. Williams, A. B. Yelikar, and A. Zimmerman, "General-relativistic precession in a black-hole binary", Nature **610**, 652–655 (2022).

[314] V. Varma, S. Biscoveanu, T. Islam, F. H. Shaik, C.-J. Haster, M. Isi, W. M. Farr, S. E. Field, and S. Vitale, "Evidence of large recoil velocity from a black hole merger signal", Phys. Rev. Lett. **128**, 191102 (2022).

[315] I. M. Romero-Shaw, P. D. Lasky, and E. Thrane, "Four Eccentric Mergers Increase the Evidence that LIGO–Virgo–KAGRA's Binary Black Holes Form Dynamically", Astrophys. J. **940**, 171 (2022).

[316] E. Maggio, H. O. Silva, A. Buonanno, and A. Ghosh, "Tests of general relativity in the nonlinear regime: a parametrized plunge-merger-ringdown gravitational waveform model", Phys. Rev. D **108**, 024043 (2023).

[317] E. Payne, S. Hourihane, J. Golomb, R. Udall, D. Davis, and K. Chatziioannou, "Curious case of gw200129: interplay between spin-precession inference and data-quality issues", Phys. Rev. D **106**, 104017 (2022).

[318] R. Macas, A. Lundgren, and G. Ashton, "Revisiting the evidence for precession in gw200129 with machine learning noise mitigation", Phys. Rev. D **109**, 062006 (2024).

[319] I. Mandel and A. Farmer, "Merging stellar-mass binary black holes", Phys. Rept. **955**, 1–24 (2022).

[320] M. Mapelli, "Binary Black Hole Mergers: Formation and Populations", Front. Astron. Space Sci. **7**, 38 (2020).

[321] M. Zevin, J. Samsing, C. Rodriguez, C.-J. Haster, and E. Ramirez-Ruiz, "Eccentric Black Hole Mergers in Dense Star Clusters: The Role of Binary–Binary Encounters", Astrophys. J. **871**, 91 (2019).

[322] N. C. Stone, A. H. W. Küpper, and J. P. Ostriker, "Formation of Massive Black Holes in Galactic Nuclei: Runaway Tidal Encounters", Mon. Not. Roy. Astron. Soc. **467**, 4180–4199 (2017).

[323] L. Wen, "On the eccentricity distribution of coalescing black hole binaries driven by the Kozai mechanism in globular clusters", Astrophys. J. **598**, 419–430 (2003).

[324] J. H. VanLandingham, M. C. Miller, D. P. Hamilton, and D. C. Richardson, "The Role of the Kozai–lidov Mechanism in Black Hole Binary Mergers in Galactic Centers", Astrophys. J. **828**, 77 (2016).

[325] A. H. Nitz, C. D. Capano, S. Kumar, Y.-F. Wang, S. Kastha, M. Schäfer, R. Dhurkunde, and M. Cabero, "3-ogc: catalog of gravitational waves from compact-binary mergers", The Astrophysical Journal **922**, 76 (2021).

[326] A. H. Nitz, S. Kumar, Y.-F. Wang, S. Kastha, S. Wu, M. Schäfer, R. Dhurkunde, and C. D. Capano, "4-ogc: catalog of gravitational waves from compact binary mergers", The Astrophysical Journal **946**, 59 (2023).

[327] T. Venumadhav, B. Zackay, J. Roulet, L. Dai, and M. Zaldarriaga, "New binary black hole mergers in the second observing run of Advanced LIGO and Advanced Virgo", Phys. Rev. D **101**, 083030 (2020).

[328] S. Olsen, T. Venumadhav, J. Mushkin, J. Roulet, B. Zackay, and M. Zaldarriaga, "New binary black hole mergers in the LIGO-Virgo O3a data", Phys. Rev. D **106**, 043009 (2022).

[329] D. Wadekar, J. Roulet, T. Venumadhav, A. K. Mehta, B. Zackay, J. Mushkin, S. Olsen, and M. Zaldarriaga, *New black hole mergers in the LIGO-Virgo O3 data from a gravitational wave search including higher-order harmonics*, Dec. 2023.

[330] A. K. Mehta, S. Olsen, D. Wadekar, J. Roulet, T. Venumadhav, J. Mushkin, B. Zackay, and M. Zaldarriaga, "New binary black hole mergers in the LIGO-Virgo O3b data", Phys. Rev. D **111**, 024049 (2025).

[331] A. V. Tutukov and L. R. YungelSon, "The merger rate of neutron star and black hole binaries", Monthly Notices of the Royal Astronomical Society **260**, 675–678 (1993).

[332] N. Ivanova, S. Justham, X. Chen, O. De Marco, C. L. Fryer, E. Gaburov, H. Ge, E. Glebbeek, Z. Han, X.-D. Li, G. Lu, T. Marsh, P. Podsiadlowski, A. Potter, N. Soker, R. Taam, T. M. Tauris, E. P. J. van den Heuvel, and R. F. Webbink, "Common envelope evolution: where we stand and how we can move forward", The Astronomy and Astrophysics Review **21**, 59 (2013).

[333] M. Mapelli and N. Giacobbo, "The cosmic merger rate of neutron stars and black holes", Monthly Notices of the Royal Astronomical Society **479**, 4391–4398 (2018).

[334] T. Fragos, J. J. Andrews, E. Ramirez-Ruiz, G. Meynet, V. Kalogera, R. E. Taam, and A. Zezas, "The complete evolution of a neutron-star binary through a common envelope phase using 1d hydrodynamic simulations", The Astrophysical Journal Letters **883**, L45 (2019).

[335] F. S. Broekgaarden, E. Berger, S. Stevenson, S. Justham, I. Mandel, M. Chruślińska, L. A. C. van Son, T. Wagg, A. Vigna-Gómez, S. E. de Mink, D. Chattopadhyay, and C. J. Neijssel, "Impact of massive binary star and cosmic evolution on gravitational wave observations – ii. double compact object rates and properties", Monthly Notices of the Royal Astronomical Society **516**, 5737–5761 (2022).

[336] S. E. de Mink and I. Mandel, "The chemically homogeneous evolutionary channel for binary black hole mergers: rates and properties of gravitational-wave events detectable by advanced ligo", Monthly Notices of the Royal Astronomical Society **460**, 3545–3553 (2016).

[337] I. Mandel and S. E. de Mink, "Merging binary black holes formed through chemically homogeneous evolution in short-period stellar binaries", Monthly Notices of the Royal Astronomical Society **458**, 2634–2647 (2016).

[338] P. Marchant, N. Langer, P. Podsiadlowski, T. M. Tauris, and T. J. Moriya, "A new route towards merging massive black holes", Astronomy and Astrophysics **588**, A50 (2016).

[339] E. P. J. van den Heuvel, S. F. Portegies Zwart, and S. E. de Mink, "Forming short-period wolf–rayet x-ray binaries and double black holes through stable mass transfer", Monthly Notices of the Royal Astronomical Society **471**, 4256–4264 (2017).

[340] Y. Shao and X.-D. Li, "Stable mass transfer can explain massive binary black hole mergers with a high-spin component", The Astrophysical Journal **930**, 26 (2022).

[341] H. Tagawa, T. R. Saitoh, and B. Kocsis, "Compact object mergers driven by gas fallback", Phys. Rev. Lett. **120**, 261101 (2018).

[342] K. Kremer, C. S. Ye, N. Z. Rui, N. C. Weatherford, S. Chatterjee, G. Fragione, C. L. Rodriguez, M. Spera, and F. A. Rasio, "Modeling dense star clusters in the milky way and beyond with the cmc cluster catalog", The Astrophysical Journal Supplement Series **247**, 48 (2020).

[343] F. Santoliquido, M. Mapelli, Y. Bouffanais, N. Giacobbo, U. N. Di Carlo, S. Rastello, M. C. Artale, and A. Ballone, "The cosmic merger rate density evolution of compact binaries formed in young star clusters and in isolated binaries", The Astrophysical Journal **898**, 152 (2020).

[344] B. McKernan, K. E. Saavik Ford, J. Bellovary, N. W. C. Leigh, Z. Haiman, B. Kocsis, W. Lyra, M.-M. Mac Low, B. Metzger, M. O'Dowd, S. Endlich, and D. J. Rosen, "Constraining stellar-mass black hole mergers in agn disks detectable with ligo", The Astrophysical Journal **866**, 66 (2018).

[345] A. Antonelli, M. van de Meent, A. Buonanno, J. Steinhoff, and J. Vines, "Quasicircular inspirals and plunges from nonspinning effective-one-body hamiltonians with gravitational self-force information", Phys. Rev. D **101**, 024024 (2020).

[346] A. Ramos-Buades, S. Husa, G. Pratten, H. Estellés, C. García-Quirós, M. Mateu-Lucena, M. Colleoni, and R. Jaume, "First survey of spinning eccentric black hole mergers: Numerical relativity simulations, hybrid waveforms, and parameter estimation", Phys. Rev. D **101**, 083015 (2020).

[347] I. Hinder, L. E. Kidder, and H. P. Pfeiffer, "Eccentric binary black hole inspiral-merger-ringdown gravitational waveform model from numerical relativity and post-Newtonian theory", Phys. Rev. D **98**, 044015 (2018).

[348] E. A. Huerta et al., "Eccentric, nonspinning, inspiral, Gaussian-process merger approximant for the detection and characterization of eccentric binary black hole mergers", Phys. Rev. D **97**, 024031 (2018).

[349] A. Placidi, S. Albanesi, A. Nagar, M. Orselli, S. Bernuzzi, and G. Grignani, "Exploiting Newton-factorized, 2PN-accurate waveform multipoles in effective-one-body models for spin-aligned noncircularized binaries", Phys. Rev. D **105**, 104030 (2022).

[350] M. Khalil, A. Buonanno, J. Steinhoff, and J. Vines, "Radiation-reaction force and multipolar waveforms for eccentric, spin-aligned binaries in the effective-one-body formalism", Phys. Rev. D **104**, 024046 (2021).

[351] S. Albanesi, A. Nagar, and S. Bernuzzi, "Effective one-body model for extreme-mass-ratio spinning binaries on eccentric equatorial orbits: Testing radiation reaction and waveform", Phys. Rev. D **104**, 024067 (2021).

[352] A. Nagar and P. Rettegno, "Next generation: Impact of high-order analytical information on effective one body waveform models for noncircularized, spin-aligned black hole binaries", Phys. Rev. D **104**, 104004 (2021).

[353] X. Liu, Z. Cao, and Z.-H. Zhu, "A higher-multipole gravitational waveform model for an eccentric binary black holes based on the effective-one-body-numerical-relativity formalism", Class. Quant. Grav. **39**, 035009 (2022).

[354] D. Chiaramello and A. Nagar, "Faithful analytical effective-one-body waveform model for spin-aligned, moderately eccentric, coalescing black hole binaries", Phys. Rev. D **101**, 101501 (2020).

[355] T. Hinderer and S. Babak, "Foundations of an effective-one-body model for coalescing binaries on eccentric orbits", Phys. Rev. D **96**, 104048 (2017).

[356] A. Ramos-Buades, A. Buonanno, M. Khalil, and S. Ossokine, "Effective-one-body multipolar waveforms for eccentric binary black holes with nonprecessing spins", Phys. Rev. D **105**, 044035 (2022).

[357] G. Carullo, S. Albanesi, A. Nagar, R. Gamba, S. Bernuzzi, T. Andrade, and J. Trenado, "Unveiling the Merger Structure of Black Hole Binaries in Generic Planar Orbits", Phys. Rev. Lett. **132**, 101401 (2024).

[358] X. Liu, Z. Cao, and L. Shao, "Upgraded waveform model of eccentric binary black hole based on effective-one-body-numerical-relativity for spin-aligned binary black holes", International Journal of Modern Physics D **32**, 2350015 (2023).

[359] P. C. Peters and J. Mathews, "Gravitational radiation from point masses in a Keplerian orbit", Phys. Rev. **131**, 435–439 (1963).

[360] C. W. Lincoln and C. M. Will, "Coalescing binary systems of compact objects to $(\text{post})^{5/2}$-newtonian order: late-time evolution and gravitational-radiation emission", Phys. Rev. D **42**, 1123–1143 (1990).

[361] T. Damour and N. Deruelle, "General relativistic celestial mechanics of binary systems. II. The post-Newtonian timing formula.", Annales de L'Institut Henri Poincare Section (A) Physique Theorique **44**, 263–292 (1986).

[362] M. Tessmer, J. Hartung, and G. Schafer, "Motion and gravitational wave forms of eccentric compact binaries with orbital-angular-momentum-aligned spins under next-to-leading order in spin-orbit and leading order in spin(1)-spin(2) and spin-squared couplings", Class. Quant. Grav. **27**, 165005 (2010).

[363] M. Tessmer, J. Hartung, and G. Schafer, "Aligned Spins: Orbital Elements, Decaying Orbits, and Last Stable Circular Orbit to high post-Newtonian Orders", Class. Quant. Grav. **30**, 015007 (2013).

[364] A. Klein and P. Jetzer, "Spin effects in the phasing of gravitational waves from binaries on eccentric orbits", Phys. Rev. D **81**, 124001 (2010).

[365] R.-M. Memmesheimer, A. Gopakumar, and G. Schaefer, "Third post-Newtonian accurate generalized quasi-Keplerian parametrization for compact binaries in eccentric orbits", Phys. Rev. D **70**, 104011 (2004).

[366] A. Klein, Y. Boetzel, A. Gopakumar, P. Jetzer, and L. de Vittori, "Fourier domain gravitational waveforms for precessing eccentric binaries", Phys. Rev. D **98**, 104043 (2018).

[367] G. Morras, G. Pratten, and P. Schmidt, "Improved post-Newtonian waveform model for inspiralling precessing-eccentric compact binaries", Phys. Rev. D **111**, 084052 (2025).

[368] N. Loutrel, S. Liebersbach, N. Yunes, and N. Cornish, "The eccentric behavior of inspiralling compact binaries", Class. Quant. Grav. **36**, 025004 (2019).

[369] T. Mora and C. M. Will, "A PostNewtonian diagnostic of quasiequilibrium binary configurations of compact objects", Phys. Rev. D **69**, [Erratum: Phys.Rev.D 71, 129901 (2005)], 104021 (2004).

[370] C. M. Will and M. Maitra, "Relativistic orbits around spinning supermassive black holes. Secular evolution to 4.5 post-Newtonian order", Phys. Rev. D **95**, 064003 (2017).

[371] N. Wex, "The second post-newtonian motion of compact binary-star systems with spin", Classical and Quantum Gravity **12**, 983 (1995).

[372] T. Damour, A. Gopakumar, and B. R. Iyer, "Phasing of gravitational waves from inspiralling eccentric binaries", Phys. Rev. D **70**, 064028 (2004).

[373] C. Konigsdorffer and A. Gopakumar, "Phasing of gravitational waves from inspiralling eccentric binaries at the third-and-a-half post-Newtonian order", Phys. Rev. D **73**, 124012 (2006).

[374] E. Poisson, "Measuring black hole parameters and testing general relativity using gravitational wave data from space based interferometers", Phys. Rev. D **54**, 5939–5953 (1996).

[375] M. Boyle, D. A. Brown, L. E. Kidder, A. H. Mroue, H. P. Pfeiffer, M. A. Scheel, G. B. Cook, and S. A. Teukolsky, "High-accuracy comparison of numerical relativity simulations with post-Newtonian expansions", Phys. Rev. D **76**, 124038 (2007).

[376] H. P. Pfeiffer, D. A. Brown, L. E. Kidder, L. Lindblom, G. Lovelace, and M. A. Scheel, "Reducing orbital eccentricity in binary black hole simulations", Class. Quant. Grav. **24**, edited by M. Campanelli and L. Rezzolla, S59–S82 (2007).

[377] W. Tichy and P. Marronetti, "A Simple method to set up low eccentricity initial data for moving puncture simulations", Phys. Rev. D **83**, 024012 (2011).

[378] A. Buonanno, L. E. Kidder, A. H. Mroue, H. P. Pfeiffer, and A. Taracchini, "Reducing orbital eccentricity of precessing black-hole binaries", Phys. Rev. D **83**, 104034 (2011).

[379] A. Ramos-Buades, S. Husa, and G. Pratten, "Simple procedures to reduce eccentricity of binary black hole simulations", Phys. Rev. D **99**, 023003 (2019).

[380] L. Smarr, "Space-times generated by computers: black holes with gravitational radiation", Annals of the New York Academy of Sciences **302**, 569–604 (1977).

[381] J. Healy, J. Levin, and D. Shoemaker, "Zoom-Whirl Orbits in Black Hole Binaries", Phys. Rev. Lett. **103**, 131101 (2009).

[382] U. Sperhake, V. Cardoso, F. Pretorius, E. Berti, T. Hinderer, and N. Yunes, "Cross section, final spin and zoom-whirl behavior in high-energy black hole collisions", Phys. Rev. Lett. **103**, 131102 (2009).

[383] E. A. Huerta et al., "Physics of eccentric binary black hole mergers: A numerical relativity perspective", Phys. Rev. D **100**, 064003 (2019).

[384] T. Dietrich, N. Moldenhauer, N. K. Johnson-McDaniel, S. Bernuzzi, C. M. Markakis, B. Brügmann, and W. Tichy, "Binary Neutron Stars with Generic Spin, Eccentricity, Mass ratio, and Compactness - Quasi-equilibrium Sequences and First Evolutions", Phys. Rev. D **92**, 124007 (2015).

[385] M. A. Shaikh, V. Varma, H. P. Pfeiffer, A. Ramos-Buades, and M. van de Meent, "Defining eccentricity for gravitational wave astronomy", Phys. Rev. D **108**, 104007 (2023).

[386] A. Ramos-Buades, M. van de Meent, H. P. Pfeiffer, H. R. Rüter, M. A. Scheel, M. Boyle, and L. E. Kidder, "Eccentric binary black holes: Comparing numerical relativity and small mass-ratio perturbation theory", Phys. Rev. D **106**, 124040 (2022).

[387] A. Bonino, R. Gamba, P. Schmidt, A. Nagar, G. Pratten, M. Breschi, P. Rettegno, and S. Bernuzzi, "Inferring eccentricity evolution from observations of coalescing binary black holes", Phys. Rev. D **107**, 064024 (2023).

[388] A. Bonino, P. Schmidt, and G. Pratten, "Mapping eccentricity evolutions between numerical relativity and effective-one-body gravitational waveforms", Phys. Rev. D **110**, 104002 (2024).

[389] T. Islam and T. Venumadhav, "Post-Newtonian theory-inspired framework for characterizing eccentricity in gravitational waveforms", (2025).

[390] A. M. Knee, I. M. Romero-Shaw, P. D. Lasky, J. McIver, and E. Thrane, "A Rosetta Stone for Eccentric Gravitational Waveform Models", Astrophys. J. **936**, 172 (2022).

[391] T. Mora and C. M. Will, "Numerically generated quasiequilibrium orbits of black holes: Circular or eccentric?", Phys. Rev. D **66**, 101501 (2002).

[392] T. A. Clarke, I. M. Romero-Shaw, P. D. Lasky, and E. Thrane, "Gravitational-wave inference for eccentric binaries: the argument of periapsis", Mon. Not. Roy. Astron. Soc. **517**, 3778–3784 (2022).

[393] T. Damour, "Coalescence of two spinning black holes: an effective one-body approach", Phys. Rev. D **64**, 124013 (2001).

[394] A. Taracchini, Y. Pan, A. Buonanno, E. Barausse, M. Boyle, T. Chu, G. Lovelace, H. P. Pfeiffer, and M. A. Scheel, "Prototype effective-one-body model for nonprecessing spinning inspiral-merger-ringdown waveforms", Phys. Rev. D **86**, 024011 (2012).

[395] T. Damour, A. Nagar, and S. Bernuzzi, "Improved effective-one-body description of coalescing nonspinning black-hole binaries and its numerical-relativity completion", Phys. Rev. D **87**, 084035 (2013).

[396] A. Taracchini et al., "Effective-one-body model for black-hole binaries with generic mass ratios and spins", Phys. Rev. D **89**, 061502 (2014).

[397] Y. Pan, A. Buonanno, A. Taracchini, L. E. Kidder, A. H. Mroué, H. P. Pfeiffer, M. A. Scheel, and B. Szilágyi, "Inspiral-merger-ringdown waveforms of spinning, precessing black-hole binaries in the effective-one-body formalism", Phys. Rev. D **89**, 084006 (2014).

[398] T. Damour, P. Jaranowski, and G. Schäfer, "Fourth post-Newtonian effective one-body dynamics", Phys. Rev. D **91**, 084024 (2015).

[399] A. Nagar, T. Damour, C. Reisswig, and D. Pollney, "Energetics and phasing of nonprecessing spinning coalescing black hole binaries", Phys. Rev. D **93**, 044046 (2016).

[400] M. Pürrer, "Frequency domain reduced order model of aligned-spin effective-one-body waveforms with generic mass-ratios and spins", Phys. Rev. D **93**, 064041 (2016).

[401] S. Babak, A. Taracchini, and A. Buonanno, "Validating the effective-one-body model of spinning, precessing binary black holes against numerical relativity", Phys. Rev. D **95**, 024010 (2017).

[402] W. Del Pozzo and A. Nagar, "Analytic family of post-merger template waveforms", Phys. Rev. D **95**, 124034 (2017).

[403] T. Damour and A. Nagar, "The Effective-One-Body Approach to the General Relativistic Two Body Problem", Lect. Notes Phys. **905**, 273–312 (2016).

[404] A. Nagar, G. Riemenschneider, and G. Pratten, "Impact of Numerical Relativity information on effective-one-body waveform models", Phys. Rev. D **96**, 084045 (2017).

[405] S. Akcay, S. Bernuzzi, F. Messina, A. Nagar, N. Ortiz, and P. Rettegno, "Effective-one-body multipolar waveform for tidally interacting binary neutron stars up to merger", Phys. Rev. D **99**, 044051 (2019).

[406] A. Nagar and P. Rettegno, "Efficient effective one body time-domain gravitational waveforms", Phys. Rev. D **99**, 021501 (2019).

[407] R. Cotesta, S. Marsat, and M. Pürrer, "Frequency domain reduced order model of aligned-spin effective-one-body waveforms with higher-order modes", Phys. Rev. D **101**, 124040 (2020).

[408] A. Bohé, M. Hannam, S. Husa, F. Ohme, M. Puerrer, and P. Schmidt, *Phenompv2 - technical notes for lal implementation*, tech. rep. LIGO-T1500602 (LIGO Project, 2016).

[409] S. Khan, K. Chatziioannou, M. Hannam, and F. Ohme, "Phenomenological model for the gravitational-wave signal from precessing binary black holes with two-spin effects", Phys. Rev. D **100**, 024059 (2019).

[410] S. Khan, K. Chatziioannou, M. Hannam, and F. Ohme, "Phenomenological model for the gravitational-wave signal from precessing binary black holes with two-spin effects", Phys. Rev. D **100**, 024059 (2019).

[411] G. Pratten, S. Husa, C. Garcia-Quiros, M. Colleoni, A. Ramos-Buades, H. Estelles, and R. Jaume, "Setting the cornerstone for a family of models for gravitational waves from compact binaries: The dominant harmonic for nonprecessing quasicircular black holes", Phys. Rev. D **102**, 064001 (2020).

[412] M. Rosselló-Sastre, S. Husa, and S. Bera, "Waveform model for the missing quadrupole mode from black hole coalescence: Memory effect and ringdown of the (ℓ=2,m=0) spherical harmonic", Phys. Rev. D **110**, 084074 (2024).

[413] J. Yoo, V. Varma, M. Giesler, M. A. Scheel, C.-J. Haster, H. P. Pfeiffer, L. E. Kidder, and M. Boyle, "Targeted large mass ratio numerical relativity surrogate waveform model for GW190814", Phys. Rev. D **106**, 044001 (2022).

[414] J. Yoo et al., "Numerical relativity surrogate model with memory effects and post-Newtonian hybridization", Phys. Rev. D **108**, 064027 (2023).

[415] D. P. Mihaylov, S. Ossokine, A. Buonanno, H. Estelles, L. Pompili, M. Pürrer, and A. Ramos-Buades, "pySEOBNR: a software package for the next generation of effective-one-body multipolar waveform models", (2023).

[416] C. García-Quirós, S. Tiwari, and S. Babak, *Gpu-accelerated lisa parameter estimation with full time domain response*, 2025.

[417] S. E. Field et al., "GWSurrogate: A Python package for gravitational wave surrogate models", J. Open Source Softw. **10**, 7073 (2025).

[418] M. van de Meent, A. Buonanno, D. P. Mihaylov, S. Ossokine, L. Pompili, N. Warburton, A. Pound, B. Wardell, L. Durkan, and J. Miller, "Enhancing the seobnrv5 effective-one-body waveform model with second-order gravitational self-force fluxes", Phys. Rev. D **108**, 124038 (2023).

[419] M. Davis, R. Ruffini, W. H. Press, and R. H. Price, "Gravitational radiation from a particle falling radially into a schwarzschild black hole", Phys. Rev. Lett. **27**, 1466–1469 (1971).

[420] R. H. Price and J. Pullin, "Colliding black holes: the close limit", Phys. Rev. Lett. **72**, 3297–3300 (1994).

[421] T. Damour and A. Gopakumar, "Gravitational recoil during binary black hole coalescence using the effective one body approach", Phys. Rev. D **73**, 124006 (2006).

[422] T. Damour and A. Nagar, "Faithful effective-one-body waveforms of small-mass-ratio coalescing black-hole binaries", Phys. Rev. D **76**, 064028 (2007).

[423] M. Haberland, A. Buonanno, and J. Steinhoff, "Modeling matter(s) in SEOBNRv5THM: Generating fast and accurate effective-one-body waveforms for spin-aligned binary neutron stars", (2025).

[424] T. Damour and A. Nagar, "New effective-one-body description of coalescing nonprecessing spinning black-hole binaries", Phys. Rev. D **90**, 044018 (2014).

[425] S. Albanesi, "Real modes and null memory contributions in effective-one-body models", (2024).

[426] E. Grilli, A. Placidi, S. Albanesi, G. Grignani, and M. Orselli, "Direct current memory effects in effective-one-body waveform models", Phys. Rev. D **111**, 044045 (2025).

[427] M. Khalil, A. Buonanno, H. Estelles, D. P. Mihaylov, S. Ossokine, L. Pompili, and A. Ramos-Buades, "Theoretical groundwork supporting the precessing-spin two-body dynamics of the effective-one-body waveform models SEOBNRv5", Phys. Rev. D **108**, 124036 (2023).

[428] S. E. Field, C. R. Galley, J. S. Hesthaven, J. Kaye, and M. Tiglio, "Fast prediction and evaluation of gravitational waveforms using surrogate models", Phys. Rev. X **4**, 031006 (2014).

[429] J. Tissino, G. Carullo, M. Breschi, R. Gamba, S. Schmidt, and S. Bernuzzi, "Combining effective-one-body accuracy and reduced-order-quadrature speed for binary neutron star merger parameter estimation with machine learning", Phys. Rev. D **107**, 084037 (2023).

[430] T. Damour and A. Nagar, "Effective One Body description of tidal effects in inspiralling compact binaries", Phys. Rev. D **81**, 084016 (2010).

[431] T. Damour and A. Nagar, "Relativistic tidal properties of neutron stars", Phys. Rev. D **80**, 084035 (2009).

[432] T. Hinderer et al., "Effects of neutron-star dynamic tides on gravitational waveforms within the effective-one-body approach", Phys. Rev. Lett. **116**, 181101 (2016).

[433] P. Ajith et al., "Phenomenological template family for black-hole coalescence waveforms", Class. Quant. Grav. **24**, edited by B. Krishnan, M. A. Papa, and B. F. Schutz, S689–S700 (2007).

[434] P. Ajith et al., "A Template bank for gravitational waveforms from coalescing binary black holes. I. Non-spinning binaries", Phys. Rev. D **77**, [Erratum: Phys.Rev.D 79, 129901 (2009)], 104017 (2008).

[435] M. Colleoni, F. A. R. Vidal, N. K. Johnson-McDaniel, T. Dietrich, M. Haney, and G. Pratten, "IMRPhenomXP_NRTidalv2: An improved frequency-domain precessing binary neutron star waveform model", (2023).

[436] A. Abac, T. Dietrich, A. Buonanno, J. Steinhoff, and M. Ujevic, "New and robust gravitational-waveform model for high-mass-ratio binary neutron star systems with dynamical tidal effects", Phys. Rev. D **109**, 024062 (2024).

[437] S. Isoyama, R. Fujita, A. J. K. Chua, H. Nakano, A. Pound, and N. Sago, "Adiabatic Waveforms from Extreme-Mass-Ratio Inspirals: An Analytical Approach", Physical Review Letters **128**, 231101, 231101 (2022).

[438] L. Barack and A. Pound, "Self-force and radiation reaction in general relativity", Reports on Progress in Physics **82**, 016904 (2018).

[439] H. Yu, J. Roulet, T. Venumadhav, B. Zackay, and M. Zaldarriaga, "Accurate and efficient waveform model for precessing binary black holes", Phys. Rev. D **108**, 064059 (2023).

[440] D. Ferguson, E. Allsup, S. Anne, G. Bouyer, M. Gracia-Linares, H. Iglesias, A. Jan, P. Laguna, J. Lange, E. Martinez, F. Meoni, R. Nowicki, D. Shoemaker, B. Steadham, M. L. Trostel, B.-J. Tsao, and F. Valorz, "Second maya catalog of binary black hole numerical relativity waveforms", (2023).

[441] A. Gonzalez, F. Zappa, M. Breschi, S. Bernuzzi, D. Radice, A. Adhikari, A. Camilletti, S. V. Chaurasia, G. Doulis, S. Padamata, A. Rashti, M. Ujevic, B. Brügmann, W. Cook, T. Dietrich, A. Perego, A. Poudel, and W. Tichy, "Second release of the core database of binary neutron star merger waveforms", Classical and Quantum Gravity **40**, 085011 (2023).

[442] C. O. Lousto and J. Healy, "Study of the intermediate mass ratio black hole binary merger up to 1000:1 with numerical relativity", Class. Quant. Grav. **40**, 09LT01 (2023).

[443] J. Healy, C. O. Lousto, and Y. Zlochower, "Remnant mass, spin, and recoil from spin aligned black-hole binaries", Physical Review D **90**, 104004, 104004 (2014).

[444] Y. Zlochower and C. O. Lousto, "Modeling the remnant mass, spin, and recoil from unequal-mass, precessing black-hole binaries: the intermediate mass ratio regime", Phys. Rev. D **92**, 024022 (2015).

[445] F. Hofmann, E. Barausse, and L. Rezzolla, "The final spin from binary black holes in quasi-circular orbits", The Astrophysical Journal Letters **825**, L19 (2016).

[446] L. Haegel and S. Husa, "Predicting the properties of black-hole merger remnants with deep neural networks", Class. Quant. Grav. **37**, 135005 (2020).

[447] A. Apte and S. A. Hughes, "Exciting black hole modes via misaligned coalescences. i. inspiral, transition, and plunge trajectories using a generalized ori-thorne procedure", Phys. Rev. D **100**, 084031 (2019).

[448] H. Lim, G. Khanna, A. Apte, and S. A. Hughes, "Exciting black hole modes via misaligned coalescences. ii. the mode content of late-time coalescence waveforms", Phys. Rev. D **100**, 084032 (2019).

[449] W. Schmidt, "Celestial mechanics in kerr spacetime", Classical and Quantum Gravity **19**, 2743–2764 (2002).

[450] J. Mathews, A. Pound, and B. Wardell, "Self-force calculations with a spinning secondary", Phys. Rev. D **105**, 084031 (2022).

[451] L. Werneck et al., *The einstein toolkit*, version The "Karl Schwarzschild" release, ET_2023_05, To find out more, visit http://einsteintoolkit.org, May 2023.

[452] S. Ossokine, M. Boyle, L. E. Kidder, H. P. Pfeiffer, M. A. Scheel, and B. Szilágyi, "Comparing post-newtonian and numerical relativity precession dynamics", Physical Review D **92**, 10.1103/physrevd.92.104028 (2015).

[453] J. W. York Jr., "Conformal 'thin sandwich' data for the initial-value problem", Phys. Rev. Lett. **82**, 1350–1353 (1999).

[454] G. Lovelace, R. Owen, H. P. Pfeiffer, and T. Chu, "Binary-black-hole initial data with nearly-extremal spins", Phys. Rev. D **78**, 084017 (2008).

[455] J. M. Bowen and J. W. York, "Time-asymmetric initial data for black holes and black-hole collisions", Phys. Rev. D **21**, 2047–2056 (1980).

[456] D. Pollney, C. Reisswig, E. Schnetter, N. Dorband, and P. Diener, "High accuracy binary black hole simulations with an extended wave zone", Phys. Rev. D **83**, 044045 (2011).

[457] J. Thornburg, "A Fast apparent horizon finder for three-dimensional Cartesian grids in numerical relativity", Class. Quant. Grav. **21**, 743–766 (2004).

[458] R. H. Boyer and R. W. Lindquist, "Maximal analytic extension of the Kerr metric", J. Math. Phys. **8**, 265 (1967).

[459] S. Drasco and S. A. Hughes, "Gravitational wave snapshots of generic extreme mass ratio inspirals", Phys. Rev. D **73**, [Erratum: Phys.Rev.D 88, 109905 (2013), Erratum: Phys.Rev.D 90, 109905 (2014)], 024027 (2006).

[460] A. Ori and K. S. Thorne, "Transition from inspiral to plunge for a compact body in a circular equatorial orbit around a massive, spinning black hole", Phys. Rev. D **62**, 124022 (2000).

[461] P. A. Sundararajan, G. Khanna, and S. A. Hughes, "Towards adiabatic waveforms for inspiral into kerr black holes: a new model of the source for the time domain perturbation equation", Phys. Rev. D **76**, 104005 (2007).

[462] P. A. Sundararajan, G. Khanna, S. A. Hughes, and S. Drasco, "Towards adiabatic waveforms for inspiral into kerr black holes. ii. dynamical sources and generic orbits", Phys. Rev. D **78**, 024022 (2008).

[463] M. Cabero, A. B. Nielsen, A. P. Lundgren, and C. D. Capano, "Minimum energy and the end of the inspiral in the post-Newtonian approximation", Phys. Rev. D **95**, 064016 (2017).

[464] N. K. Johnson-McDaniel, S. Kulkarni, and A. Gupta, "Inferring spin tilts at formation from gravitational wave observations of binary black holes: interfacing precession-averaged and orbit-averaged spin evolution", Physical Review D **106**, 10.1103/physrevd.106.023001 (2022).

[465] D. Kennefick and A. Ori, "Radiation reaction induced evolution of circular orbits of particles around Kerr black holes", Phys. Rev. D **53**, 4319–4326 (1996).

[466] L. C. Stein and N. Warburton, "Location of the last stable orbit in Kerr spacetime", Phys. Rev. D **101**, 064007 (2020).

[467] ". Research", *LinearModelFit*, https://reference.wolfram.com/language/ref/LinearModelFit.html, Accessed: 12-January-2024, 2008.

[468] W. Research, *Fit*, https://reference.wolfram.com/language/ref/Fit.html, Accessed: 15-January-2024, 2019.

[469] H. Akaike, "A new look at the statistical model identification", IEEE Transactions on Automatic Control **19**, 716–723 (1974).

[470] G. Schwarz, "Estimating the dimension of a model", The Annals of Statistics **6**, 461–464 (1978).

[471] A. R. Liddle, "Information criteria for astrophysical model selection", Monthly Notices of the Royal Astronomical Society: Letters **377**, L74–L78 (2007).

[472] The LIGO Scientific Collaboration, "Advanced ligo", Classical and Quantum Gravity **32**, 074001 (2015).

[473] Virgo Collaboration, "Advanced virgo: a second-generation interferometric gravitational wave detector", Classical and Quantum Gravity **32**, 024001 (2014).

[474] KAGRA Collaboration, "Overview of kagra: detector design and construction history", Progress of Theoretical and Experimental Physics **2021**, 05A101 (2020).

[475] S. Stevenson, A. Vigna-Gómez, I. Mandel, J. W. Barrett, C. J. Neijssel, D. Perkins, and S. E. de Mink, "Formation of the first three gravitational-wave observations through isolated binary evolution", Nature Commun. **8**, 14906 (2017).

[476] M. Colleoni, M. Mateu-Lucena, H. Estellés, C. García-Quirós, D. Keitel, G. Pratten, A. Ramos-Buades, and S. Husa, "Towards the routine use of subdominant harmonics in gravitational-wave inference: Reanalysis of GW190412 with generation X waveform models", Phys. Rev. D **103**, 024029 (2021).

[477] S. Tiwari and A. Gopakumar, "Combining post-circular and Padé approximations to compute Fourier domain templates for eccentric inspirals", Phys. Rev. D **102**, 084042 (2020).

[478] S. Tanay, A. Klein, E. Berti, and A. Nishizawa, "Convergence of Fourier-domain templates for inspiraling eccentric compact binaries", Phys. Rev. D **100**, 064006 (2019).

[479] B. Moore, T. Robson, N. Loutrel, and N. Yunes, "Towards a Fourier domain waveform for non-spinning binaries with arbitrary eccentricity", Class. Quant. Grav. **35**, 235006 (2018).

[480] E. A. Huerta, P. Kumar, S. T. McWilliams, R. O'Shaughnessy, and N. Yunes, "Accurate and efficient waveforms for compact binaries on eccentric orbits", Phys. Rev. D **90**, 084016 (2014).

[481] K. Paul and C. K. Mishra, "Spin effects in spherical harmonic modes of gravitational waves from eccentric compact binary inspirals", Phys. Rev. D **108**, 024023 (2023).

[482] O. Sridhar, S. Bhattacharyya, K. Paul, and C. K. Mishra, *Spin effects in the phasing formula of eccentric compact binary inspirals till the third post-newtonian order*, 2024.

[483] A. Klein, "Efpe: efficient fully precessing eccentric gravitational waveforms for binaries with long inspirals", (2021).

[484] J. N. Arredondo, A. Klein, and N. Yunes, "Efficient gravitational-wave model for fully-precessing and moderately eccentric, compact binary inspirals", Phys. Rev. D **110**, 044044 (2024).

[485] E. A. Huerta et al., "Complete waveform model for compact binaries on eccentric orbits", Phys. Rev. D **95**, 024038 (2017).

[486] A. Chattaraj, T. RoyChowdhury, Divyajyoti, C. K. Mishra, and A. Gupta, "High accuracy post-Newtonian and numerical relativity comparisons involving higher modes for eccentric binary black holes and a dominant mode eccentric inspiral-merger-ringdown model", Phys. Rev. D **106**, 124008 (2022).

[487] P. Manna, T. RoyChowdhury, and C. K. Mishra, "An improved IMR model for BBHs on elliptical orbits", (2024).

[488] K. Paul, A. Maurya, Q. Henry, K. Sharma, P. Satheesh, Divyajyoti, P. Kumar, and C. K. Mishra, "ESIGMAHM: An Eccentric, Spinning inspiral-merger-ringdown waveform model with Higher Modes for the detection and characterization of binary black holes", (2024).

[489] G. Carullo, "Ringdown amplitudes of nonspinning eccentric binaries", (2024).

[490] Y. Setyawati and F. Ohme, "Adding eccentricity to quasicircular binary-black-hole waveform models", Phys. Rev. D **103**, 124011 (2021).

[491] T. Islam and T. Venumadhav, "Universal phenomenological relations between spherical harmonic modes in non-precessing eccentric binary black hole merger waveforms", (2024).

[492] T. Islam, "Straightforward mode hierarchy in eccentric binary black hole mergers and associated waveform model", (2024).

[493] T. Islam, G. Khanna, and S. E. Field, "Adding higher-order spherical harmonics in non-spinning eccentric binary black hole merger waveform models", (2024).

[494] L. Blanchet and G. Schafer, "Gravitational wave tails and binary star systems", Classical and Quantum Gravity **10**, 2699 (1993).

[495] A. G. Wiseman, "Coalescing binary systems of compact objects to (post)$^{\frac{5}{2}}$-newtonian order. iv. the gravitational wave tail", Phys. Rev. D **48**, 4757–4770 (1993).

[496] L. Blanchet, B. R. Iyer, C. M. Will, and A. G. Wiseman, "Gravitational waveforms from inspiralling compact binaries to second postNewtonian order", Class. Quant. Grav. **13**, 575–584 (1996).

[497] K. G. Arun, L. Blanchet, B. R. Iyer, and M. S. S. Qusailah, "The 2.5PN gravitational wave polarizations from inspiralling compact binaries in circular orbits", Class. Quant. Grav. **21**, [Erratum: Class.Quant.Grav. 22, 3115 (2005)], 3771–3802 (2004).

[498] L. E. Kidder, "Using full information when computing modes of post-Newtonian waveforms from inspiralling compact binaries in circular orbit", Phys. Rev. D **77**, 044016 (2008).

[499] Y. Boetzel, C. K. Mishra, G. Faye, A. Gopakumar, and B. R. Iyer, "Gravitational-wave amplitudes for compact binaries in eccentric orbits at the third post-Newtonian order: Tail contributions and postadiabatic corrections", Phys. Rev. D **100**, 044018 (2019).

[500] M. Mateu-Lucena, S. Husa, M. Colleoni, H. Estellés, C. García-Quirós, D. Keitel, M. d. L. Planas, and A. Ramos-Buades, "Parameter estimation with the current generation of phenomenological waveform models applied to the black hole mergers of GWTC-1", Mon. Not. Roy. Astron. Soc. **517**, 2403–2425 (2022).

[501] L. Blanchet, "Post-Newtonian Theory for Gravitational Waves", Living Rev. Rel. **17**, 2 (2014).

[502] L. Blanchet, G. Faye, B. R. Iyer, and B. Joguet, "Gravitational wave inspiral of compact binary systems to 7/2 postNewtonian order", Phys. Rev. D **65**, [Erratum: Phys.Rev.D 71, 129902 (2005)], 061501 (2002).

[503] L. Blanchet, G. Faye, B. R. Iyer, and S. Sinha, "The Third post-Newtonian gravitational wave polarisations and associated spherical harmonic modes for inspiralling compact binaries in quasi-circular orbits", Class. Quant. Grav. **25**, [Erratum: Class.Quant.Grav. 29, 239501 (2012)], 165003 (2008).

[504] G. Faye, S. Marsat, L. Blanchet, and B. R. Iyer, "Post-Newtonian prediction for the (2,2) mode of the gravitational wave emitted by compact binaries", ASP Conf. Ser. **467**, edited by G. Auger, P. Binétruy, and E. Plagnol, 197–202 (2013).

[505] K. G. Arun, A. Buonanno, G. Faye, and E. Ochsner, "Higher-order spin effects in the amplitude and phase of gravitational waveforms emitted by inspiraling compact binaries: Ready-to-use gravitational waveforms", Phys. Rev. D **79**, [Erratum: Phys.Rev.D 84, 049901 (2011)], 104023 (2009).

[506] A. Buonanno, G. Faye, and T. Hinderer, "Spin effects on gravitational waves from inspiraling compact binaries at second post-Newtonian order", Phys. Rev. D **87**, 044009 (2013).

[507] J. Madore, "The equations of motion of an extended body in general relativity", en, Annales de l'institut Henri Poincaré. Section A, Physique Théorique **11**, 221–237 (1969).

[508] W. G. Dixon, "Extended bodies in general relativity: their description and motion.", in Isolated gravitating systems in general relativity, edited by J. Ehlers (Jan. 1979), pp. 156–219.

[509] B. Moore, M. Favata, K. G. Arun, and C. K. Mishra, "Gravitational-wave phasing for low-eccentricity inspiralling compact binaries to 3PN order", Phys. Rev. D **93**, 124061 (2016).

[510] A. Gamboa, M. Khalil, and A. Buonanno, "Third post-Newtonian dynamics for eccentric orbits and aligned spins in the effective-one-body waveform model SEOBNRv5EHM", (2024).

[511] M. Boschini, N. Loutrel, D. Gerosa, and G. Fumagalli, "Orbital eccentricity in general relativity from catastrophe theory", Phys. Rev. D **111**, 024008 (2025).

[512] P. Virtanen, R. Gommers, T. E. Oliphant, M. Haberland, T. Reddy, D. Cournapeau, E. Burovski, P. Peterson, W. Weckesser, J. Bright, S. J. van der Walt, M. Brett, J. Wilson, K. J. Millman, N. Mayorov, A. R. J. Nelson, E. Jones, R. Kern, E. Larson, C. J. Carey, İ. Polat, Y. Feng, E. W. Moore, J. VanderPlas, D. Laxalde, J. Perktold, R. Cimrman, I. Henriksen, E. A. Quintero, C. R. Harris, A. M. Archibald, A. H. Ribeiro, F. Pedregosa, P. van Mulbregt, and SciPy 1.0 Contributors, "SciPy 1.0: Fundamental Algorithms for Scientific Computing in Python", Nature Methods **17**, 261–272 (2020).

[513] Q. Henry et al., "In preparation (2025)Spin effects in gravitational waveforms and fluxes for binaries on eccentric orbits to the third post-Newtonian order", In preparation (2025).

[514] B. S. Sathyaprakash and S. V. Dhurandhar, "Choice of filters for the detection of gravitational waves from coalescing binaries", Phys. Rev. D **44**, 3819–3834 (1991).

[515] L. S. Finn and D. F. Chernoff, "Observing binary inspiral in gravitational radiation: One interferometer", Phys. Rev. D **47**, 2198–2219 (1993).

[516] M. Evans, R. Sturani, S. Vitale, and E. Hall, *Unofficial sensitivity curves (ASD) for aLIGO, Kagra, Virgo, Voyager, Cosmic Explorer, and Einstein Telescope*, Available online, 2023.

[517] C. Capano, Y. Pan, and A. Buonanno, "Impact of higher harmonics in searching for gravitational waves from nonspinning binary black holes", Phys. Rev. D **89**, 102003 (2014).

[518] I. Harry, J. Calderón Bustillo, and A. Nitz, "Searching for the full symphony of black hole binary mergers", Phys. Rev. D **97**, 023004 (2018).

[519] I. Hinder, S. Ossokine, H. P. Pfeiffer, and A. Buonanno, "Gravitational waveforms for high spin and high mass-ratio binary black holes: a synergistic use of numerical-relativity codes", Phys. Rev. D **99**, 061501 (2019).

[520] J. Veitch et al., "Parameter estimation for compact binaries with ground-based gravitational-wave observations using the LALInference software library", Phys. Rev. D **91**, 042003 (2015).

[521] D. Shoemaker.

[522] The LIGO Scientific Collaboration, the Virgo Collaboration, "Open data from the first and second observing runs of advanced ligo and advanced virgo", SoftwareX **13**, 100658 (2021).

[523] R. O'Shaughnessy, J. Healy, L. London, Z. Meeks, and D. Shoemaker, "Is J enough? comparison of gravitational waves emitted along the total angular momentum direction with other preferred orientations", Phys. Rev. D **85**, 084003 (2012).

[524] H. A. Bethe and G. E. Brown, "Evolution of binary compact objects which merge", Astrophys. J. **506**, 780–789 (1998).

[525] K. Belczynski, T. Bulik, and B. Rudak, "First stellar binary black holes: strongest gravitational wave burst sources", Astrophys. J. Lett. **608**, L45–L48 (2004).

[526] H. V. Zeipel, "Sur l'application des séries de m. lindstedt à l'étude du mouvement des comètes périodiques", Astronomische Nachrichten **183**, 345–418 (1909).

[527] Y. Kozai, "Secular perturbations of asteroids with high inclination and eccentricity", The Astronomical Journal **67**, 591–598 (1962).

[528] M. L. Lidov, "The evolution of orbits of artificial satellites of planets under the action of gravitational perturbations of external bodies", Planetary and Space Science **9**, 719–759 (1962).

[529] M. Bošković, M. Koschnitzke, and R. A. Porto, "Signatures of Ultralight Bosons in the Orbital Eccentricity of Binary Black Holes", Phys. Rev. Lett. **133**, 121401 (2024).

[530] E. Payne, C. Talbot, and E. Thrane, "Higher order gravitational-wave modes with likelihood reweighting", Phys. Rev. D **100**, 123017 (2019).

[531] A. Borchers, F. Ohme, J. Mielke, and S. Ghosh, "Observability of spin precession in the presence of a black-hole remnant kick", Phys. Rev. D **110**, 024037 (2024).

[532] B. P. Abbott et al. (LIGO Scientific, Virgo), "GW150914: The Advanced LIGO Detectors in the Era of First Discoveries", Phys. Rev. Lett. **116**, 131103 (2016).

[533] D. Davis, T. B. Littenberg, I. M. Romero-Shaw, M. Millhouse, J. McIver, F. Di Renzo, and G. Ashton, "Subtracting glitches from gravitational-wave detector data during the third LIGO-Virgo observing run", Class. Quant. Grav. **39**, 245013 (2022).

[534] A.-K. Malz, G. Ashton, and N. Colombo, *Classification uncertainty for transient gravitational-wave noise artefacts with optimised conformal prediction*, 2024.

[535] D. Davis, T. J. Massinger, A. P. Lundgren, J. C. Driggers, A. L. Urban, and L. K. Nuttall, "Improving the Sensitivity of Advanced LIGO Using Noise Subtraction", Class. Quant. Grav. **36**, 055011 (2019).

[536] N. J. Cornish and T. B. Littenberg, "BayesWave: Bayesian Inference for Gravitational Wave Bursts and Instrument Glitches", Class. Quant. Grav. **32**, 135012 (2015).

[537] P. J. GREEN, "Reversible jump markov chain monte carlo computation and bayesian model determination", Biometrika **82**, 711–732 (1995).

[538] M. de Lluc Planas et al., "In preparation (2025). Discerning eccentricity in neutron star-black hole mergers: GW200105 is eccentric, GW200115 is not.", In preparation (2025).

[539] J. C. Bustillo, N. Sanchis-Gual, A. Torres-Forné, and J. A. Font, "Confusing head-on collisions with precessing intermediate-mass binary black hole mergers", Phys. Rev. Lett. **126**, 201101 (2021).

[540] I. M. Romero-Shaw, D. Gerosa, and N. Loutrel, "Eccentricity or spin precession? Distinguishing subdominant effects in gravitational-wave data", Mon. Not. Roy. Astron. Soc. **519**, 5352–5357 (2023).

[541] H. L. Iglesias et al., "Eccentricity Estimation for Five Binary Black Hole Mergers with Higher-order Gravitational-wave Modes", Astrophys. J. **972**, 65 (2024).

[542] M. d. L. Planas, A. Ramos-Buades, C. García-Quirós, H. Estellés, S. Husa, and M. Haney, *Data release for the article: Eccentric or circular? A reanalysis of binary black hole gravitational wave events for orbital eccentricity signatures*, 2025.

[543] B. Zackay, T. Venumadhav, L. Dai, J. Roulet, and M. Zaldarriaga, "Highly spinning and aligned binary black hole merger in the Advanced LIGO first observing run", Phys. Rev. D **100**, 023007 (2019).

[544] A. H. Nitz, T. Dent, G. S. Davies, S. Kumar, C. D. Capano, I. Harry, S. Mozzon, L. Nuttall, A. Lundgren, and M. Tápai, "2-OGC: Open Gravitational-wave Catalog of binary mergers from analysis of public Advanced LIGO and Virgo data", Astrophys. J. **891**, 123 (2020).

[545] A. H. Nitz, C. D. Capano, S. Kumar, Y.-F. Wang, S. Kastha, M. Schäfer, R. Dhurkunde, and M. Cabero, "3-OGC: Catalog of Gravitational Waves from Compact-binary Mergers", Astrophys. J. **922**, 76 (2021).

[546] A. E. Koloniari, E. C. Koursoumpa, P. Nousi, P. Lampropoulos, N. Passalis, A. Tefas, and N. Stergioulas, "New gravitational wave discoveries enabled by machine learning", Mach. Learn. Sci. Tech. **6**, 015054 (2025).

[547] K. Belczynski, V. Kalogera, and T. Bulik, "A Comprehensive study of binary compact objects as gravitational wave sources: Evolutionary channels, rates, and physical properties", Astrophys. J. **572**, 407–431 (2001).

[548] M. Dominik, K. Belczynski, C. Fryer, D. Holz, E. Berti, T. Bulik, I. Mandel, and R. O'Shaughnessy, "Double Compact Objects I: The Significance of the Common Envelope on Merger Rates", Astrophys. J. **759**, 52 (2012).

[549] I. Hinder, B. Vaishnav, F. Herrmann, D. M. Shoemaker, and P. Laguna, "Circularization and final spin in eccentric binary-black-hole inspirals", Phys. Rev. D **77**, 081502 (2008).

[550] J. M. B. Downing, M. J. Benacquista, M. Giersz, and R. Spurzem, "Compact binaries in star clusters – ii. escapers and detection rates", Monthly Notices of the Royal Astronomical Society **416**, 133–147 (2011).

[551] C. L. Rodriguez, M. Morscher, B. Pattabiraman, S. Chatterjee, C.-J. Haster, and F. A. Rasio, "Binary Black Hole Mergers from Globular Clusters: Implications for Advanced LIGO", Phys. Rev. Lett. **115**, [Erratum: Phys.Rev.Lett. 116, 029901 (2016)], 051101 (2015).

[552] D. Chattopadhyay, J. Stegmann, F. Antonini, J. Barber, and I. M. Romero-Shaw, "Double black hole mergers in nuclear star clusters: eccentricities, spins, masses, and the growth of massive seeds", Mon. Not. Roy. Astron. Soc. **526**, 4908–4928 (2023).

[553] M. C. Miller and D. P. Hamilton, "Four-body effects in globular cluster black hole coalescence", Astrophys. J. **576**, 894 (2002).

[554] J. Samsing, M. MacLeod, and E. Ramirez-Ruiz, "The Formation of Eccentric Compact Binary Inspirals and the Role of Gravitational Wave Emission in Binary-Single Stellar Encounters", Astrophys. J. **784**, 71 (2014).

[555] P. Mahapatra, D. Chattopadhyay, A. Gupta, F. Antonini, M. Favata, B. S. Sathyaprakash, and K. G. Arun, "Possible binary neutron star merger history of the primary of GW230529", (2025).

[556] K. Silsbee and S. Tremaine, "Lidov-Kozai Cycles with Gravitational Radiation: Merging Black Holes in Isolated Triple Systems", Astrophys. J. **836**, 39 (2017).

[557] T. O. Kimpson, M. Spera, M. Mapelli, and B. M. Ziosi, "Hierarchical black hole triples in young star clusters: impact of Kozai–Lidov resonance on mergers", Mon. Not. Roy. Astron. Soc. **463**, 2443–2452 (2016).

[558] B.-M. Hoang, S. Naoz, B. Kocsis, F. A. Rasio, and F. Dosopoulou, "Black Hole Mergers in Galactic Nuclei Induced by the Eccentric Kozai–Lidov Effect", Astrophys. J. **856**, 140 (2018).

[559] M. Zevin, I. M. Romero-Shaw, K. Kremer, E. Thrane, and P. D. Lasky, "Implications of Eccentric Observations on Binary Black Hole Formation Channels", Astrophys. J. Lett. **921**, L43 (2021).

[560] M. Zeeshan and R. O'Shaughnessy, "Eccentricity matters: Impact of eccentricity on inferred binary black hole populations", Phys. Rev. D **110**, 063009 (2024).

[561] I. M. Romero-Shaw, N. Farrow, S. Stevenson, E. Thrane, and X.-J. Zhu, "On the origin of GW190425", Mon. Not. Roy. Astron. Soc. **496**, L64–L69 (2020).

[562] A. K. Lenon, A. H. Nitz, and D. A. Brown, "Measuring the eccentricity of GW170817 and GW190425", Mon. Not. Roy. Astron. Soc. **497**, 1966–1971 (2020).

[563] T. Yamamoto, M. Shibata, and K. Taniguchi, "Simulating coalescing compact binaries by a new code SACRA", Phys. Rev. D **78**, 064054 (2008).

[564] M. Thierfelder, S. Bernuzzi, and B. Bruegmann, "Numerical relativity simulations of binary neutron stars", Phys. Rev. D **84**, 044012 (2011).

[565] F. Foucart, M. D. Duez, L. E. Kidder, S. M. Nissanke, H. P. Pfeiffer, and M. A. Scheel, "Numerical simulations of neutron star-black hole binaries in the near-equal-mass regime", Phys. Rev. D **99**, 103025 (2019).

[566] L. Barack, "Gravitational self force in extreme mass-ratio inspirals", Class. Quant. Grav. **26**, 213001 (2009).

[567] E. Rantsiou, S. Kobayashi, P. Laguna, and F. Rasio, "Mergers of Black Hole - Neutron Star binaries. 1. Methods and First Results", Astrophys. J. **680**, 1326 (2008).

[568] M. Shibata and K. Taniguchi, "Merger of black hole and neutron star in general relativity: Tidal disruption, torus mass, and gravitational waves", Phys. Rev. D **77**, 084015 (2008).

[569] Z. B. Etienne, Y. T. Liu, V. Paschalidis, and S. L. Shapiro, "General relativistic simulations of black hole-neutron star mergers: Effects of magnetic fields", Phys. Rev. D **85**, 064029 (2012).

[570] F. Foucart, M. D. Duez, L. E. Kidder, and S. A. Teukolsky, "Black hole-neutron star mergers: effects of the orientation of the black hole spin", Phys. Rev. D **83**, 024005 (2011).

[571] K. Kyutoku, H. Okawa, M. Shibata, and K. Taniguchi, "Gravitational waves from spinning black hole-neutron star binaries: dependence on black hole spins and on neutron star equations of state", Phys. Rev. D **84**, 064018 (2011).

[572] F. Pannarale, "Black hole remnant of black hole-neutron star coalescing binaries with arbitrary black hole spin", Phys. Rev. D **89**, 044045 (2014).

[573] F. Foucart, T. Hinderer, and S. Nissanke, "Remnant baryon mass in neutron star-black hole mergers: Predictions for binary neutron star mimickers and rapidly spinning black holes", Phys. Rev. D **98**, 081501 (2018).

[574] F. Foucart, "A brief overview of black hole-neutron star mergers", Front. Astron. Space Sci. **7**, 46 (2020).

[575] Y. Huang, C.-J. Haster, S. Vitale, V. Varma, F. Foucart, and S. Biscoveanu, "Statistical and systematic uncertainties in extracting the source properties of neutron star - black hole binaries with gravitational waves", Phys. Rev. D **103**, 083001 (2021).

[576] A. Gonzalez, R. Gamba, M. Breschi, F. Zappa, G. Carullo, S. Bernuzzi, and A. Nagar, "Numerical-relativity-informed effective-one-body model for black-hole–neutron-star mergers with higher modes and spin precession", Phys. Rev. D **107**, 084026 (2023).

[577] M. Dax, S. R. Green, J. Gair, J. H. Macke, A. Buonanno, and B. Schölkopf, "Real-time gravitational wave science with neural posterior estimation", Phys. Rev. Lett. **127**, 241103 (2021).

[578] J. Skilling, "Nested sampling for general Bayesian computation", Bayesian Analysis **1**, 833–859 (2006).

[579] W. Gropp, E. Lusk, N. Doss, and A. Skjellum, "A high-performance, portable implementation of the MPI message passing interface standard", Parallel Computing **22**, 789–828 (1996).

[580] T. L. Collaboration, *Data release for gw200105_162426 and gw200115_042309*, 2021.

[581] T. L. Collaboration, *Data release for gw230529_181500*, 2025.

[582] J. E. Thompson, E. Fauchon-Jones, S. Khan, E. Nitoglia, F. Pannarale, T. Dietrich, and M. Hannam, "Modeling the gravitational wave signature of neutron star black hole coalescences", Physical Review D **101**, 124059, 124059 (2020).

[583] M. d. L. Planas, S. Husa, A. Ramos-Buades, and J. Valencia, *Data release for article: First eccentric inspiral-merger-ringdown analysis of neutron star-black hole mergers*, 2025.

[584] N. J. Cornish, T. B. Littenberg, B. Bécsy, K. Chatziioannou, J. A. Clark, S. Ghonge, and M. Millhouse, "BayesWave analysis pipeline in the era of gravitational wave observations", Phys. Rev. D **103**, 044006 (2021).

[585] C. Shannon, “Communication in the Presence of Noise”, Proceedings of the IRE **37**, 10–21 (1949).